Max-Planck-Institut für Meteorologie
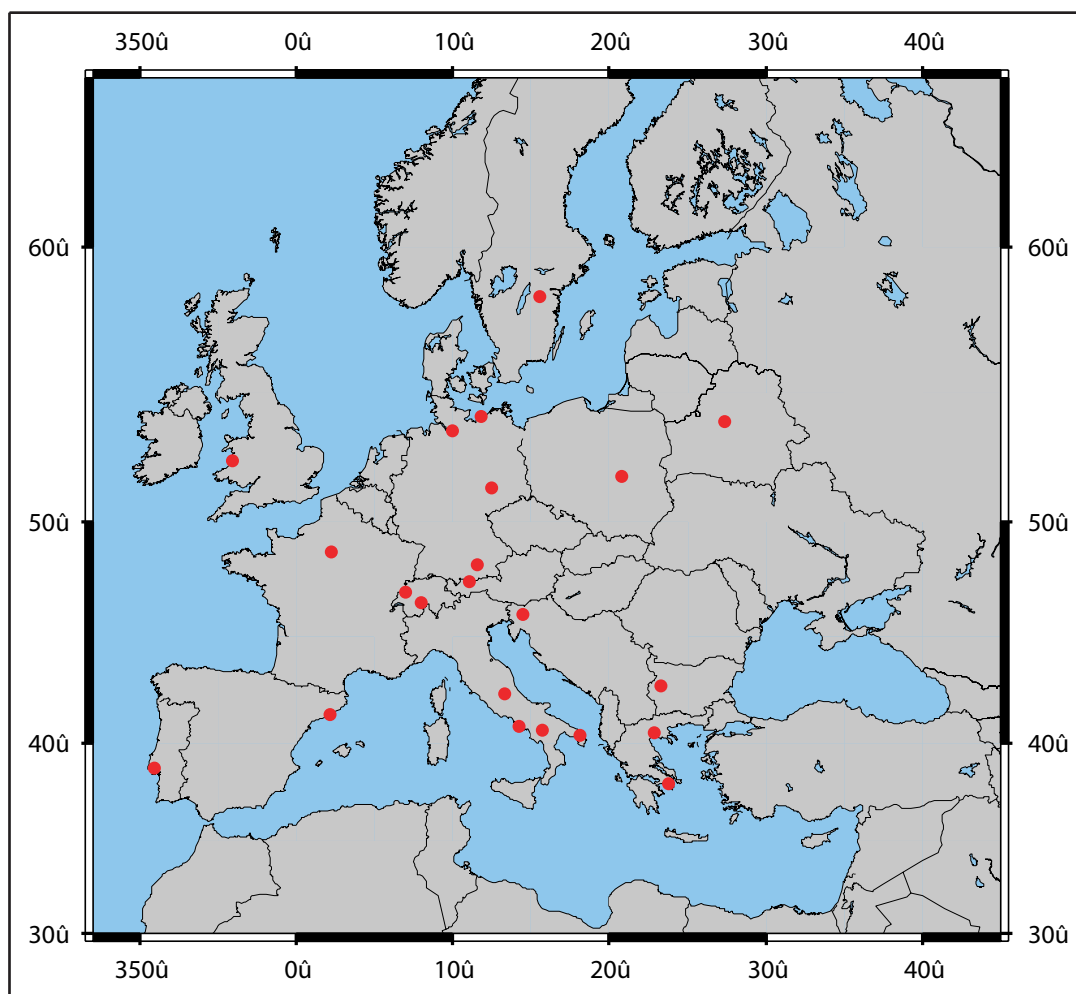*Max Planck Institute for Meteorology*

Report No. 348

EARLINET:
A European Aerosol Research Lidar Network
to Establish an Aerosol Climatology

by

Jens Bösenberg • Volker Matthias • et al.

Authors

J. Bösenberg, H. Linné, V. Matthias

Max-Planck Institut für Meteorologie

C. Böckmann, I. Mironova, L. Schneidenbach, A. Kirsche, A. Mekler

Universität Potsdam, Institut für Mathematik, Potsdam, Germany

M. Wiegner, V. Freudenthaler, I. Stachlewska, W. Kumpf

Meteorologisches Institut der Maximilians-Universität, München, Germany

G. Pappalardo, A. Amodeo, L. Mona, M. Pandolfi

Istituto di Metodologie per l'Analisi Ambientale - C.N.R., Tito Scalo (Potenza), Italy

D. Balis, V. Amoiridis, C. Zerefos

Aristotele University of Thessaloniki, Laboratory of Atmospheric Physics, Thessaloniki, Greece

A. Ansmann, I. Mattis, U. Wandinger, D. Müller

Institut für Troposphärenforschung, Leipzig, Germany

N. Spinelli, X. Wang, A. Boselli

Istituto Nazionale per la Fisica della Materia, Complesso Universitario di Monte S. Angelo, Napoli, Italy

A. Chaikovsky

Institute of Physics, National Academy of Sciences of Belarus, Minsk, Minsk, Belarus

A. Comeron, F. Rocadenbosch, C. Pérez, J.M. Baldasano

Universitat Politécnica de Catalunya, Barcelona, Spain

J. Pelon, L. Sauvage

Institut Pierre Simon Laplace, Laboratoire de la Météorologie Dynamique, Palaiseau cedex, France

R. M. Perrone, Ferdinando de Tomasi

Istituto Nazionale per la Fisica della Materia, Universita' di Lecce, Lecce, Italy

R. Eixmann

Leibniz-Institut für Atmosphärenphysik, Kühlungsborn, Germany

V. Mitev, R. Matthey

Observatoire de Neuchâtel, Neuchâtel, Switzerland

A. Hagard, R. Persson, G. Carlsson

FOI, Swedish Defence Research Agency, Division of Sensor Technology, Linköping, Sweden

V. Rizi, M. Iarlori

Universitat Degli Studi - L'Aqulia, Dipartimento di Fisica, L'Aqulia, Italy

G. Vaughan

Physics Department of the University of Wales, Aberystwyth Ceredigion, U.K.

T. Trickl, S. Kreipl, H. Giehl

Fraunhofer Institut für Atmosphärische Umweltforschung, Garmisch Partenkirchen, Germany

V. Simeonov

Ecole Polytechnique Fédérale de Lausanne, ENAC - SSIE, Lausanne, Switzerland

D. P. Resendes, J. A. Rodrigues

Centro de Fisica de Plasmas - Instituto Superior Técnico, Lisboa, Portugal

P. Sobolewski, S. Nickovic, S. Music

Institute of Geophysics, Polish Academy of Sciences, Euro Mediterranean Centre on Insular Coastal Dynamics, University of Malta, La Valletta, Malta

M. Zavrtanik

Polytechnic Nova Gorica, Nova Gorica, Slovenia

D. Stoyanov, I. Grigorov, G. Kolarov

Laser Radars Laboratory, Institute of Electronics, Bulgarian Academy of Sciences, Sofia, Bulgaria

A. Papayannis

National Technical University of Athens, LAG-LIDAR Group, Athens, Greece

EARLINET:
A European Aerosol Research Lidar Network
to Establish an Aerosol Climatology.

J. Bösenberg, V. Matthias, A. Amodeo, V. Amoiridis, A. Ansmann,
J. M. Baldasano, I. Balin, D. Balis, C. Böckmann, A. Boselli, G. Carlsson,
A. Chaikovsky, G. Chourdakis, A. Comerón, F. De Tomasi, R. Eixmann,
V. Freudenthaler, H. Giehl, I. Grigorov, A. Hågård, M. Iarlori, A. Kirsche,
G. Kolarov, L. Komguem, S. Kreipl, W. Kumpf, G. Larchevêque, H. Linné,
R. Matthey, I. Mattis, A. Mekler, I. Mironova, V. Mitev, L. Mona, D. Müller,
S. Music, S. Nickovic, M. Pandolfi, A. Papayannis, G. Pappalardo, J. Pelon,
C. Pérez, R. M. Perrone, R. Persson, D. P. Resendes, V. Rizi, F. Rocadenbosch,
J. A. Rodrigues, L. Sauvage, L. Schneidenbach, R. Schumacher,
V. Shcherbakov, V. Simeonov, P. Sobolewski, N. Spinelli, I. Stachlewska,
D. Stoyanov, T. Trickl, G. Tsaknakis, G. Vaughan, U. Wandinger, X. Wang,
M. Wiegner, M. Zavrtanik, and C. Zerefos

Contents

1 Executive summary

by Jens Bösenberg

1.1 Objectives

The main objectives of EARLINET are the establishment of a comprehensive and quantitative statistical data base of the horizontal and vertical distribution of aerosols on the European scale using a network of advanced laser remote sensing stations, and the use of these data for studies related to the impact of aerosols on a variety of environmental problems. This also includes the creation of a suitable research infrastructure comprising quality controlled instruments and evaluation procedures as well as the establishment of a common data base. Also important is a system of internal communication for exchange of technical know-how and data as well as for the performance of joint analyses using data from several groups.

1.2 Scientific achievements

EARLINET is the first aerosol lidar network which attempts to retrieve quantitative data on the vertical distribution of aerosol optical properties in a systematic and statistically significant approach. Therefore the main effort as well as the main achievements are in the development of methods. Strong emphasis is on making the results from all stations and all times comparable, because this is essential for the use of joint data sets in all studies involving several stations. Regarding the development of methodologies for aerosol lidar networking the major achievements of EARLINET are:

- Advanced lidar systems for regular use are finally implemented at 22 permanent and 3 temporary stations in 12 European countries including the Newly Associated States. A large part of Europe is thus covered by the observation network. 13 stations are now using detection channels for Raman scattering to retrieve aerosol extinction quantitatively rather than crudely estimating it from attenuated backscatter measurements. With respect to the quantitative retrieval of optical properties this is a major improvement compared to the standard approach with simple backscatter lidar measurements. It is also important because it provides key information for the retrieval of aerosol microphysical properties. Detailed information about the system properties is documented in a "Handbook of Instruments" that is publicly available at the project website *http://lidarb.dkrz.de/earlinet*.

- An extensive quality assurance program at instrument and retrieval algorithm levels was conducted. In spite of the large logistical problems caused by the immobility of most systems almost all lidars have been compared directly. It is for the first time that so many lidar systems have been compared, and considerable progress has been achieved in the idenfication of possible problems in system components and operation procedures. All algorithms for backscatter retrieval from lidar signals have undergone a rigorous intercomparison procedure based on synthetic lidar signals. In the beginning the exercise revealed several problems in various aspects of the implementation, finally it resulted in considerable improvement of results for practically all groups. It was also demonstrated again that backscatter measurements alone are not sufficient for achieving high quality optical properties for aerosols: large discrepancies occur in the results from different researchers in the corresponding parts of the retrievals where

the required information about the aerosol properties had to be guessed. The algorithms to retrieve aerosol extinction from Raman measurements were tested using a similar approach. Here it was mainly the assessment of temporal and vertical resolution in combination with remaining statistical errors that caused initial discrepancies in the results, but the problems were solved so that now well established procedures for this important task exist.

- A schedule is established for making the measurements on the one hand in a way to minimize bias in statistical evaluations due to selective measurement conditions, and on the other hand to make special measurements for various dedicated studies. For establishing an aerosol climatology a regular schedule is chosen with 3 measurements per week at preselected times. For the special measurements dedicated to various process studies an alerting system is established which is used by the corresponding work package leaders to inform the relevant groups about important measurement opportunities. About 30% of all profiles are collected on the regular schedule, the remainder is dedicated to special studies, to a large part with many stations observing simultaneously. Examples for such special measurements are given below.

- For the lidar profiles from all stations a data base is established that is suitable for automated processing. A common platform independent file format is used, the files containing either profiles or time series of profiles are prepared and made accessible by the individual institutions. These files are collected in a common data base which is automatically updated every night. Automatic check procedures are installed to increase data consistency and compatibility. Controlled access to these data by all participants and by approved external users is provided.

- To provide important information about the history of the observed air mass back-trajectories were compiled for each station, 2 daily arrival times, and 6 pressure levels. They are provided by the German Weather Service on the basis of the hourly wind fields of the global weather prediction model. This important support is gratefully acknowledged by the EARLINET community. All trajectories are stored in a data base and tools are provided to access and use these data. For special studies trajectories with higher resolution, flexible arrival times and levels, and longer history were obtained through cooperation with the group of A. Stohl (TU München).

  An adaption of cluster analysis is developed for application to all trajectories ending at a single station. In this way the typical transport patterns are identified. Correlation with observed aerosol load shows that only a small fraction of the aerosol variability can be explained simply by transport patterns. Obviously other features of the air mass history play a major role, too, so that more sophisticated modeling is needed to explain or predict the aerosol load.

- Sophisticated algorithms are developed to extract information on the aerosol microphysical properties from multi-wavelength lidar profiles. Minimum requirements on the distribution of measurement wavelengths, type of observation, and accuracy are derived. Results show that independent extinction measurements are mandatory for a retrieval of microphysical parameters. They show further that for a moderate system using the 3 emission wavelengths of a Nd:YAG laser in combination with Raman measurements at 2 wavelengths a microphysical retrieval with adequate accuracy is feasible. These important new results have been verified using data from the network. A special report describing details of the underlying mathematics and the practical implementation is published.

- A lidar network is a valuable instrument for ground truthing of satellite retrievals of the aerosol distribution. The high variability of aerosol profiles observed in EARLINET is identified as a major problem for direct intercomparisons, at least for instruments having coarse horizontal resolution like limb sounders. Nevertheless data were collected to provide ground truth for ENVISAT and SAGE III. Very unfortunately the carefully prepared intercomparison with a high resolution sounder, CHRIS on PROBA, was cancelled because of satellite failure. Radiative transfer calculations revealed that the aerosol type and abundance affect the radiance at the top of the atmosphere significantly. The vertical layer structure is equally important whenever layers with different aerosol properties exist. The analysis of data from spaceborne optical sensors which are used for many purposes often requires corrections for aerosols. Our results show that these depend on the vertical structure and type of aerosol so that information from a lidar network can be very beneficial for the analysis.

Special data sets are collected for process studies addressing various topics such as Saharan dust, forest fires, urban photosmog, volcanic aerosol from the Mount Etna eruption, stratospheric aerosols, diurnal cycles, differences between rural and urban aerosol distributions, and cirrus clouds. Data collection targeted at these studies was very successful, but of course the analysis is not complete so shortly after the data collection phase. The main results, which in part are preliminary only, are:

- A very large data set of Saharan dust observations is established covering 85 cases of dust outbreaks over the Mediterranean. In the first part of the project it was recognised that dust transport to regions north of the Alps occurred more often than expected, so finally 19 stations were involved in the measurement program instead of the 8 stations planned initially. About 50 events are documented at the most prominent stations in the Mediterranean, of course for higher latitudes the number of cases was much smaller. It is for the first time that sufficient material is collected to establish a statistically significant distribution of Saharan dust over Europe, including the seasonal dependence. Significant amounts of dust were found in elevated layers up to about 5km over the Mediterranean and up to 7km north of the Alps. The material is also used to assess the major pathways of dust transport, to compare with satellite observations, and to validate an advanced dust transport model. Forecasts based on the analysis of a variety of observational and modeling results were very successful, leading to an excellent success rate for the alerting system.

- For one selected case the observations of Saharan dust outbreaks are used to compare with the results of an advanced regional dust forecast model (DREAM). The agreement of model output and measurements is generally good, both for the column amount and the profile characteristics. This indicates that advanced models are likely to be useful in quantifying the impact of Saharan dust on the aerosol load over Europe. Comparisons for cases are necessary to confirm this results, the necessary data are available.

- Aerosol layers generated by wild fires were observed in many cases (174 profiles). The importance of long range transport, e.g. from North America, is confirmed. The pyrogenic aerosols originating from large fires in Russia and Belarus are well characterised by observations.

- Detailed studies of the aerosol layer over the city of Athens during smog episodes, covering the temporal and spatial development as well as the optical properties, clearly demonstrated the importance of photochemistry for its formation.

8

- The eruption of Mount Etna triggered intensive observations at the nearby stations. The flow pattern happened to be such that none of the stations could observe the volcano plume directly, but layers with enhanced aerosol load were observed some time after the eruption and were identified as volcanic aerosol using backtrajectories. However, because of the prevailing southward flow pattern it was not possible to quantify the importance of these probably secondary aerosols.

- Observations of stratospheric aerosols are routinely performed at 8 stations including Garmisch-Partenkirchen where the long term record starting in 1976 was continued. The initial objective was to use these stations for investigations of the fine structure of stratospheric aerosol layers. However, it happened that at the start of the project the stratospheric aerosol load was rather low and continued to decrease. So there was no chance to observe fine structures as intended, but the opportunity was taken to assess the background level of stratospheric aerosol unaffected by major volcano eruptions.

- A common procedure is established to retrieve the height of the boundary layer from lidar data. This parameter is now routinely reported in the data from many stations at least for the cases where the idenfication appears reliable. Since this parameter is important for transport studies of many substances the data set is considered very valuable for corresponding model validation. Measurements extending over a large part of the day were coordinated for up to 11 stations under weather conditions where no distortions by frontal passages were expected. Typical patterns for the development of the ABL are derived and growth rates are determined. Local effects, e.g. induced by special orography, are identified for several stations.

- Differences between rural und urban aerosols are explored using additional measurements in the vicinity of big cities (Paris, Hamburg, Athens). On the average only minor spatial variations are observed, but in individual cases differences can be large with no obvious explanation. The measurements inside the cities are found to be representative for a larger urban and suburban area unless special orography has a major influence on the flow pattern.

- Local orographic wind systems have major influence on the aerosol vertical distribution, examples are Barcelona, Athens (both also influenced by land-sea-breeze effects), Neuchâtel, and Garmisch-Partenkirchen. The observations confirm the injection of boundary layer air into the free troposphere induced by orography. In particular in the Alpine region the wind field can be very complex and extensive dedicated studies are required to explain the upward transport of aerosol from the PBL to the FT in sufficient detail.

- An analysis of selected cases demonstrates that aerosols can be transported over large distances. At present mainly the major pathways are established, a quantification of the impact of long range transport is not yet attempted. Long range transport is frequently observed and takes place in elevated layers (typ. 2- 5 km asl). Intercontinental transport, usually from North America, can also occur at higher altitudes (5-8 km). Compared to the PBL, only a small fraction of aerosol can be found in higher altitudes and the occurance of aerosol layers in the FT is mostly connected with single events like wild fires or Saharan dust outbreaks.

The dataset that was collected on a regular schedule is used for statistical analyses and, in conjunction with additional non-lidar measurements for other important studies. The main results obtained so far are:

- A combination of lidar observations and spectrophotometer measurements in the UV is used to assess the impact of aerosols on the UV radiation field. The importance of information about the single scattering albedo of the aerosol is demonstrated, and procedures are developed to improve the retrievals of this parameter from the combined measurements. The accuracy of calculated radiation fields is significantly enhanced.

- A new method is developed to estimate the average impact of Western Europe on the aerosol load which is based on the combined use of backtrajectories and aerosol profiles from selected stations. A very significant increase of the aerosol load from the western coast line to the eastern continental sites is observed, reflected in both increased backscatter coefficient and extension of the dust layer. Seasonal dependence is assessed and major source regions are identified.

- The ratio of aerosol extinction to backscatter, the so called lidar ratio, is derived from independent measurements of the backscatter and extinction coefficient. From the observations at 10 stations the first statistically significant data set on the distribution of this parameter is established, which is very important for the characterization of the aerosol type (it depends mainly on microphysical parameters), and is vitally important for the estimation of aerosol extinction from pure backscatter lidar measurements. Presently planned spaceborne lidar retrievals of aerosol extinction depend completely on information about the applicable lidar ratio for the observed aerosol type. The statistical distribution of the lidar ratio is broad for all stations, occasionally even exceeding the range from 10 to 100sr. Mean values range from 32sr to 76sr. No significant dependence on season is observed, and simple sector analysis fails to explain the variability. Correlation with air mass origin looks more promising as expected from the dependence of the lidar ratio on aerosol microphysics. The results demonstrate again that only independent measurements of aerosol extinction can yield reliable values, estimates from backscatter measurements have a very large uncertainty, depending on the available information about the aerosol microphysics.

- Main statistical properties of the temporal and spatial distribution of boundary layer heights and aerosol extinction are derived. The boundary layer height shows a sinusoidal annual cycle for almost all stations, but the scatter for individual cases is very large. The distribution function is close to Gaussian, mean and standard deviation are derived for many stations. For the aerosol optical depth (AOD) the distribution shows large scatter as well, the distribution function is close to lognormal. AOD for the boundary layer is similar for northern and southern European stations, but southern stations show significantly larger AOD in upper layers. Correlation of the time series at different stations is high only for very small distances, e.g. 0.96 for a distance of 25km, but decreases rapidly and is not significant for distances larger than some 100km. This is in accordance with the generally large scatter observed in aerosol fields.

1.3 Socio-economic relevance and policy implications

The main achievement is the installation of a network providing the aerosol vertical distribution based on homogeneous, quality controlled procedures. It is for the first time worldwide that such a network is established, and this contributes significantly to enhanced understanding of the aerosol distribution, the processes controlling it, and the impact of aerosol on human life.

Because aerosol plays a role in many atmospheric processes there is a large number of research areas that need to be addressed by special studies, not all of which are actually covered within EARLINET. To mention just a few:

- observations of the aerosol distribution allow to retrieve boundary layer characteristics, which in turn are most important for the distribution of pollutants.

- Studies of Saharan dust outbreaks allow to address directly the mechanisms of mineral dust formation, long range transport, and impact on solar radiation and climate. Using the particles as tracers also serves to study long range transport of many other pollutants.

- Observations of the modification of aerosol properties when air masses pass over Europe provide excellent material to improve air pollution and climate prediction models, and thus help to develop abatement strategies.

- Observations of elevated aerosol layers in combination with trajectory analysis permit to study long range transport of pollutants on a hemispherical scale. Again this is important material to improve air pollution and climate prediction models.

- The development of methods to retrieve microphysical properties of aerosol will lead to a much better characterization of the aerosol distribution, providing additional information about the composition and origin of the particles. This will help to identify major sources of aerosol and hence support the development of suitable abatement strategies.

Apart from the individual studies that have been initialized on the basis of the large data set, an important achievement of the project is the establishment of a real network with fairly homogeneous operation, evaluation, and analysis procedures and with comparable and well assessed data quality, despite of the widely varying starting conditions for the participating groups. It is also emphasized that very good cooperation is achieved. It is now standard that several groups perform coordinated measurements for special purposes, and that data from several groups are used for joint analyses. Thus a new community is formed that is truly European, spanning a major part of the continent including the Newly Associated States. It is particularly encouraging to see a large number of young scientists involved, demonstrating the transfer of know-how between different groups as well as between generations. EARLINET has turned out as an excellent training ground for the application of high-tech methodology to environmental problems.

1.4   Conclusions

The project has made very good progress in many areas of research. An infrastructure has been developed that is truly unique worldwide. The selection of measurement methods, the extensive quality control, and the establishment of a common data base served to create an excellent basis for a wide range of scientific studies related to the vertical distribution of aerosols.
The strategy for setting up the network operation has proven successful, only minor modifications were necessary. The suitability of the collected data for the intended studies has been demonstrated. New methodology for the using the unique data set is being developed, first preliminary results have become available.
EARLINET and the institutions that are active within this project have contributed significantly to the making Europe the leader in a broad and important area of aerosol studies and related applications. The project has also contributed to strengthen the European capabilities in the trendsetting area of laser remote sensing of the atmosphere.

2 Hardware setup

by Jens Bösenberg

2.1 Objective

The main goal of this work package, the preparation of lidar systems at all sites for regularly scheduled operation as well as for special observations, has already been reached about three months after the beginning of the project. However, to achieve a very early start for establishing an aerosol climatology over a long period of time some compromises had to be made regarding the technical properties of the systems which were quite different when the project was initialized. This was due to the fact that only previously existing systems were used. In the course of the project opportunities were taken to install a number of important upgrades. In addition, with the project extension to the Newly Associated States (NAS), 3 additional stations were brought into operation, again whithin very short time.

2.2 Approach

For the establishment of a climatological data set of the aerosol vertical distribution on a continental scale it is required that a rather large number of stations is operated and that the data taken at different stations or different times are comparable. Considering the limited resources and the limited project period it was necessary to make use of existing lidar equipment and operation by groups with experienced lidar researchers. It was also necessary to resort to quantitative lidar methods to the largest possible extent, and to apply strict quality control (treated in a separate dedicated work package).

The most widely used lidar technique, the pure backscatter lidar, certainly has the advantages of being the simplest lidar measurement and coming as a byproduct of more sophisticated methods anyway. But it also has the disadvantage of being not quantitative, the 2 unknowns, backscatter and extinction coefficients, cannot be retrieved unambigously from a single measurement. It is only appropriate to retrieve backscatter for layers with small optical depth, e.g. in rather clean areas of the upper troposphere or the stratosphere. The aerosol extinction, which is the more important parameter in aerosol research, can only be estimated when microphysical parameters of the aerosol are known. The results of this project demonstrate very clearly that the necessary parameter for the conversion from backscatter to extinction is highly variable and can hardly be guessed reliably unless detailed knowledge about the aerosol composition is available.

Two lidar methods have been used in this project to make quantitative retrievals of aerosol optical properties: Raman scattering from nitrogen and multi-angle measurements. The Raman technique is used now at !? stations and serves as the backbone for quantitative measurements.

In the multi-angle method the extinction is calculated from the signals measured at different zenith angles. When sufficient temporal averaging is applied it may be assumed under many conditions that the aerosol properties are the same for both directions. The set of two lidar equations can be solved directly to yield extinction and backscatter profiles. This method is also used at some stations, and is considered particularly useful for longer wavelengths where Raman scattering is too weak. Two stations made regular use of this technique, although some others have the necessary beam steering capabilities.

2.3   Achievements

At almost all stations the lidar systems were ready for operation as scheduled. The details of the used instruments are described in the handbook of instruments which has been published in September 2000 and which is available at *http://lidarb.dkrz.de/earlinet*. Table 1 provides an overview over the present status of the hardware at the individual stations. Comparison with the status at the beginning of the project reveals that substantial progress has been made in the installation of Raman measurement capabilities which have turned out as the backbone of quantitative aerosol profiling. Fourteen stations presently have the possibility to determine true extinction profiles independently from backscatter profiles.

A total of 22 permanent plus 3 temporary stations in 13 countries covering a large part of Europe including NAS are operational and contribute actively to the measurement program. This is a real success!

Station	ab	at	at.2	ba	gp	hh	hb	ju	kb	la	lc	le	li	lk	mi	mi.2	mu	mu.2	na	ne	pl	po	th	be	ng	sf	sf.2
Detection channels																											
elastic backscatter																											
UV	x	x			x	x	x	x	x	x	x	x		x			x	u	x	x		x	u		x		
VIS		x	u	u	x	x		x	x			x	u		x	x	x			x	x	x	u	x		x	x
IR				x	x	x		x	x			x	x		x	x	x			x	x		x				
N$_2$ Raman scattering																											
UV	x	x			x			x	x	x	x	x							x	u		x	u				
VIS				u				u	x			x															
water vapor channel	x					u		x		x	u	x															
liquid water channel									u																		
temperature channel								u	x			x															
depolarisation channel								x	x			x								x	x						
Other system parameters																											
scanning capability				x	x								x	x	x	x	x	x						x	x	x	
system transportable			x	x	x	x							x	x	x	x	x	x			x						
alt. limit low / m	0.5	0.5	0.5	.25	0.2	0.3	0.3	4.0	1.0	0.3	0.4	0.3	0.3	0.1	0.1	0.5	0.2	0.07	.25	1.0	0.5	1.2	0.7	0.2	0.4	0.4	1.0
alt. limit high / m	8.0	12.0	5.0	10.	10.	10.0	9.0	11.	35.	12.	7.0	12.	5.0	10.	30.	10.	5.0	15.0	3.0	10.	15.	8.0	8.0	10.0	5.0	5.0	10.0
range res. (raw) / m	30	15	7.5	7.5	15	15	15	7.5	50	300	15	60	1.5	7.5	15	15	3.75	7.5	15	30	15	15	7.5	7.5	7.5	120	150
time res. (raw) / s	330	300	360	1800	10	10	10	100	33	300	180	30	1	.1	10	200	0.1	60	60	200	10	60	240	1	1	ng	ng

Table 1: Overview over main system characteristics. x = existing at beginning, u = upgrade during project, ng = not given

ab	Aberystwyth	at	Athens
hb	Hamburg-Bergedorf	ju	Jungfraujoch
le	Leipzig	li	Lisboa
na	Napoli	ne	Neuchâtel
be	Belsk	ng	Nova Gorica

ab Aberystwyth   at Athens   ba Barcelona   gp Garmisch-Partenkirchen   hh Hamburg

hb Hamburg-Bergedorf   ju Jungfraujoch   kb Kühlungsborn   la L'Aquila   lc Lecce

le Leipzig   li Lisboa   lk Linköping   mi Minsk   mu München

na Napoli   ne Neuchâtel   pl Palaiseau   po Potenza   th Thessaloniki

be Belsk   ng Nova Gorica   sf Sofia

3 Regular measurements

by Jens Bösenberg

3.1 Objective

The goal of this work package is the establishment of a comprehensive climatological database of the vertical distribution of aerosol over all stations of the network.

3.2 Scientific Achievements

In order to establish a climatological data set it is required that measurements are made under a broad range of meteorological conditions. It is one of the important advantages of lidar over passive remote sensing methods that it can yield reliable results even in case of the presence of complex cloud fields which are variable in height and extension. In order to minimize the bias in the results due to the selection of specific measurement conditions the climatological data set is collected on a regular schedule on preselected dates, regardless of weather conditions. If weather conditions do not permit lidar operation during the scheduled period, e.g. due to rain, fog, or low clouds, this fact is noted in the data record, thus providing a statistics of occasions when aerosols do not play a major role for most atmospheric processes. The selected schedule of 3 measurement per week on 2 different days (Mondays at noontime and at sunset, Thursdays at sunset) turned out very appropriate. With the present status of instruments and the available manpower the selected schedule was about the maximum that could be achieved on a regular basis, considering that many requests for special measurements came from other work packages.

The main achievement is that regularly scheduled measurements to establish the aerosol climatology have been performed at all stations, although with some differences in the resulting number of profiles. Mainly this is due to restrictions caused by weather (low clouds or precipitation), but some interruptions have been caused by other events, ranging from system breakdown over unavailability of personnel to blockage of premises by students on strike. However, the overall performance is good, the part of the data set addressing the regular measurements comprises 5435 profiles, and about 30% of them are accompanied by independent measurements of aerosol extinction. This is by far the largest data set on the aerosol vertical distribution, and it is the only one which is collected systematically and is covering a whole continent.

4 Quality Assurance

Homogeneous and well established data quality is one of the key conditions for the combined use of data originating from different systems. Because the establishment of a joint dataset and its use in comparative studies are major objectives of EARLINET, specific attention is given to data quality assurance. Comparisons have been performed on algorithm and system level. The algorithms have been tested in two separate excercises, one for the backscatter algorithms and one for the extinction algorithms starting from Raman lidar measurements.

4.1 System intercomparison

by Volker Matthias

The performance of the individual instruments has been tested in several intercomparison experiments. Two lidar systems which already had been compared during the LACE 98 field campaign (Ansmann, 2002) served as "standard systems". EARLINET lidar systems had to meet predefined quality criteria when being compared to these standards.

4.1.1 Organisation

Because most of the EARLINET lidar systems are not transportable, it was not possible to perform one large intercomparison experiment with all the instruments at one site. Instead, the lidar systems from MPI Hamburg and University of Munich travelled to several different lidar sites to perform simultaneous measurements with the local lidars. Both systems are emitting three laser wavelengths at 355 nm, 532 nm and 1064 nm. The MPI lidar is additionally equipped with a UV Raman channel to derive aerosol extinction profiles.

The intercomparison procedure can be followed in the diagram in Figure 1. Most of the comparisons have been performed with the instruments from Hamburg and Munich. Additionally, instruments which passed the quality assurance could serve as standard systems themselves and test the performance of other systems. This has been used for the second round of intercomparisons in 2002, which was necessary because two instruments (from LMD and IST) did not fulfill the quality criteria from the beginning. Additionally, the lidar on Jungfraujoch has been compared to the very compact microlidar from OCN, because it is impossible to bring a larger system to that mountain station.

An exception to this quality assurance procedure has been made for the group from Minsk. It was regarded virtually impossible to go there with a lidar system and therefore internal intercomparisons performed by two different systems (one for the lower troposphere and one for the upper troposphere and stratosphere) have been accepted as quality test for this station.

In 2002, the EARLINET project could be extended by three new lidar stations. Groups from Belsk/Poland, Nova Gorica/Slovenia and Sofia/Bulgaria came into the project and performed additional lidar observations. These systems have undergone a different quality control procedure. The Belsk lidar has been built by the lidar group from Minsk. Regular technical inspections and also the data evaluation are done by them. Data from Belsk has been sent to the EARLINET data base since October 2000, so a first check of the system performance could be done already from the quality of the profiles stored in the data base. The EARLINET quality assurance has here been done by inspection of the lidar system by an experienced lidar scientist.

The lidar from Slovenia has been compared to a new portable system from Munich, which makes intercomparisons which much lower logistical effort possible. The Bulgarian group performed internal intercomparisons, similar to what has been done in Minsk. Their systems operate at 510 nm
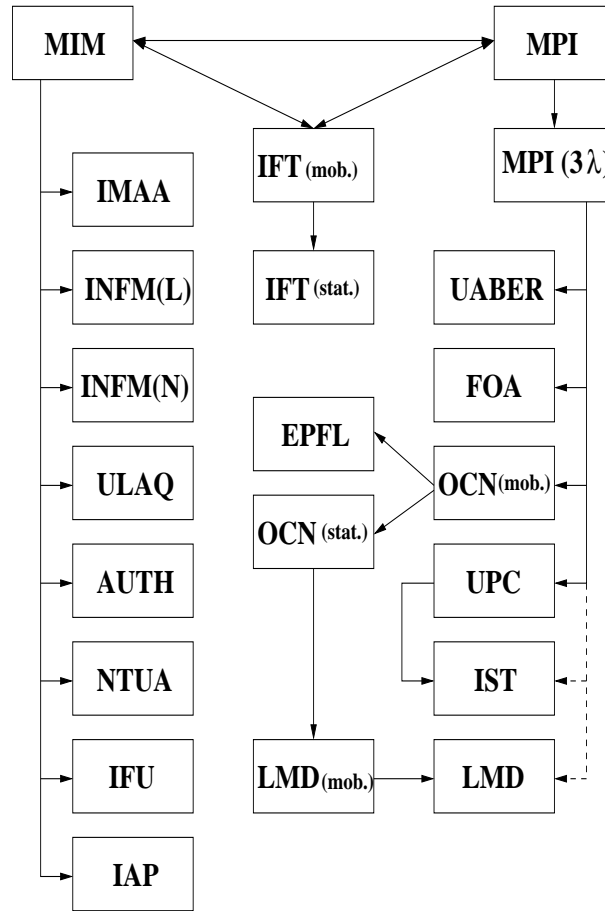
Figure 1: Diagram of intercomparison experiments performed for the EARLINET quality assurance.

and 532 nm, respectively. Therefore intercomparisons of those systems in in common height ranges are possible.

Beneath the lidar intercomparisons, the systems from MPI and IFT have also been compared to optical depth measurements performed either by a sun photometer or a star photometer for night time measurements.

4.1.2 Quality criteria

The quality criteria have been fixed before the intercomparisons started and all groups agreed on reaching those values. They have been defined on the basis of results which have been achieved during the LACE experiment and on typical statistical errors of lidar measurements. All values are given in Table 2. Compared quantities were (if measured):

- aerosol backscatter at 355 nm, 532 nm and 1064 nm

- aerosol extinction at 355 nm

- aerosol optical depth (in comparison with sun photometer)

All values for the maximum allowed deviations are given in Table 2. They had to be fulfilled for at least three different periods with significant aerosol load in the dust layer. Also the minimum height

17

Table 2: Maximum deviations allowed for the different compared quantities during the lidar inter-comparison experiments.

quantity	mean deviation	std. deviation	min. height interval
aerosol extinction (355 nm)	$< 20\ \% \ / \ 5 \cdot 10^{-5} \mathrm{m}^{-1}$	$< 25\ \% \ / \ 1 \cdot 10^{-4} \mathrm{m}^{-1}$	1000 m
aerosol backscatter (355 nm)	$< 20\ \% \ / \ 5 \cdot 10^{-7} (\mathrm{m} \cdot \mathrm{sr})^{-1}$	$< 25\ \% \ / \ 5 \cdot 10^{-7} (\mathrm{m} \cdot \mathrm{sr})^{-1}$	2000 m
aerosol backscatter (532 nm)	$< 20\ \% \ / \ 5 \cdot 10^{-7} (\mathrm{m} \cdot \mathrm{sr})^{-1}$	$< 25\ \% \ / \ 5 \cdot 10^{-7} (\mathrm{m} \cdot \mathrm{sr})^{-1}$	2000 m
aerosol backscatter (1064 nm)	$< 30\ \% \ / \ 5 \cdot 10^{-7} (\mathrm{m} \cdot \mathrm{sr})^{-1}$	$< 30\ \% \ / \ 5 \cdot 10^{-7} (\mathrm{m} \cdot \mathrm{sr})^{-1}$	2000 m
aerosol optical depth (355 nm)	$< 30\ \% \ / \ 0.1$	$< 30\ \% \ / \ 0.1$	2000 m

interval for the calculation of mean differences and their standard deviation has been prescribed. The aerosol backscatter profiles have been calculated with common lidar ratios and calibration values, for the aerosol extinction, no assumptions have been made. Comparisons of the optical depth between lidar and sun photometer could only be made in cases with stable aerosol distribution to avoid large errors due to the necessary temporal difference between the measurement.

The intercomparison experiments were mainly done for aerosol backscatter profiles. This is due to the fact that Raman lidar systems usually are much larger and more complex than pure backscatter lidars are. The MPI lidar was the only transportable Raman lidar available in this project. This system is built into a 20-feet-container and is not as easy transportable as the Munich system which is built onto a small trailer. Because the main goal was to verify optical setup, alignment and data acquisition systems of the lidars, it is sufficient to test the channels for elastically backscattered light.

4.1.3 Results

All results of the first phase of the intercomparison experiments (up to summer 2001) are documented in Matthias et al. (2002). Some typical results are shown here to illustrate the main findings of the EARLINET quality assurance.

The intercomparisons between the Munich (MIM) and the Napoli (INFM(N)) lidars (Fig. 2) show very good agreement in the range between 1000 m and 4500 m with mean deviations of less than 5 %. In the upper part of the atmosphere, lidar signals generally are very weak which leads to large fluctuations of the calculated aerosol backscatter around zero. The amplitude of the fluctuations depends on lidar system parameters like emitted laser energy, diameter of the receiving mirrors, detector efficiency and preamplifier noise. It can be reduced by further avering in time and/or in space and is not a severe problem on cloud-free days. Under conditions with broken clouds, it can limit the achievable altitude range, if measurements of only few minutes have to be used to probe the whole troposphere.

In the lower range, some deviations can be seen, especially on October 13, 2000. On October 14, 2000 the signals below 1000 m could not be used for the intercomparison. Also the comparisons between MIM and INFM(P) (Fig. 3) show these differences in the low range due to different height regions with full overlap of laser beam and telescope. These differences are typical in the near range and are mainly attributed to incomplete overlap between the laser beam and the field of view of the telescope. There is always a tradeoff between a low height in which full overlap is achieved and a good signal statistics in the uppper range. This is attributed to the high signal dynamics of lidar signals. Some systems use two different telescopes for different height ranges or measurements under different zenith angles to overcome this problem.

The intercomparisons between MPI and the University of Wales in Aberystwyth (UABER) included both aerosol backscatter and extinction measurements at 355 nm. Some results are displayed in Fig.
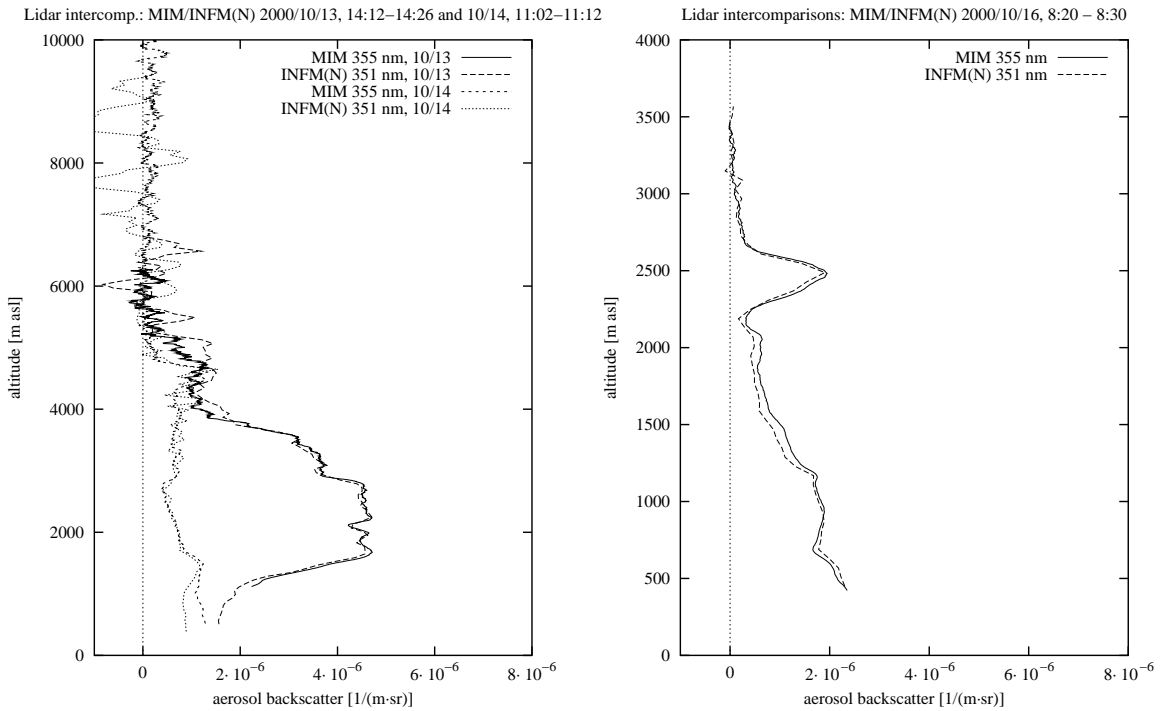
Figure 2: Intercomparison of aerosol backscatter profiles at 351 nm and 355 nm, respectively, between MIM and INFM(N) on October 13, 14 and 16, 2000.
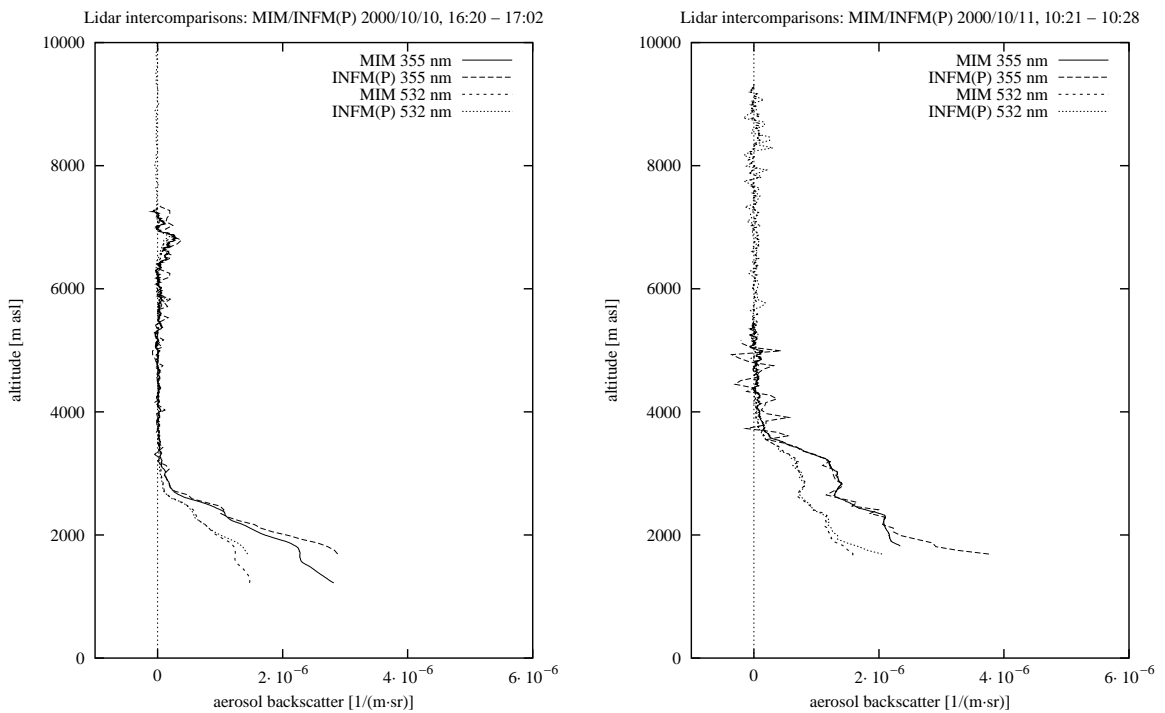

Figure 3: Intercomparison of aerosol backscatter profiles at 355 nm and 532 nm between MIM and INFM(P) on October 10 and 11, 2000.
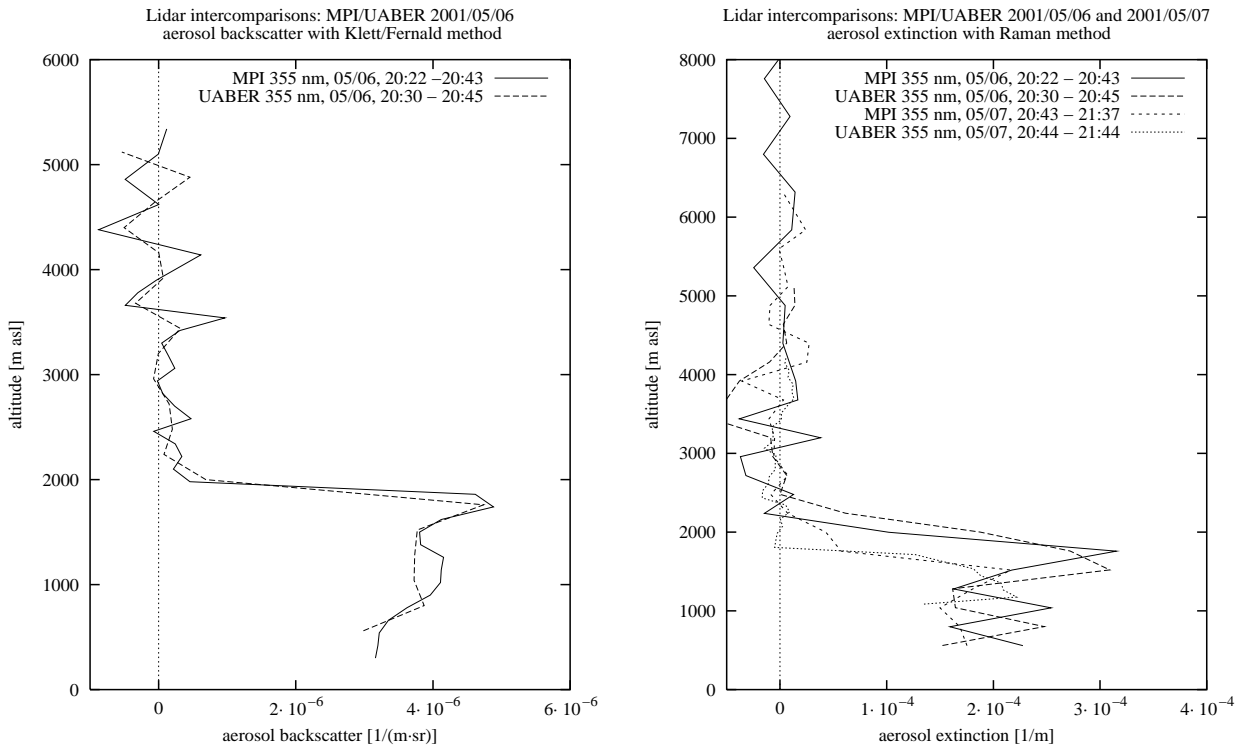
Figure 4: Intercomparison of aerosol backscatter profiles at 355 nm between MPI and UABER on May 8, 2001 and of aerosol extinction profiles on May 6 and 7, 2001.

4. During this intercomparison, measurements have mostly been restricted to nighttime, because the Raman channels can only be operated with very low background light. Additionally, the elastic channels of the UABER lidar operate only in photon counting mode and therefore give best results during nighttime. Most of the profiles shown here are measured with a small near range telescope and limited in range. High standard deviations in the upper heights are due to the low signal level achieved with the small telescope.

Good agreement could be found for the average values of the extinction profiles in the PBL. The standard deviation shows high relative deviations of up to 35 %, but they stay within the predefined maximum absolute deviation of $1.0 \cdot 10^{-4} \mathrm{m}^{-1}$.

Besides the good agreement of the measured profiles, the intercomparison was also successful in determining an adjustment error of the big telescope of UABER which could be corrected after the experiment.

The results of all intercomparison experiments in terms of mean deviation and standard deviation at the individual wavelengths are given in Fig. 5 for the dust layer and in Fig. 6 for the free troposphere. Almost all results stay within the given limits. In those cases where the relative deviations in the dust layer exceeded the predefined threshold, the aerosol backscatter was very low and the absolute deviations stayed within the given limits.

Here also the results from the second round of intercomparisons in 2002, when the new IST lidar has been compared to the Barcelona system and the LMD stationary lidar has been tested via their microlidar (see IC diagram in Fig. 1) are included. These systems passed the quality assurance after major modifications had been applied.

Also the system from the new EARLINET partners from Belsk, Nova Gorica and Sofia passed the quality assurance. High quality of the lidar system could be stated for the Polish system, although

Mean deviations in the dust layer
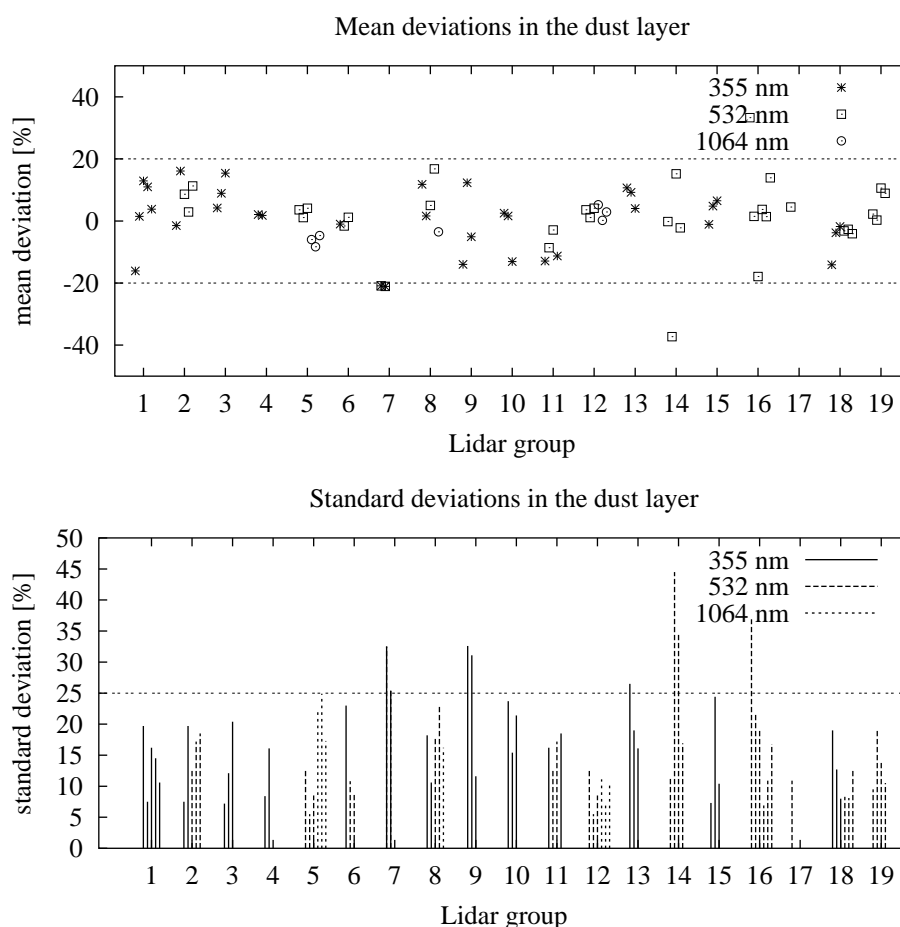

Standard deviations in the dust layer

Figure 5: Mean deviations and standard deviations of all aerosol backscatter intercomparisons in the dust layer. 1: MPI, 2: MIM, 3: UABER, 4: NTUA, 5: UPC, 6: IFU, 7: EPFL, 8: IAP, 9: ULAQ, 10: INFM(L), 11: IFT, 12: IST, 13: FOI, 14: IPNANB, 15: INFM(N), 16: OCN, 17: LMD, 18: IMAA, 19: AUTH.

some recommendations have been given for further improvements, especially of the data acquisition. Comparisons of the lidar from Slovenia to the Munich portable lidar (POLIS) gave sufficiently good results in the upper troposphere, however the system can only be operated at nighttime and the data acquisition via the existing oscilloscope shows clear limitations. Reconstructions are necessary and will be applied to participate in EARLINET also in the future. The system will then be tested again, similar to the two lidars from Sofia. At this stage internal intercomparisons have been accepted as quality control for Sofia. In two cases from summer 2002 the mean and standard deviations stayed within the given limits. Nevertheless direct measurements at the location of the lidar systems give a better impression on the quality of the lidar and are therefore the preferred measure of quality control, also in the future.

Comparisons of optical depth between lidar and photometer could only been done once during the EARLINET period. In September 2000, the integrated extinction profile from the MPI Raman lidar has been compared to the sunphotometer from Palaiseau (Fig. 7). The intercomparisons suffered from the time difference of 3-4 hours and the different wavelengths used for the measurement. The Palaiseau photometer is only equipped with for channels between 440 nm and 1020 nm while the lidar profile is taken at 355 nm. An extrapolation of the sunphotometer optical depth into the UV
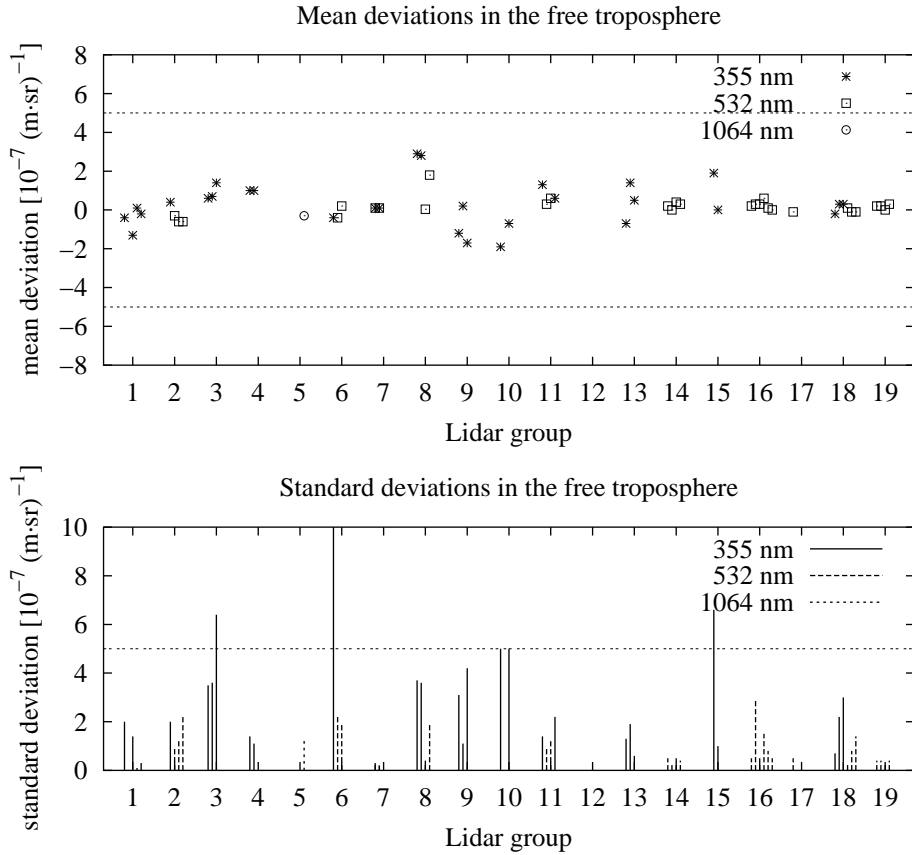
Figure 6: Mean deviations and standard deviations of all aerosol backscatter intercomparisons in the free troposphere. 1: MPI, 2: MIM, 3: UABER, 4: NTUA, 5: UPC, 6: IFU, 7: EPFL, 8: IAP, 9: ULAQ, 10: INFM(L), 11: IFT, 12: IST, 13: FOI, 14: IPNANB, 15: INFM(N), 16: OCN, 17: LMD, 18: IMAA, 19: AUTH.

using the Ångstrøm coefficient which fits best between 440 nm and 1020 nm had to be applied. Nevertheless the comparison shows relatively good agreement. Other cases from the LACE experiment are shown in Wandinger et al. (2002a) and Matthias et al. (2003).

4.2 Aerosol backscatter lidar algorithm intercomparison

by Christine Böckmann

4.2.1 Principle of backscatter coefficient retrieval from lidar signals

The basis of any lidar signal analysis is the lidar equation which describes the receiver signal as a function of atmospheric and system parameters. The lidar equation in its simplest form is valid for quasimonochromatic emission of the laser light, instantaneous scattering, and negligible multiple scattering and coherence:

$$P(\lambda, z) = P_0(\lambda) C \frac{O(z)}{z^2} \beta(\lambda, z) \exp\left(-2 \int_0^z \alpha(\lambda, \zeta) \, \mathrm{d}\zeta\right) \qquad (1)$$

22

Intercomparison of sunphotometer optical depth with Raman lidar optical depth, Palaiseau 2000/09/11 and 2000/09/14

Palaiseau Sunphotometer 2000/09/11, average 15:50 − 16:51 UT ○
Fit to Sunphototmeter 2000/09/11, k = 0.92 ——
MPI Lidar 2000/09/11 19:04 −20:20 UT ●
Palaiseau Sunphotometer 2000/09/14, average 14:47 − 16:45 UT ▢
Fit to Sunphototmeter 2000/09/14, k = 1.68 - - - - -
MPI Lidar 2000/09/14 18:20 − 19:05 UT ■

Figure 7: Intercomparison of aerosol optical depth measurements with the MPI Raman lidar and the sunphotometer from LMD Palaiseau.

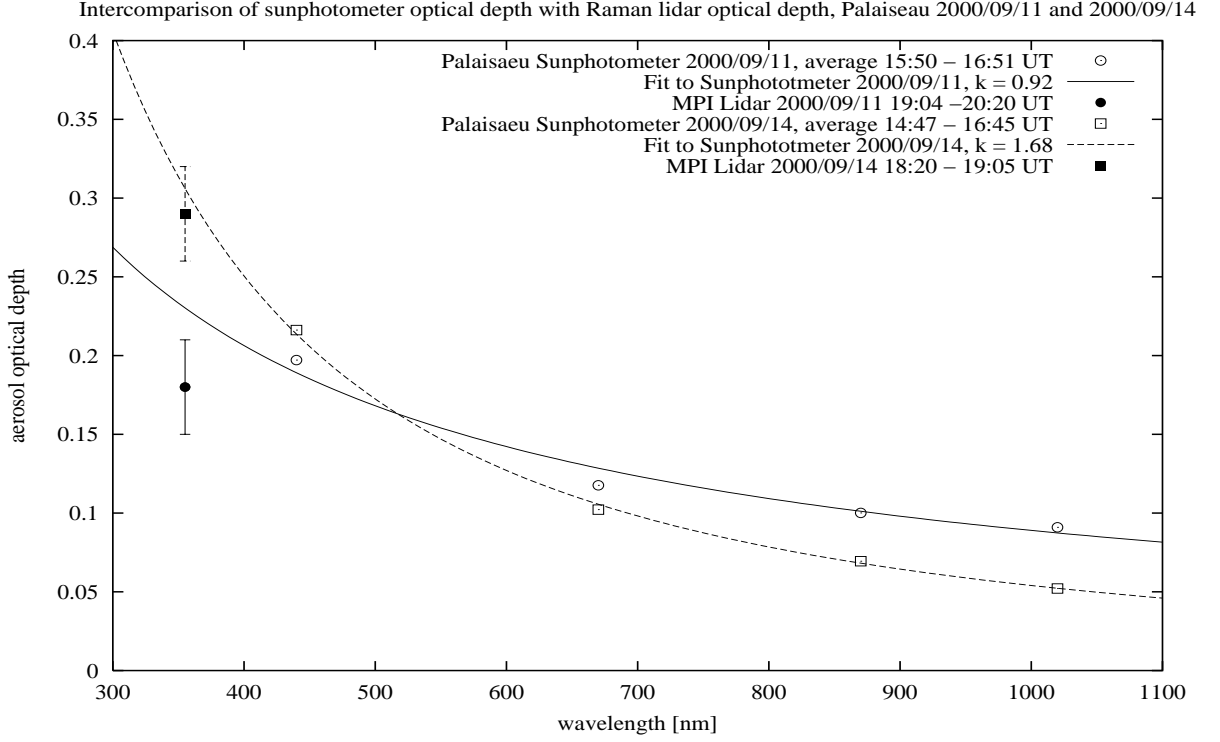where $P(\lambda, z)$ is the backscattered laser power at wavelength λ from range z and $P_0(\lambda)$ is the emitted laser power at wavelength λ. C is the range independent system constant and $O(z)$ the overlap function. $\beta(\lambda, z)$ stands for the backscatter coefficient and $\alpha(\lambda, \zeta)$ for total extinction coefficient. $C = \eta A c \tau_L / 2$ depends on the efficiency η of the detector system, the receiving telescope area A and the pulsewidth of the laser τ_L. c is the velocity of light.

Different methods can be applied to derive aerosol vertical profiles from lidar measurements. If only elastically backscattered light at one laser wavelength is available, aerosol backscatter profiles can only be calculated if assumptions are made about the relation between aerosol extinction and backscatter coefficients (lidar ratio) and for the backscatter coefficient at a calibration range. Because in particular the lidar ratio generally is not sufficiently well known, this method is not really quantitative. However, it is widely used because single wavelength backscatter lidars are the systems that are easiest to operate, and because it is at least a by-product of any lidar measurement.

To solve the lidar equation for one wavelength in the simplest case of no gaseous absorption, it is useful to split the backscatter and extinction in their molecular and aerosol parts and use only that part of the profile where the laser beam fully overlaps with the field of view of the receiving telescope, i.e., $O(z) = 1$,

$$P(\lambda, z) = P_0(\lambda) C \frac{\beta_{aer}(\lambda, z) + \beta_{mol}(\lambda, z)}{z^2} \exp\left(-2 \int_0^z \alpha_{aer}(\lambda, \zeta) + \alpha_{mol}(\lambda, \zeta) \, d\zeta \right) \quad (2)$$

with the extinction coefficient

$$\alpha(\lambda, z) = \alpha_{mol}(\lambda, z) + \alpha_{aer}(\lambda, z) = \alpha_{mol}^{abs}(\lambda, z) + \alpha_{mol}^{sca}(\lambda, z) + \alpha_{aer}^{abs}(\lambda, z) + \alpha_{aer}^{sca}(\lambda, z). \quad (3)$$

23

Assuming the molecular part of this equation can be calculated using standard atmosphere conditions or an atmospheric density profile from nearby launched radiosondes, $\alpha_{aer}(z)$ and $\beta_{aer}(z)$ remain as two height dependent unknowns while one signal has been measured. This problem is usually solved by assuming a (a priori unknown) relationship between aerosol backscatter and extinction. $S_{aer}(\lambda, z) = \alpha_{aer}(\lambda, z)/\beta_{aer}(\lambda, z)$ is usually called the lidar ratio. It is wavelength and height dependent. The determination of $\beta_{aer}(z)$ for one wavelength from Eq. (2) requires the additional assumption of an unknown constant, representing the height independent system parameters. To solve the equation for $\beta_{aer}(z)$, usually a so called calibration or reference value $\beta_{aer}(\lambda, z_0)$ is chosen which prescribes the aerosol backscatter in a certain height z_0.

Under these assumptions, the equation for $\beta_{aer}(z)$ can be solved following Klett (1981) and Fernald (1984). One gets for all heights where $z_0 > z$, i.e., calibration in the far range,

$$
\beta_{aer}(z) = -\beta_{mol}(z) +
$$
$$
\frac{P(z)z^2 \exp\left[-2(S_{aer} - S_{mol}) \int_0^z \beta_{mol}(\zeta)\, \mathrm{d}\zeta\right]}{P_0 C - 2 S_{aer} \int_0^z P(\zeta)\zeta^2 \exp[-2(S_{aer} - S_{mol}) \int_0^\zeta \beta_{mol}(z')\, \mathrm{d}z']\, \mathrm{d}\zeta} \qquad . \tag{4}
$$

where $S_{mol} = \alpha_{mol}(\lambda, z)/\beta_{mol}(\lambda, z) = 8\pi/3$. Calibration in height z_0 gives the system constants $P_0(\lambda)C$. Writing $X(z) = P(z)z^2$ gives

$$
\beta_{aer}(z) = -\beta_{mol}(z) +
$$
$$
\frac{X(z) \exp\left[-2(S_{aer} - S_{mol}) \int_{z_0}^z \beta_{mol}(\zeta)\, \mathrm{d}\zeta\right]}{\frac{X(z_0)}{\beta_{aer}(z_0)+\beta_{mol}(z_0)} - 2 S_{aer} \int_{z_0}^z X(\zeta) \exp[-2(S_{aer} - S_{mol}) \int_{z_0}^\zeta \beta_{mol}(z')\, \mathrm{d}z']\, \mathrm{d}\zeta} \qquad . \tag{5}
$$

This equation can then be solved iteratively down- or upward from z_0. Molecular absorption is neglected here. Molecular scattering can be calculated from

$$
\alpha_{mol}^{sca}(z, \lambda; p, T) = \frac{8\pi^3 (m_{air}^2 - 1)^2}{3\lambda^4 N_S^2} \frac{6 + 3\gamma}{6 - 7\gamma} N_S \frac{T_0}{p_0} \frac{p(z)}{T(z)} \tag{6}
$$

with the refractive index of the air m_{air}, the depolarization factor γ (γ is 0.0301, 0.0284 and 0.0273 for 350, 550 and 1000 nm, respectively), and the molecular number density N_s= 2.547×10^{19}cm^{-3} for standard atmospheric conditions at ground level (p_0=1013.25 hPa, T_0=15°C, 0.03% CO_2). Profiles of temperature $T(z)$ and pressure $p(z)$ are taken from actual radiosonde measurements or from a standard atmosphere with actual ground values of temperature and pressure (Edlen, 1953; Bodhaine et al., 1999). We emphasize once again that two unknown quantities, the particle lidar ratio and the particle backscatter coefficient $\beta_{aer}(z_0)$ at a suitable reference height z_0, have to be estimated in the determination of the particle backscatter-coefficient profile after Eq. (5). The numerical application of Eq. (5) has been discussed in the literature as Fernald or Klett algorithm for more than 20 years. Contributions to the problem are also given by Sasano et al. (1985) and Bösenberg et al. (1997). They are usually considered in the algorithms.

4.2.2 Data simulation and evaluation procedure

The determination of the particle backscatter coefficient from a single elastic backscatter signal was investigated in the algorithm intercomparison. All participating groups processed three sets of synthetic lidar data using their individual algorithms. Some specific details of the groups' individual algorithms are presented in Table 3. Thereby, synthetic lidar signals were used to test the numerical

(a)
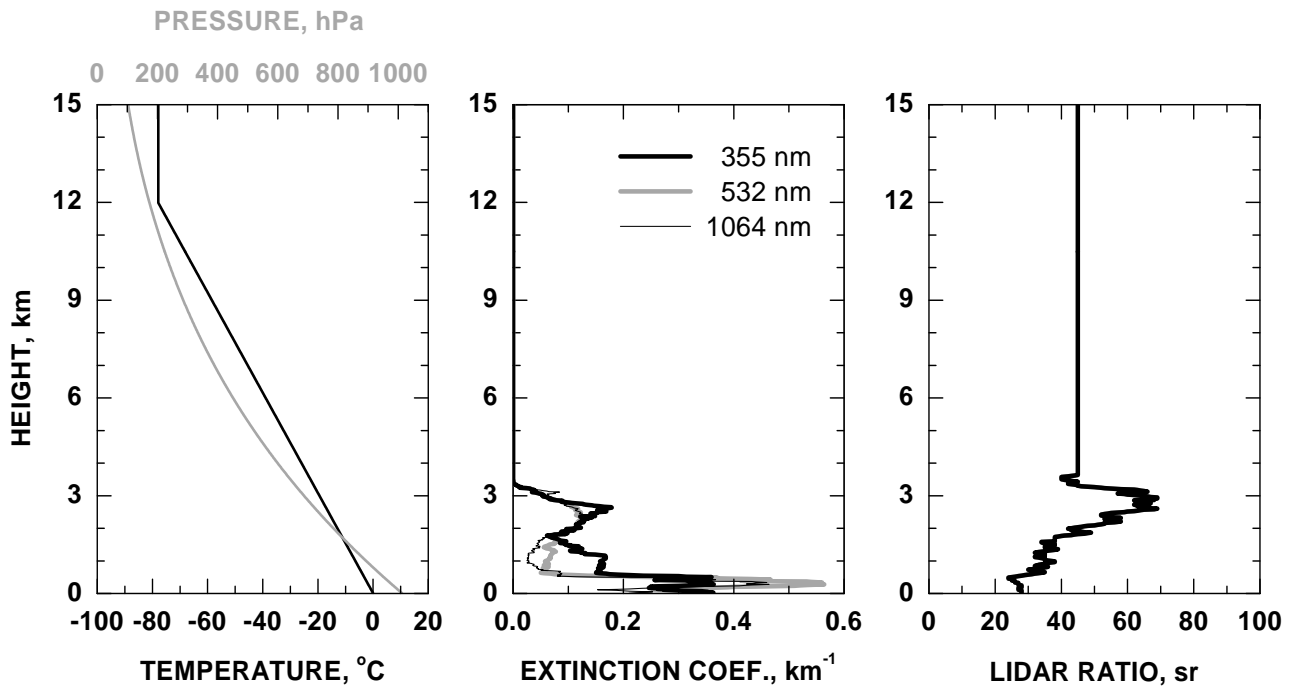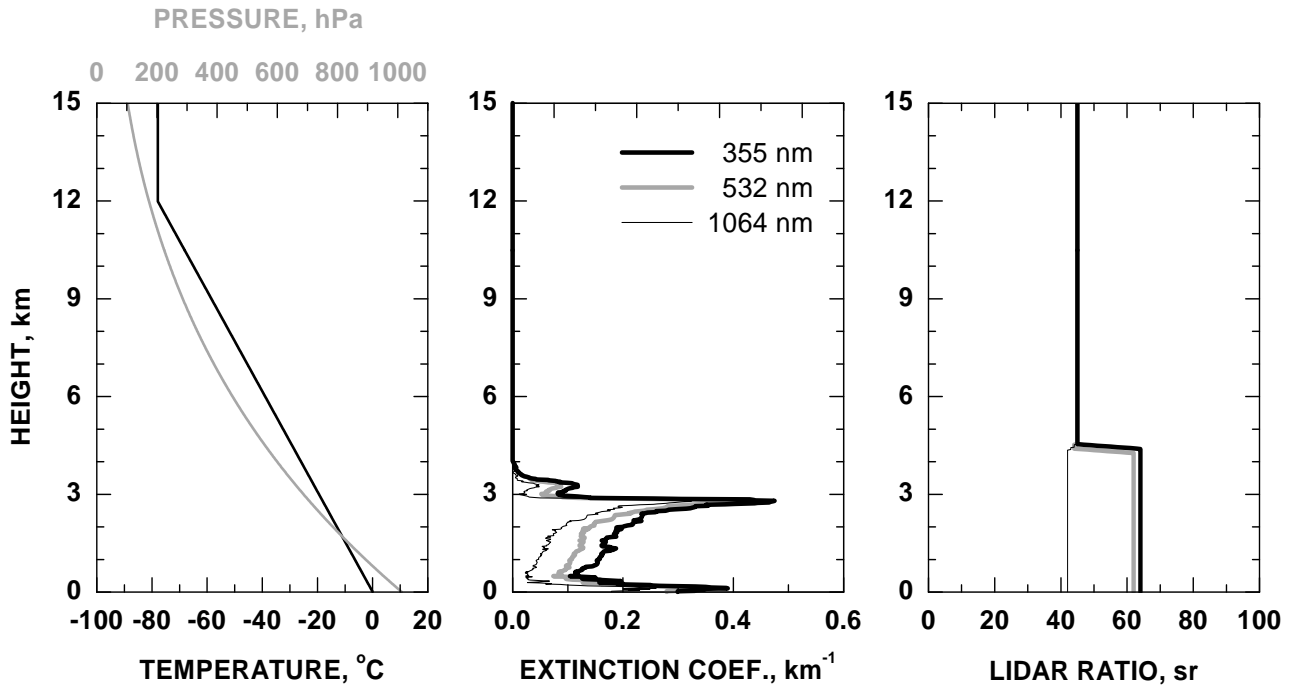
(b)

Figure 8: Input data for (a) simulation case 2 and (b) simulation case 3.

Table 3: Participating groups and capabilities of their processing algorithms: height dependent lidar ratio, both integration directions from the calibration point and possibility to include radiosonde data.

	Lidar group	lidar ratio	integration direction	radio-sonde
A1	École Polytechnique Fédérale de Lausanne, Switzerland	yes	yes	yes
A2	Observatory of Neuchâtel, Switzerland	yes	yes	yes
A3	Institute for Tropospheric Research, Leipzig, Germany	yes	yes	yes
A4	Physics Department, National Technical University of Athens, Greece	yes	no	no
A5	Max-Planck-Institut für Meteorologie, Hamburg, Germany	yes	yes	yes
A6	Leibniz-Institute für Atmosphärenphysik, Kühlungsborn, Germany	yes	yes	yes
A7	Departimento di Fisica, Università degli Studi, L'Aquila, Italy	yes	yes	yes
A8	Institute of Physics, National Academy of Sciences, Minsk, Belarus	yes	yes	yes
A9	Laboratory of Atmospheric Physics, University of Thessaloniki, Greece	yes	yes	yes
A10	Meteorologisches Institut der Universität München, Germany	yes	yes	yes
A11	I.N.F.M., Complesso Universitario di Monte S. Angelo, Napoli, Italy	yes	yes	yes
A12	I.N.F.M., Dipartimento di Fisica, Università di Lecce, Italy	yes	yes	yes
A13	Institut für Meteorologie und Klimaforschung Garmisch-Partenkirchen, Germany	yes	yes	no
A14	Universitat Politècnica de Catalunya, Barcelona, Spain	yes	no	no
A15	Institute Pierre Simone Laplace, Palaiseau cedex, France	yes	yes	yes
A16	Physics Department, University of Wales, Aberystwyth, United Kingdom	yes	yes	yes
A17	Istituto di Metodologie per l'Analisi Ambientale, Potenza, Italy	yes	yes	yes
A18	Division of Sensor Technology, Linköping, Sweden	yes	yes	yes
A19	Centro de Física de Plasmas, Instituto Superior Técnico, Lisboa, Portugal	yes	yes	yes
A20	Laboratory for Astroparticle Physics, Nova Gorica Polytechnic, Slowenia	yes	yes	yes
A21	Institute of Electronics, Bulgarian Academy of Sciences, Sofia, Bulgaria	yes	no	yes
A22	Institute of Geophysics, Polish Academy of Sciences, Warsaw, Poland	yes	yes	yes

correctness and accuracy of the algorithms as well as the experience of the groups and the limits of the method itself. Three examples with different degree of difficulty were calculated with the lidar simulation model of the Institute of Tropospheric Research Leipzig, Germany. The simulations were performed by a person who was not involved in the evaluation of these data for the intercomparison study and the input data were not known to other persons. This software permits to simulate and to evaluate elastically and inelastically backscattered lidar signals at arbitrary wavelengths in dependence on a variety of system parameters for a variable model atmosphere with arbitrary aerosol and cloud layers. Sky background, background noise, and signal noise are considered as well. Atmospheric input parameters are profiles of temperature and pressure to calculate Rayleigh scattering and profiles of extinction coefficients and lidar ratios for the simulation of aerosol and cloud layers. For the algorithm intercomparison three different data sets of elastic backscatter signals at wavelengths of 355, 532, and 1064 nm were simulated. A US standard atmosphere (United States Committee on Extension to the Standard Atmosphere, 1976), with a ground pressure of 1013 hPa and a ground temperature of 0 °C, a tropopause height of 12.0 km, and isothermal conditions above was assumed. The signal profiles were simulated without signal noise. An incomplete overlap of laser beam and receiver field of view below 250 m was introduced. Typical system parameters, e.g., laser power and telescope diameter, were used for the calculations. However, they are not of importance for the algorithm intercomparison.

In all cases, only boundary-layer aerosols in heights below 4.5 km were simulated. Minor particle

scattering in the free troposphere and the stratosphere was introduced and no clouds were considered. The three simulation cases represent different atmospheric conditions with increasing degree of difficulty in data evaluation:

Case 1: The first case did not represent realistic atmospheric conditions. The extinction coefficient was independent of wavelength and changed stepwise from 3×10^{-4} m^{-1} below 1500 m to 3.5×10^{-4} m^{-1} between 1500 and 2000 m and 4×10^{-4} m^{-1} between 2000 and 2440 m, and decreased to values below 10^{-6} m^{-1} above. The lidar ratio had a constant value of 50 sr for all heights and all wavelengths.

Case 2: In the second case, significant aerosol load up to 4000 m was simulated, see Fig. 8(a). A more realistic, height-dependent extinction coefficient was assumed. In addition, the extinction coefficient changed with wavelength, with highest values for the shortest wavelength and lowest values for the longest wavelength. The lidar ratio was height-independent in the aerosol layer, but took different values of 64 sr for 355 nm, 62 sr for 532 nm, and 42 sr for 1064 nm. Above 4500 m the lidar ratio was 45 sr for all wavelengths.

Case 3: In case 3, significant aerosol load up to 3300 m was simulated, see Fig. 8(b). Realistic, height-dependent extinction coefficients and lidar ratios were introduced. The extinction coefficient varied quite differently with wavelength in different heights. The lidar ratio took values between 24 and 69 sr, but did not vary with wavelength. Above 3600 m the lidar ratio was set to 45 sr for all wavelengths.

Case 4: Case 4 is an additional case for the groups which join in the EARLINET community later as mentioned above and will only be briefly discussed. In case 4 a realistic EARLINET evening winter measurement was simulated in central Europe around sunset without clouds, but with a dominating high-pressure system and a variable, visible and stable aerosol layering up to 2000 m. Additionally, a Saharian dust layer, a weak aerosol layer, was simulated between 3000 and 4500 m. Whereas the lower layer showed a strong wavelength dependence of the extinction coefficient for the upper layer it was only weak. The lidar ratio was height- and wavelength-dependent in the aerosol layers, but constantly in each case over certain heigh ranges and took values between 48 and 79 sr or 40 and 65 sr, respectively, for 355 nm or 532 nm. The ground temperature was -2 ºC, the ground pressure 1025 hPa. The measurement lasted 30 min, signal profiles were stored with 2-min and 15-m resolution. Moreover, a realistic signal noise, but no background noise was simulated.

For the first case which is not shown here the input profiles of extinction coefficient and lidar ratio were provided to the participants to allow an exercise with known solutions. Cases 2-4 were used for the intercomparison. The results are discussed here. The procedure of the algorithm intercomparison was as follows.

Stage 1: The simulated signals were distributed to all groups without any information on the input parameters, except the used standard atmosphere. Each group calculated particle backscatter coefficient profiles using their own algorithm.

Stage 2: The prescribed lidar ratio profile was provided to all groups. Evaluation was repeated.

Stage 3: The reference value at calibration height was also provided. Evaluation was repeated.

27

For each stage the results were collected evaluated by the Institute of Mathematics of the Potsdam University, Germany, because this group is not involved in experimental lidar work and acted as the referee. The first stage was the most difficult and most realistic one, because lidar-ratio profiles and reference values were unknown. Therefore, not only the correctness and accuracy of the algorithms was proven but also the dependence of the solution on estimates of the lidar ratio and the reference value. In the third and final stage all parameters were known. So the numerical correctness and stability of the algorithms was definitely tested. The results of each group from each step were compared with the input data in order to determine the systematic errors. They are discussed in the next section.

4.2.3 Intercomparison results

The numerical schemes differ from each other only in some details. Before Eq. (5) can be applied to measured lidar signals, the signals are averaged over the time interval of interest, corrected for background, and usually spatially averaged, i.e., smoothed. For the synthetic data used here, this procedure was not necessary except for case 4. In Table 3, three details of the individual algorithms concerning the following questions are given.

- Is the determination of the backscatter-coefficient profile with height-dependent lidar-ratio S_{aer} possible?

- Is the integration in Eq. 5 in forward and backward direction possible?

- Is it possible to use temperature and pressure values from radiosonde ascent?

Tables 4 – 6 and Figs. 9 to 12 summarize the results of the algorithm intercomparison.

The results for case 2 are shown in detail in the six parts of Fig. 9 and 10 as well as in columns 2 and 3 of Tables 4 – 6. In the first stage, the mean deviations from the correct solution, see Fig. 9 first column, were between 0% and 120%. Especially for the wavelength 355 nm the deviations are very large whereas with increasing wavelength the mean errors become smaller. The mean errors over all groups for the wavelengths of 355, 532, and 1064 nm are about 65%, 30%, and 15%, respectively. In the second stage with known lidar-ratio profile but still unknown reference value the mean deviations from the correct solution, see Fig. 9 second column, become visibly smaller and were approximately between 0%, and 30% only. The mean errors over all groups for the wavelengths of 355, 532, and 1064 nm are about 7%, 5%, and 8%, respectively.
The final stage is shown in Fig. 10 in more detail including relative error profiles. First, with increasing knowledge on the input parameters in stages 2 and 3, the errors decreased to a few percent, in almost all individual algorithms well below 5% for all wavelengths in the range between 0.3075 and 3.4875 km, see Fig. 10 and Tables 4 – 6. The mean error over all groups stays well below 2% for all wavelengths. Second, in the range from 3.5025 to 15.0675 km the mean absolute error over all groups is smaller than $1 \times 10^{-5} (\text{km sr})^{-1}$. Both facts indicate that all algorithms work well and can generally reproduce the simulated profiles of case 2 if all input parameters are known.
Finally, it has to be stated that the retrieval of the backscatter coefficient profile in the range between 0 and 250 m is impossible for these simulations, because an incomplete overlap between the laser beam and the receiver field of view was included in the model. The overlap function was not known by the groups, hence, it could not be corrected for. The simulation of the incomplete overlap should remind the groups that one has to take great care in the near range, i.e., 100 to several 100 m, where

Figure 9: Retrieved particle backscatter-coefficient profiles at all three wavelengths in comparison to the simulation input profiles of example 2 concerning the first stage (a),(c),(e) and the second one (b),(d),(f).

29

Figure 10: Retrieved particle backscatter-coefficient profiles at all three wavelengths in comparison to the simulation input profiles (a),(c),(e) and respective relative errors (b),(d),(f) of example 2 for the third stage.
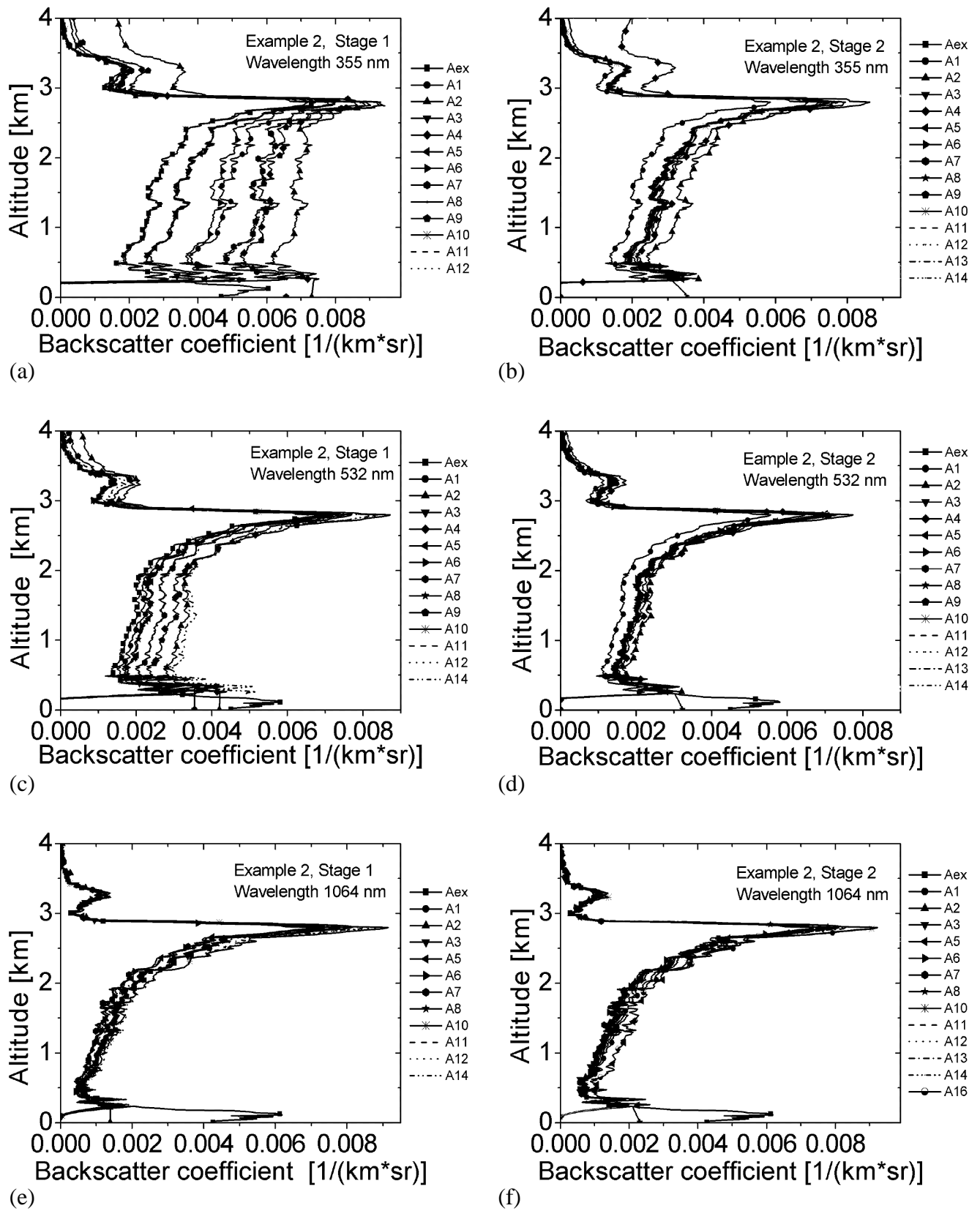
30

Figure 11: Retrieved particle backscatter-coefficient profiles at all three wavelengths in comparison to the simulation input profiles of example 3 concerning the first stage (a),(c),(e) and the second one (b),(d),(f).
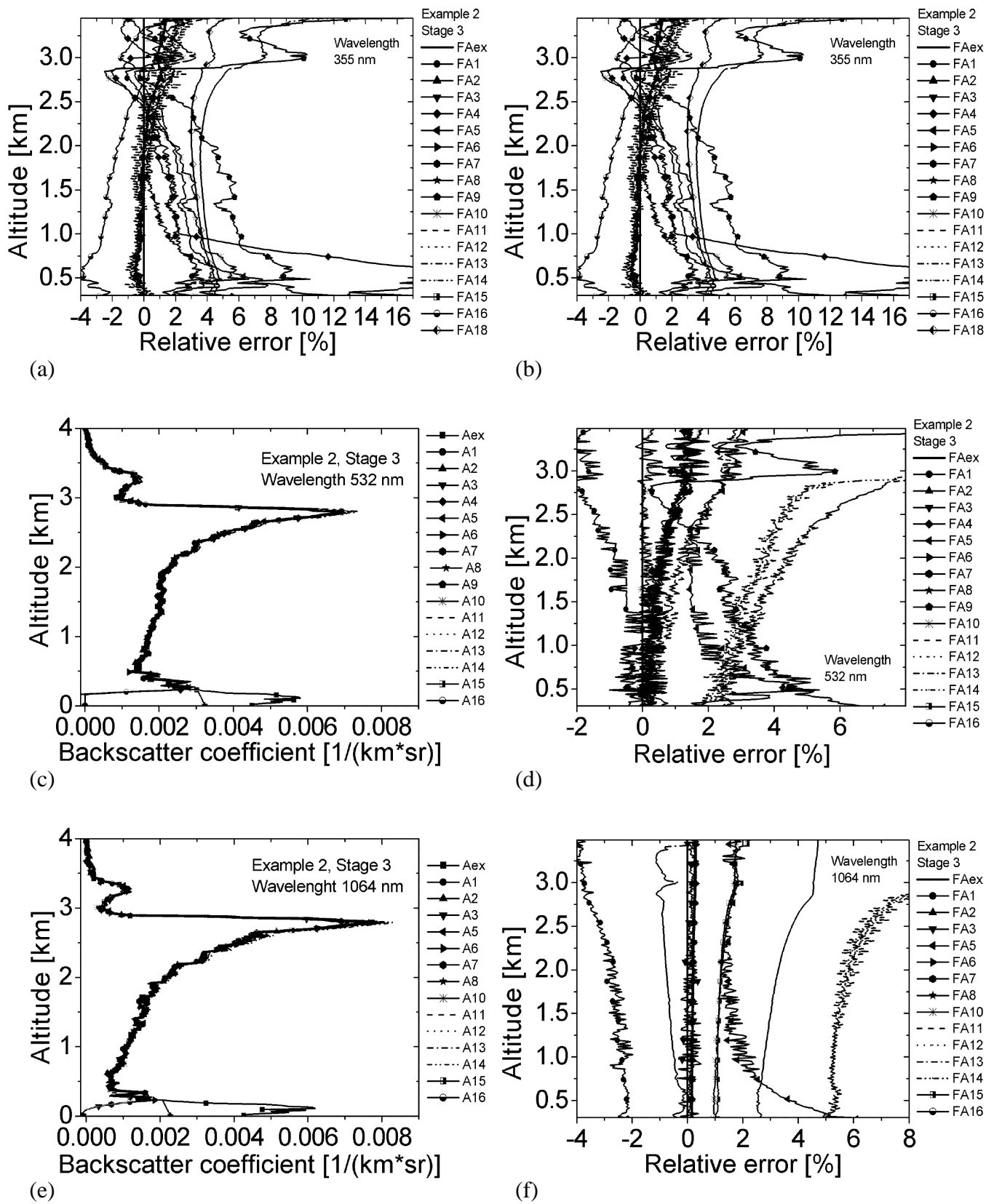
31

Figure 12: Retrieved particle backscatter-coefficient profiles at all three wavelengths in comparison to the simulation input profiles (a),(c),(e) and respective relative errors (b),(d),(f) of example 3 for the third stage.
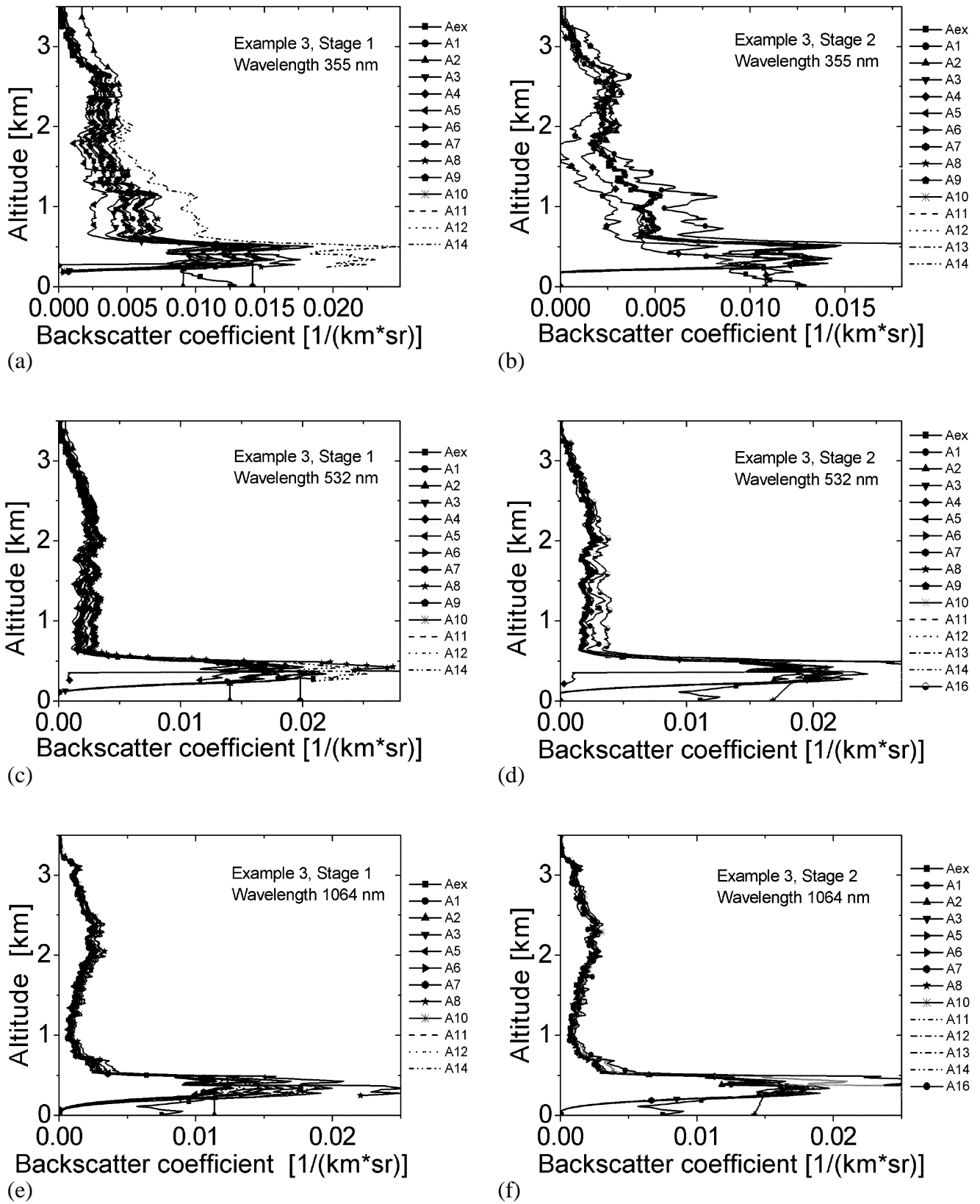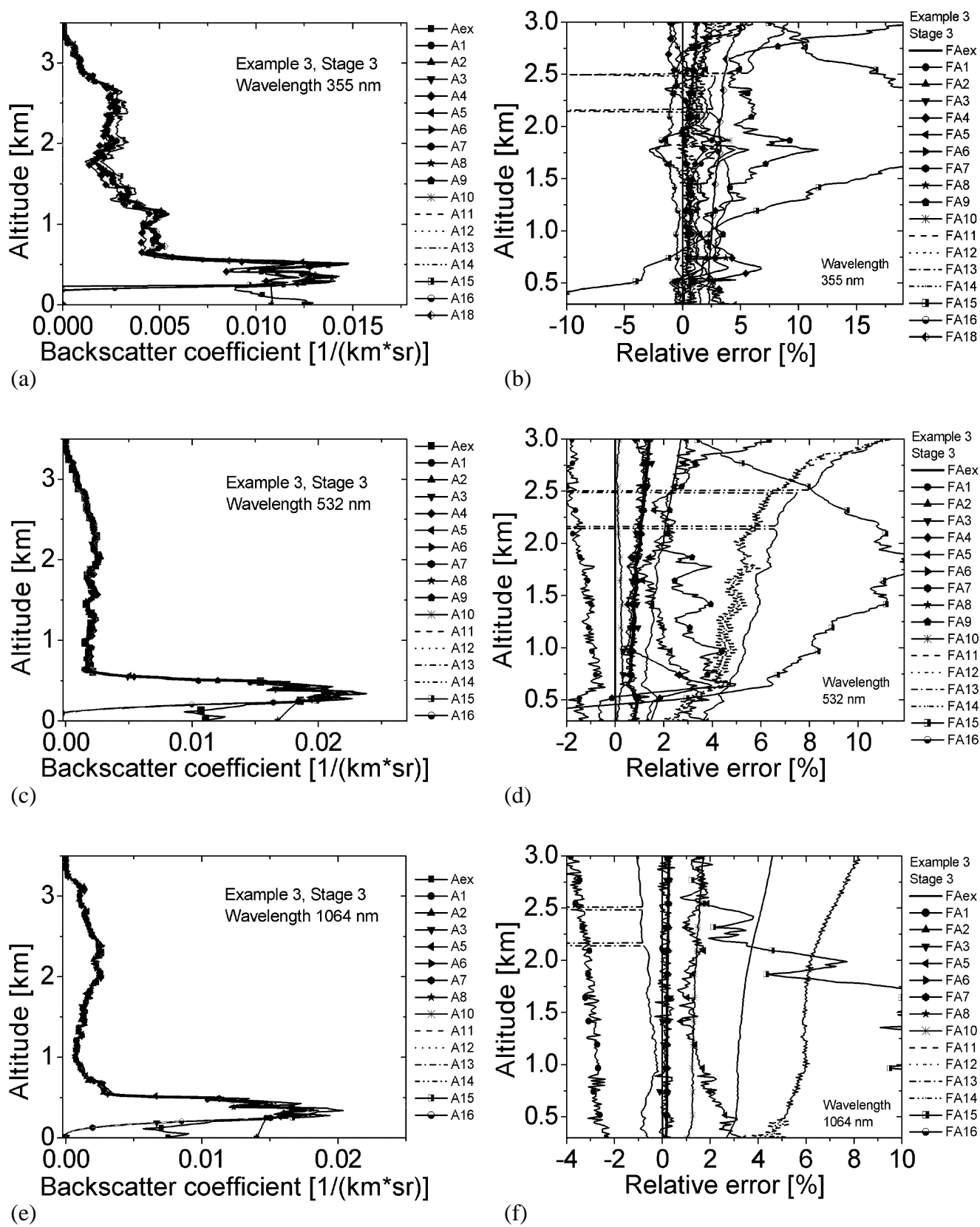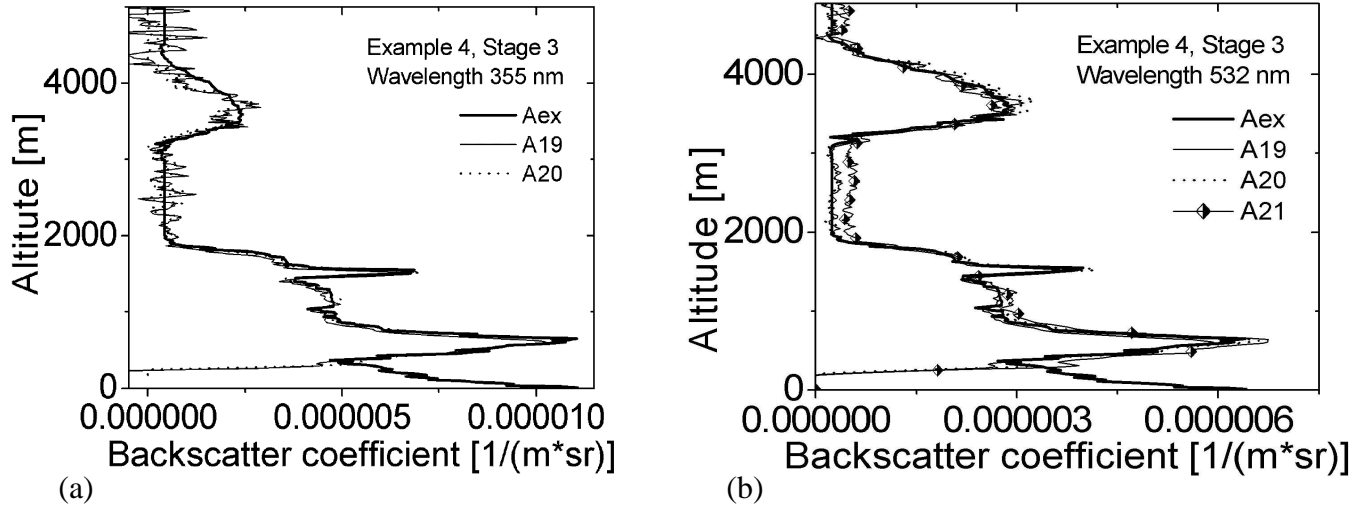
Figure 13: Retrieved particle backscatter-coefficient profiles in comparison to the simulation input profiles for the wavelength 355 nm (a) and for the wavelength 532 nm (b) of case 4 for the third stage.

the overlap function is generally not known.

Table 4: Mean errors of cases 2 and 3 for the wavelength 355 nm in stage 3

	Stage 3: 355 nm			
	Case 2		Case 3	
	mean relative error [%]	mean absolute error [1/(km*sr)]	mean relative error [%]	mean absolute error [1/(km*sr)]
Group	0.3075-3.4875km	3.5025-15.0675km	0.3075-3.0075km	3.0225-15.0675km
A1	1.54±0.91	1.72e-5±1.28e-5	1.01±0.85	1.85e-5±1.41e-5
A2	0.46±0.40	1.43e-7±5.42e-7	0.63±0.29	2.38e-7±1.24e-6
A3	0.45±0.38	3.94e-7±5.42e-7	0.60±0.30	4.94e-7±1.14e-6
A4	3.73±5.65	8.76e-7±2.56e-6	1.39±1.45	1.92e-6±4.73e-6
A5	1.84±2.14	3.91e-6±2.59e-6	1.51±0.79	4.14e-6±3.15e-6
A6	0.46±0.40	2.59e-7±5.20e-7	0.63±0.28	3.43e-7±1.22e-6
A7	0.46±0.40	1.41e-7±5.36e-7	0.63±0.28	2.34e-7±1.22e-6
A8	0.45±0.41	4.27e-7±6.52e-7	0.68±0.47	5.41e-7±1.34e-6
A9	5.57±3.25	2.18e-5±4.62e-5	5.34±3.86	2.89e-5±5.67e-5
A10	2.45±1.56	2.79e-5±2.08e-5	1.58±1.32	2.99e-5±2.26e-5
A11/A17	2.25±1.21	2.28e-5±1.71e-5	1.86±1.21	2.44e-5±1.86e-5
A12	0.45±0.40	2.95e-7±5.76e-7	0.63±0.28	9.31e-7±2.17e-6
A13	4.82±1.85	4.41e-5±1.71e-5	3.76±2.14	3.15e-5±2.58e-5
A14	0.90±0.80	6.73e-5±3.76e-5	0.96±0.72	6.53e-5±3.81e-5
A15	0.48±0.42	2.32e-6±1.42e-6	12.88±8.27	7.44e-6±1.40e-5
A16	1.76±1.05	5.01e-6±4.27e-6	0.72±0.47	5.07e-6±3.81e-6
A18	3.66±0.62	6.65e-6±4.85e-6	3.11±0.72	6.46e-6±5.64e-6
mean values	1.87	1.30e-5	2.23	1.33e-5

33

Table 5: Mean errors of both cases for the wavelenth 532 nm in stage 3

| | Stage 3: 532 nm | | | |
| | Case 2 | | Case 3 | |
Group	mean relative error [%] 0.3075-3.4875km	mean absolute error [1/(km*sr)] 3.5025-15.0675km	mean relative error [%] 0.3075-3.0075km	mean absolute error [1/(km*sr)] 3.0225-15.0675km
A1	0.91±0.72	9.68e-7±1.00e-6	1.36±0.39	1.24e-6±1.80e-6
A2	0.71±0.46	1.16e-7±6.13e-7	0.97±0.23	2.12e-7±1.33e-6
A3	0.62±0.47	2.24e-7±4.92e-7	0.88±0.28	3.32e-7±1.14e-6
A4	0.71±0.48	1.80e-7±5.69e-7	1.17±3.35	2.97e-7±1.28e-6
A5	2.34±1.07	9.97e-7±1.39e-6	2.24±0.66	1.29e-6±2.96e-6
A6	0.72±0.46	1.75e-7±6.20e-7	0.98±0.24	2.74e-7±1.36e-6
A7	0.71±0.46	1.13e-7±6.12e-7	0.97±0.23	2.11e-7±1.34e-6
A8	0.68±0.43	1.23e-7±5.92e-7	0.94±0.23	2.16e-7±1.28e-6
A9	2.90±1.59	5.54e-6±1.22e-5	2.88±3.41	7.31e-6±5.30e-6
A10	0.16±0.14	4.90e-7±4.61e-7	0.19±0.08	5.34e-7±5.04e-7
A11/A17	1.36±0.82	3.98e-7±1.24e-6	1.84±0.44	5.95e-7±2.57e-6
A12	0.70±0.44	1.27e-7±6.04e-7	0.95±0.23	2.14e-7±1.31e-6
A13	5.22±2.73	1.92e-5±1.15e-5	6.39±1.73	1.45e-5±1.65e-5
A14	4.54±2.78	3.44e-5±1.53e-5	5.45±1.78	3.49e-5±1.67e-5
A15	0.81±0.52	2.28e-6±1.91e-6	8.18±2.88	4.36e-6±7.19e-6
A16	0.63±0.46	1.98e-7±7.77e-7	0.90±0.25	3.57e-7±1.70e-6
A18	-	-	-	-
mean values	1.48	4.10e-6	2.27	4.18e-6

The results for case 3, which is a more realistic one with a height dependent lidar ratio but still without statistical noise and without clouds, are shown in Fig. 11, 12 and at Tables 4 – 6 in columns 4 and 5. For the stages 1 and 2 the mean errors are more or less in the same range as for case 2. In detail, the mean errors over all groups for the first stage for the wavelengths of 355, 532, and 1064 nm are approximately 40%, 20%, and 17%, respectively. Moreover, for stage 2 the respective errors are about 10%, 8%, and 7%. For the third stage, the errors are somewhat larger than for case 2, which is mainly caused by the height-dependent lidar ratio. In the range between 0.3075 and 3.0075 km, see Fig. 12 and Tables 4 – 6, the mean error over all groups stays well below 3% for all wavelengths. Only the group A15 has still some problems, especially for the wavelength 355 nm, which have to be improved in the future. In the range from 3.0225 to 15.0675 km the mean absolute error over all groups is smaller than $1 \times 10^{-5} (\mathrm{km\,sr})^{-1}$. Finally, in the range between 0 and 250 m the retrieval of the backscatter coefficient again is impossible because of the unknown overlap function.

The algorithm intercomparison shows that in general the data evaluation schemes of the different groups work well. Differences in the solutions can mainly be attributed to differences in the estimation of input parameters. If the input parameters are known, remaining errors are in the order of a few percent. The unknown height-dependent lidar ratio had the largest influence on the solutions, which demonstrates the need for independent measurements of the particle extinction coefficient, e.g., with the Raman method (Ansmann et al., 1992a). To overcome this problem, independent measurements of the particle extinction coefficient with the Raman method are or will be performed at most of the network stations.

The unknown reference value was of minor importance for the examples presented here, because height regions with dominating Rayleigh scattering were present in all cases. It should be mentioned, however, that this is not necessarily the case under realistic atmospheric conditions. Especially at

Table 6: Mean errors of both cases for the wavelength 1064 nm in stage 3

	Stage 3: 1064 nm			
	Case 2		Case 3	
	mean relative error [%]	mean absolute error [1/(km*sr)]	mean relative error [%]	mean absolute error [1/(km*sr)]
Group	0.3075-3.4875km	3.5025-15.0675km	0.3075-3.0075km	3.0225-15.0675km
A1	2.88±0.60	1.18e-7±7.29e-7	3.05±0.39	7.02e-7±5.10e-6
A2	0.21±0.04	8.89e-9±5.31e-8	0.22±0.03	5.29e-8±3.75e-7
A3	0.15±0.11	1.54e-8±4.81e-8	0.17±0.12	4.95e-8±3.99e-7
A4	-	-	-	-
A5	1.94±0.85	1.01e-7±3.29e-7	1.57±0.55	3.57e-7±2.16e-6
A6	0.22±0.05	1.36e-8±5.59e-8	0.23±0.03	5.80e-8±3.86e-7
A7	0.22±0.04	8.89e-9±5.35e-8	0.22±0.03	5.13e-8±3.72e-7
A8	0.19±0.04	9.86e-9±4.63e-8	0.21±0.04	4.95e-8±3.51e-7
A9	-	-	-	-
A10	1.29±0.27	5.25e-8±3.19e-7	1.38±0.15	3.08e-7±2.23e-6
A11/A17	3.44±0.74	1.37e-7±8.64e-7	3.56±0.50	8.31e-7±6.03e-6
A12	0.23±0.05	9.25e-9±5.61e-8	0.23±0.03	5.42e-8±3.93e-7
A13	0.66±0.27	1.19e-6±7.53e-7	0.83±1.72	1.14e-6±3.33e-6
A14	6.42±1.48	3.05e-6±2.40e-6	6.25±0.87	4.21e-6±1.05e-5
A15	1.31±0.28	1.51e-6±9.12e-7	8.33±5.22	4.35e-6±6.35e-6
A16	0.19±0.04	1.34e-8±6.28e-8	0.19±0.03	7.77e-8±4.28e-7
A18	-	-	-	-
mean values	1.38	4.46e-7	1.89	8.78e-7

1064 nm, particle scattering often dominates the signals in the entire measurement range, which may cause additional errors that are not discussed here.

Case 4, the additional intercomparison, showed more or less the same qualitative behaviour between the stages 1,2 and 3. In Fig. 13 the results of stage 3 for 355 nm and 532 nm show that the data evaluation schemes of the groups A19-A21 works well, too. In detail, the mean relative errors in stage 3 in the ranges between 322.5 and 1987.5 m, i.e., in the lower layer, and between 3217.5 and 3892.5 m, i.e., in the upper layer, are 11.35 ± 12.6 % and 15.2 ± 10.6 % for group A19 and 6.14 ± 8.9 % and 26.8 ± 29.2 % for group A20 concerning the wavelength 355 nm or 7.35 ± 6.3 % and 11.7 ± 16.2 % for group A19, 6.8 ± 6.7 % and 10.8 ± 8.0 % for group A20 and 14.51 ± 19.61 % and 10.96 ± 12.3 % for group A21 concerning the wavelength 532 nm, respectively. The mean relative errors show the same qualitative behaviour as for case 3 with respect to the wavelengths 355 and 532 nm. They are bigger for the smaller one. Furthermore, the errors in general are smaller in the lower layer. In contrast to case 3, case 4 includes additionally realistic signal noise. For this reason the values of the mean relative errors are bigger as for case 3 and therefore, not directly comparable.

Some additional remarks are given now. Firstly, during the algorithm intercomparison some groups developed or improved their algorithms so that a few groups are not present in stages 1 and 2, see Figs. 9,11. Secondly, the groups A4 and A9 use only the wavelengths 355 nm and 532 nm at their lidar stations, the group A18 lidar emits only at 355 nm and the group A21 lidar only at 532 nm. Therefore, they did not perform evaluations at 1064 nm, 532 nm or 355 nm, respectively. Finally, the groups A11 and A17 as well as the groups A8 and A22 used the same algorithm.

4.2.4 Conclusion

The backscatter algorithm intercomparison has been performed in three stages with increasing knowlegde on the necessary input parameters. In stage one neither the necessary reference value nor the height dependent lidar ratio was given. In stage two the prescribed lidar ratio was provided and in stage 3 also the reference value was given. It became again clear that the estimation of the lidar ratio which is required for real measurements has a large effect on the calculated aerosol backscatter profile. The calculated profiles can differ by more than 50 % if no information on the lidar ratio is available. This effect decreases with increasing wavelength. Therefore, independent measurements of the particle extinction coefficient with the Raman method or with a multi-angle scanning technique are urgently necessary.

The effect of the reference value was rather small in the chosen examples, however, at 1064 nm the result can depend strongly on this value which also has to be estimated for real measurements. The errors of the algorithms themselves have been tested in stage 3 with knowledge of all input parameters. The remaining calculation errors in case 2 and 3 stay in the order of 2-4 % and can be regarded as negligible when compared to the uncertainties caused by wrong estimation of the input parameters lidar ratio and reference value.

4.3 Raman algorithm intercomparison

by Gelsomina Pappalardo

The main goal of the Raman algorithm intercomparison experiment is to test the correctness and accuracy of the algorithms used by each group within the EARLINET network for the retrieval of the aerosol extinction profile starting from nitrogen Raman lidar signals (Ansmann et al., 1990; Bösenberg, 1998; Godin et al., 1999; Measures, 1984; Bösenberg and Theopold, 1988; Wandinger, 1998; Whiteman, 1999). For this purpose, synthetic lidar signals were calculated covering a wide variety of experimental conditions, such as different level of noise and aerosol properties that vary with time. In particular three different cases have been studied and the results are reported in the previous scientific reports and in the MPI report No. 337 (Matthias et al., 2002). This work has been continued during the last year of the project and a further simulation has been prepared. In this case the algorithms have been tested using synthetic lidar data that have been simulated taking into account realistic experimental and atmospheric conditions. Moreover, with this last experiment we have tested the correctness and accuracy of the algorithm used for the independent retrieval of the aerosol backscatter and extinction profiles and then of the lidar ratio profiles. For this reason both elastic and Raman lidar signal have been simulated at 355 nm and 532 nm (Ansmann et al., 1992a). In Table 7, the groups which participated in this intercomparison for the extinction retrieval are listed with the indication of the used algorithm.

Figure 14 shows all the extinction profiles provided by different groups at both 355 nm and 532 nm for this intercomparison, compared with the solution. In the first height range up to 2000 m of height, differences among the extinction profiles are always within 10% and no significant bias has been observed for both wavelengths. In the height range 3000 - 4400 m, where an aerosol layer is present in the solution, differences among the extinction profiles are always within 20% and again, no significant bias has been observed for both wavelengths. With the detection of the Raman scattered light, independent aerosol extinction profiles can be determined. This information can be used to derive also the aerosol backscatter without any assumption on the extinction-to-backscatter ratio (lidar ratio). The retrieved aerosol backscatter profiles obtained with the combined Raman elastic-backscatter lidar method are reported in Figure 15 compared with the solution; this figure

Table 7: Participating groups and the used averaging procedure in Raman algorithm intercomparison

LIDAR STATIOn		DATA PROCESSING in RAMAN ALORITHM
ABERYSTWYTH	ab	Linear and quadratic fit
ATHENS	at	Sliding average filter and polynomial fit
BARCELONA	ba	Weighted gliding window for spatial averaging. Least-squares linear fit
HAMBURG	hh	Sliding average
L'AQUILA	la	2nd order digital filter Savitzky-Golay
LECCE	lc	Sliding linear least-squares fit
LEIPZIG	le	Sliding linear least-squares fit
NAPOLI	na	Sliding linear fit
NEUCHATEL	ne	Sliding average
POTENZA	po	Sliding linear least-squares fit
THESSALONIKI	th	Least-square fit

shows a quite good intercomparison among all groups, for both wavelengths, even if in this case no reference values for the backscatter has been provided. Starting from aerosol extinction and backscatter profiles obtained by each group, lidar ratio profiles have been calculated up 2 km as reported in Figure 16.

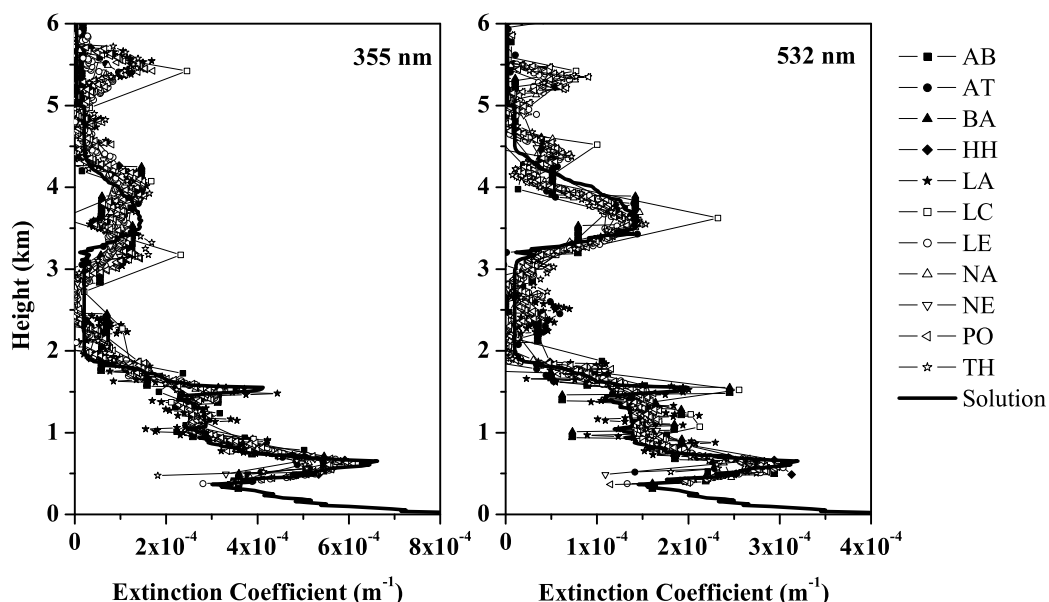This intercomparison showed that the aerosol extinction evaluation can be accomplished with good

Figure 14: Comparison between the extinction coefficients profiles retrieved at 355 nm (a) and 532 nm (b), by each lidar station, and the corresponding solutions.
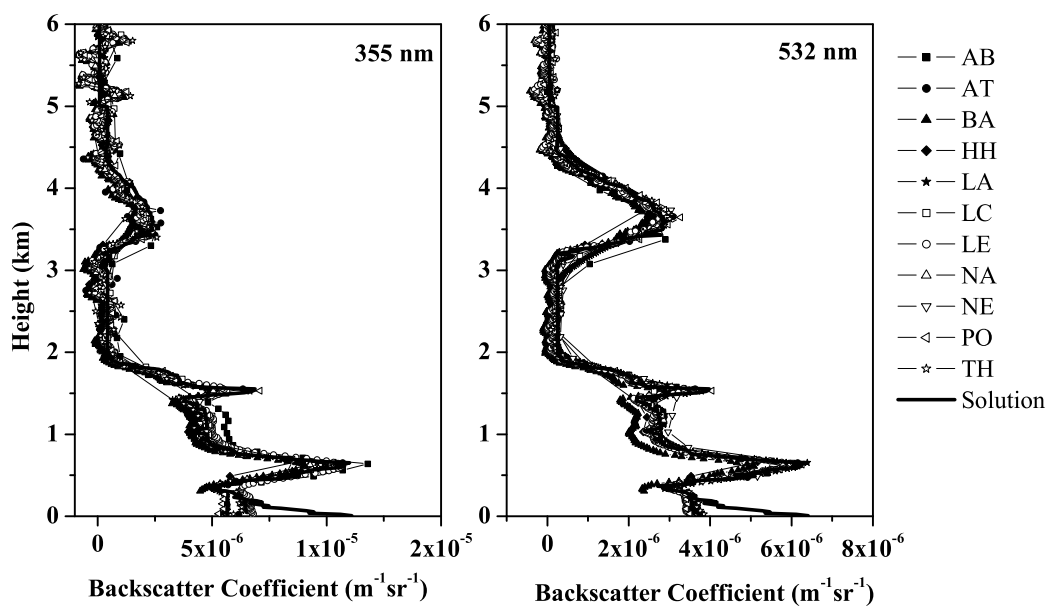
Figure 15: Comparison between the backscatter coefficients profiles retrieved at 355 nm (a) and 532 nm (b), by each lidar station, and the corresponding solutions.
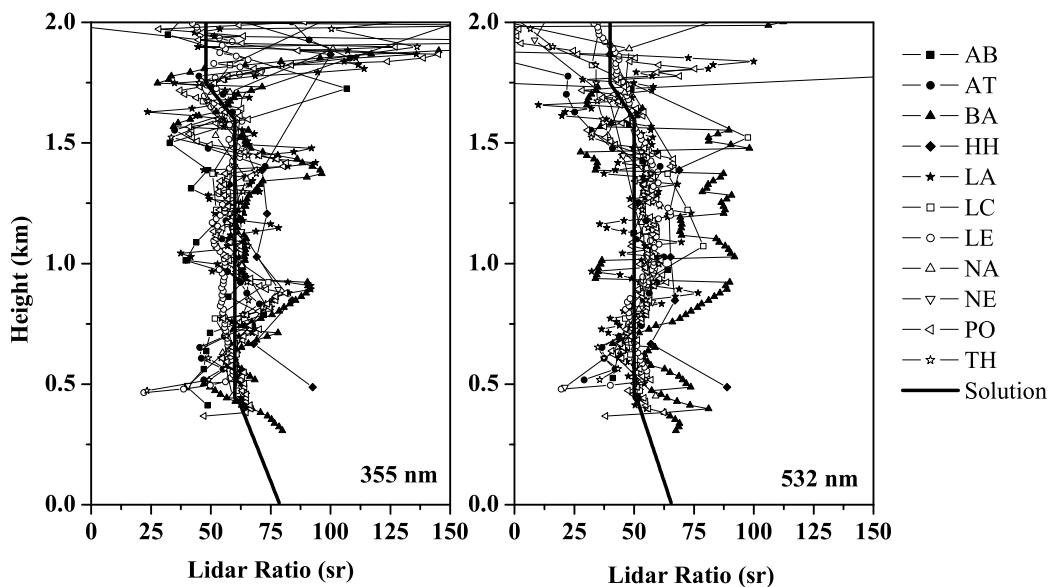

Figure 16: Comparison between the lidar ratio profiles, at 355 nm (a) and 532 nm (b) for each lidar station, and the corresponding solutions.

accuracy for all participating groups. Moreover, this intercomparison showed that, also without any further information about the reference value for the backscatter, the combination of the Raman elastic-backscatter lidar technique allows the independent retrieval of the aerosol extinction and backscatter profiles with good accuracy. Finally, quite good results for the intercomparison of the lidar ratio profiles demonstrate the capability for each participating group to obtain lidar ratio profiles in the whole aerosol dust layer with a mean deviation from the solution within 30 %. A more detailed analysis on the results of this intercomparison is still in progress and final results will be published in the next future.

5 Compilation of trajectory data

by Ina Mattis

5.1 Objectives

Atmospheric trajectories provide information on the origin of observed aerosols. Thus they are a very useful tool for the interpretation of measured profiles of aerosol optical properties.

In the framework of EARLINET trajectories are mainly used for the identification and interpretation of long-range aerosol transport events (section 8), for studying air-mass modification processes over the European continent (section 10). In addition trajectories can be used not only for the interpretation of special events, but also to perform climatological studies on the relationship between aerosol profiles and the origin of the observed air masses.

5.2 Methodology

The atmospheric trajectories, which are used for the EARLINET project, are calculated by the German Weather Service (DWD) for all EARLINET lidar sites for six arrival pressure levels between 975 and 200 hPa and for two arrival times per day. The latter correspond approximately to the times of the routine lidar observations at noon and at sunset. The DWD trajectories are 4-day backward trajectories and are calculated from the hourly wind fields of the global numerical weather prediction model of the German Weather Service (Kottmeier and Fay, 1998). The trajectories are available since May 2000 for all EARLINET participants. The trajectories are stored in a data base at IfT Leipzig. All EARLINET partners have access to the trajectory archive via an interactive web page (http://earlinet.tropos.de:8084).

There is a cooperation between EARLINET and the group of Andreas Stohl (Technical University of Munich, Germany), whose trajectory model FLEXTRA (Stohl et al., 1995) provides 10-day backward trajectories, which are calculated from the wind fields of the ECMWF model. FLEXTRA trajectories have a height resolution of 250 m and arrival-time steps of 3 hours and are therefore more appropriate for a comprehensive discussion of special events than the standard DWD trajectories. The trajectories are available for two periods of major Saharan dust outbreaks from July 27, 2001 to August 5, 2001 and from October 11, 2001 to October 16, 2001 for all 20 EARLINET stations.

Both types of trajectories are calculated on a 3-dimensional grid. This calculation method leads to lower uncertainties in comparison to those of other methods, e.g. isentropic calculation. The accuracy of the calculated trajectories also depends on the synoptic conditions. The higher the wind speed the lower in general the uncertainty of the trajectories. Usually the deviation between the calculated and the actual track of an air parcel is about 10% to 20% of the trajectory length (Stohl, 1998).

5.3 Scientific achievements

5.3.1 Combined statistical analysis of trajectories and lidar profiles

Because the quantity of available trajectory data sets (two per day) is much larger than the number of measured aerosol profiles (usually not more than three per week), we applied statistical analysis primarily to the trajectories and not directly to the lidar profiles. The DWD trajectories provide information on the synoptic patterns corresponding to the measurements (Dorling et al., 1992). Therefore

the trajectories should be used to classify profiles of optical aerosol properties derived by the routine observations in dependence on the large-scale weather regime (Mattis et al., 2001). For that purpose, the trajectories were divided into distinct clusters by means of cluster analysis. Each lidar profile then was assigned to the cluster of its corresponding trajectory. Because a trajectory cluster represents one large-scale atmospheric transport pattern, each of the profiles within the corresponding class of optical aerosol properties was obtained from a lidar observation under similar large-scale synoptic conditions. Investigations of the properties of these aerosol classes show the dependence of optical aerosol properties on the corresponding weather regime.

Cluster analysis provides algorithms to separate a large number of data sets (in our case sets of trajectories) into groups, the so-called clusters. The separation of the data sets has to be done in such a way that similar trajectories are merged within one cluster and dissimilar ones belong to different clusters. In this study, a clustering algorithm for atmospheric trajectories recommended by (Dorling et al., 1992) was used. Modifications concerning the starting conditions provide additional information on the uncertainty of the derived results (Mattis, 2002). An advantage of the used clustering algorithm is, that the optimum number of clusters follows from the algorithm itself and has not to be assumed.

The cluster analysis was applied to all 1812 trajectories which end at Leipzig at 850 hPa between April 2000 and September 2002. In this case only the trajectory data of the last 48 hours before arrival were used for the calculation of the trajectory similarities. The 850-hPa trajectories are believed to be the most representative ones for the main air transport in the upper part of the atmospheric boundary layer. The optimum number of clusters for Leipzig was found to be six. Figure 17 illustrates, how the Leipzig trajectories are assigned to the six clusters.

The six clusters represent weather regimes with different wind directions and speeds. Clusters A and D contain all trajectories with very low speed coming to Leipzig from easterly and westerly parts of Central Europe. Air parcels which were transported to Germany from the north with higher wind speeds are merged within cluster B. Cluster C combines trajectories
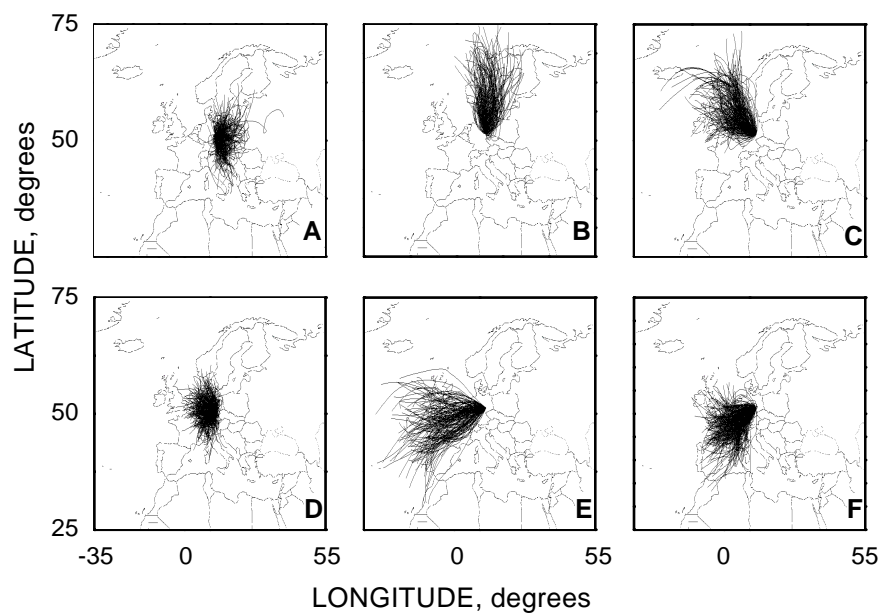

Figure 17: All 2-day backward trajectories arriving at Leipzig at 850 hPa between April 2000 and September 2002 in the six clusters identified by the clustering algorithm.

41

which crossed Great Britain and the North Sea. Those trajectories, which are characterized by very high wind speeds and have their origin over the Atlantic ocean are combined in cluster E. Cluster F combines trajectories from the Mediterranean Sea and from North Africa as well as slow trajectories from western Europe.

Figure 18 illustrates the characteristics of the groups of dust-layer mean extinction values at 532 nm and dust-layer mean values of the Ångström exponents which were assigned to the cluster of their corresponding trajectories. The extinction values are highest in clusters A, C, and D, which correspond to highly polluted air masses. This result agrees with the large Ångström exponents in these clusters. In contrast, in the clusters B and E—which are characterized by cleaner air masses— the lowest extinction values and Ångström exponents were found. The results of cluster F are difficult to interprete because this cluster contains different aerosol types like mineral dust from Africa or southwest Europe and industrial aerosols from western Europe.
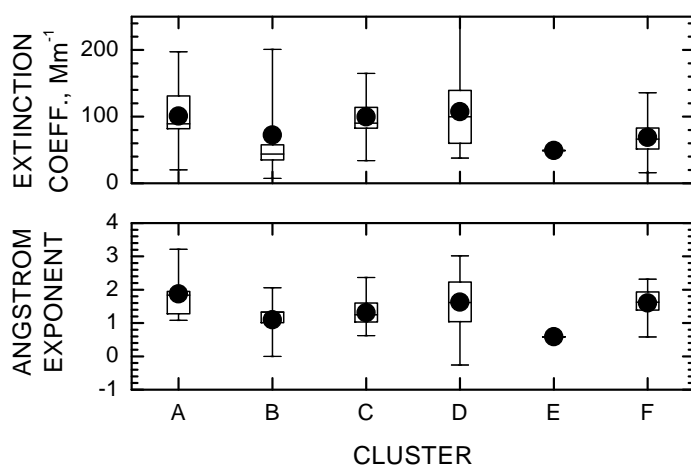

Figure 18: Characteristics of the groups of dust-layer mean extinction values at 532 nm (top) and dust-layer mean values of the Ångström exponents (bottom) which were assigned to the cluster of their corresponding trajectories. The dots represent group mean values. The boxes show the median, the 25%, and the 75% percentiles. The error bars indicate the minimum and maximum values of each group.

5.3.2 Major Saharan dust outbreak between July 27 and August 5, 2001

Dust layers covered almost the whole European continent for a period of several days during the Saharan dust outbreak between July 27 and August 5, 2001, (see section 8). The detailed FLEXTRA trajectories are used for all lidar stations to identify the origin of the observed aerosol layers in the free troposphere.

As an example Figure 19 shows a time series of the backscatter coefficient at 532 nm observed at Leipzig. Two Saharan dust layers, each with an optical depth of 0.13 at 532 nm, could be observed. The first layer stretched from 6 to 10-km height. Later a second layer appeared between 3 and 6-km height. The colored symbols indicate the arrival heights and times of selected FLEXTRA-trajectories shown in Figure 20. The trajectories show that the aerosols within the layers were advected from arid regions of the African continent. In contrast, the trajectory arriving at 18 UTC in 3-km height illustrates that the relatively clean region between the boundary layer and the Saharan dust layer originated from the Atlantic Ocean.
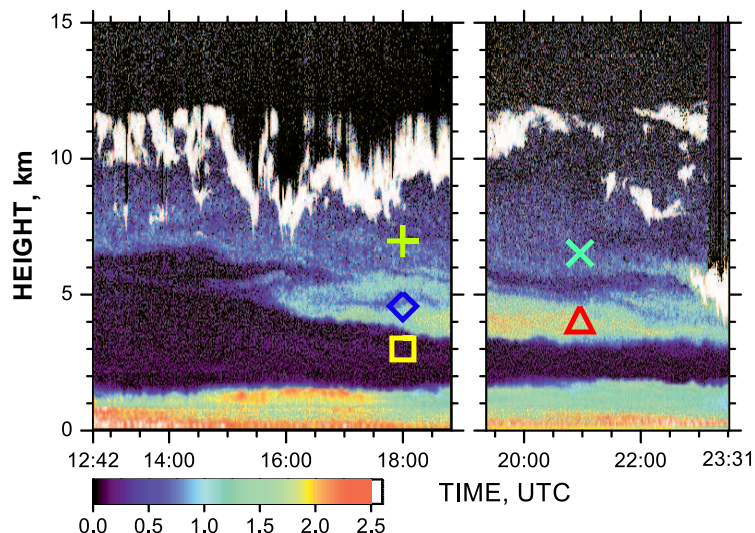
Figure 19: Time series of the particle backscatter coefficient at 532 nm in Mm^{-1}sr^{-1} observed at Leipzig on August, 2–3, 2001. White colors indicate clouds. The symbols show the arrival heights and times of selected FLEXTRA-trajectories.
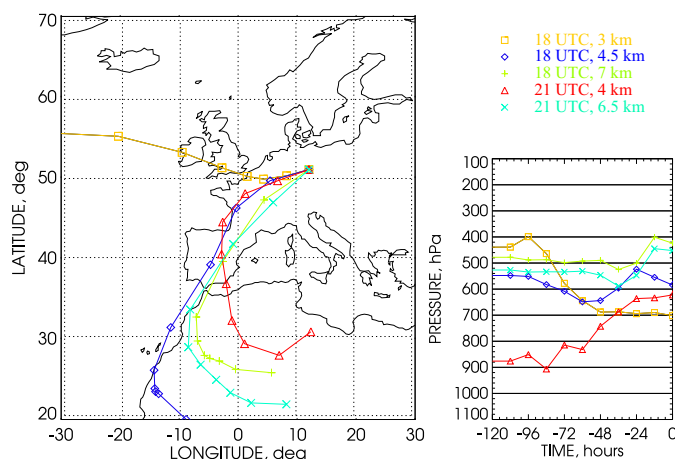

Figure 20: FLEXTRA trajectories, arriving at Leipzig on August 2, 2001. Arrival times and heights are given in the legend.

5.4 Conclusions

Within EARLINET two types of trajectories are used. The DWD trajectories which are available for all routine observations are used for the statistical interpretation of these routine lidar measurements. In section 10 they are used for a study of aerosol modification processes. In this section was demonstrated that a combined statistical analysis of such DWD trajectories and lidar profiles may indicate correlations between optical aerosol properties and the origin of the observed air masses. A similar study was performed with the 1454 trajectories which end at Barcelona at 850 hPa between May 2000 and April 2002.

The more detailed FLEXTRA trajectories are a very useful tool for case studies. They are used for the interpretation of measurements during special events in the framework of section 8. As an example the observation of an Saharan dust layer at Leipzig on August, 2–3, 2001 was presented.

43

6 Compilation of aerosol profile data

by Jens Bösenberg and Holger Linné

6.1 Objectives

The goal of this work package is the establishment of a large data base on aerosol profiles in a way that allows easy access and automated processing of the results from all different stations. Selection for special conditions should be possible, e.g. for climatology, Saharan dust events, forest fires, photochemical smog events, studies of the diurnal cycle, special stratospheric measurements, studies of the differences rural/urban aerosols, studies of the eruption of mount Etna, or files containing cirrus cloud observations.

6.2 Methodology

A statistical analysis of a large data set requires automated processing of files originating from many different stations. Therefore it is a crucial requirement that a common format is used by all parties. Netcdf was chosen as a professionally designed and maintained, platform-independent, self-describing format that offers sufficient flexibility for later additions as they become necessary. While the main part of the file structure is the same for all stations the format gives room for individual extensions whithout affecting the standard usage. In this way additional information is easily introduced whenever this appears necessary. A documentation of the mandatory and optional file structure components is available at the project internal website,
http://lidarb.dkrz.de/earlinet/earlinet_intern/rules,
which is accessible for all project participants and other authorised users.
Responsibility for maintenance of the individual sets is with the participating institutions. This was decided in the beginning because the data producers can make the best of their data. During the course of the project a number of changes had to be introduced in many data files, because improved methods of processing and the need for extra information developed. The approach of a decentralised data base proved very appropriate to mitigate such problems. For ease of access all data files are additionally collected in a single data base at MPI Hamburg, which is automatically updated every night from the data stored at the participating institutions. Selection for special conditions is made possible through special category files, in which all files from all sites belonging to one of the abovementioned categories are listed. These files are also updated automatically, so that at any time a complete list of measurements for selected conditions is available.

6.3 Scientific achievements

At the formal end of the observation period, December 31, 2002, a total of 14637 profiles is collected in the data base. The number of climatology files, based only on the regularly scheduled measurements, is 5435, and for studies of Saharan dust events 2235 profiles have been collected. For both areas the EARLINET data base is by far the largest existing collection. Table 8 gives an overview over the number of files collected for other special observation categories.
By application of automated check procedures it is verified that the data base is internally consistent. E.g., it is checked that measurement times and dates are meaningful, duration is not excessive, mandatory parameters can be retrieved, climatology files have been labeled correctly, etc. As can be expected for a large data base constructed from many individual contributions there are certainly

Table 8: number of files collested for special observation categories

All	14637
Cirrus	399
Climatology	5435
Diurnal cycles	2010
Etna eruption	143
Forest fires	174
Photosmog	99
Rural/urban	568
Saharan dust	2235
Stratosphere	73

some inconsistencies within the files, but through automated checking and notification of the data producers these inconstiencies have been minimised.

It is a major achievement that three years after the start of the project a fairly homogeneous data base is established from a large number of initially quite heterogeneous contributions. The data base and the necessary software tools are very useful now, and they are used extensively for various studies related to the aerosol vertical distribution. The content of the data base is still growing in spite of the formal end of the project.

7   Temporal cycles

by Jacques Pelon and Laurent Sauvage

7.1   Introduction

In this workpackage the task performed is related to the analysis of observations of the aerosol properties in the lower troposphere and more particularly in the planetary at different time scales. This encompasses the diurnal and seasonal cycle of aerosols in the boundary layer as it is controlled by solar and synoptic forcing.

All groups but one were involved in this workpackage. The main focus of this workpackage is put on the aerosol in the atmospheric boundary layer (ABL). The terminology "boundary layer" means the layer directly coupled in terms of energy transfers with the surface over a diurnal cycle. However in our analysis we also include the residual layer observed above the boundary layer during the day as a result of growth cycles over the previous days. Aerosol properties are different in both layers helping characterising the difference between the various layers.

Periods of observations are related to unperturbed weather conditions, ideally in a high pressure system. This allows to favour simultaneous observations at different stations and quantify the behaviour of aerosol at the regional scale.

Ideally, the objective is to make observations during the whole day starting before sunrise and ending after sunset to observe the transition between the stable night-time and the unstable daytime boundary layer. As this represents a long observation period, and as processes involved are differently phased, the observations can be separated in several sets: transition in the morning, development of the ABL, stabilisation and decay phase.

The ABL development is conditioned by several parameters, as it reflects the local thermal and dynamical forcings but also the forcing at the synoptic scale. In the ABL, aerosols and pollutants are mixed during daytime, when the local forcing is important leading to turbulence production in the whole ABL. The ABL top height is thus marked by a gradient in aerosol particle concentration, which leads to a gradient in the backscattering and extinction coefficients derived from lidar measurements. This gradient may be enhanced by the effect of relative humidity (RH) on particle size. As aerosol particles are hygroscopic their size varies with RH, and so do their optical properties. It is thus important to take into account this parameter in the analysis. Aerosol particles and gases trapped in the ABL are then transported. The whole evolution process of the ABL is discussed in the next section.

Backscatter measurements can be used directly to derive the ABL height using different methods which will be discussed in the third section. Backscattering lidar measurements during daytime can also be reinforced by Raman lidar measurements before and/or after sunset, whenever possible. In this second case, the ABL developed during the day is identified as the residual layer in the evening Raman measurement.

In the fourth section we will illustrate results obtained during the diurnal cycle alerts with observations at different stations. Finally we will discuss in a fifth section the characteristics observed on a seasonal basis at selected stations.

Temporal variations due to special events such as the transport of aerosols linked to the occurrence of fronts, the seasonal transport of desert dust or of particles produced by biomass burning and production due to photochemical pollution are not included in this workpackage. The analysis of the statistics of lidar derived parameters on a seasonal basis is detailed in section 15.
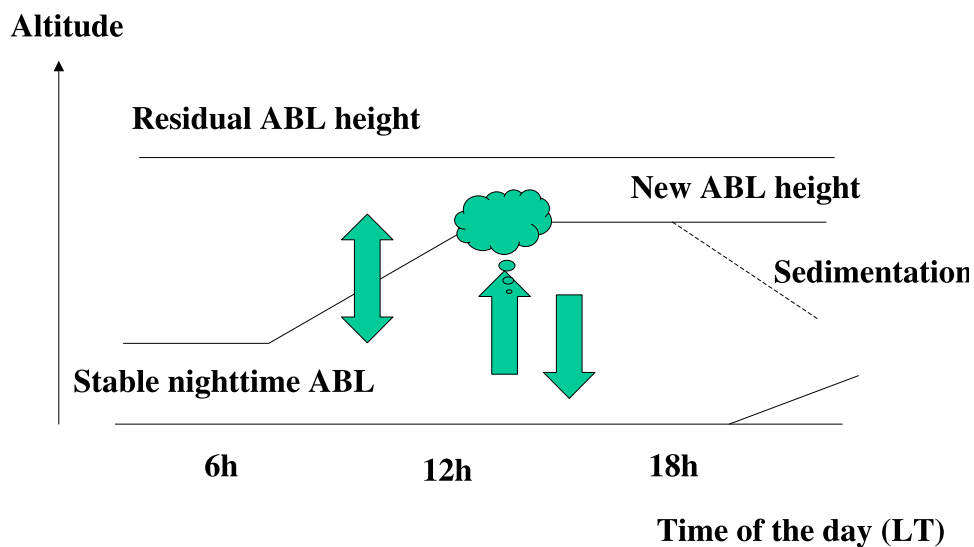
Altitude

Residual ABL height

New ABL height

Sedimentation

Stable nighttime ABL

6h   12h   18h

Time of the day (LT)

Figure 21: Evolution of the boundary layer height and modification of its main structural and optical characteristics during the diurnal cycle.

7.2   The diurnal cycle of the boundary layer

Let us first consider the daily evolution of the boundary layer. The accumulation of the aerosol load during the day in the planetary boundary layer (PBL) is depending on the strength of the aerosol source itself (number of particles of natural or man-made origin), surface wind speed (dynamical forcing at the surface), and solar flux (thermal forcing) leading to turbulence development and mixing. The vertical stability (linked to the potential temperature gradient) and synoptic forcing are critical to the development of the boundary layer, and may lead to an increase of the number of aerosol particles and of pollutant concentration when the growth of the boundary layer is blocked, assuming the source is kept constant. The variation of the optical properties of the aerosols which is observed by lidar is further depending on moisture. The development of the boundary layer may be identical at different places or for several days in terms of the top altitude reached, but the optical properties may differ. Periods of observations are related to unperturbed weather conditions, ideally in a high pressure system. This allows to favour simultaneous observations at different stations and quantify the behaviour of aerosol at a regional scale.

In our analysis we need to differentiate the residual layer and the active boundary layer formed during the day. The residual layer is a result of growth cycles over the previous days leading to an increased number of particles and pollutant concentration in the upper atmosphere. As a result from the local scale dynamics, moistening and larger scale transport, aerosol properties are different in both layers helping to characterise the difference between the various layers.

During the morning, the growing boundary layer is eroding the stable and residual layers of the previous night and day, respectively. This is illustrated on the idealised evolution shown in Figure 21.

In the evening, the detrainment of the ABL and the sedimentation of large particles occurs during the

47

WP6 : DIURNAL CYCLES ALERTS

IOPs	SEASON	Number of stations involved
IOP1 : 02 April 2001	SPRING	11
IOP2 : 28 May 2001	SPRING	10
IOP3 : 14 – 15 August 2001	SUMMER	4
IOP4 : 16 Nov. 2001	AUTUMN	6
IOP5 : 3 & 4 Jan. 2002	WINTER	6
IOP6 : 4 March 2002	WINTER	5
IOP7 : 11 March 2002	WINTER	5
IOP8 : 16 May 2002	SPRING	7
IOP7B : 08 April 2002	SPRING	8
IOP9 : 30 May 2002	SPRING	5
IOP9B : 03 June 2002	SUMMER	4
IOP10 : 30 Sep 2002	SUMMER	4

Table 9: IOPs and measurements made in the frame of WP6.

stabilisation of the residual layer. In both transition phases the profile of the extinction coefficient is not constant with altitude. Morning transitions are important as particles and pollutants formed during daytime can be stored in the upper part of the residual boundary layer and further transported (possibly in the middle or upper troposphere, this topic is linked with section 17 objectives about long range transport). During the formation of the stable nocturnal layer, this layer may include less particles and pollutants as no photochemical production will occur (although there could well be more emissions). In this case, the erosion of the residual layer above it whereas the following cycle may lead to a pollution increase near the surface, as the residual layer is mixed with the new growing active boundary layer. The structural and optical properties of these aerosol layers are thus important to be measured especially in the transition phases.

7.2.1   Observations performed

The strategy for the measurements needed within this workpackage is aiming at getting information at short time scales comparing diurnal cycles at different locations and analysing climatological characteristics over the whole data set for selected stations.

In the first year of the EARLINET programme, the focus has been set on the methods of acquisition of known quality lidar data from all stations. As all the station did not have the same experience in lidar, consolidation of system operation and analysis methods were prioritised as compared to scientific analysis to get quality measurements and compare results. This is necessary to successfully analyse data, and not misinterpret the obtained results.
While all EARLINET lidar systems had to be checked for quality in the first year of the project diurnal scycles have only been observed on an individula basis by some of the groups. In 2001 and 2002 the focus has been set on the acquisition of new, coordinated data sets and the consolidation of the methods to analyse lidar data from all stations. Several alerts have been given to include more
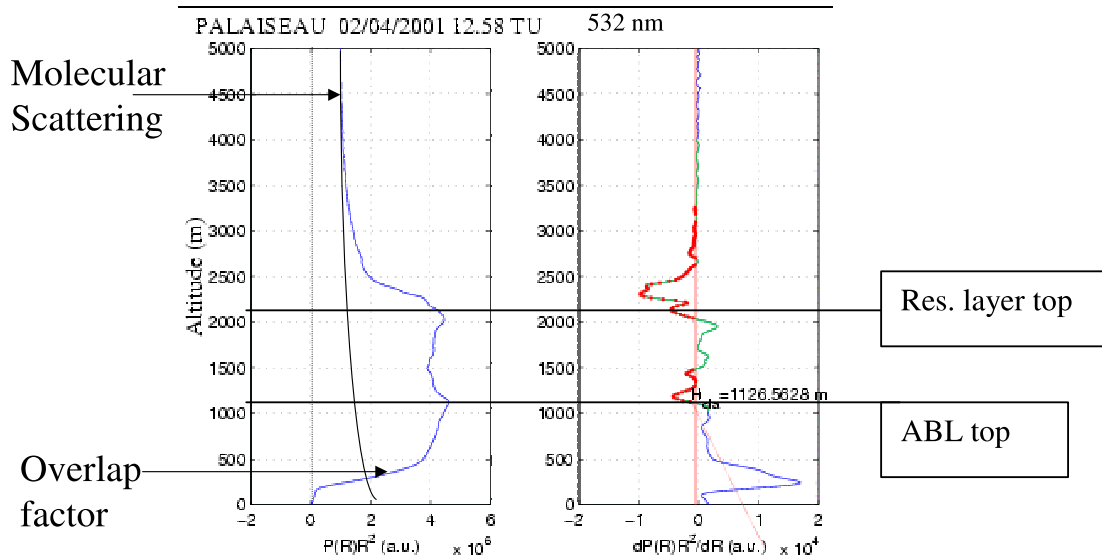
Figure 22: Left : Example of range corrected signal proportional to attenuated backscatter showing the increase in signal in the developed boundary layer observed during IOP 2 at Palaiseau. Right : First order derivative and determination of PBL and dust layers top heights from the analysis.

comprehensive diurnal cycle observations. The observations made are summarised in Table 7.2.1. All data has been stored in the common database.

7.3   Methods for retrieving the boundary layer height

As seen in Figure 21 the development of the ABL is eroding the stable nigttime layer. This layer is controlled by the radiative cooling of the surface during the night and additional dynamics of thermal forcings (in case of an urban aera). This layer usually has a small depth and requires to be detected to perform measurements in the first hundreds of meters. This is a problem for lidar since an incomplete overlap between laser beam and telescope field of view can prevent the analysis of lower atmospheric layers and the detection of the ABL evolution during wintertime (smaller vertical development). This may be partly accounted for by using a correction of the overlap function before determining the ABL by taking the derivative of the corrected term.

Assuming a typical situation, where the solar heating of the surface leads to the mixing of the aerosols, the ABL height can be defined from the gradient of the particle concentration mixed in the ABL by turbulence up to its top. This leads to a sharp gradient in particle extinction and backscattering coefficients. To retrieve the ABL top height, one can work on vertical profiles of range corrected lidar signals (attenuated range corrected backscattering) or particle backscattering coefficients or extinction coefficients.

 In the example of range corrected signal (RCS) reported in Figure 22, the ABL height is about 1100 m and the residual layer about 2100 m. The lowest minimum of the derivative of the RCS and the highest minimum, respectively, correspond to these altitudes.

It may be thus difficult to identify the boundary layer from a single average measurement, as it

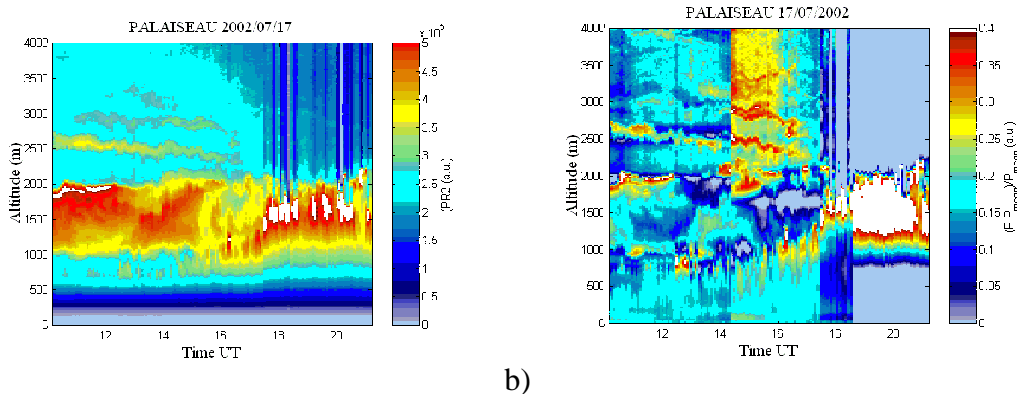a)   b)

Figure 23: Backscattered lidar signal obtained at Palaiseau a) with the small size telescope and b) with the large size telescope after application of expression 7 on the signal.

would be the case from the averaged backscattering profiles defining the climatology in the database. The ABL height may better be identified from other features such as the variability of the aerosol backscattering at the top of the unstable boundary layer.

To overcome the problem of incomplete overlap in the lowest few hundred meters a new method has been proposed by U. Wandinger (IfT, Germany). The idea is to work on the relative signal variation in the vertical which should reflect the decrease in particle scattering and allows to eliminate the overlap function.

$$S = PR^2 \longrightarrow S' = \frac{S - S_{ave}}{S_{ave}} \tag{7}$$

A test has been done to check this procedure on lidar signals measured with the dual telescope configuration used at Palaiseau. The larger size telescope has an overlap factor of about 1500 m. The lidar signal measured with this telescope is limited to altitudes larger than 500 m The variation in aerosol scattering in the lower layer is less easily evidencing the ABL height as compared to the signal obtained in the lower range allowed by the small size telescope (Figure 23a).

The relative signal obtained from the expression (7) above with a moving average over consecutive files (Figure 23b) shows a more continuous pattern down to the surface. The gradient algorithm can then be applied to the signal more efficiently to retrieve the ABL height as shown in Figure 24 where a comparison of the three derived ABL heights for the signals measured is shown for the large and small size telescope and for the modified signal.

7.3.1   Data analysis

A simple analysis model of ABL Dynamics   A zero- (or first) order jump model is well suited to represent the convective PBL and interpret its evolution (Fig. 25). In this model the ABL is divided into three layers : the surface layer where the fluxes are almost constant, the mixed layer, where the potential temperature (water vapour mixing ratio or wind) are constant, and the entrainment layer where the vertical gradient is well marked. The boundary layer evolution can be represented by a set of equations governing the mixed layer potential temperature Θ , moisture q and wind U(u,v) and the temperature, moisture and wind jumps ($\Delta \Theta$, Δq, Δu, Δv) in the entrainment layer (Driedonks, 1982; Diak and Stewart, 1986). The evolution of these parameters is depending on their gradient above the ABL and by fluxes at the surface.
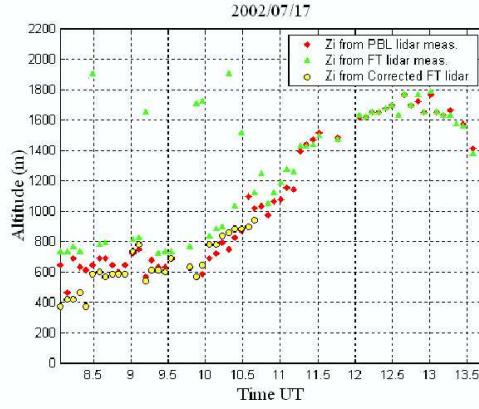
50

Figure 24: Comparison of the values of the ABL height derived from the three signals reported in Figure 23.

There is a direct relationship between the surface heat fluxes and the ABL height, through the vertically integrated equations of conservation of heat and moisture. We can write for the potential temperature

$$\frac{d\Theta}{dt} = u\frac{\partial\Theta}{\partial x} + v\frac{\partial\Theta}{\partial y} + \frac{\partial\Theta}{\partial t} = \frac{1}{h}(H_s - H_h) + S_\Theta \quad , \tag{8}$$

where H_s is the sensible heat flux at the surface, H_h the sensible heat flux at the top h of the mixed layer and S the other sources (sinks) of heat (radiation, phase change) which are neglected in clear air.

Using the parameterised kinetic energy budget at the ABL top reduced to the balance between Buoyancy flux and flux convergence of kinetic energy, we can write the sensible heat flux in the entrainment layer so that it is proportional to the surface flux $H_h = -C_\Theta H_s$, we then obtain the surface fluxes from the equation

$$H_s = \frac{h}{(1 + c_\Theta)}\left(u\frac{\partial\Theta}{\partial x} + v\frac{\partial\Theta}{\partial y} + \frac{\partial\Theta}{\partial t} - S_\Theta\right) \tag{9}$$

An accurate determination of this flux thus requires accurate determination of the advection and temporal evolution terms from measurements or from a model. It requires furthermore the knowledge of the ratio of fluxes c_Θ from the analysis of the turbulent kinetic energy budget (Driedonks, 1982; Flamant et al., 1997). In the absence of wind and forcing, in a steady situation, sensible heat flux is balanced by radiative cooling, but this term is not introduced here because it gives only a minor contribution in clear air.

At the boundary layer top, the gradient in potential temperature $\Delta\Theta$ varies as the ABL develops as

$$\frac{d(\Delta\Theta)}{dt} = \gamma\left(\frac{dh}{dt} - w\right) - \frac{d\Theta}{dt} \tag{10}$$

where γ is the vertical gradient of the undisturbed potential temperature profile above the boundary layer. Combining equations (8) and (9) assuming no source of heating and no vertical speed, and using a relationship between heat flux and gradient as given by

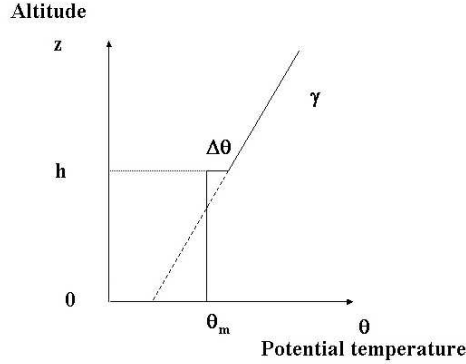$$H_h = -\Delta\Theta\left(\frac{dh}{dt} - w\right) \tag{11}$$

51

Figure 25: First order model representation of the temperature increase in the convective atmospheric boundary layer.

in the same conditions, we obtain the increase in boundary layer height as a function of time due to the surface thermal forcing as

$$h^2(t) - h_0^2 = \frac{2}{\gamma}(1 + 2c) \int\limits_0^t H_s(t')dt' \qquad (12)$$

It has to be noticed that this expression can be used to interpret observations at different time scales. As far as diurnal cycle is considered, the evolution of the sensible heat flux can be assumed to be linear with time in the morning phase. This implies that the growth of the height of the ABL top is almost linear with time. This allows to estimate surface sensible heat flux. In the afternoon, when H_s is almost constant, h is varying as the square root of time. The ABL height remains constant when the surface flux has vanished.

Assuming a given flux variation with time, the evolution of the heating as a function of season is reflected in a higher boundary layer height. This will be discussed in the climatological analysis. Expression (12) is however simplified as neglecting contributions such as the vertical speed, and some sites may experience forcings which would reflect different behaviours as detailed in the case study herebelow.

7.4 Analysis at the European scale

16 May 2002 Additional measurements are required for the analysis. Namely, radio-sonde measurements of pressure, temperature, moisture and wind speed at least twice a day and better is the analysis obtained from a meteorological centre. Measurements of radiation and turbulent fluxes at the surface are also to be considered.

From the measurement database, the 16 May 2002 was selected as presenting a number of measurements homogeneously distributed over Europe. This is due to the presence of a high pressure system over central Europe extending to northern Germany and England as shown in Figure 26.

A low pressure system is located west of Brittany moving to the north-east and bringing warm air
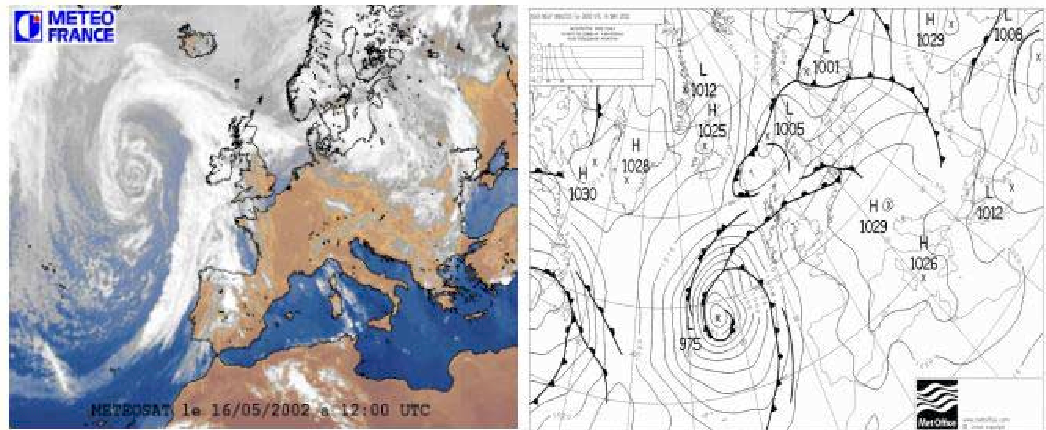
Figure 26: Meteorological situation on 16 May 2003 as evidenced a) from Meteosat observations at 12 UTC (Eumetsat/Meteo-France) and b) surface pressure analysis from UKMO.

over western Europe up to England. The Meteosat image also reported in Figure 26 is evidencing the presence of the cloud bands associated with the frontal system, and of the clear air area over most EARLINET stations at 12 UTC.

Measurements performed over 16 May 2002 at the different EARLINET stations are reported in Figure 27. They show various features reflecting the different forcings.

In Aberystwyth the diurnal evolution of the boundary layer is showing the existence of two regimes with a transition at 12 UTC. In the first regime large values of backscattering coefficients are ob-
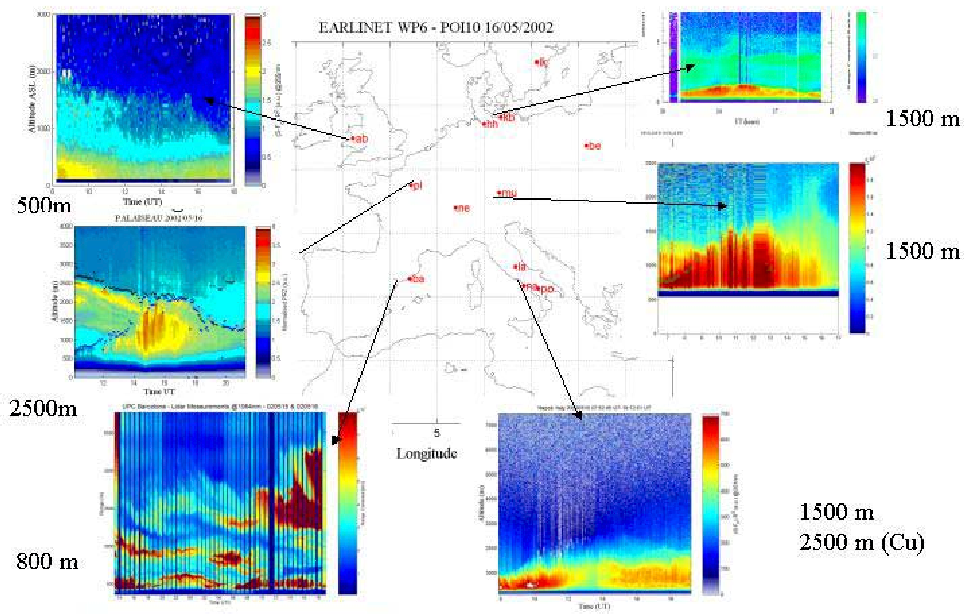

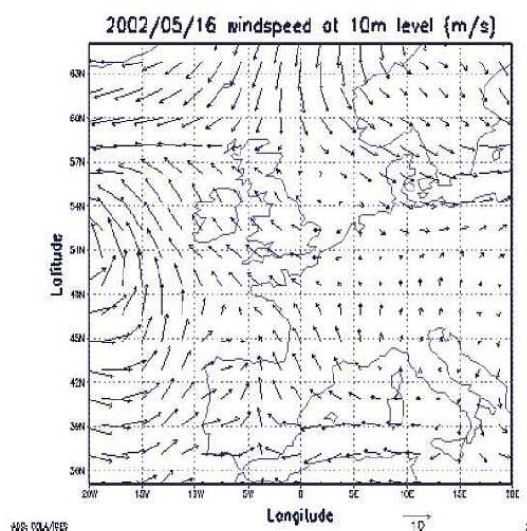Figure 27: Measurements performed on the 16 May 2002 during IOP 8.

Figure 28: Wind field at 10 m level above the surface from NCEP analyses.

served up to altitudes of 2000 m, with a boundary layer height of about 500 m decaying with time. In the second regime, the ABL height is growing. This difference may reflect the influence of advection more important before 12 UTC, and local forcing dominating in the second regime. The rate of increase with time of the ABL h is very small (less than 40m/h), and probably still constrained by a vertical subsidence.

A few stations are experiencing similar evolution of the boundary layer height. In Kühlungsborn the rate is about 300 m/h, with a steady increase of the ABL h between 8:30 UTC and 14:00 UTC allowing to reach a value of 1500 m above ground level (AGL). In Palaiseau the height reached is about 2000 m AGL. After a slow evolution in the morning, the hourly rate of increase at 13 UTC is about 350 m/h. However, referring to a larger period of time ($\pm$ 6h), it is reduced to 230 m/h, but extending later in the afternoon. This behaviour is comparable to the one observed in Munich, although the ABL height is reaching 1500 m AGL.

The wind field controlling advection is given in Figure 28. One can see that its strength rapidly decreases as one moves from the low pressure system to the high pressure system. Advection is very weak in eastern Germany. Temperature gradients (not shown) are also small in this area. Since the vertical wind speed in this area is also weak as shown in Figure 29, it is expected that one can use the equation (12) to derive the boundary layer height knowing surface fluxes. The fluxes obtained from NCEP analyses at 12 UTC are about 200 W/m^2 in this area. Looking to the radiosonde measurements in Lindenberg and Munich in Germany allows to derive a vertical gradient of potential temperature above the ABL of about 6 K/km. Assuming peak fluxes are reached after 6h and then decreases to zero in the same time duration, equation (12) gives a maximal boundary layer height of about 1500 m.

Particular behaviours : orography effects   Several stations in the EARLINET network are under the influence of mountains (Neuchâtel), or of the sea (Naples, Aberystwyth, Kühlungsborn) or of both (Barcelona, Athens). It is generally difficult to neglect these forcings as they will induce specific behaviours in the evolution of the ABL height. We describe some particular events observed at some
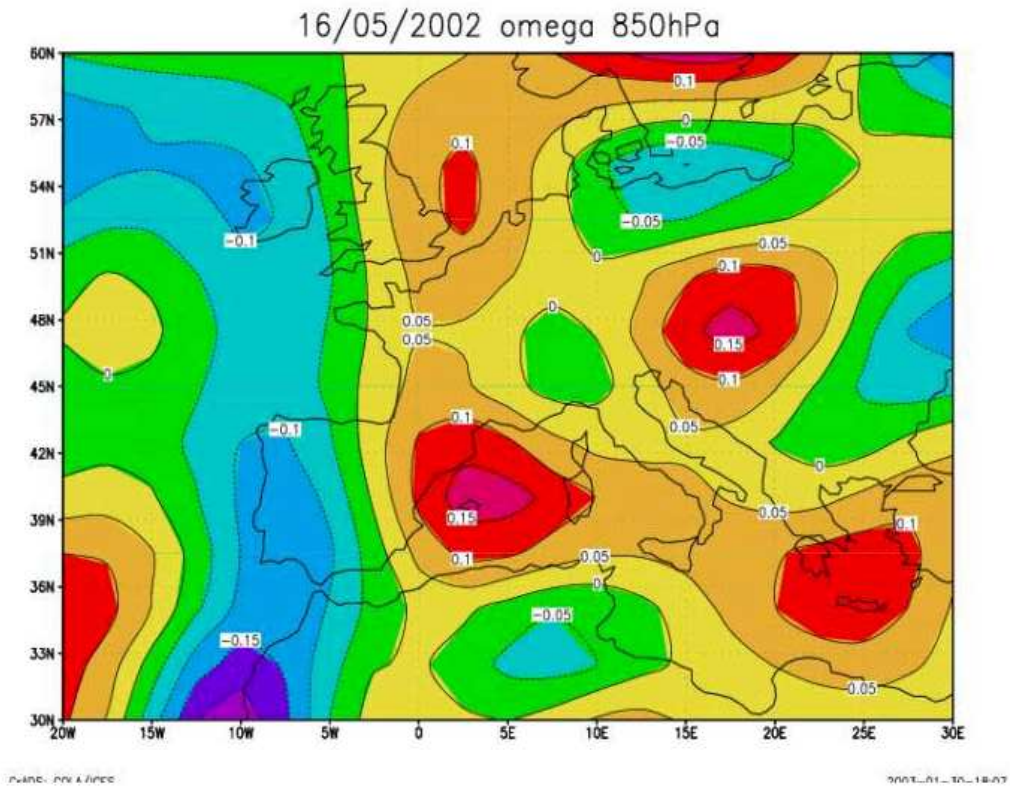
54

Figure 29: Vertical wind speed as derived from NCEP analyses for 16 May 2002.

of these stations.

In Barcelona the rate of increase with time of the ABL h is about 100m/h, which is also much smaller than the average value observed over the continent. As seen in Figure 29 a strong downward velocity was given by NCEP analyses on the area, which may explain such a small growth rate of the ABLh. It is further stopped well before noon due to the development of secondary circulations due to orography (see breeze and mountain flow return).

In Naples, the rate of increase of the ABL height is larger in the early morning and seems to end well before 14 UTC. However, a dual layer structure appears early in the morning hours (10 UTC) which further develops in the afternoon, the top of the inversion being at 2500 m AGL. The upper layer is capped buy clouds between 10 and 12 UTC. This structure is also observed in the radiosonde measurements of temperature and humidity at 12 UTC. Humidity is much lower in the upper layer above 1500m, than below. This vertical structure is also observed on the horizontal wind. Easterly winds are blowing in the upper layer, whereas westerly winds are observed below. Such features can be explained by sea breeze development as land becomes warmer than the sea and as the sea breeze front propagates inland to the east and passes over the lidar station.

In Athens, measurements on the 16 May 2002 were not possible due to cloud cover. However, a total of 24 days were covered by diurnal lidar measurements for the purpose of evaluating the mixing layer height over Athens. These days covered a variety of cases and corresponded to various atmospheric conditions (clear skies, Saharan dust outbreaks, photochemical smog, volcanic eruption, etc.). Continuous lidar measurements under clear sky conditions were then limited to 6 days. Each day of measurements was examined subjectively to see whether any repeated patterns occurred
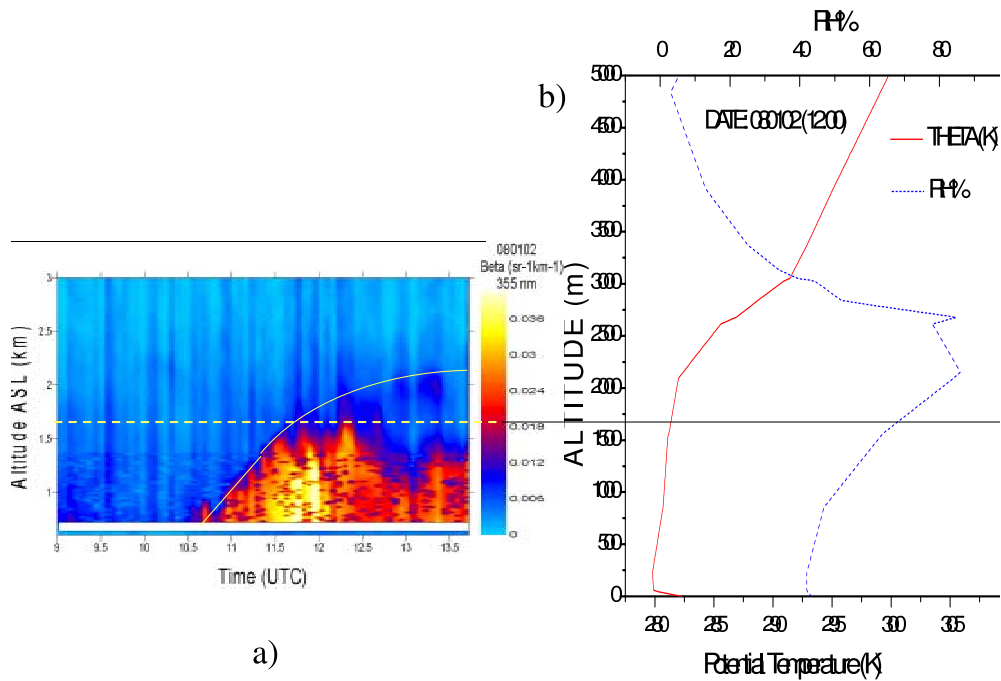
Figure 30: a) : Evolution of the aerosol backscatter coefficient over Athens at 355 nm, from 09:00 to 14:00 UT on 080102. b)Potential temperature and relative humidity profiles taken at the Hellinikon Airport, on 080102 at 12:00 UT.

during the observing period.

From this examination we identified some common features of the diurnal evolution of the ABL for the site of Athens:

- Intense convective boundary layer during early morning hours, implying the presence of strong convection, is observed, between 06:00 and 10:30 UT, especially during summer time. This is confirmed by local radiosonde data. The general afternoon behaviour of the ABL was characterized by the persistence of strong lidar signal gradients at the height of the top of the late-morning PBL. From mid-afternoon (around 13:00 UT) to late after-noon hours (around 15:00 UT) the PBL height was steadily decreasing.

- Around 11:00-12:00 UT a discernible and coherent pattern could be seen, related to the arrival of the sea-breeze circulation over the Greater Athens Area (GAA). This resulted, in some cases, in the splitting-up of the top of the PBL aerosol layer into two layers. This observation is similar to the one noticed on Naples observations.

- A typical diurnal evolution of the aerosol backscatter coefficient over Athens (080102) is presented in Figure 30 at 355 nm, from 09:00 to 14:00 UT, from 0.5 to 3 km asl. In this figure the daytime evolution of the ABL is clearly seen. The corresponding vertical profiles of the potential temperature and the relative humidity (RH) at 12:00 UT are given in Figure 31, by the local radiosonde data taken at the Hellinikon Airport, located 20 km from our measuring site.

56

The potential temperature (theta) profile (Figure 30b) shows a convective Boundary Layer around 12:00 UT, up to a height of approximately 1800-2000 m, which is consistent with the aerosol backscatter profile shown in Figure 30 taken at the same time. The RH profile increases up to 2500 m. The daytime evolution of the wind direction- speed and that of RH and potential temperature, taken at the lidar site at ground level (220 m asl.), are showing the arrival of the sea-breeze front from the SW direction, around 13:00 LST (11:00 UT) together with the arrival of the return flow near ground (from northern directions) over the lidar site. This arrival around 13:00 LST is accompanied by a sudden drop of the RH values (due to overpass over the Greater Athens Area) and an increase of the temperature near ground level.

7.5   Climatological analysis

An example of seasonal evolution of the boundary layer height is reported in Figure 31. Data have been obtained at Palaiseau during daytime using backscatter lidar (Figure 31a). Hamburg data from almost five years of post sunset observations are compared (Figure 31b). The boundary layer height obtained at sunset corresponds to the well developed ABL at the end of the day. It is seen that a seasonal increase in summer due to a larger heating of the surface can clearly be observed on the averaged data. Further analysis should be made using the standard backscatter and Raman lidar measurements performed at the different stations.

It is possible to check coherence of the developed ABL height with the forcing at the surface using Eq. (12):

$$< h^2(t) >= \frac{2}{\gamma}(1 + 2c) < H_s > \Delta T \quad .$$ (13)

Using similar values of fluxes and temperature gradient on a climatological basis would lead to the same results in terms of average ABL height.

The strength of EARLINET is that backscatter measurements during daytime have been reinforced by Raman measurements before and/or after sunset. This avoids hypothesis to retrieve the extinction in the boundary layer and allows a survey of the evolution of extinction by particles in the PBL at

a)   b)
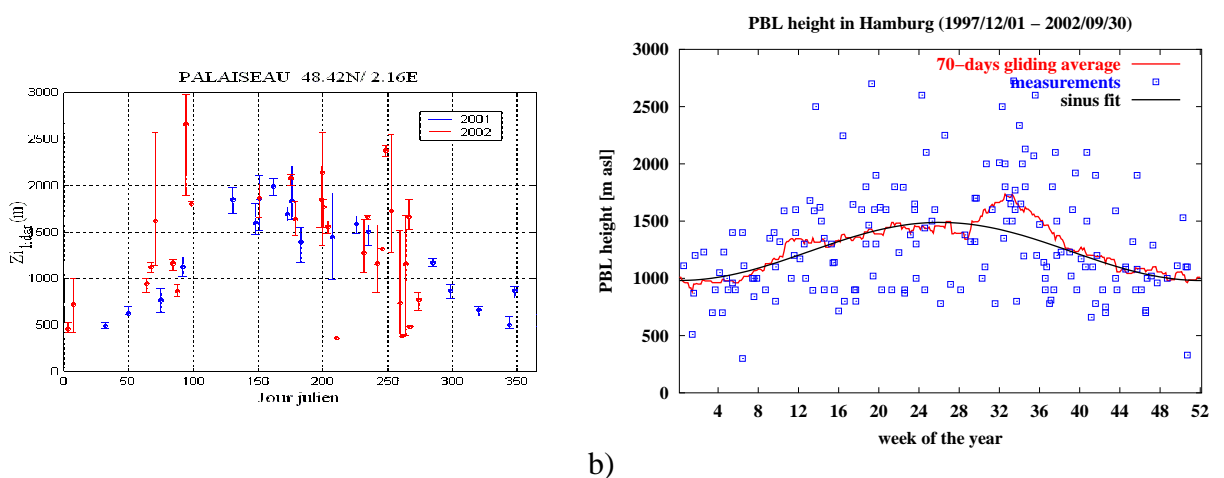
Figure 31: Evolution of the PBL top height as a function of the month of the year as analysed a) at Palaiseau and b) Hamburg from the routine operation measurements using the first derivative analysis.
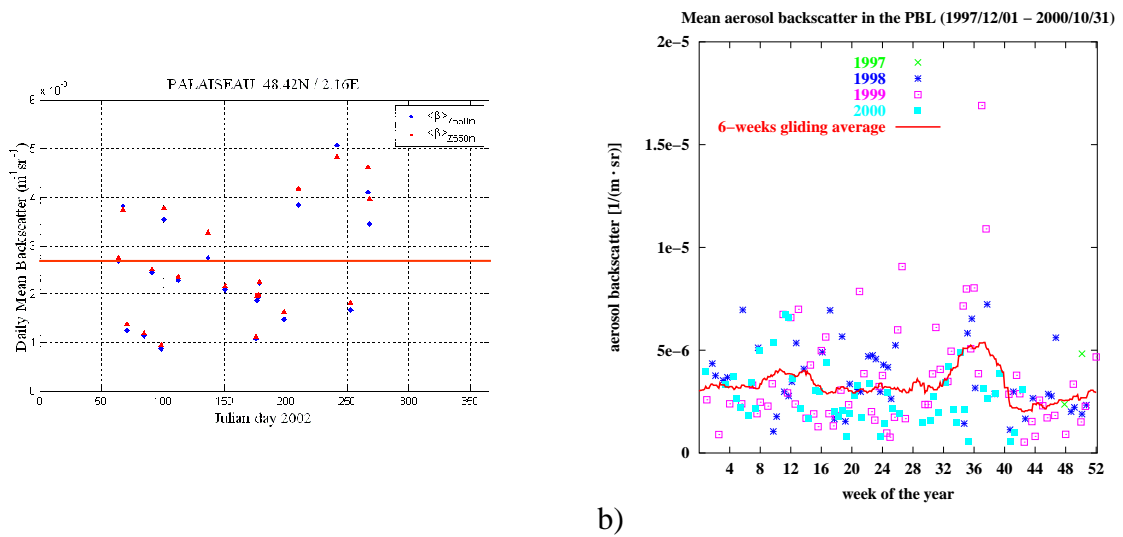
57

Figure 32: a) Backscatter coefficient measured in the ABL in 2002 at Palaiseau during daytime with the backscattering lidar and b) at Hamburg between Dec. 1997 and October 2000 as a function of the week of the year.

several locations. An example is reported in Fig. 32 from observations made at Hamburg. Again a large dispersion is observed but an average distribution showing two peaks in spring and autumn can be observed. As observations are made after sunset, the reformation of the stable layer in the mixed PBL and the sedimentation of large particles may induce some additional effects to analyse in more detail. Observations made in Palaiseau with the backscattering lidar operated during daytime give a comparable average value. This type of analysis is being done by the different groups involved in WP14 (statistical analysis) and WP6.

The typical evolution of the mean Mixing Layer Height over Athens during EARLINET, based on the RCS-derivative method, is presented in Figure 33 for different seasons. The same behaviour is observed with a summer maximum.
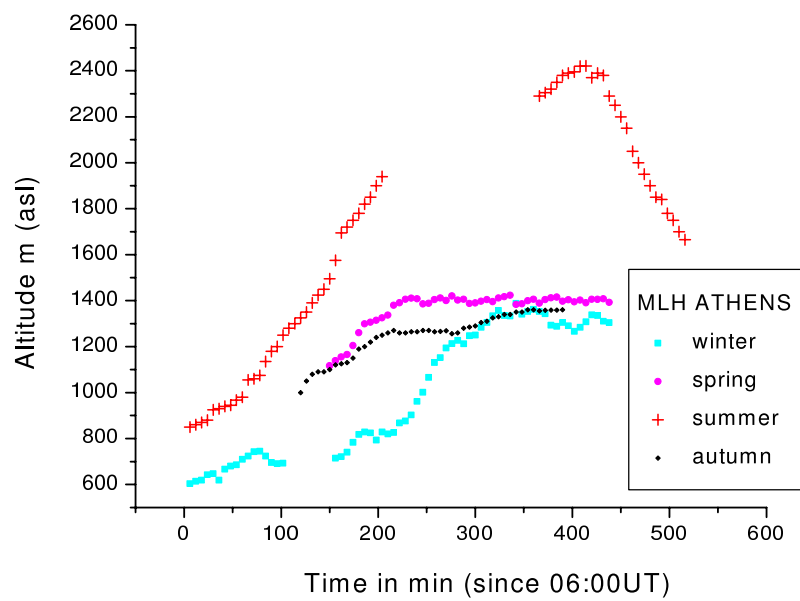
Figure 33: Evolution of the mean Mixing Layer Height over Athens during EARLINET, based on the RCS-derivative method.

8 Observation of special events

by Alexandros Papayannis

8.1 Executive Summary

During the whole EARLINET period, this work package showed a strong activity with contributions from all EARLINET stations. Since May 1, 2000, more than 105 Saharan dust outbreaks were successfully forecasted, while 85 of them were followed by most of the stations of the network. This has established the largest data set on the vertical and horizontal distribution of Saharan dust aerosols observed over the European continent. More than 30 important cases have been analyzed, using lidar and ancillary data (sun photometers, satellite and meteorological data) thus leading to major results concerning the vertical and horizontal distribution of Saharan dust aerosols over Europe. The material collected so far forms a very solid basis for a detailed analysis of Saharan dust episodes occurring over Europe. This material was published or submitted for publication to various scientific Journals (see list of publications). It was also presented, through several oral and poster presentations, mainly at the 21st International Laser Radar Conference (Qu´ebec, Canada) in July 2002, as well as at the IGAC 2002 International Symposium and the SPIE Remote Sensing of the Atmosphere Conference, both in September 2002 (Crete, Greece). A major part of this work will be submitted for a presentation at the 6th International Symposium on Tropospheric Profiling to be held in September 2003 (Leipzig, Germany). It is interesting to note the seasonal distribution of the Saharan dust outbreaks over Europe, which show a maximum during the autumn and summer months. The second activity of this work package concerns the detection of aerosols emitted by forest fires. During the project period, such aerosols were detected in more than 12 cases, the origin of such particles being mostly the U.S., Belarus and Russian wildfires, which occurred during summers 2001 and 2002. Rainy weather during autumn and winter 2002/2003 over Europe and particularly over S. Europe did not permit the detection of aerosol related to special events during this specific period. Photochemical smog episodes were detected only over Athens (13 cases), while volcanic dust was detected by several S-SE European stations during 2001 and 2002 eruptions of the Etna volcano. Arctic haze aerosols were detected over Leipzig (April 2002).

8.2 Objectives

The main objectives of this work package are focused on the implementation of a routine monitoring scheme, mainly in the south and central European region for the observation of specifically high aerosol loads in the lower troposphere, resulting from extreme dust events (transport of Saharan dust, break of forest/industrial fires, intense photochemical smog episodes, Arctic haze, volcanic eruptions, etc.).

8.3 Methodology

To achieve the objectives of this work package, 8 of the EARLINET lidar stations located in southern Europe (Portugal, Spain, France, Italy and Greece) have been selected to perform extra lidar soundings, under conditions of particularly high aerosol loads. The measurement frequency was initially set to 6-8 events/year, with 4-6 h measurements per event. Additional lidar stations were also
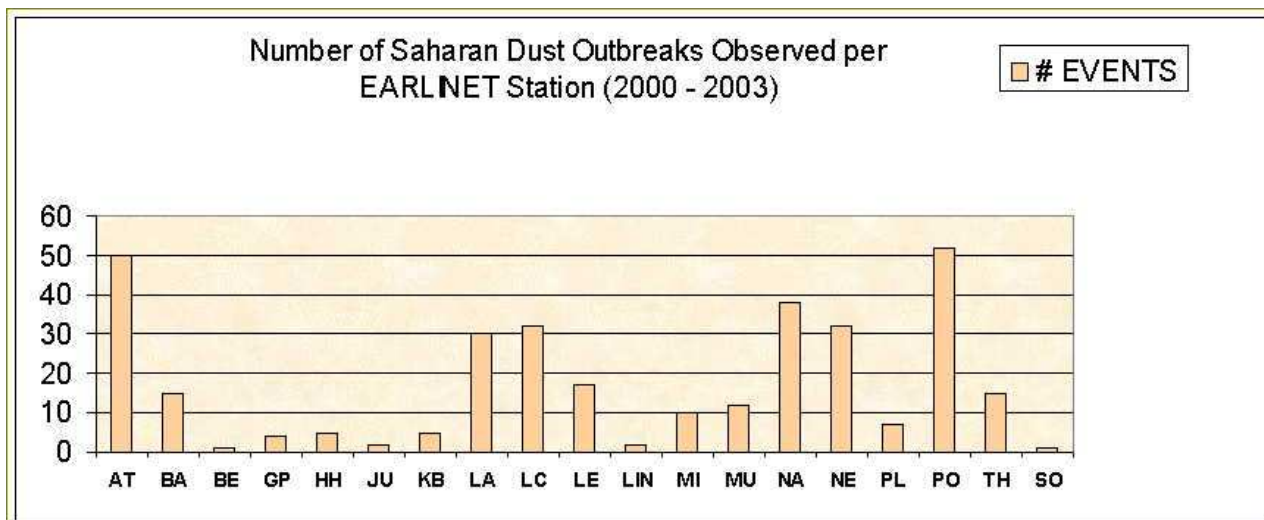
60

Figure 34: Total number of Saharan dust events detected by each EARLINET station.

selected in central and northern European sites (Switzerland, Germany, Sweden, Poland, Belarus), to investigate the long-range transport of Saharan dust aerosols across the European continent. The coordination of the special lidar measurements was performed by the NTUA group, using forecasted Saharan dust events data available on the World Wide Web (http://www.nrlmry.navy.mil/aerosol/, http://forecast.uoa.gr), validation data from satellite measurements (Aerosol Optical Thickness data: NOAA/AVHRR http://psbsgi1.nesdis.noaa.gov:8080/PSB/EPS/Aerosol/data/aerday.html; Aerosols Index data: http://jwocky.gsfc.nasa.gov/ from the TOMS instrument; Visible Images of Saharan dust storms at http://seawifs.gsfc.nasa.gov/SEAWIFS/IMAGES/IMAGES.html from the SeaWIFS instrument; Meteorological Observations from METEOSAT satellite at http://www.wetterzentrale.de/), meteorological forecast data from ECMWF/UK, (http://grads.iges.org/pix/euro.fcst.html) and historic meteorological analysis data from Infomet, Spain (http://www.infomet.fcr.es/arxiu/).

At the final phase of the project Saharan dust forecast was also performed by the DREAM model of ICOD/Malta. Ancillary measurements included routine observations of the aerosol optical depth at several UV/VIS/IR wavelengths using automated sun-tracking photometers (including some AERONET stations) and spectral UV radiance measurements, at selected EARLINET sites (IPSL/France, INFM/Italy, AUTH/Greece).

8.4 Scientific achievements

8.4.1 Saharan dust events

The NTUA group, right from the start of the lidar measurements, on May 1, 2000, was in charge of the emission of special warnings, forecasting the time the Saharan dust events would overpass the respective EARLINET lidar sites. Figure 34 presents a summary of the Saharan dust events occurred during the project period. In total, more than 105 Saharan dust episodes (each event having a duration from 1 to 5 days) were successfully forecasted by NTUA, while 85 of them were subsequently identified and observed by the EARLINET stations. In the remaining cases no observations were possible due to bad weather conditions (rain, low clouds etc.).

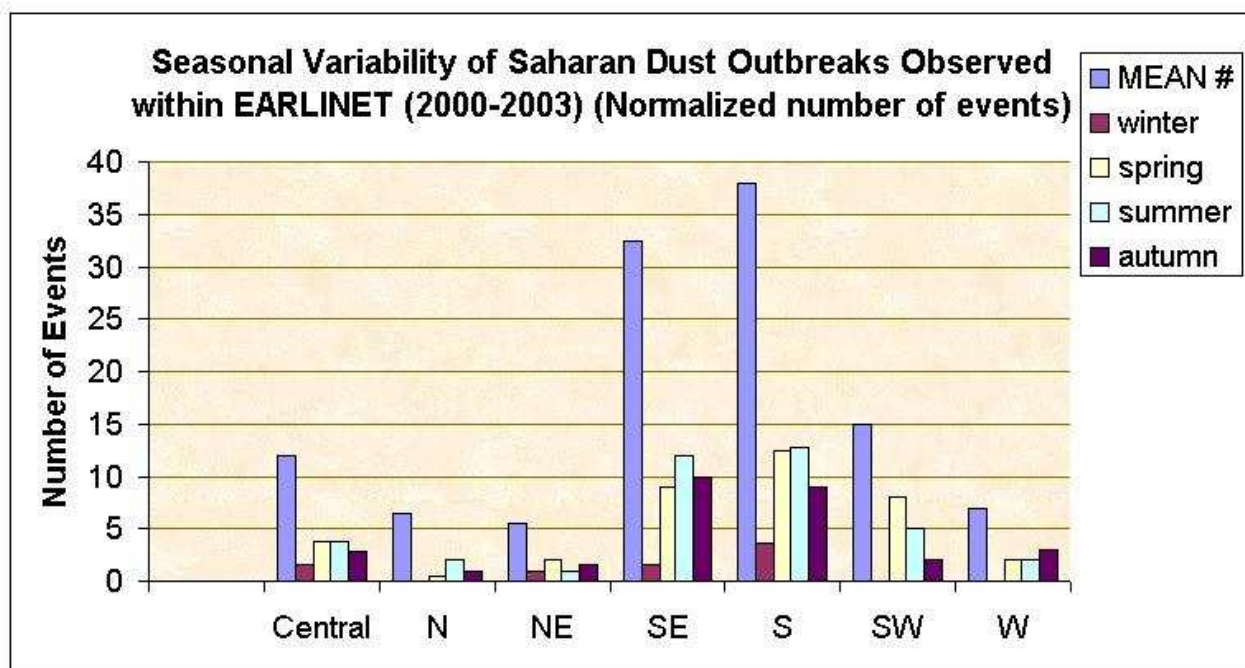Special attention should be paid to the following four special cases:

Figure 35: Seasonal distribution of detected Saharan dust outbreaks per geographical section (normalized number of events).

8.4.2 CASE I

This was a case lasting as long as five days (08-12.05.00) which was successfully followed by 7 lidar stations in south/southeastern, central and western Europe. In this successful case distinct Saharan dust layers were observed in the height region from 2.5 km up to 5 km ASL (over the Mediterranean area), while they reached heights between 3-6 km ASL, when they overpassed central Europe.

8.4.3 CASE II

This case again lasting as long as five days (01-05.10.00), was successfully followed by 3 lidar stations in southeastern and eastern Europe. In this case distinct Saharan dust layers were observed in the height region from 2.5 up to 5.5 km asl. (over the Mediterranean area), while they reached heights between 3-7 km asl when they overpassed eastern Europe (Poland, Belarus). This is the first case of a Saharan dust event to be detected by lidars, both in the southeastern (Greece) and eastern (Poland, Belarus) Europe.

8.4.4 CASE III

Case III lasted for three days (12-14.10.00) and was successfully followed by 7 lidar stations in south/southeastern, central and western Europe. Several distinct Saharan dust layers were observed in the height region from 2.5 km up to 5 km ASL (over the Mediterranean area), while they reached heights between 3.5-7 km ASL, when they overpassed central (Alps region) and western Europe.
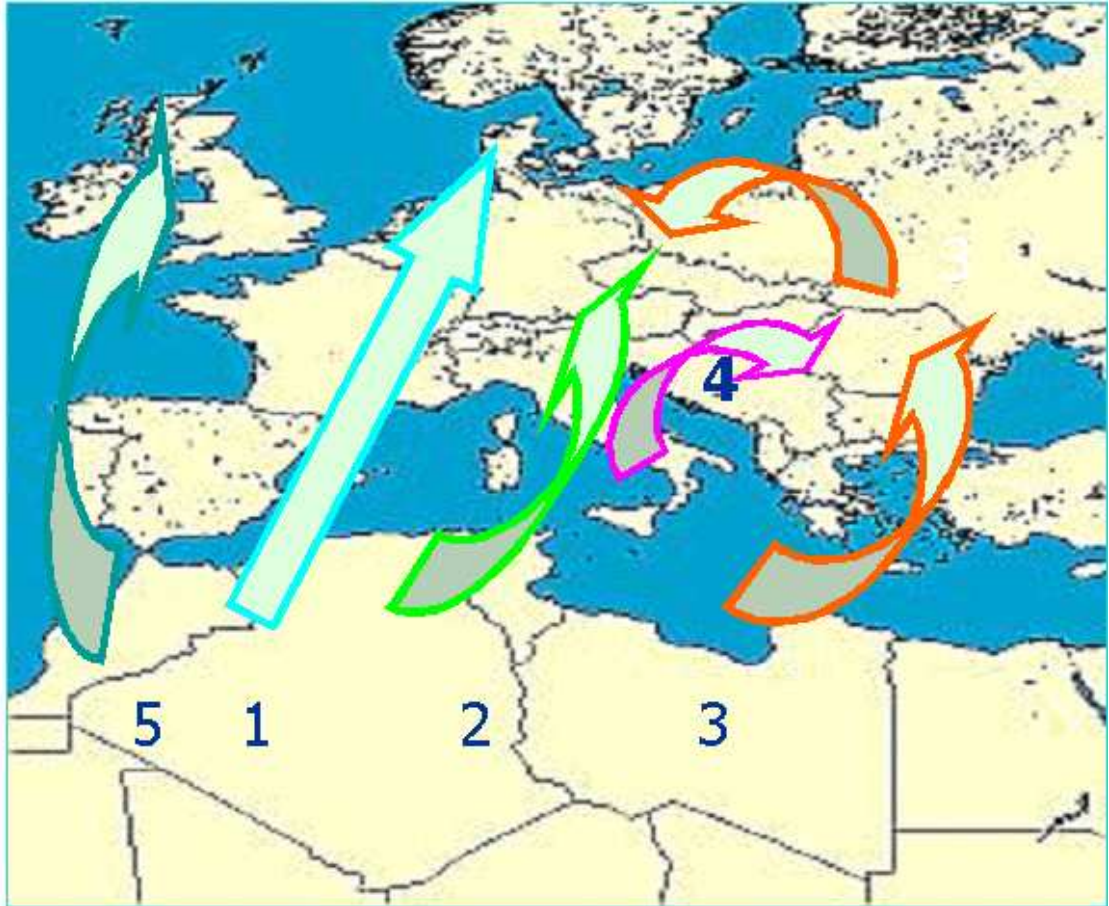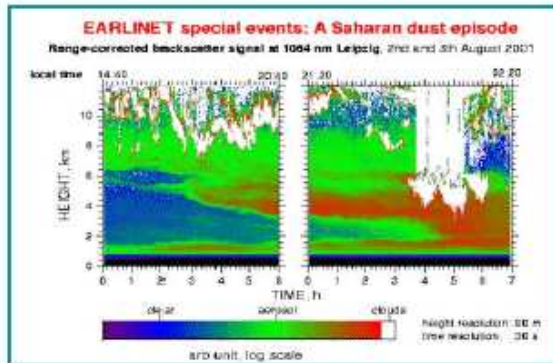
Figure 36: Main pathways of Saharan dust outbreaks to Europe.
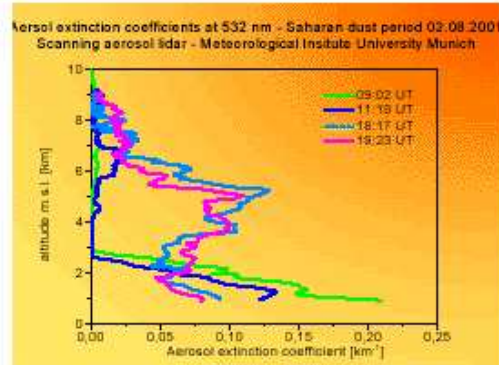
8.4.5 CASE IV

This was a major dust event case which lasted as long as 10 days (28.07-07.08.01) and was success-fully followed by 13 lidar stations within EARLINET. In this successful case distinct dust layers were observed from 2.5 to 5.0 km asl (over the Mediterranean region), while they reached heights between 3-7 km asl (and locally up to 8-10 km) when they overpassed central Europe.

In support to the lidar observations, backward air-mass trajectory analysis was performed (see section 5) by the German Weather Service (DWD), valid every day for each lidar station at 13:00 UT and 19:00 UT. In the case of the detected Saharan dust layers, nearly all backward trajectory air masses (2-4 days earlier) had the Saharan region as origin. Additionally, the day-to-day analysis of the available meteorological and satellite observations (i.e. TOMS aerosol index, NOAA aerosol optical thickness, SeaWifs images) verified the lidar observations, and confirmed the horizontal extent of Saharan dust events over Europe.

It is also interesting to note the seasonal distribution of the Saharan dust outbreaks over Europe shows a maximum during the autumn and summer months (35). The main 5 pathways of the Sa-haran dust outbreaks to Europe are presented in Fig.36. Fig. 37 and Fig.38 show a selection of Saharan dust profiles, air mass backtrajectories and the corresponding satellite aerosol index data (EP/TOMS).
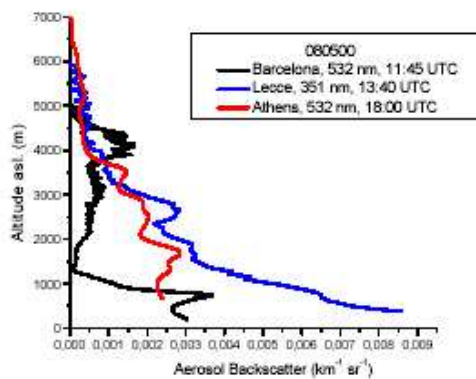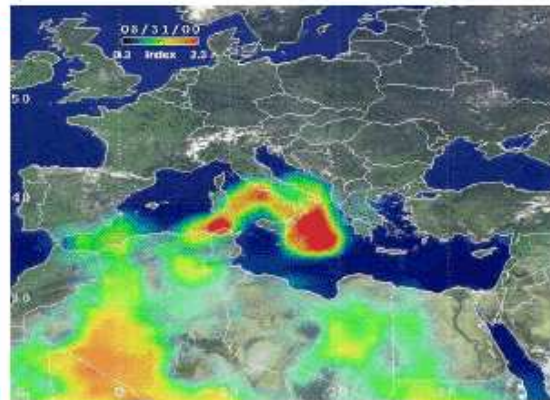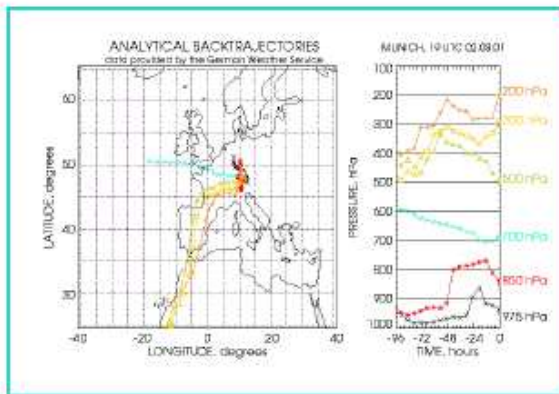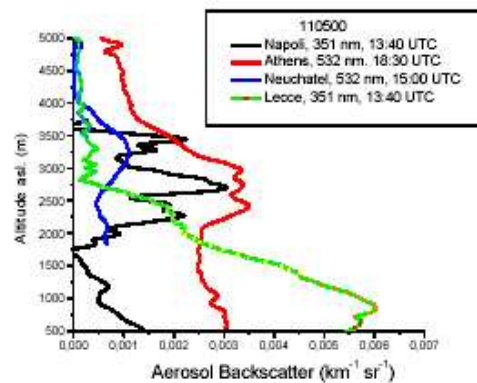
Figure 37: Selection of Saharan dust profiles, air masses backtrajectories and aerosol index satellite data (EP/TOMS).
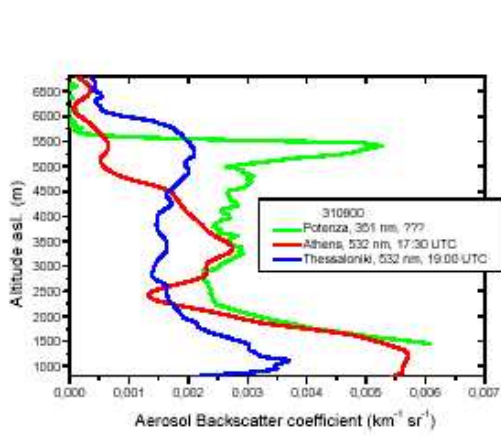
(Potenza, Thessaloniki, Athens)

(Hamburg)

(Garmish-Patternkirchen)
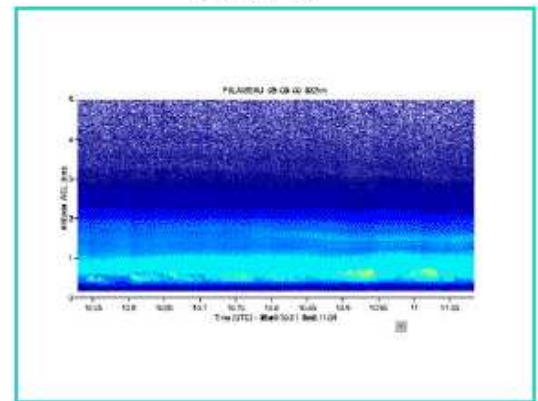
(Palaiseau)
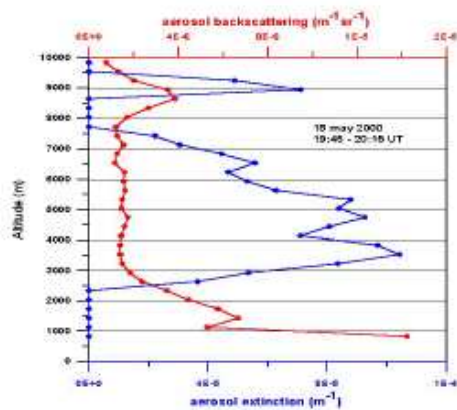
(Laquila)
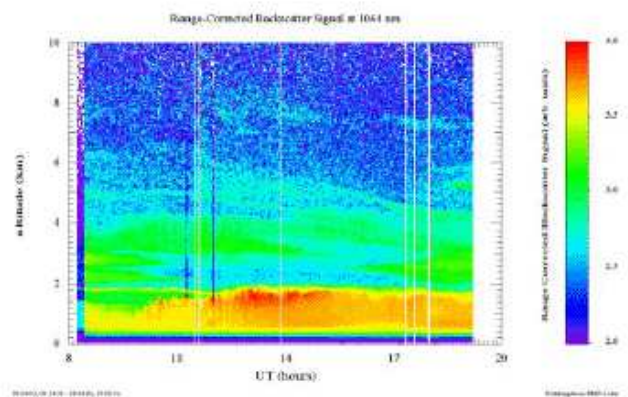
(Kuehlungsborn)

Figure 38: Selection of Saharan dust profiles, air masses backtrajectories and aerosol index satellite data (EP/TOMS).
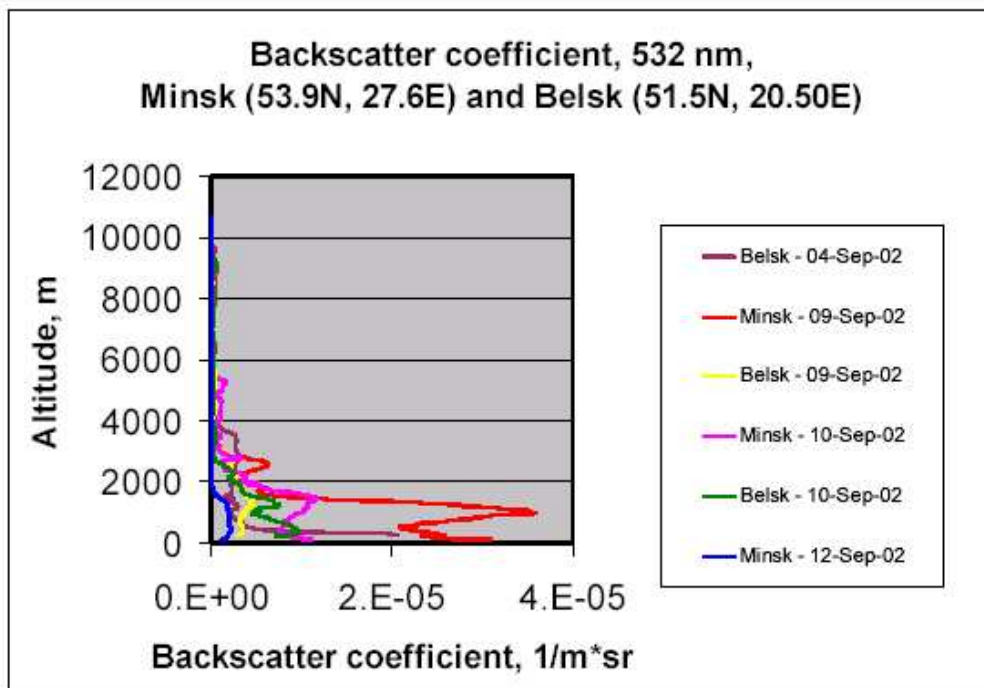
Figure 39: Biomass burning aerosols (aerosol backscatter coefficient) detected over Belarus and Poland (September 2002).
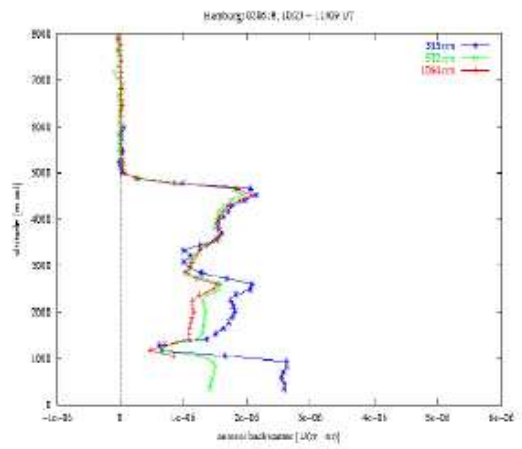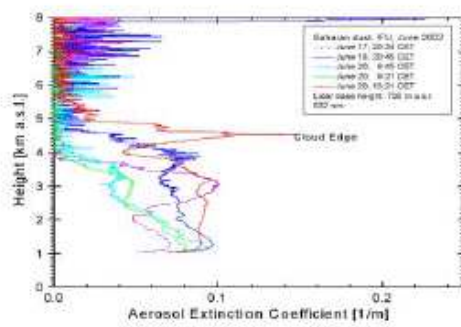
8.4.6 Forest fires

In addition, during the project period, several plumes from forest fires were observed by the lidar systems network. The largest of these forest fires occurred over United States, Belarus and Russia during summer 2002. Such aerosols were detected in more than 12 cases particularly by stations situated in central and eastern Europe. In the cases of fires in eastern Europe the corresponding aerosol optical depth (AOD) reached a value of 3 at 440 nm. Pyrogenic aerosols were found in altitudes of 1.7-2 km, while in some cases they reached 3-3.5 km (39).

8.4.7 Photochemical smog episodes

Regarding photochemical smog episodes 13 important cases were monitored by the NTUA's lidar group in Athens, Greece. In all cases the aerosol backscatter coefficients observed at 532 nm, over-passed the mean values (0.005 - 0.01 $km^{-1}sr^{-1}$) valid for the city of Athens, by a factor at least 1.5 to 3. In all cases, the highest aerosol concentrations were observed between 1.5-2.5 km ASL, around 13:00-14:00 UT, while the ABL height reached maximum values of 2.5-3 km ASL (spring/summer seasons) and 2-2.5 km ASL (autumn season) around 13:00 UT (40). These results show that photo-chemistry over Athens plays a very important role in the air pollution levels in this city.
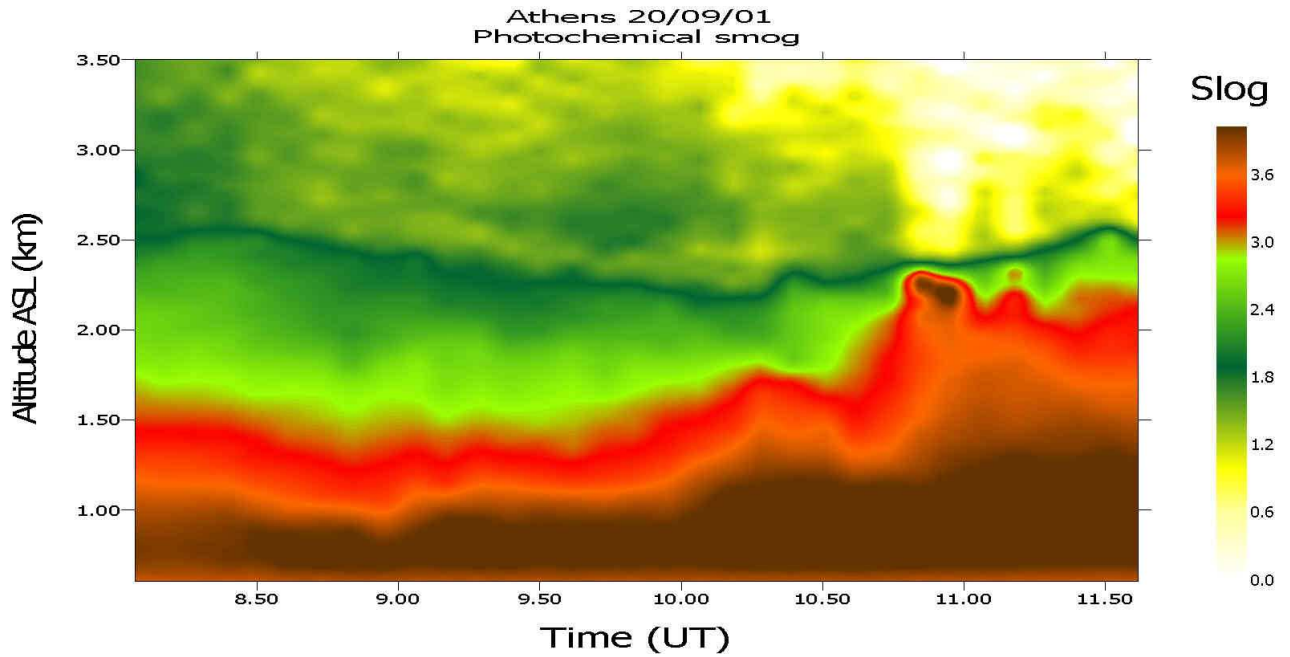
Figure 40: Photochemical smog detected over Athens.

8.4.8 Volcanic dust

Volcanic dust was systematically observed over several stations located in southern and south-eastern Europe during the Etna volcano eruption (summer 2001 and 2002). The Italian stations were the most privileged ones to follow this event, since they are located around the Etna volcano. Volcanic dust was injected and subsequently detected at altitudes between 2 and 4 km. Fig. 41 shows the diurnal variation of these aerosol layers over Athens on July 26, 2001.
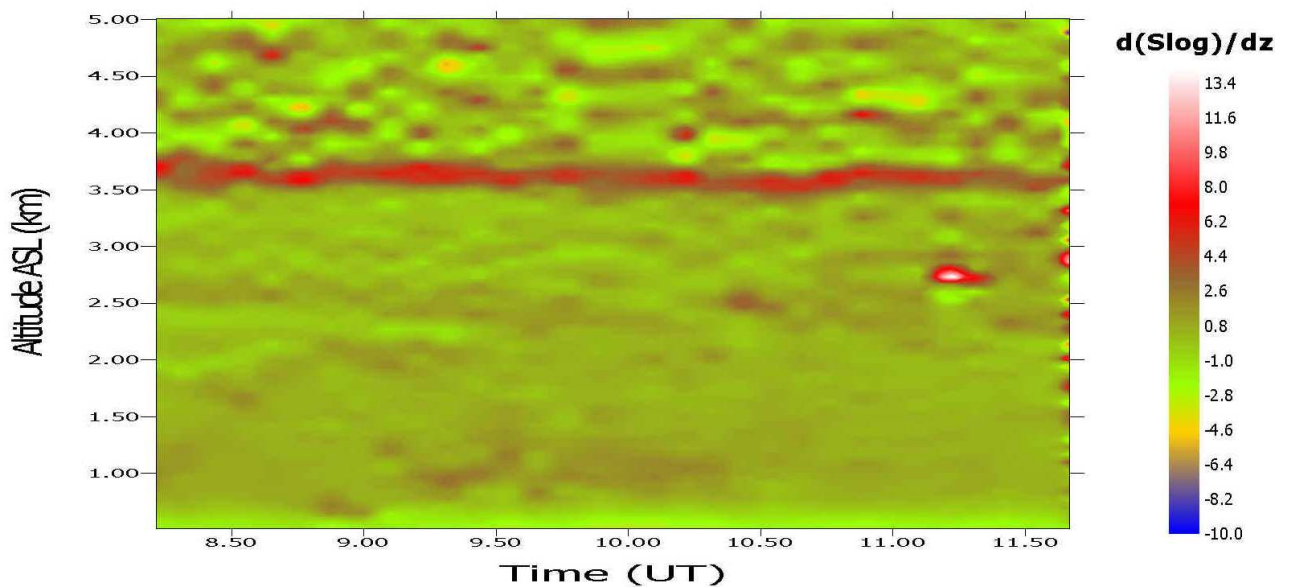
Figure 41: Diurnal variation of volcanic aerosols over Athens (summer 2001).

8.5 Socio-economic relevance and policy implication

The main direct product of this work package is a data set on the vertical, horizontal and temporal distribution of aerosols, occurred during special events (Saharan dust outbreaks, forest/industrial fires, photochemical smog episodes, volcanic eruptions, Arctic haze, etc.) over Europe. This is the first data set of such measurements on a continental scale, therefore there will be significant interest in the science community to use these data, for the improvement of global/regional atmospheric or of climate prediction models. Scientific publications and conference presentations, resulting from this work package, give the opportunity to the science community to address the mechanisms of local aerosol formation, to study the trans-boundary transport processes of air pollution over Europe and to study the impact of aerosol loads in the earth's radiation budget and their link to Global Change issues. Finally, the necessary measures could be proposed for an air pollution abatement strategy in Europe, in compliance with the EU air pollution abatement/Climate Change policy.

8.6 Discussion and conclusion

Important activities, in full accordance with the contract, were implemented right from the start of the project within this work package. The NTUA group organized the forecast procedure regarding the Saharan dust events over Europe. In total, more than 105 Saharan dust episodes were successfully forecasted, while 85 of them were identified and observed by various lidar stations around Europe. According to the observations it seems that the southern and south-eastern stations are the best located to detect such events, due to their vicinity to the Saharan region. These observations enabled the establishment of the largest data set, available so far, on simultaneous lidar observations, regarding the horizontal and vertical (altitude-resolved) distribution of free tropospheric Saharan dust layers over Europe. The Saharan dust layers were systematically found between 2.5 and 5-6 km asl. (over the Mediterranean region). They raised up to 3 to 7 km over central Europe, while overpassing the Alps, even reaching locally 8-11 km asl. The seasonal distribution of the Saharan dust outbreaks over Europe showed a maximum around summer and autumn months. Aerosols emitted by biomass burning (wildfires) were also detected in 12 cases. The origin of such particles was mostly the U.S., Belarus and Russian wildfires. Photochemical smog episodes were detected only over Athens (13 cases), while volcanic dust was detected by several southern and south-eastern European stations during 2001 and 2002 eruptions of the Etna volcano. Arctic haze aerosols were detected over Leipzig in April 2002.

For better interpretation of the lidar observations, backward air-mass trajectory analysis, as well as meteorological and satellite observations were analysed and strongly supported our observations and our conclusions about the origin of the air masses probed.

The scientific material collected so far, for all three subsets (Saharan dust events, photochemical smog episodes, forest/industrial fires), forms already a very solid basis for relevant detailed studies of the associated meteorological and photochemical processes over Europe. An important part of this material has been presented at International Conferences in 2002 and 2003 and has been (or will be) published in major international scientific journals. The output of this work package could be directly used for the quantification of the Saharan dust transported from Africa to the European continent.

9 Impact on satellite retrievals

by Matthias Wiegner

9.1 Introduction and rationale

Aerosols play an important role in our climate system by influencing the radiation budget, atmospheric chemistry and the hydrological cycle. To aim at a continuous and global aerosol climatology, satellite remote sensing is indispensable.

Spectral radiances at a satellite's sensor $L_\lambda^\uparrow$ are described by the radiative transfer equation which reads

$$\mu \, \frac{dL_\lambda^\uparrow(\tau, \mu, \varphi)}{d\tau} = L_\lambda^\uparrow(\tau, \mu, \varphi) - J_\lambda^\uparrow(\tau, \mu, \varphi) \tag{14}$$

where $J_\lambda^\uparrow$ is the source function. It is defined as

$$
\begin{aligned}
J_\lambda^\uparrow(\tau, \mu, \varphi) \;=\;& \frac{\omega_0(\tau)}{4\pi} \, E_{\odot,\lambda} \, e^{-\tau/\mu_\odot} \, p(\tau, \mu, \varphi, -\mu_\odot, \varphi_\odot) \\
+\;& \frac{\omega_0(\tau)}{4\pi} \int_0^{2\pi} \int_0^1 L_\lambda^\uparrow(\tau, \mu', \varphi') \, p(\tau, \mu, \varphi, \mu', \varphi') \, d\mu' d\varphi' \\
+\;& \frac{\omega_0(\tau)}{4\pi} \int_0^{2\pi} \int_0^1 L_\lambda^\downarrow(\tau, \mu', \varphi') \, p(\tau, \mu, \varphi, -\mu', \varphi') \, d\mu' d\varphi'
\end{aligned}
\tag{15}
$$

The terms on the right hand side of (15) describe primary scattering, multiple scattering from the lower hemisphere and multiple scattering from the upper hemisphere, respectively. The angular distribution of the scattering is given by the height-dependent phase function p. $E_{\odot,\lambda}$ is the incoming solar radiation, τ the optical depth (with $\tau=0$ at the top of the atmosphere and τ_1 at the lower boundary), and $\mu = \cos\vartheta$ and φ are the zenith and azimuth angles of the radiances. ω_0 is the single scattering albedo, describing the fraction of extinction which is not absorbed. It is also height dependent.

Introducing (15) into (14) and solving for $L_\lambda^\uparrow$ leads to

$$
\begin{aligned}
L_\lambda^\uparrow(\tau, \mu, \varphi) \;=\;& L_\lambda^\uparrow(\tau_1, \mu, \varphi) \, e^{-(\tau_1 - \tau)/\mu} \\
+\;& \frac{1}{\mu} \int_\tau^{\tau_1} J_\lambda^\uparrow(\tau', \mu, \varphi) \, e^{-(\tau' - \tau)/\mu} \, d\tau'
\end{aligned}
\tag{16}
$$

The first term on the right hand side of (16) is the contribution from the surface, the second from the atmosphere. Thus, radiances at the satellite depend in a non-linear way on properties of the atmosphere and the surface, that means, if an atmospheric parameter is to be retrieved, the surface properties must be considered as well and vice versa.

From the above it is also obvious, that the potential of aerosol remote sensing from space is controlled by the following:

- Radiances depend on the height distribution of aerosols which differs from the air density profile (Rayleigh scattering)

- Radiances depend on the optical properties of aerosols (number density, chemical composition, shape) as they determine ω_0, τ and p as a function of height

- Remote sensing is influenced by surface properties (bidirectional reflectance distribution function, orography), in first approximation the more, the higher the albedo is.

Consequently, the number of controlling variables is significantly higher than the number of observables. Accordingly, aerosol retrievals must rely on several assumptions and approximations, and therefore calibration and validation is essential.

Even the most basic optical parameter of aerosols, the optical depth, is difficult to derive. While retrievals are almost operational over dark homogeneous areas such as oceans, they are hampered over land due to the relative high and inhomogeneous surface albedo and the complex influences of the orography. As a consequence, inversion algorithms must rely on several assumptions, must apply simplifications and can only be used in special cases. Therefore, they require independent high-quality aerosol data for validation.

With respect to the vertical distribution of aerosols, satellite retrievals are restricted to the stratosphere: limb sounding can identify aerosol layers, but only with a limited spatial resolution. Thus, validation is also desirable. Satellite remote sensing of the vertical structure of tropospheric aerosols was not successful until now and is impossible in most cases for physical reasons. For this reason, lidar data can complement satellite information.

Summarizing, spaceborne aerosol observations can benefit from any additional aerosol information, be it for the validation of aerosol retrievals or as input for the satellite retrieval algorithms to characterize the state of the atmosphere (atmospheric correction). The latter is also required for remote sensing of land surfaces. EARLINET as a lidar network of more than 20 quality assured systems can offer outstanding possibilities for this purpose. This workpackage provides this link between active remote sensing from ground and passive remote sensing from space.

It should be mentioned in this context that the partnership between ground based lidars and passive radiometry has also been beneficial for EARLINET. Images of SeaWIFS were quite helpful to support the identification of Saharan dust transport over Europe – though no quantitative aerosol parameters can be derived from these data. The same is true for the TOMS aerosol index, which gives a rough estimate of the (absorbing) aerosol load and was used to trace aerosol plumes from the Sahara as well.

Due to the limited resources of this workpackage, we have focussed on potential applications of lidar data to improve satellite retrievals. Examples of our activities are briefly outlined in the following.

9.2 Ground Truth Experiments

One scientific goal of this workpackage was the performance of ground truth experiments. In this context, ground truth means that EARLINET aerosol optical properties (particle extinction coefficient $\alpha_p(z)$ or optical depth τ_p) are compared with the corresponding quantity from the satellite retrieval. This requires co-incident and co-located measurements. In particular, co-location implies some difficulties: in most cases, the spatial resolution of the satellite sensor and the lidar are quite different. In cases, where the satellite pixel is between a few and several hundreds of square-kilometers, adequate temporal averages of the lidar must be considered. Then, it is possible to determine the homogeneity and stability of the aerosol distribution and to study to which extent a validation is

allowed, i.e., whether the lidar measurement is representative for the satellite measurement or not. Only in cases of high resolution imagers (pixel diameter below 100 m) co-location and co-incidence can be strictly achieved.

To demonstrate the benefit of lidars for high resolving satellites that are primarily used for land surface remote sensing, a complete ground truth campaign was planned for CHRIS (Compact High Resolution Imaging Spectrometer) onboard of the PROBA (Project for On-Board Autonomy) Small Satellite Mission. CHRIS was launched on October 22, 2001. It provides a spatial resolution of 25 m and delivers images in 19 spectral bands between 0.4 μm and 1.05 μm under five different angles along track.

For this ground truth campaign four overpasses between May and August 2002 were envisaged. The main goal was the verification of retrievals of plant properties and BRDF models. It included a full characterization of relevant surface parameters such as leaf area index, leaf angle distribution, gap fraction, tree distribution, BRDF, and several radiative flux measurements. Radiance measurements from aircrafts were included as well as lidar measurements from the Munich EARLINET lidar group. Partners were Vito (Belgium), the Universities of Zurich and Munich (TUM) and the 'Ground Truth Center Oberbayern' (GTCO, Germering).

Unfortunately, the ground truth campaigns finally could not be performed, because – due to satellite problems – no data from CHRIS were available until October 2002.

Ground truth experiments by several EARLINET lidar stations were initiated in the framework of ENVISAT, which was launched on March 1, 2002 and carries three instruments aiming at atmospheric research (MIPAS, GOMOS and SCIAMACHY). All these instruments provide only medium spatial resolution, which in principle complicates the validation (see above).

With respect to MIPAS, corresponding activities were conducted by the EARLINET sites in L'Aquila (Rizi et al.) and Potenza (Pappalardo et al.). Since MIPAS is a limb sounder it provides vertically resolved information (nominal vertical resolution is 3 to 8 km in the range from 6 to 68 km) but the pixels are relatively large ($3 * 30$ km^2). MIPAS focusses mainly on stratospheric chemistry including measurements of O_3, N_2O, NO_2, HNO_3, H_2O and CH_4 concentrations, aerosols are only of secondary importance so that aerosol data did not become available during EARLINET. On the other hand it should be noted, that comparisons of stratospheric water vapor profiles were attempted though this task is extremely difficult because the lowest height levels available so far from MIPAS were at the far end of the lidar range.

A space mission that is more directly devoted to aerosols is SAGE III, launched December 10, 2001. It measures in limb sounding configuration aerosol extinction at 8 wavelengths in the solar spectrum between 0.29 μm and 1.03 μm. The vertical range covers the whole stratosphere, where limited horizontal resolution is not a major issue. Since summer 2002 stratospheric aerosol profiles are provided from the EARLINET site in Garmisch-Partenkirchen (Trickl et al.). They are collected to build up a long time series for validation purposes.

9.3   Radiative Transfer Modelling

The second topic of this workpackage concentrates on the modelling of the influence of different aerosol properties on radiances at the top of the atmosphere. Our investigations focus mainly on the assessment of the relevance of the vertical aerosol distribution because this is the main outcome of the EARLINET data base.

The modelling of the aerosol influence was performed with RSTAR (courtesy of Dr. Frank Wagner, GTCO). This code is based on the adding and doubling method and provides radiances with a high angular resolution. Aerosols distributions (vertical profile, optical properties) can be handled quite
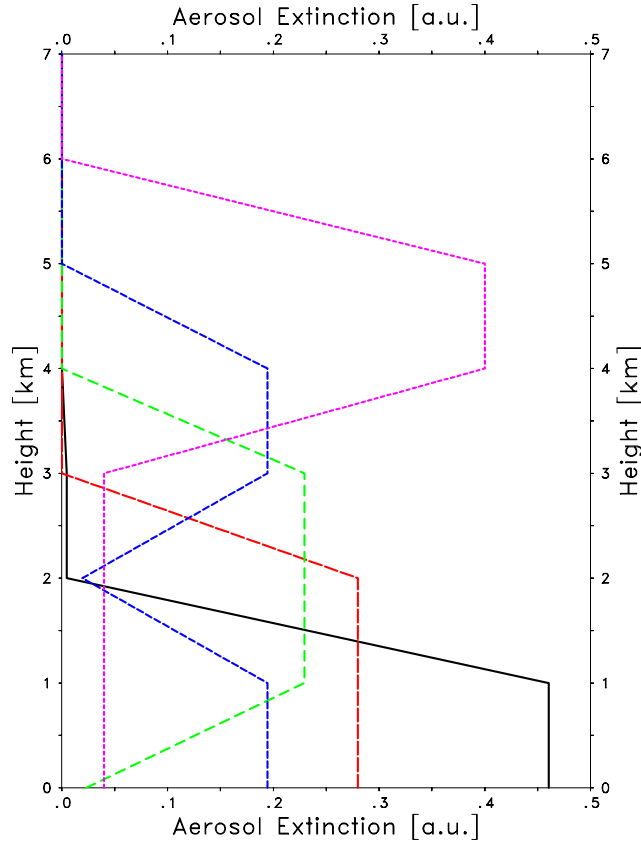
Figure 42: Vertical profiles of the aerosol extinction coefficient used in the model calculations, profile '1' is the full line: most aerosols below 1 km

flexible.

Five profiles as shown in Fig.42 were used for the simulations. Furthermore, aerosol optical depth, aerosol type (i.e., ω_0 and p), surface albedo and solar zenith angle were varied. The wavelength was selected as 532 nm.

Only two examples illustrating the influence of the vertical distribution are shown here. Fig.43 shows the difference of the isotropic radiance $L_{iso}^{\uparrow}$ (i.e., irradiance divided by π) with an aerosol optical depth as indicated minus $L_{iso}^{\uparrow}$ if no aerosols are present. Units are $W\,m^{-2}\,\mu m^{-1}$. The different lines are for the five vertical profiles from Fig.42. In Fig.43 two aerosol types, a weak absorbing (right panel) and an strong absorbing aerosol (left panel), were selected, furthermore α_{surf}=0.15 and $\vartheta_{\odot}$=32.5° were used. It can be clearly seen, that in case of nearly conservative scattering the sensitivity of the radiance on the aerosol profile is virtually zero. In case of strong absorption, the effect increases but is smaller than the sensitivity on the optical depth.

We have also modelled a situation which was frequently observed during the EARLINET project: a layer of Saharan dust. The simulations show, that in the presence of such a moderately absorbing, elevated aerosol layer the influence of the vertical distribution on the top of the atmosphere-radiance is stronger. Again, two examples are shown in Fig. 44; as in the previous figure we have considered a weak absorbing (right panel) and an strong absorbing aerosol (left panel) in the lowermost kilometer (i.e., profile '1'), and an additional layer between 4 km and 5 km of a desert aerosol. Shown are different fractions of aerosols in the elevated layer with respect to the total aerosol optical depth (as indicated on the abscissa), ranging from 1% (i.e., almost no aerosols are concentrated in the layer)

Figure 43: Change of the radiance at the top of the atmosphere in case of a weak absorbing (left panel) and a strong absorbing aerosol (right panel: profile '1' is the uppermost curve); see text for details

to 99% (i.e., almost all aerosols are between 4 and 5 km). The 99%-line is virtually the same in both panels as expected. It is obvious that in cases of a pronounced layering of different aerosol types the radiance is strongly affected. This highlights the relevance of the vertical distribution. It also shows, that the vertical distribution can significantly complicate the evaluation of satellite data: if a wrong aerosol distribution is assumed, the evaluation of satellite radiances can be misleading. Unknown vertical aerosol distributions can therefore be a serious error source.

It can be concluded from the calculations that the aerosol type and the optical depth are very important to correctly describe the aerosol influence on the radiance field at satellite level. The vertical layering is of similar importance if layers of different aerosol types (e.g. absorbing and non-absorbing particles) exist.

9.4 Conclusions and Outlook

This workpackage was very ambitious, in particular in view of the very limited resources allocated to it. Nevertheless, several ground truth experiments could be initiated. Moreover, it was outlined by model calculations how ground based lidar networks like EARLINET can lead to a significant progress in the description of the atmosphere's vertical structure and thus support satellite remote sensing algorithms.
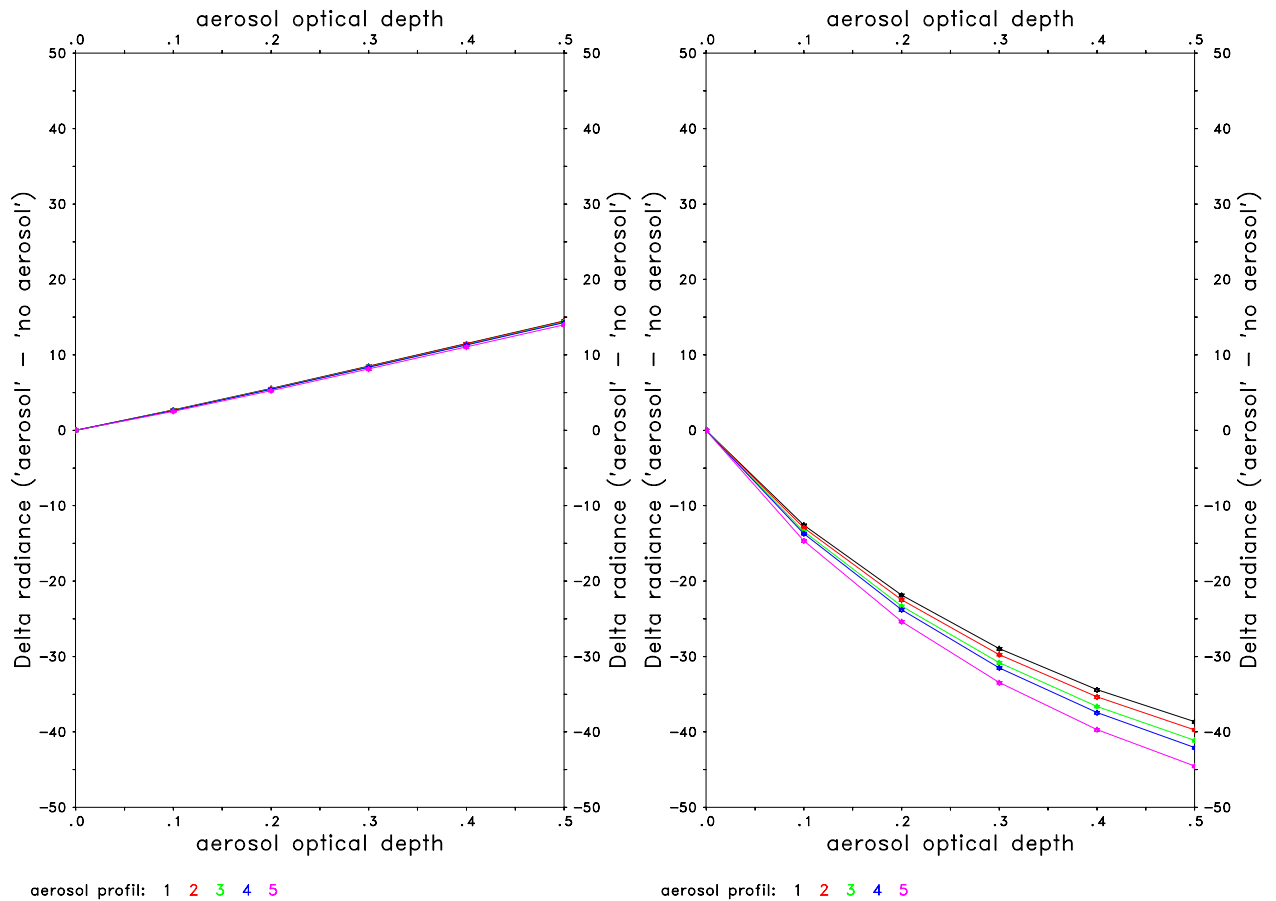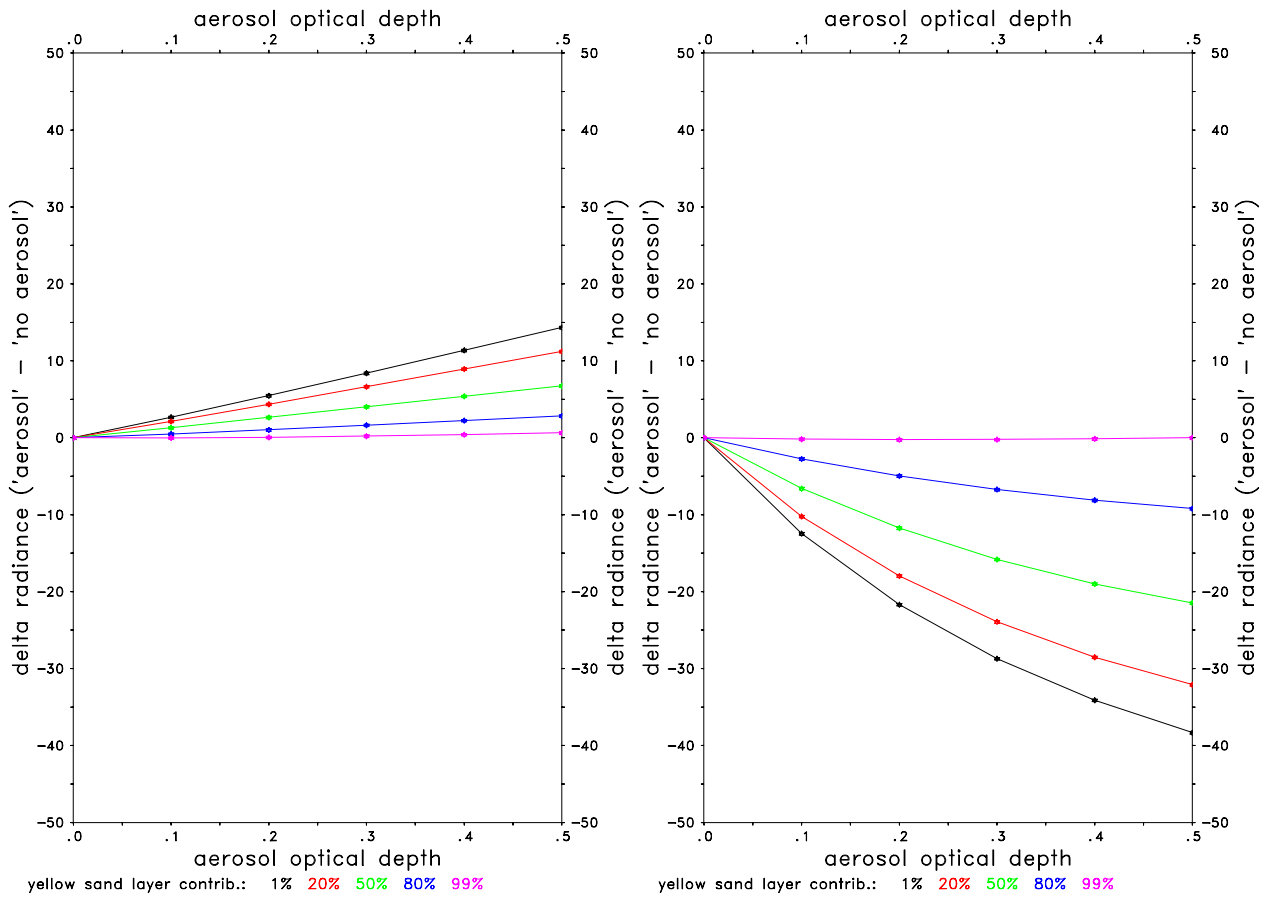
73

Figure 44: Change of the radiance at the top of the atmosphere in case of a weak absorbing (left panel) and a strong absorbing aerosol (right panel); see text for details

Within EARLINET, ground truth campaigns for MIPAS and SAGE have begun. An extensive campaign for CHRIS has failed for reasons beyond the responsibility of the contractor. The full benefit of the lidar-satellite partnership will, of course, be visible on a long term basis. For the time period from 2000 until 2002, there is a data base of high-quality aerosol profiles available. This data base offers also the possibility of validations on the basis of temporal averages: it should be investigated in future projects whether the comparison of weakly or monthly means on a larger spatial scale will be of use. On the one hand, the short term variability of the atmosphere is smoothed out, on the other hand, adequate temporal and spatial grids have to be selected very carefully. Because of different scales of variations, the benefit will depend on the quantity to be compared (tropospheric or stratospheric aerosol parameter) and will be influenced by orbital characteristics of the satellite sensor (repeat cycle). Finally, it should be stressed that joint applications of lidar measurements and mesoscale models should be exploited (data assimilation).

With the availability of data from Meteosat Second Generation (MSG) and aerosol products from ENVISAT and other polar satellites, several applications can be expected. Interesting candidates are in particular nadir looking radiometers with high or moderate spatial resolution, if they succeed to sense the troposphere. SeaWIFS, MODIS or POLDER, the latter exploiting the state of polarization of the radiation field, are promising partners for a cooperation. The main focus should be on synergistic exploitation of passive sensors with high spectral resolution, sensors with high spatial resolution and lidar data.

Another important contribution is the support of the upcoming spaceborne lidar systems. Since CALIPSO – the launch is expected for the end of 2004 – will only be a conventional backscatter lidar, the assumption of correct lidarratios will be required. EARLINET can serve here twice: first, the datasets of lidarratios build up during EARLINET can establish a basis of a climatology to be applied to the spaceborne data, and second, a follow-up of the lidar network can be used for ground truth validation.

However, due to the complexity of these tasks and the long term perspective, an EARLINET-type network should be maintained and – if possible – extended. It is hoped that the EARLINET lidar systems will remain operational at the high level reached during the last three years, and that the funding for a follow-on project can be raised. The benefit over a long period can be fully expected when partners from the satellite community can rely on a continuous flow of high quality lidar data and can consider this fact in future proposals.

10   Air mass modification processes

by Ulla Wandinger

10.1   Objectives

The distribution of the lidar network stations in Europe gives the opportunity to study the anthropogenic influence on the aerosol. Clean (pristine) air arriving from maritime and polar regions is detected by the most northerly and westerly stations. Travelling across Europe, these air masses are modified through anthropogenic activities, by which precursor gases and particles are emitted into the atmosphere. Depending on travel distance and residence time over the source regions, particle number concentrations, the physical and chemical state, and thus the optical properties of the aerosol change. The comparison of particle backscatter and extinction profiles measured at the stations in central and eastern Europe with those at the boundaries of the network permits us to quantify the anthropogenic impact on the aerosol properties. The investigations are limited to the northern part of the network, where orographic effects on aerosol modification processes are of minor importance.

10.2   Methodology

On the basis of the routine, long-term measurements at different stations (data from section 3 and 6) and an appropriate analysis of analytical backward trajectories (data from section 5), the increase of the aerosol load in air masses that cross Europe from (north)west to (south)east is quantified. In Table 10 the stations participating in this approach are listed. The stations were chosen from the

Table 10: EARLINET stations and measurement parameters for the investigation of aerosol modification over Europe

Station	Altitude, m asl	Backscatter wavelength, nm	Evaluation method	Lowest meas. height, m above ground
Aberystwyth	15	355	Raman	0–400
Hamburg	25	355, 532, 1064	Fernald/Raman	200–300
Paris	156	532, 1064	Fernald	300–600
Leipzig	90	355, 532, 1064	Raman	100–300
Munich	549	355, 532, 1064	Fernald	0–200
Belsk	188	532, 694	Fernald	200
Minsk	200	532, 694	Fernald	100

following criteria:

- The station is located in the northern part of the network. Orographic effects (mountains) can be assumed to have a minor influence with respect to aerosol modification in the air mass.

- The station delivers particle backscatter-coefficient profiles at 355 and/or 532 nm with a lowest measurement height of <500 m above ground, i.e., the planetary boundary layer is well covered by the measurements.

Linköping and Kühlungsborn were excluded from the investigation because the lowest measurement height at these stations is about 1000 m above ground. All other EARLINET stations not listed in Tab. 10 are located either within the Alps or south of the Alps and the Pyrenees.

The measurements at each of the seven stations in Tab. 10 were investigated in the following way:

- Backscatter profiles were taken from the data base (section 6) for five summer and winter seasons of the EARLINET measurement period (May 2000–December 2002). The seasons are defined as:

  - summer 2000 (measurements from May–September 2000),
  - winter 2000/01 (measurements from October 2000–March 2001),
  - summer 2001 (measurements from April–September 2001),
  - winter 2001/02 (measurements from October 2001–March 2002),
  - summer 2002 (measurements from April–September 2002).

- Only nighttime measurements, i.e., measurements taken shortly after sunset usually on Monday and Thursday within the regular EARLINET time frame, were considered. Thus a well-developed dust layer and a minor influence of the diurnal cycle (see section 7) is expected. Each individual profile was inspected. Profiles which could bias the statistical approach were omitted. Especially, profiles which did not cover the entire dust layer because of the presence of clouds below 3 km height were excluded.

- The measurements were classified with the help of the analytical 96-h backward trajectories arriving at each station at 19 UTC. Only the lowest two pressure levels, i.e., 975 and 850 hPa, were considered (see section 5). These trajectories mainly characterize the air-mass history for the planetary boundary layer below 1500 m. Typical air flows representing the transport of clean marine air masses into the European continent and the air-mass transport across western and central Europe were defined. The geographical conditions for each individual station were taken into account, e.g., by distinguishing flows from marine and continental regions.

- All backscatter profiles which belong to a specific air flow and season were averaged. The profiles were extrapolated down to the ground by assuming a constant value between the lowest measurement height and the ground. Mean profiles between 0 and 3000-m height above ground of all five winter and summer seasons as well as mean summer (from 3 summer seasons) and mean winter profiles (from 2 winter seasons) were calculated. Heights above 3000 m were not included, because air flows in the free troposphere are often different from those below, and aerosol layers in the free troposphere often result from long-range transport (see section 8 and 17).

- The mean backscatter-coefficient profiles were converted to optical depths for the column from 0–3000-m height above ground with the help of typical lidar ratios for the individual air flows (see section 17).

- For stations which provide measurements at 532 nm only, the backscatter-coefficient profiles were converted to 355 nm by the use of Ångström exponents for backscattering. The Ångström exponent characterizes the spectral slope of an optical parameter and is defined in our case as $k = -\ln[\beta(\lambda_1)/\beta(\lambda_2)]/\ln(\lambda_1/\lambda_2)$, with the backscatter coefficient β and the wavelength λ. Typical Ångström exponents were derived from measurements at 355 and 532 nm at Leipzig.

- Finally, the aerosol modification for specific flows across Europe was quantified by comparing the measurement results of the different stations with respect to mean backscatter-coefficient profiles at 355 nm, column-integrated backscatter coefficients and optical depths for the 0–3000-m height range, and mean dust-layer heights.

10.3 Scientific achievements

10.3.1 Aberystwyth

Aberystwyth is the most northwesterly station of the network and is located directly at the west coast of Wales. The arriving air masses very often did not have any land contact for several days before detection. The measurements at this site can therefore be used to define reference profiles which represent the properties of air masses entering Europe from clean environments in the North Atlantic.

Figure 45 shows the measurements of the particle backscatter coefficient at 355 nm performed at Aberystwyth in summer 2001 and in winter 2001/02 together with the corresponding backward trajectories for the 975-hPa level. Maximum values of the backscatter coefficient in the dust layer vary by about one order of magnitude. The column-integrated mean backscatter profiles were multiplied with a lidar ratio of 30 sr, which is typical for slightly polluted marine aerosols, and optical depths of 0.12 and 0.14 for the summer 2001 and the winter 2001/02 were obtained, respectively.

In Fig. 46 the mean backscatter-coefficient profiles for all five seasons are shown. Whereas the two winter profiles are very similar, the profiles of the summers 2000 and 2002 deviate from the profile of the summer 2001 and give significantly higher optical depths of about 0.2. From the trajectories shown in Fig. 45 it is obvious that the measurements in summer 2001 were mainly taken in northerly and westerly flows. In contrast, during the other two summers a considerable number of measurements were taken in southerly and easterly flows, which transported polluted air from Europe to the Aberystwyth site and caused higher mean backscatter-coefficient and optical-depth values. For all five seasons, those measurements were selected which showed the lowest backscattering values. In summer 2001, eight out of 20 measurements had maximum backscatter coefficients of <2 $\mathrm{Mm}^{-1}\mathrm{sr}^{-1}$, in winter 2001/02 only two out of 16 profiles showed such low values (see Fig. 45). In winter 2000/01, four out of 14 profiles were below 2 $\mathrm{Mm}^{-1}\mathrm{sr}^{-1}$. In contrast, in summer 2000 and in summer 2002 all profiles showed backscatter coefficients above 4 $\mathrm{Mm}^{-1}\mathrm{sr}^{-1}$. In the right panel of Fig. 46 the mean backscatter-coefficient profiles for the clean conditions are shown. For the summers 2000 and 2002 the three cleanest profiles were averaged, for the other seasons all profiles with values below 2 $\mathrm{Mm}^{-1}\mathrm{sr}^{-1}$ were taken.

Figure 47 shows a mean summer and a mean winter backscatter-coefficient profile for the clean conditions at Aberystwyth (average of all profiles with backscatter coefficients <2 $\mathrm{Mm}^{-1}\mathrm{sr}^{-1}$ observed from May 2000–September 2002) together with the corresponding backward trajectories. Two main flows, one from the north across Scotland and one from the west across Ireland, turn out to cause the lowest observed aerosol loads at Aberystwyth. The profiles shown in Fig. 47 can be assumed to represent the reference profiles for clean air that arrives at the European continent rim from the pristine North Atlantic. A mean optical depth of about 0.04 is found for both summer and winter seasons, if a typical lidar ratio for clean marine aerosols of 25 sr is assumed.

A first modification of the clean conditions directly at the continent rim was found by investigating all observations in northerly and westerly flows with backscatter values >2 $\mathrm{Mm}^{-1}\mathrm{sr}^{-1}$, i.e., non-reference or slightly polluted conditions, at Aberystwyth. The mean profiles are shown in Fig. 48. Optical depths of 0.14 and 0.15 are found for summer and winter seasons, respectively, if a lidar ratio of 30 sr is assumed. All air masses originated in the North Atlantic and the trajectories were similar to those shown in Fig. 47 for clean conditions. The increase in aerosol load can be explained by pollution uptake during the travel over Ireland, Scotland, and northern England but also over marine sites which are influenced by the dense ship traffic in the Channel and southwest of it. In addition, an increase of the concentration of sea-salt particles in the case of strong winds over the ocean has to be taken into account as a natural source.

Figure 45: Backscatter-coefficient profiles obtained at Aberystwyth in summer 2001 (upper left panel) and in winter 2001/02 (lower left panel) and corresponding backward trajectories for the 975-hPa level (right panels).

Figure 46: Mean backscatter-coefficient profiles (left) and mean backscatter-coefficient profiles for clean conditions (right) obtained at Aberystwyth during five summer and winter seasons. The optical depth (OD) and the number of averaged measurements for each profile are given in the legend.

Figure 47: Mean backscatter-coefficient profiles for clean conditions averaged for winter and summer seasons (left) and corresponding backward trajectories (right) obtained at Aberystwyth. The optical depth (OD) and the number of averaged measurements for each profile are given in the legend.

Figure 48: Mean backscatter-coefficient profiles for slightly polluted northerly and westerly flows obtained at Aberystwyth. In the right panel the reference profiles for clean conditions are shown for comparison. The optical depth (OD) and the number of averaged measurements for each profile are given in the legend.

10.3.2 Hamburg

Hamburg is located about 100 km apart from the southeastern coast of the North Sea. Two flows were investigated for this site. Northerly and northwesterly flows arriving from the North Sea were expected to represent slightly polluted marine conditions similar to those at Aberystwyth. Westerly flows originating in the North Atlantic and travelling along the northwestern rim of the European continent were used to quantify the uptake of pollution over industrialized regions in this area.

Figure 49 shows measurements of the particle backscatter coefficient at 355 nm performed under northerly and northwesterly flows at Hamburg during summer 2001 and winter 2001/02 and the corresponding trajectories of the 975 and 850-hPa levels. The respective results for westerly flows are shown in Fig. 50.

For the northerly and northwesterly flows relatively clean air was observed in most cases indeed. The column values are similar to the mean values for northerly and westerly flows at Aberystwyth, considering both the clean and the slightly polluted cases (see Fig. 47 and 48). In comparison to the reference profiles, the uptake of aerosol particles is obvious (see Fig. 51). Optical depths of 0.09 and 0.12 in winter and summer, respectively, are found assuming a lidar ratio of 35 sr for slightly polluted marine aerosols. Industrialized regions adjacent to the North Sea, the ship traffic in the North Sea, and local sources are obviously responsible for the increased aerosol load. The dust-layer height is considerably higher in Hamburg than in Aberystwyth, which is probably caused by convection over land before the air masses reach Hamburg. The convection leads to an aerosol dilution, so that backscatter coefficients observed in Hamburg at ground are similar to those of the reference profiles.

Much higher aerosol loads are observed in Hamburg when the air is advected from the west (see
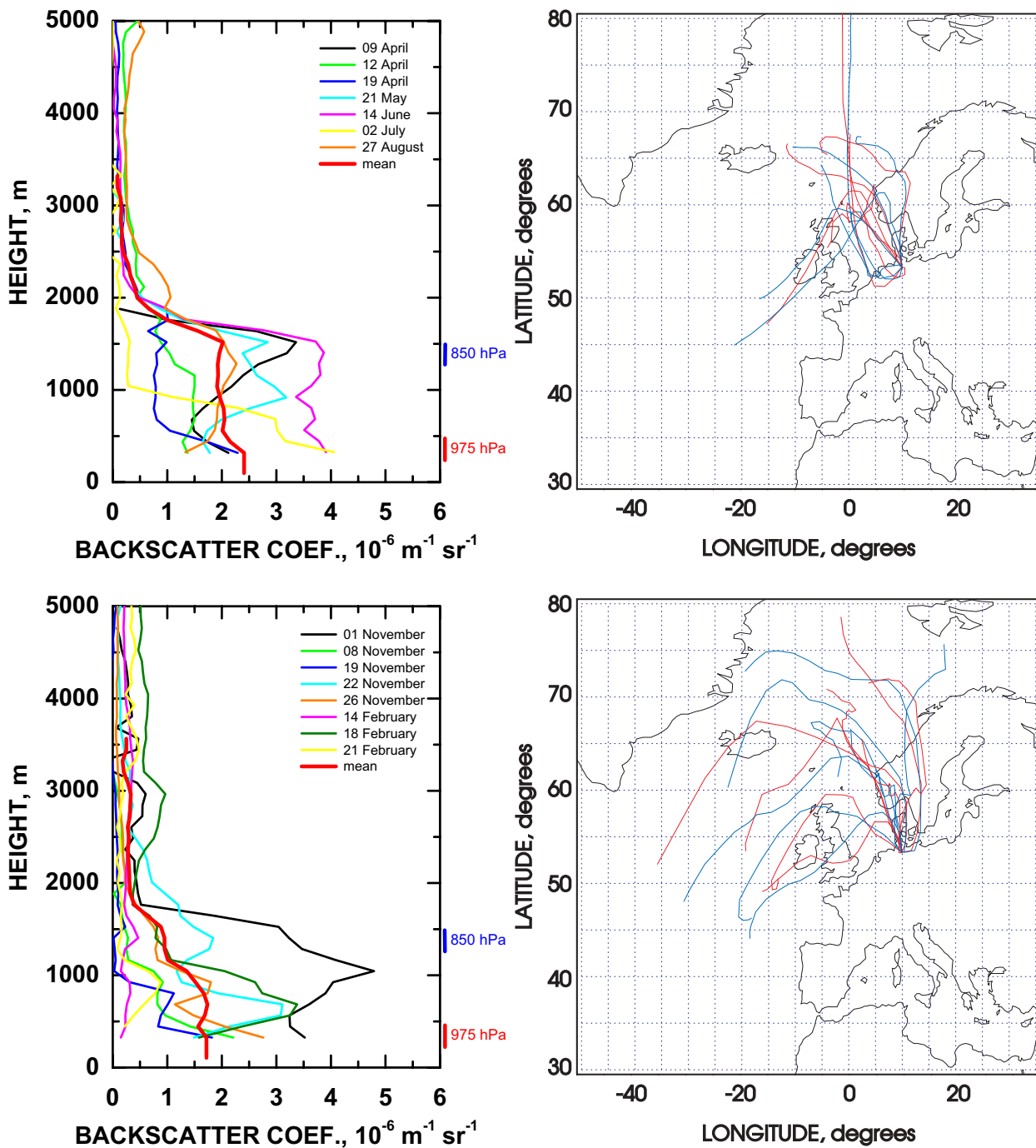
Figure 49: Backscatter-coefficient profiles obtained in northerly and northwesterly flows at Hamburg in summer 2001 (upper left panel) and in winter 2001/02 (lower left panel) and corresponding backward trajectories for the 975 (red) and 850-hPa (blue) levels (right panels).
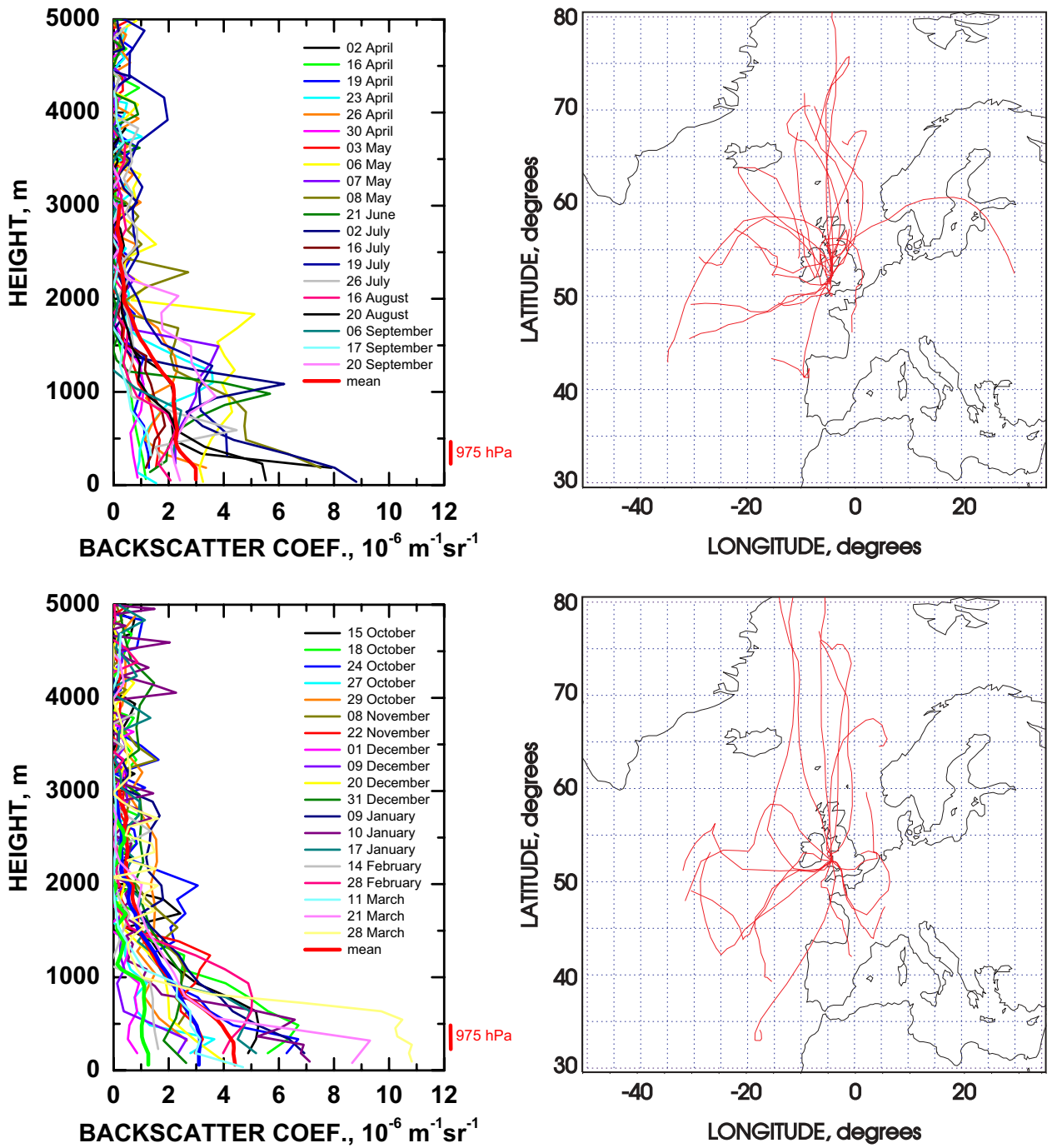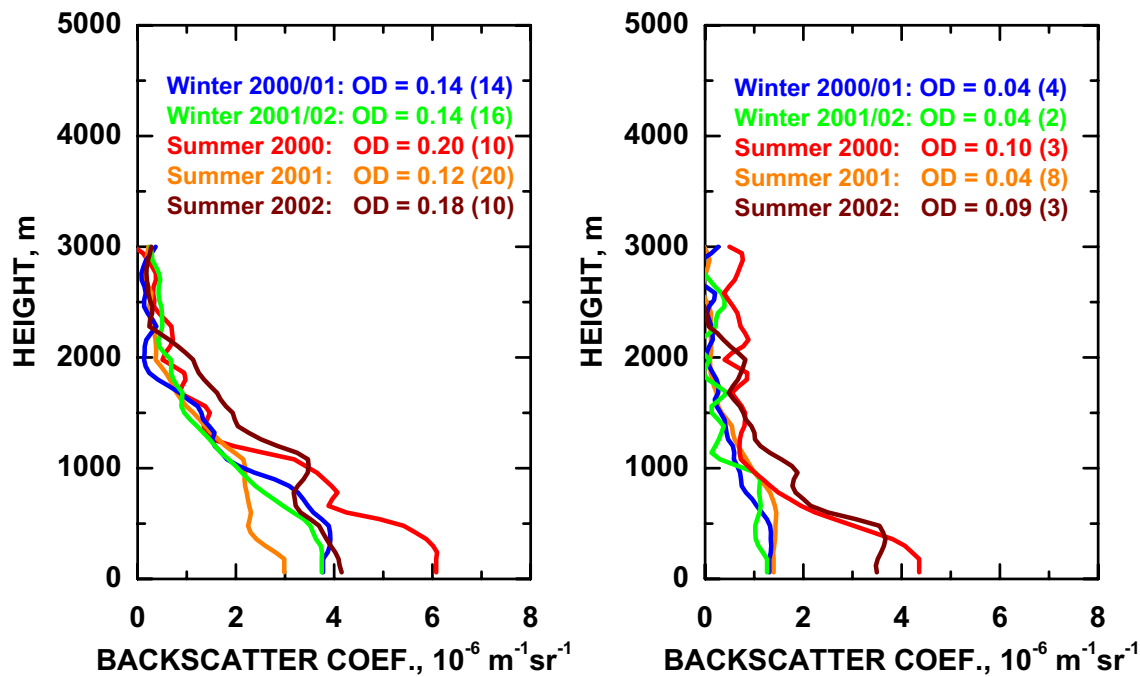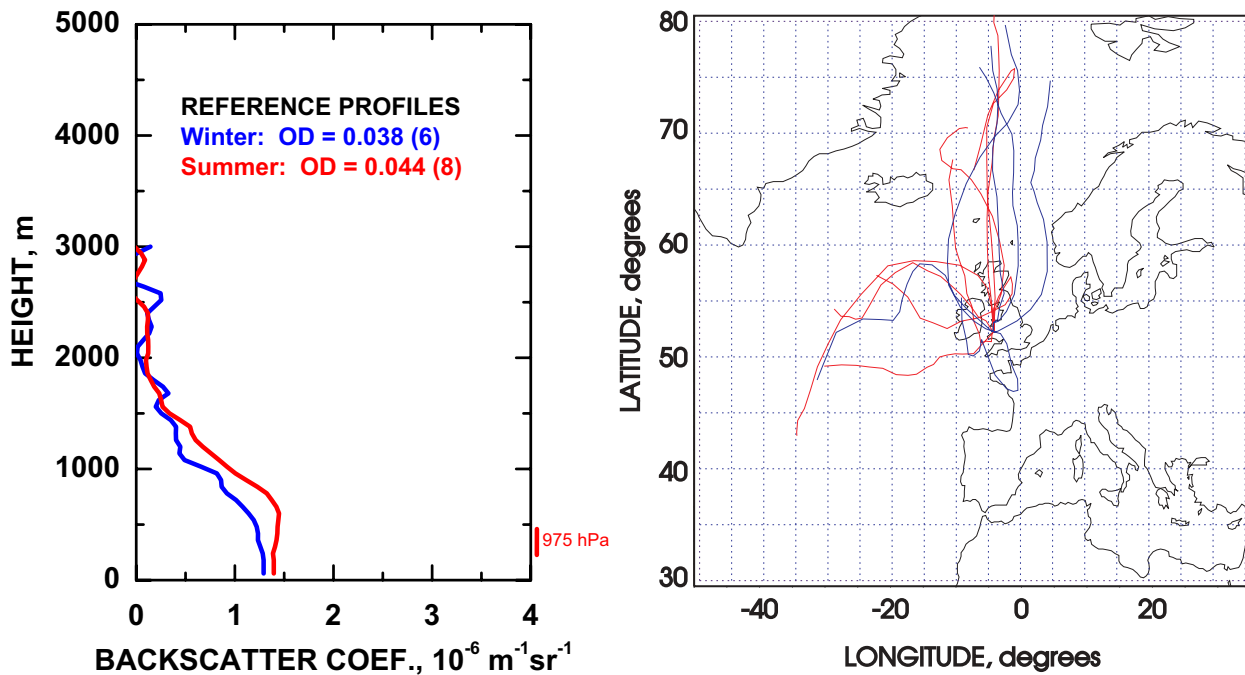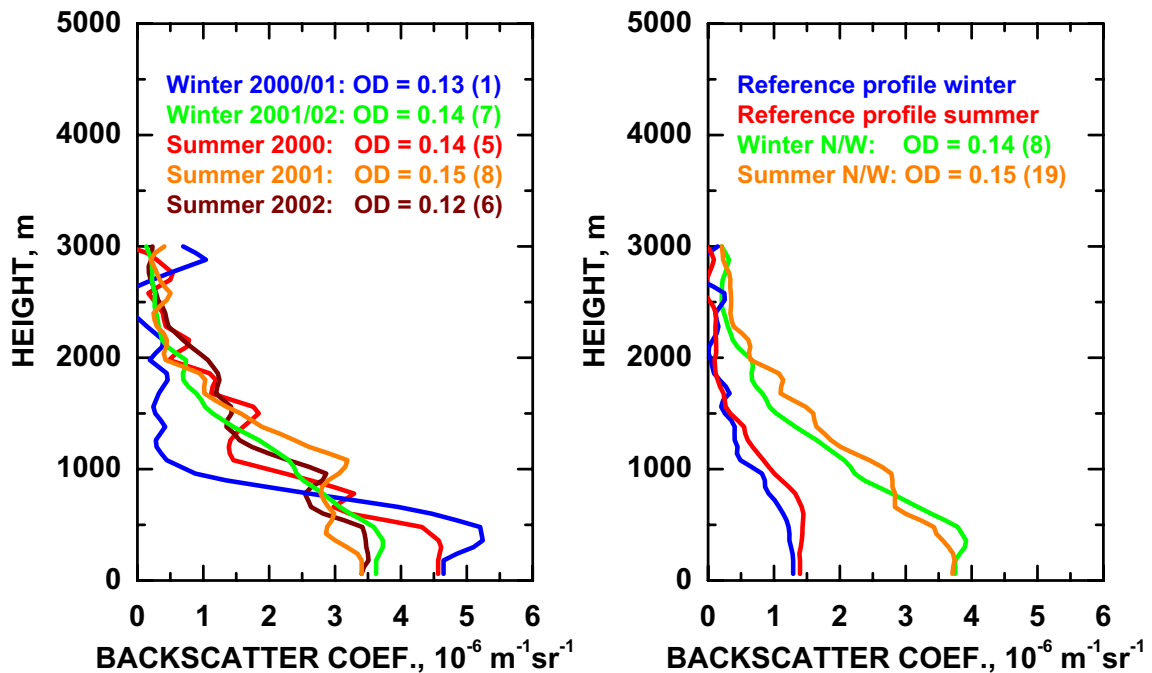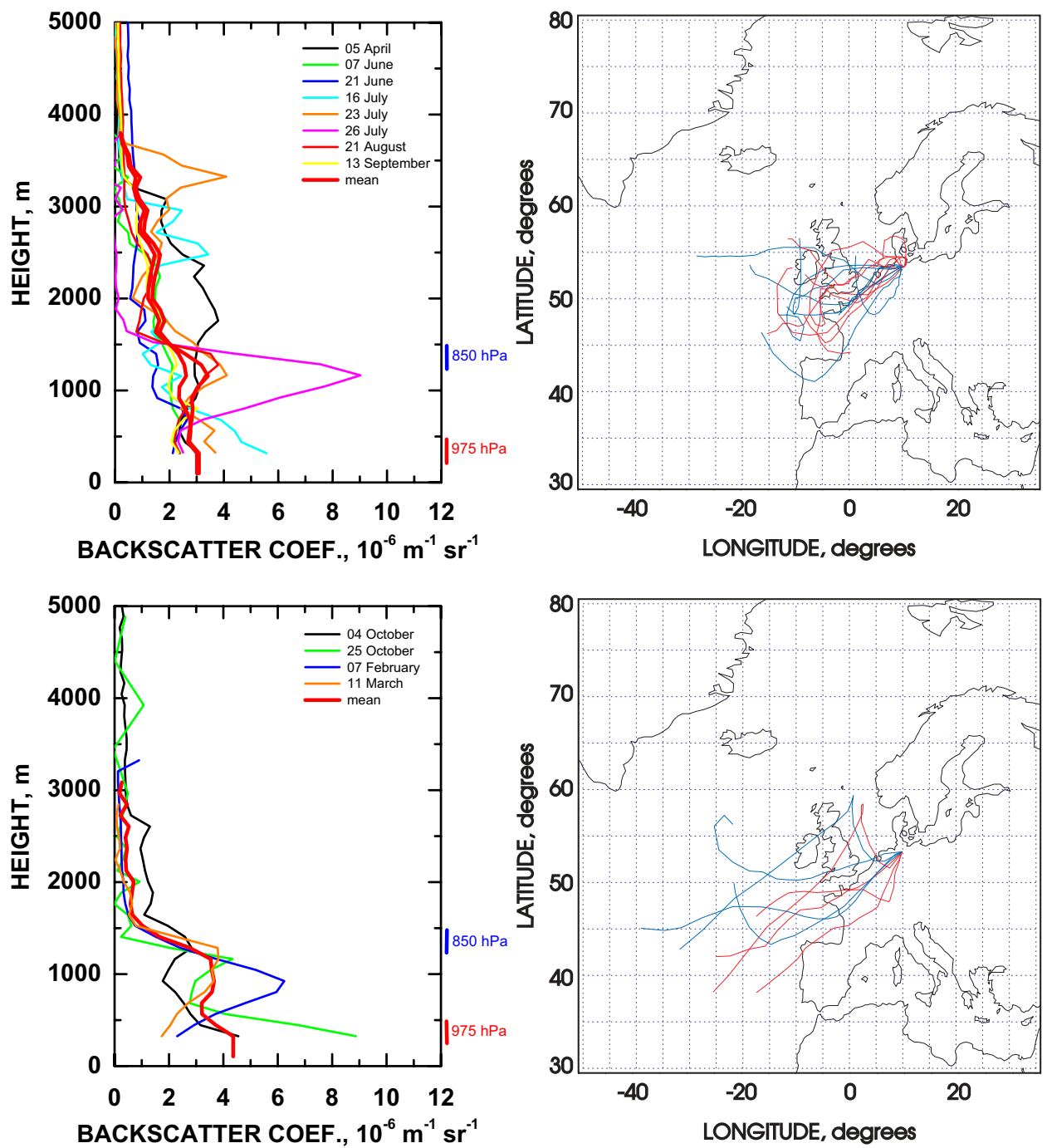
Figure 50: Backscatter-coefficient profiles obtained in westerly flows at Hamburg in summer 2001 (upper left panel) and in winter 2001/02 (lower left panel) and corresponding backward trajectories for the 975 (red) and 850-hPa (blue) levels (right panels).
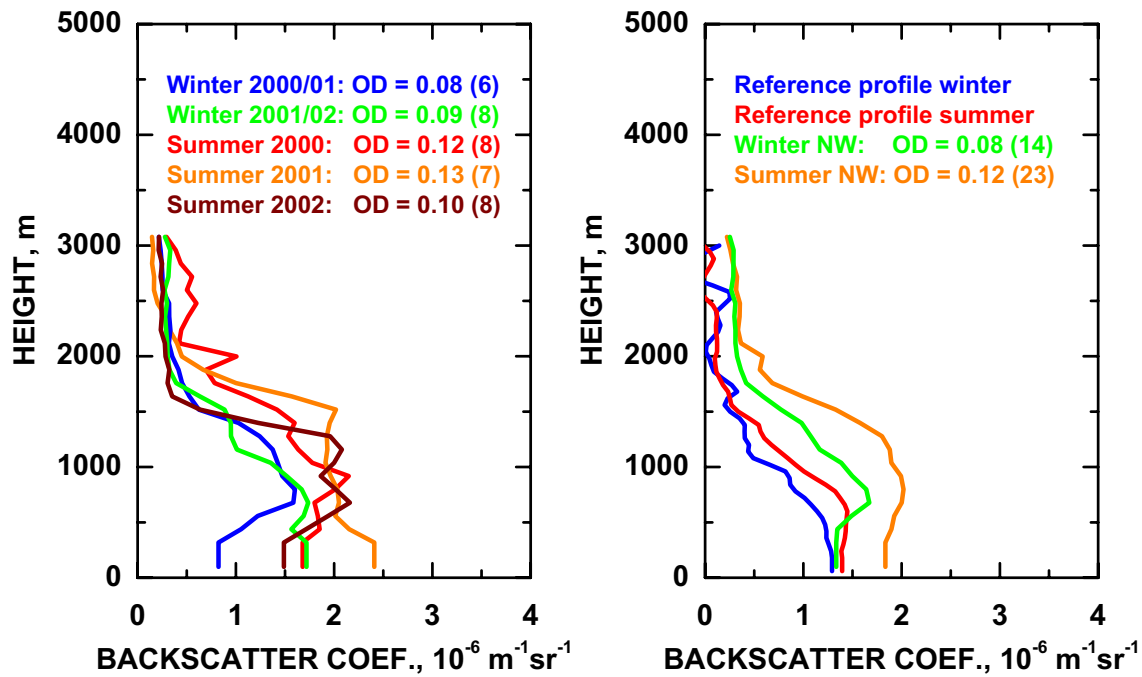
Figure 51: Mean backscatter-coefficient profiles for northerly and northwesterly flows obtained at Hamburg. In the right panel the reference profiles for clean conditions are shown for comparison. The optical depth (OD) and the number of averaged measurements for each profile are given in legend.
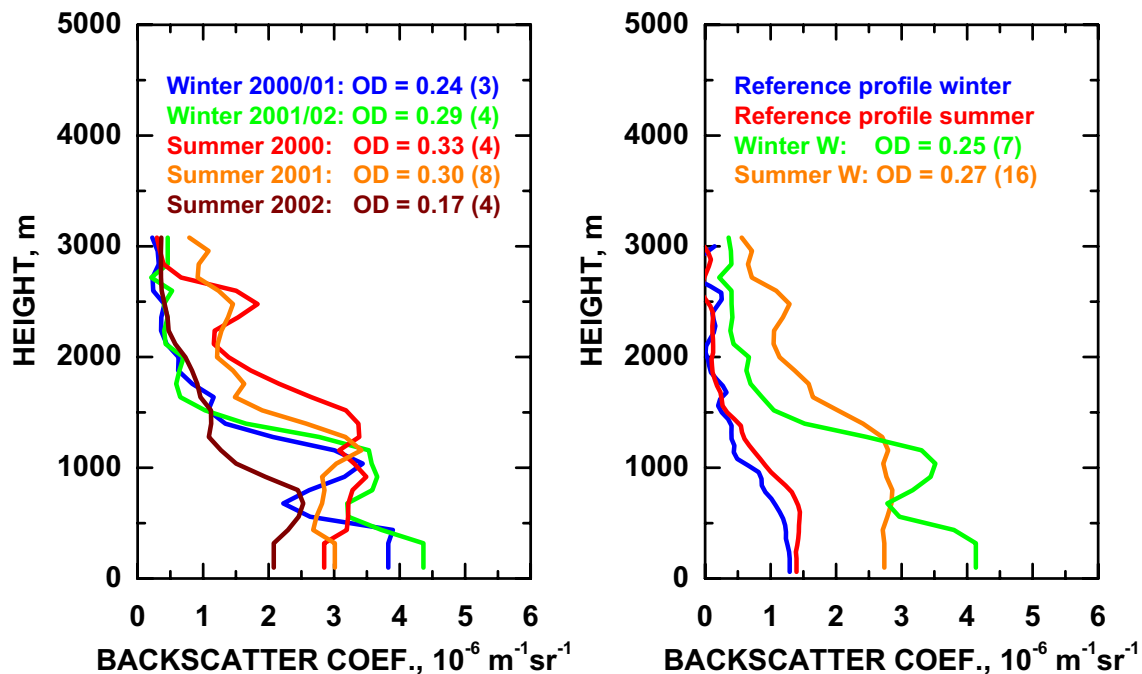
Figure 52: Mean backscatter-coefficient profiles for westerly flows obtained at Hamburg. In the right panel the reference profiles for clean conditions are shown for comparison. The optical depth (OD) and the number of averaged measurements for each profile are given in the legend.

Fig. 50 and Fig. 52). The trajectories indicate that the air masses, which originated in the North Atlantic, have passed highly industrialized regions in northwestern Europe, namely northern France, Belgium, The Netherlands, England, and northwestern Germany. The longer residence time over land leads to an increase of both aerosol load and dust-layer height. The optical depth is estimated to 0.23 and 0.25 in winter and summer, respectively, with a lidar ratio of 50 sr for polluted aerosols.

10.3.3 Leipzig

Leipzig is located in an industrialized region of central Europe. Any air arriving at this site has crossed more or less polluted regions. Three air flows were investigated in detail for this site. The first one is the northwesterly flow which brings air masses from the North Sea across northern Germany to the measurement site. The second one is the westerly flow from France, Belgium, and western Germany. In addition, local flow pattern were investigated, i.e., measurement situations during which the air masses travelled slowly for several days over central European regions.

The mean profiles for summer and winter for these three flows are shown in comparison to the reference profiles and to the profiles obtained in Hamburg for northwesterly and westerly flows in Fig. 53. The increase of the aerosol load for the air masses that cross the northwestern part of
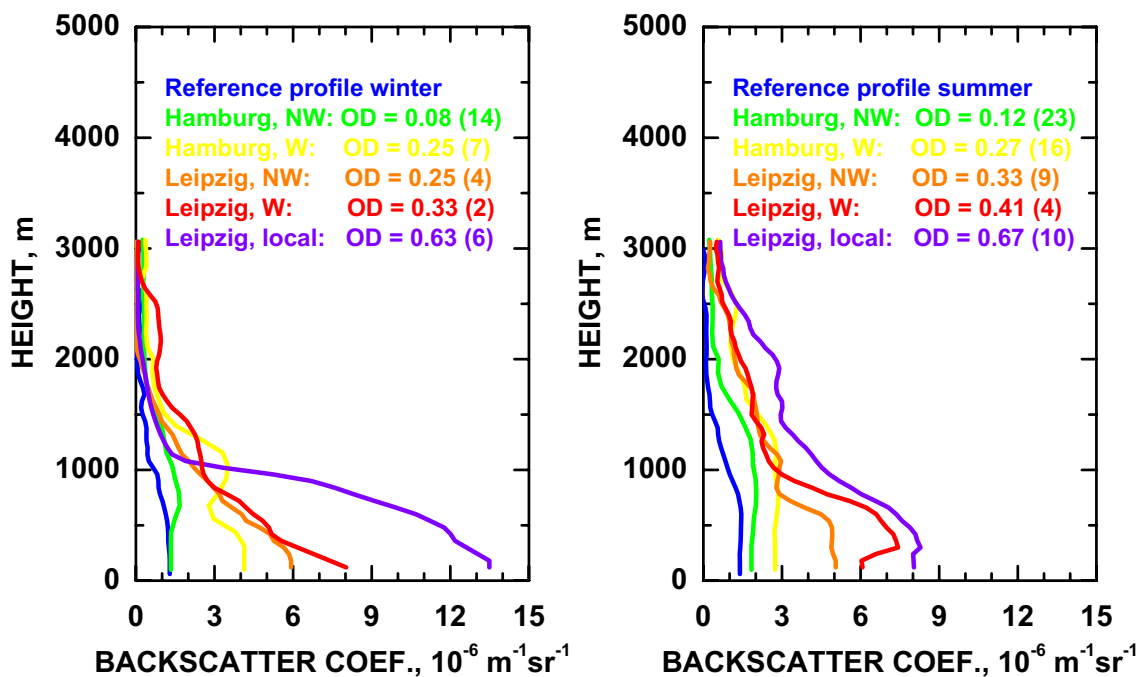
Figure 53: Mean backscatter-coefficient profiles for different flows obtained at Leipzig and Hamburg. The reference profiles for clean conditions are shown for comparison. The optical depth (OD) and the number of averaged measurements for each profile are given in the legend.

Europe is obvious. Whereas the column values are generally higher in summer than in winter, the concentration near the ground is always higher in winter. The upward mixing in the convective boundary layer leads to a dilution of the aerosol concentration in the lower heights. The enrichment of aerosols near the ground because of stable inversion situations in winter is especially visible for the local flows at Leipzig. Both a stronger mixing in summer, i.e., an increase of the dust-layer height, and a stronger enrichment of aerosol near the ground in winter is found when the air masses

have moved further into the continent. The optical depths at Leipzig given in Fig. 53 were estimated with lidar ratios of 50 sr for the northwesterly and westerly flows and 60 sr for the local flows.

10.3.4 Munich

Munich is located in central Europe far from any marine site. From the seven stations in Table 10 it has the highest altitude (549 m). Any air flow to Munich has to cross mountain sites. Even if we restrict the investigation to westerly and northerly flows, which should not be influenced by the Alps, mountain ridges of about 1000-m height will play a role for air masses transported across northwestern and central Europe to Munich. Therefore, care has to be taken in the interpretation of the findings for this site.

Four air flows have been investigated for the Munich site: 1) the westerly flow across central France and southern Germany, 2) the northwesterly flow from the North Sea region across Belgium, The Netherlands, and western Germany, 3) the easterly flow from continental sites in central and eastern Europe, and 4) local flows mainly across southern Germany. The findings are shown in Fig. 54.

In comparison to Leipzig, the observations at Munich in general show lower optical-depth values. Especially in westerly flows a very low aerosol load is observed. The values are comparable to those observed in marine flows at the continental rim. Obviously, air masses do not cross strong source regions on their way across central France and southern Germany. Local flows lead to moderate optical depths of the order of 0.2, which also indicates that the Munich site is not much influenced by strong aerosol source regions. Somewhat higher values are found for northwesterly flows which is interpreted as the influence from the source regions in The Netherlands, Belgium, and western Germany. For easterly flows, high optical depths are only observed in summer. A possible explanation is that the transport from source regions in eastern Europe, especially from the Bohemian Basin, across the mountain sites to the east and northeast of Munich can only take place if convection leads to an upward mixing of polluted air. This hypothesis is supported by the fact that the typical dust-layer height is only 200–600 m in Munich in winter, whereas in summer the aerosol typically is mixed up to 2000-3000 m above ground (see shape of the backscatter-coefficient profiles in Fig. 54).

10.3.5 Westerly flows — Paris, Belsk, Minsk

Westerly flows across the main part of the European continent were investigated with the help of measurements at the stations Paris, Belsk, and Minsk. All three station perform measurements at 532 nm but not at 355 nm. The mean profiles obtained at 532 nm were converted to 355 nm with the help of Ångström exponents of 1.5 for Paris and 1.6 for Belsk and Minsk. An increase of the Ångström exponents characterizes a decrease of the mean particle size as it is expected if marine particles are replaced by particles from continental pollution. For the same reason, a lidar ratio of 35 sr for Paris and of 60 sr for Belsk and Minsk was used to convert the column backscatter coefficient to optical depth.

The Paris region is expected to be the first highly industrialized source region which air masses cross when entering Europe from the west. The lidar station is located at Palaiseau which is to the southwest of the metropolitan and therefore not in the pollution plume for prevailing westerly winds. Westerly flows therefore represent air masses which have already passed continental sites but have not yet been strongly influenced by anthropogenic activities. The resulting profiles are shown in Fig. 55 in comparison to the profiles measured at Belsk and Minsk in westerly flows. Belsk, located south of Warsaw in Poland, and Minsk, the capital of Belarus, represent continental sites in east-central Europe. The modification of the aerosol properties in westerly flows across Europe is clearly

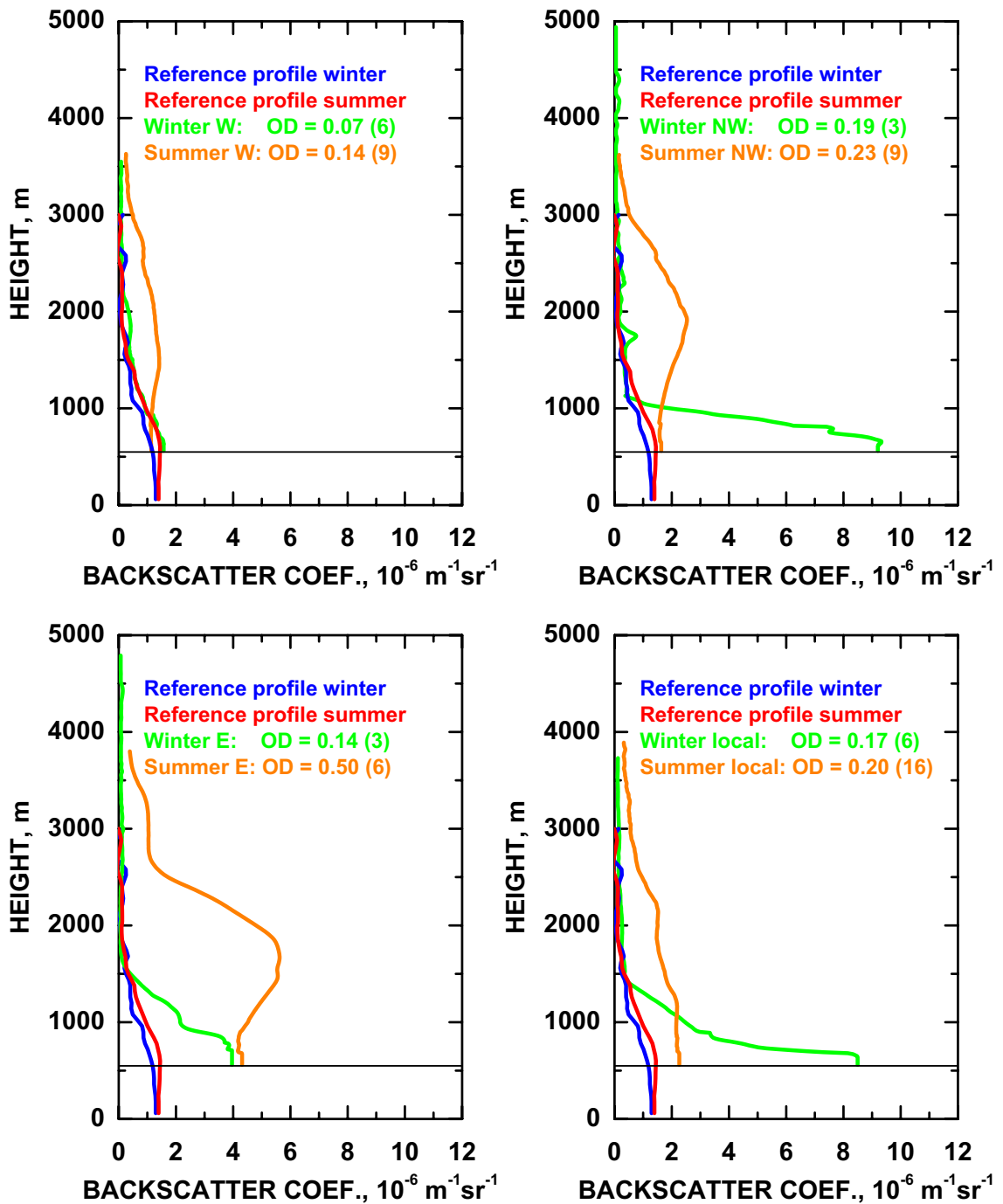Figure 54: Mean backscatter-coefficient profiles for westerly (upper left), northwesterly (upper right), easterly (lower left), and local flows (lower right) obtained at Munich. The horizontal line indicates the altitude of the lidar station. The reference profiles for clean conditions are shown for comparison. The optical depth (OD) and the number of averaged measurements for each profile are given in the legend.
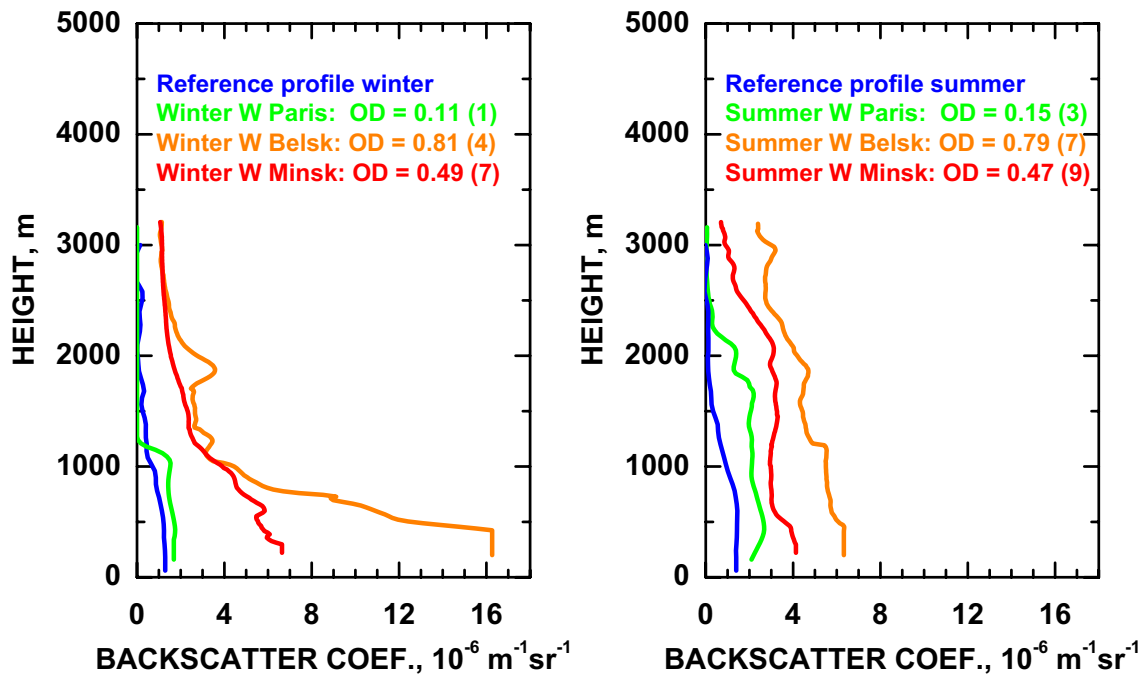
Figure 55: Mean backscatter-coefficient profiles for westerly flows across Europe as obtained at Aberystwyth (reference profile), Paris, Belsk, and Minsk. The optical depth (OD) and the number of averaged measurements for each profile are given in the legend.

visible from Fig. 55. The Belsk region shows the highest values of optical depth obtained at all. For Minsk, the values are still very high compared to most of the other stations but considerably lower than in Belsk, which indicates that the Belsk site represents the region which is most influenced from the main source regions of central Europe.

10.3.6 Summary of findings

Table 11 and Fig. 56 summarize the findings in terms of all investigated flows and the corresponding aerosol properties. In Table 11 the flows are sorted by increasing column optical properties. The typical dust-layer height is defined here as the height at which the mean backscatter coefficient has decreased to 50% of its maximum value. Fig. 56 visualizes the air-mass modification in terms of the aerosol optical depth along the different flows and indicates the core of highest pollution above eastern Germany, the Czech Republic, and southern Poland.

10.4   Socio-economic relevance and policy implication

This EARLINET workpackage delivers for the first time a coherent data set on the modification of air masses in terms of aerosol optical parameters on a continental and vertically resolved scale. The data set is of major scientific interest. It can be used to improve air-pollution and climate-prediction models, to address aerosol formation and transport mechanisms, and to calculate the impact of aerosols on the radiation budget. The data set can help to develop strategies for the reduction of air pollution in Europe.

Figure 56: Air flows across Europe and corresponding optical depths at 355 nm for winter (upper values) and summer conditions (lower values).

Table 11: Mean aerosol properties obtained at seven EARLINET stations for different air flows

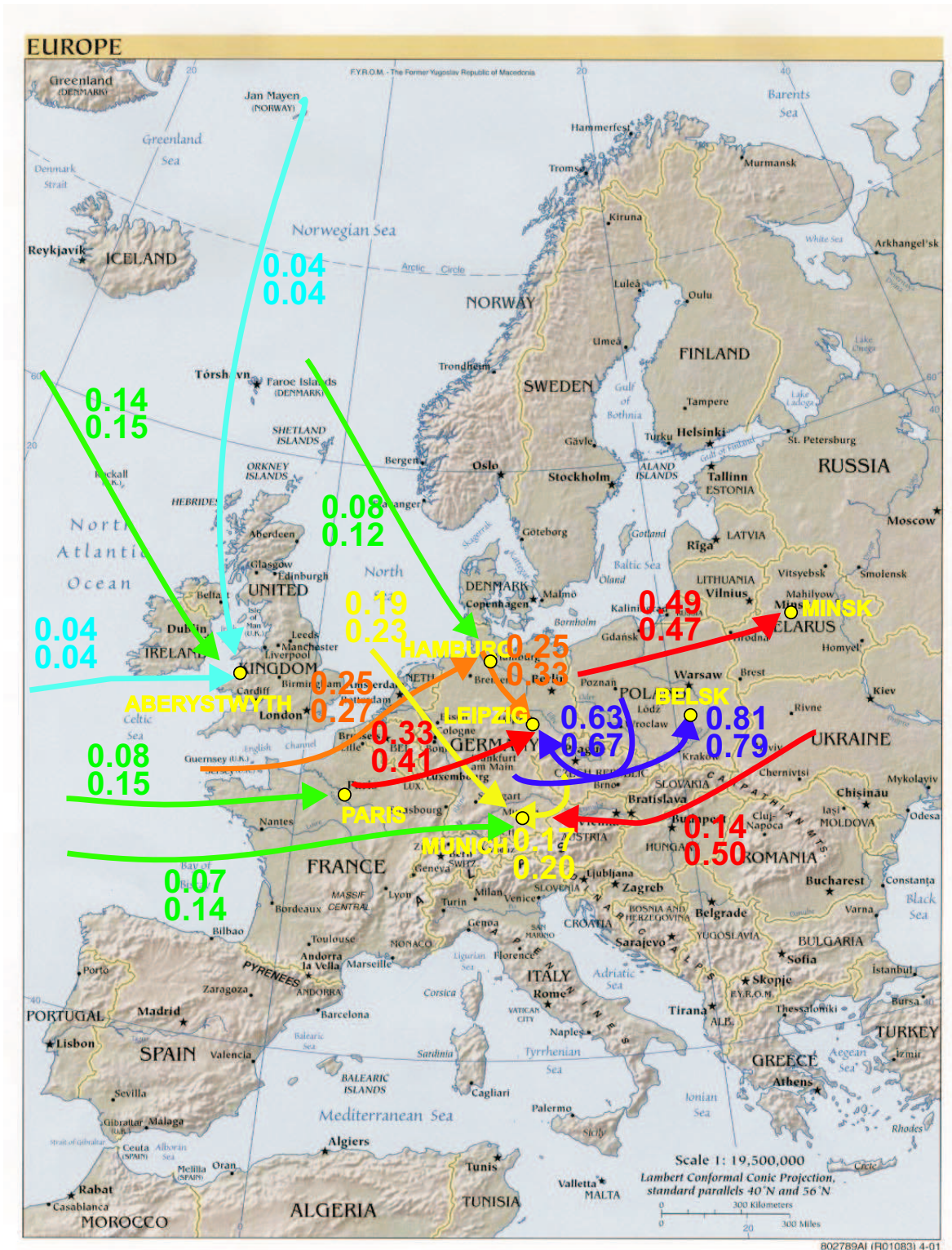| Station, flow	Integr. backsc. coef. (355 nm) 10^{-3} sr^{-1} Wi/Su	Lidar ratio (estimate) sr	Optical depth (355 nm) Wi/Su	Dust-layer height (typical) km above ground Wi/Su
Aberystwyth, N/W clean	1.6/1.8	25	0.04/0.04	1.0/1.2
Aberystwyth, N/W poll.	4.8/5.1	30	0.14/0.16	1.1/1.3
Paris, W	2.2/4.3	35	0.08/0.15	1.0/1.8
Hamburg, NW	2.4/3.3	35	0.08/0.12	1.5/1.6
Munich, W	1.3/2.9	50	0.07/0.14	0.6/2.3
Munich, local	3.4/4.1	50	0.17/0.20	0.2/1.8
Munich, NW	3.7/4.9	50	0.19/0.23	0.3/2.1
Hamburg, W	5.0/5.4	50	0.25/0.27	1.3/1.8
Leipzig, NW	4.6/6.5	50	0.25/0.33	0.8/1.1
Munich, E	2.4/9.9	50	0.14/0.50	0.6/1.8
Leipzig, W	6.7/8.2	50	0.33/0.41	0.6/0.8
Minsk, W	8.1/7.9	60	0.49/0.47	0.9/2.2
Leipzig, local	10.5/11.2	60	0.63/0.67	0.8/1.1
Belsk, W	13.5/13.1	60	0.81/0.79	0.6/2.2

10.5   Discussion and conclusion

The objectives of this workpackage were tackled on the basis of the regular measurements (section 3 and 6) and of analytical backward trajectories (section 5). In this way, statistically significant results were obtained and the aerosol modification over Europe could be quantified. Typical air flows from northwest/west to southeast/east were investigated. A strong increase in aerosol load for air masses which enter Europe from marine sites and cross highly populated, industrialized regions was found. The column backscatter coefficient increases by about a factor of 10 between the cleanest and the most polluted sites. The optical depth shows an increase of a factor of 20 due to the fact that the particle optical properties change from clean marine to polluted continental sites, i.e., the particles become smaller and more absorbing over land, which leads to an increase of the extinction-to-backscatter ratio. Column values of aerosol optical parameters are higher in summer than in winter ($\approx 30\%$) at almost all sites. Reasons might be the contribution of natural particles (biogenic particles, agricultural activities, erosion), the higher photochemical conversion rate of precursor gases into particles in summer, and/or meteorological conditions. At continental sites absolute values of the aerosol optical parameters in the lowest 500 m are a factor of 2–5 higher in winter than in summer. Inversion situations in winter and upward mixing in summer lead to an enrichment and a dilution of the aerosol, respectively.

11 Orography and Vertical Transport

by Thomas Trickl

11.1 Objectives

The local orography strongly influences the vertical aerosol distribution at stations in the vicinity of mountains. Thermally induced updrafts during daytime lead to vertical transport to, in part, considerable height and even circulation patterns may build up. During nighttime the flow is reversed pulling air from reservoir layers or the free troposphere down to the ground. For coastal stations these wind systems are additionally influenced by land-breeze - sea-breeze effects. It has been obvious that a detailed investigation of these local phenomena is essential for the understanding of the aerosol climatology of the respective station and had been, therefore, proposed by several EARLINET partners. These investigations also aimed at obtaining information on the pollution export to the free troposphere. A key topic of current atmospheric research is the hemispheric circulation of air pollution. Significant long-range transport (see also Work Package 16) takes place in the free troposphere. As a consequence, the most important mechanisms of pollution export to the free troposphere must be understood. Besides transport in frontal systems and deep convection the vertical transport in mountainous regions has been identified as one of the most efficient processes for uplifting boundary-layer air. Europe is covered by many high mountain ranges which may significantly contribute to the uplifting of boundary-layer air. The stations contributing to this work package are located within or in the vicinity of major pollution source areas which also underlines the importance of this work.

11.2 Methods

Aerosol is an excellent tracer for air pollution and atmospheric stratification, at least under conditions of low or moderate humidity. Therefore, the lidar time series, carried out at hourly or shorter intervals, are seen as the key to this work package. Meterological and complementary chemical information is provided by station measurements, radiosonde ascents, aircraft-based measurements and also backward trajectory calculations.

11.3 Scientific Achievements

11.3.1 Interaction of Coastal Winds with a Local Orographic Wind System: Barcelona

by C. Pérez, J.M. Baldasano, A. Comerón, F. Rocadenbosch

Regular aerosol backscatter measurements using an elastic-backscatter lidar were performed from May 2000 to December 2002 in Barcelona (Spain), a region with strong coastal and orographic influences. The vertical profiles retrieved on a regular schedule have confirmed the presence of multi-layered structures of aerosols above the mixing layer (ML) in numerous measurement days. The analysis of the profiles reveals that the transport of aerosols in the region is coupled to sea-breeze circulations and mountain-induced winds. Previous work interpreted some elastic-backscatter lidar vertical scans by numerical simulation of the Barcelona atmosphere with meteorological mesoscale models (Baldasano et al., 1994; Toll and Baldasano, 2000; Soriano et al., 2001; Barros et al., 2003). This study greatly extends the investigations of the multi-layer arrangement of aerosols over the city
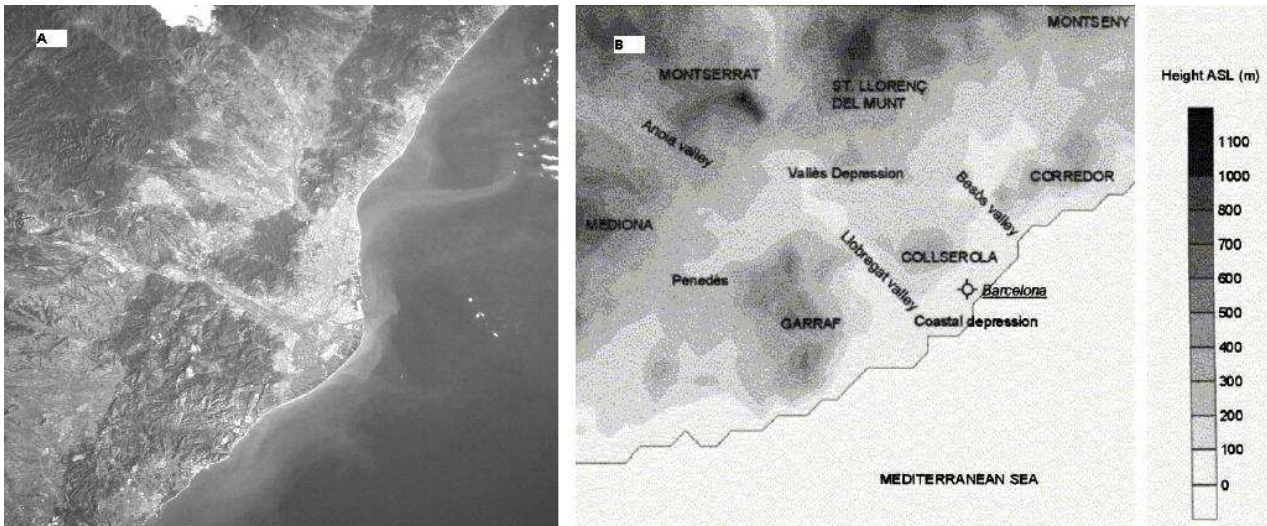
Figure 57: The Barcelona geographical area: A) Aerial view. B) Orography

which are related to the meteorological situation and the local orography. Barcelona is located on the shores of the Mediterranean Sea, on the northeastern corner of the Iberian Peninsula. Its location, together with the orography surrounding the region, contributes to the complexity of the dispersion of pollutants emitted in the region. The orography of the region is dominated by four main features arranged parallel to the coastline (Figure 57):

(1) the coastal plain, which comprises an 8 km strip of land between the sea and the first mountain range and which includes most of the cities in the greater urban area of Barcelona;

(2) the coastal mountain range with altitudes between 250 and 512 m;

(3) the pre-coastal depression, situated between the coastal mountain range; and

(4) the pre-coastal mountain range, with maximum altitudes of about 1500 m. There are two main river valleys in the area: Llobregat and Besòs. These rivers frame the city and their respective valleys play an important role in the establishment of air-flow patterns.

From spring to autumn, barometric swamps or anticyclonic situations with weak pressure gradients occur all over the region. Under this low pressure horizontal gradient scenarios, sea breeze and mountain induced winds predominate in such a way that pollutants are regionally re-circulated and polluted atmospheric layers are developed at several heights.

From 156 valid measurement days during EARLINET, 67 days presented a multi-layer arrangement of aerosols due to regional/peninsular recirculations. In some cases, the layers of regional/peninsular origin are combined with long range aerosol layers at higher altitudes (e.g Saharan dust). The resulting percentage of cases (42,9 %) is biased mainly because no measurements were performed on rainy days or with low clouds conditions. Furthermore, the measurement period did not cover three entire years and in some cases the system failed or underwent upgrades mainly in winter. Figure 58 shows selected lidar backscatter coefficient profiles averaged over 30 minutes. The profiles present vertical distributions of aerosols over the ML in layers of different height and thickness. Many aerosols are emitted into the atmosphere during the morning. As solar radiation increases, turbulence intensity increases and a ML forms. The ML over land during this time of the year in the Barcelona region grows to a maximum height of 800-1000m at about 13:00 LST (11:00 UTC) (Soriano et al., 2001).
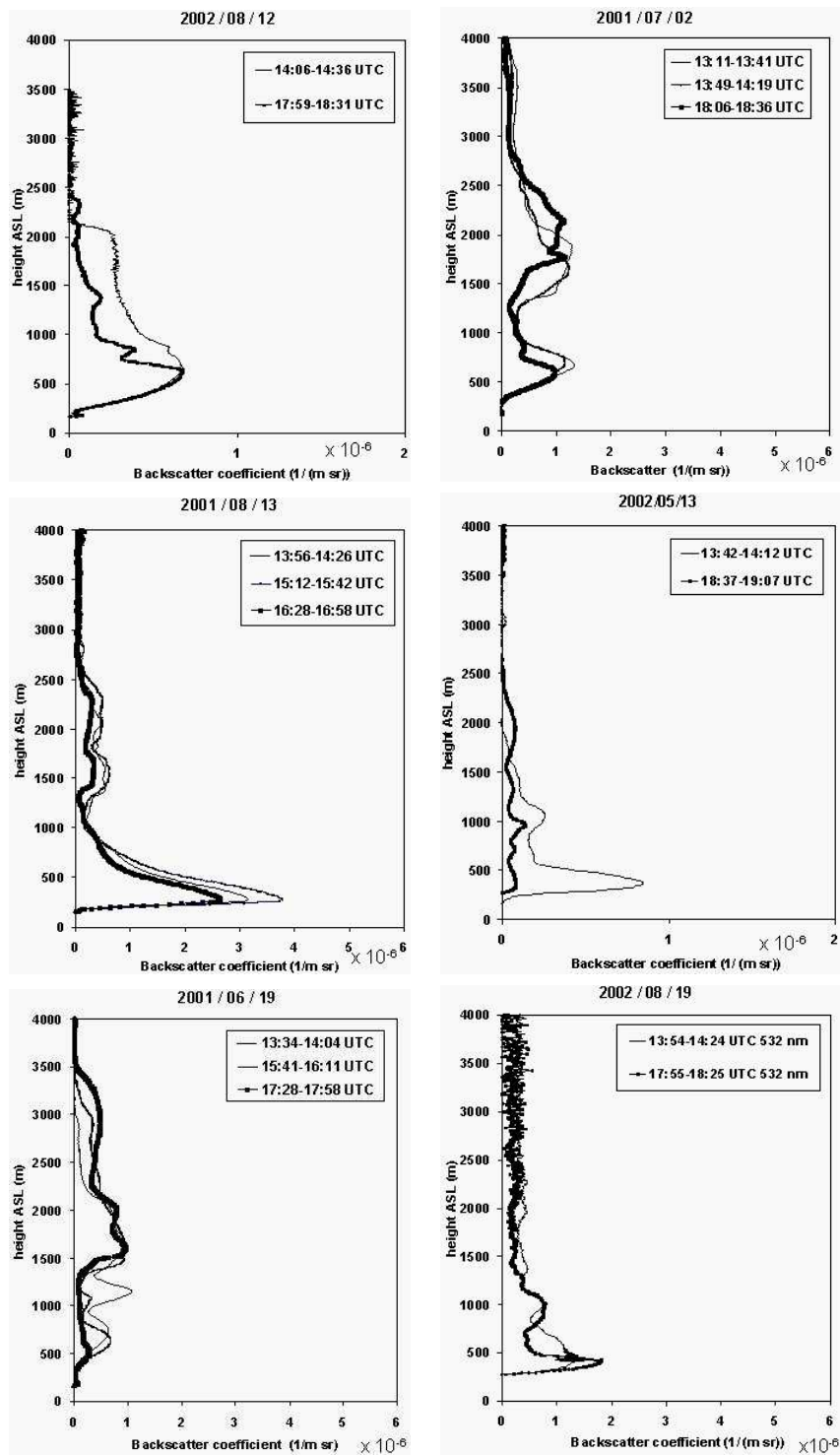
Figure 58: Selected lidar profiles: Backscatter coefficient 1064 nm or 532 nm. The full overlap is not reached up to 450 m.
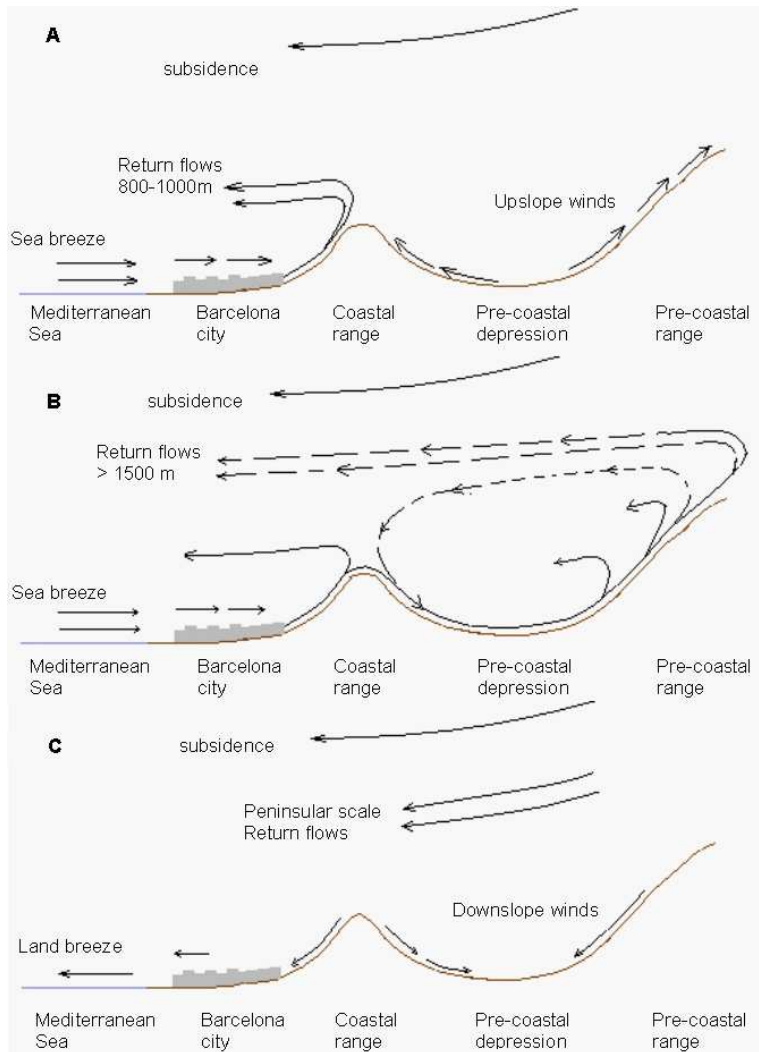
Figure 59: Schematic vertical cross-sections of atmospheric circulations in the Barcelona Air Basin during a typical summer day during (A) midday, (B) afternoon and (C) night periods.

The height of the aerosol layers vary from 1000 to 4000m and the thickness range typically from 100m to 1000m.

Information from the lidar and the numerical models were used to explain the circulatory patterns of air pollutants in the Barcelona Air Basin. Figure 59 shows schematics of the mechanisms determined as important in the development of atmospheric circulatory patterns within the Basin for a typical summertime situation.

The first mechanism is for the typical midday to early afternoon situation (Fig. 59(A)), characterized by sea-breeze inland flows, upslope winds in the mountain ranges, and up-valley winds in the river valleys. Return flows from the sea-breeze circulatory cell and from the orographic injection of the mountains of the coastal range take place between 800-1000 m, dependent on the depth of development of the circulation cell. The high-altitude situation is dominated by a general subsidence caused by the high-pressure area located above the region at the synoptic scale. The mid-afternoon situation (Fig. 59(B)) also shows a general inflow circulation typical of the daytime period. However by this time, the sea breeze has penetrated over the coastal mountains and its associated front

94
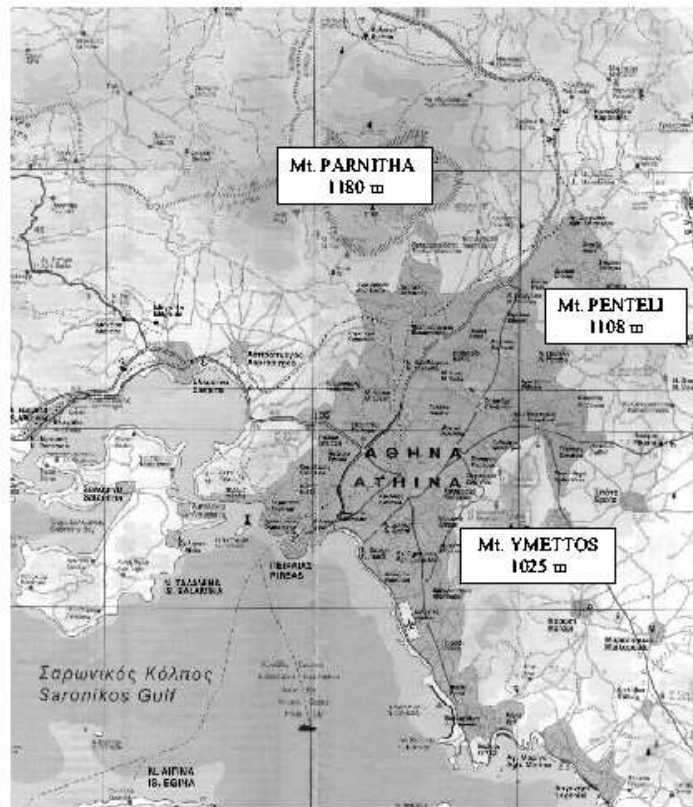
Figure 60: The topography of the Athens basin.

has reached the pre-coastal mountain range. A circulatory cell between the two mountain ranges appears. In addition, return flows produced by orographic injections of this second higher mountain range are situated at higher altitude, above 1500 m. Subsidence persists aloft. The final situation (Fig.59(C)) corresponds to the nighttime regime, i.e., the sea breeze has reversed and a general off-shore flow is now present. This offshore flow is characterized by the combined effects of land breeze, drainage valley winds, and downslope winds in the mountains. Subsidence persists on the synoptic scale, and effects from peninsular-scale phenomena are now more evident. As a consequence of the Iberian thermal low centered on the peninsula at this time of the year, pollutants from its centre rise up and then diverge toward the coast during nighttime. This return flow takes place at even higher altitudes (2000 - 4000 m) and explains some of the elevated aerosol layers imaged by the lidar. Future measurements will be performed with the recently upgraded UPC lidar system, integrating a Raman channel and scanning capabilities, in order to retrieve quantitatively optical properties of the aerosol layers and deepen in the comprehension of the transport patterns of pollutants within the region.

11.3.2 Interaction of coastal winds with a local orographic wind system: Athens basin

by A. Papayannis

The main objective of the aerosol lidar operation over Athens, in the frame of this work package, was to study air pollution export from the boundary layer into the free troposphere promoted by the mountains surrounding the Athens basin and the interaction by the synoptic wind. For this purpose more than 12 diurnal cycles were performed inside the Greater Athens Area (GAA) during the EARLINET period. Previous lidar and aircraft campaigns performed over the GAA (e.g.
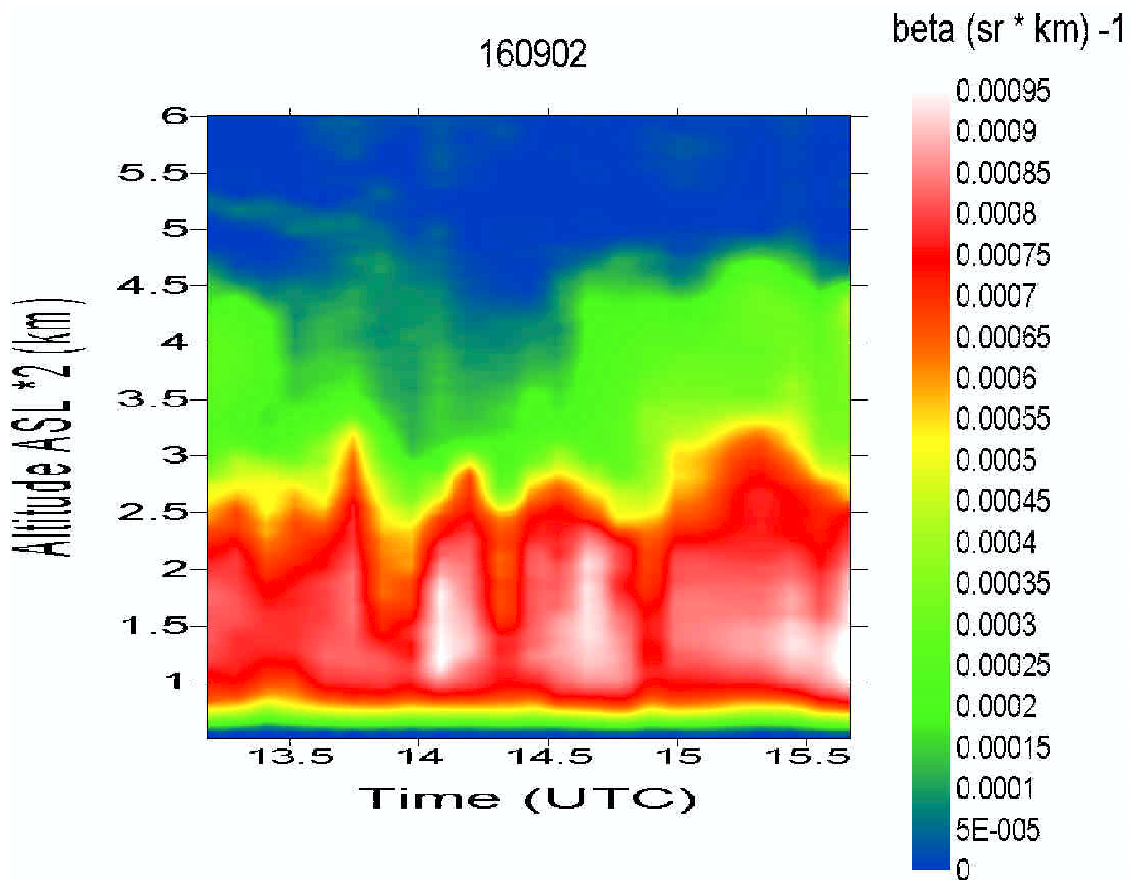
Figure 61: The temporal evolution of the aerosol backscatter coefficient over the Athens basin at 532 nm on 160902 (13:00-16:00 UT).

MEDCAPHOT-1994 and STAAARTE-HELLEN-96 campaigns) and the scientific results obtained from EARLINET measurements showed the following issues:

1) Most of the air pollutants emitted at ground within the GAA stay inside the PBL.

2) The sea-breeze circulation develops around 8-9 UT and is responsible for transporting air pollutants of various photochemical ages, further inside the GAA.

3) Under favorable meteorological conditions the sea-breeze could penetrate the entire Athens basin, resulting in an intense convergent upward flow at the foothills of the highest GAA mountains (Penteli and Parnitha mountains shown in 60. Through this process emissions from the Athens basin are transported upward, thus filling the free troposphere with high levels of air pollution at altitudes up to at least 2000 m, due to orography effects. These polluted layers can then be incorporated into the long-range transport circulation system.

4) During strong sea-breeze conditions and due to orography effects, outward flows from the GAA were observed through the valleys in between the three mountains surrounding the Athens basin (Fig. 60).

96
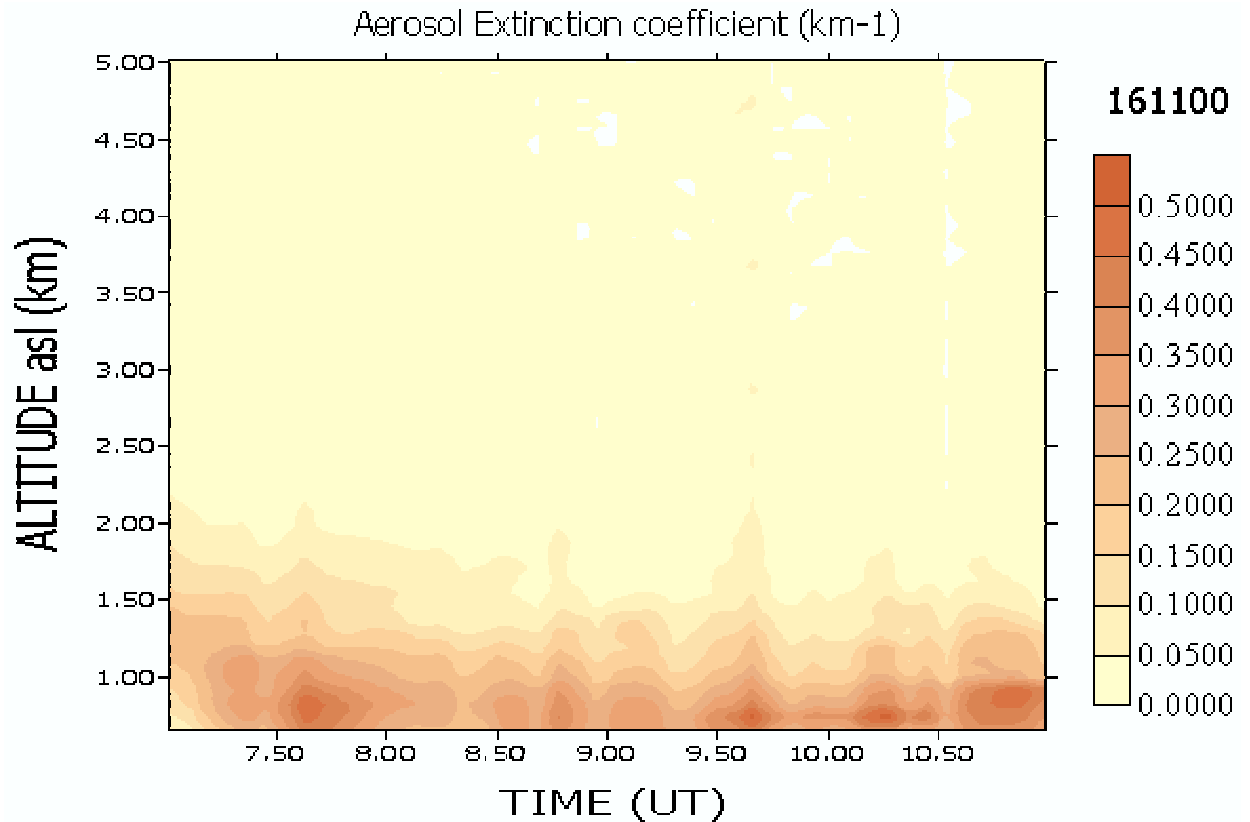
Figure 62: The temporal evolution of the aerosol extinction coefficient over the Athens basin at 532 nm on 161100 (07:00-11:00 UT).

5) Our lidar measurements over GAA validated for the first time older simulation studies by Batcharova and Gryning (1998), showing the temporal evolution of the internal boundary layer height over Athens. This simulation and our measurements showed that the temporal evolution of the internal boundary layer height over the central part of the GAA (where the lidar station is placed) is characterized by a 'pulsation' distribution, which is due to different land fetches caused by the irregular coastline and the changing wind direction (co-existence of south-west sea-breeze and northern synoptic winds occurring over the central part of the Athens basin). Some selected examples illustrating points (1), (3) and (5) are given by Figs. 61 and 62 where the temporal evolution of the aerosol backscatter and extinction coefficients at 532 nm is given over the Athens basin. Figure 61 corresponds to the day of 160902 (time period: 13:00-16:00 UT), while Fig. 62 corresponds to the day of 161100 (time period: 07:00-11:00 UT). In Fig. 61 high aerosol load is observed inside the PBL (surface up to 1.5 km), which is due to local air pollution production, while intense aerosol load is found lifted in the free troposphere up to an altitude of 2.25 km, due to orography effects. In Fig. 62 an example of air pollution export from the PBL to the free troposphere due to high convection processes inside the Athens basin is shown. The aerosol is transported up to altitudes of 2-2.25 km a.s.l. promoted by the mountains surrounding the Athens basin and the synergy of the sea-breeze circulation and the synoptic winds flow.

97

Figure 1: Sketch digram of cross section of lidar measurement site and overall topography of Neuchâtel

Figure 63: Sketch diagram of cross section of lidar measurement site and overall topography around Neuchâtel

11.3.3 Influence of the Jura mountains on the lidar observations at Neuchâtel

by S. Manoj, V. Mitev Few representative cases are presented here for lower atmosphere dynamics with evidences of orographic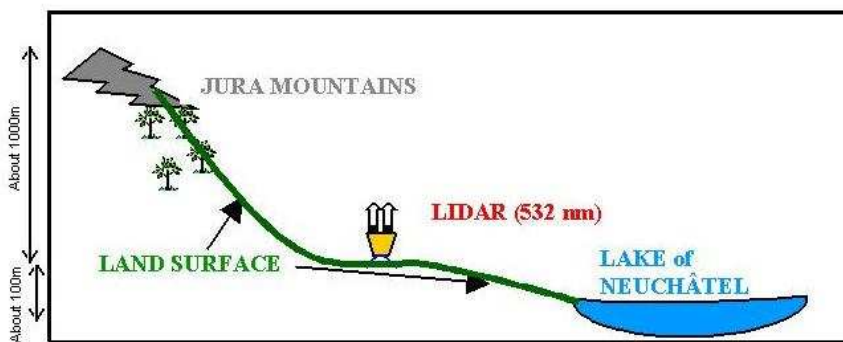 influence as observed by backscatter lidar. The observations are performed at Neuchâtel, Switzerland (47.00 N, 6.95 S, 485m asl). The lidar site at Neuchâtel is positioned between the Lake of Neuchâtel and Jura Mountains (Fig. 63; Sketch diagram) . The dynamics is presented as backscatter lidar range-corrected signal and its altitude gradient (log-derivative). Meteorological observations from Neuchâtel Stations (at the lidar site) and Chasseral Stations (47.13°N, 7.06°E, 1607m asl; Jura Mountain) are used to support these presented cases. Lidar observations and simultaneous meteorological parameters reveal the influence of convective and advective processes during the various phases of the PBL development cycle.

Figure 64a) shows several layers sliding down from about 0300H to about 0830H on May 29, 2001. The layers are converging towards the rising mixed layer. The measurements are done in calm weather (i.e., low synoptic wind at the surface). These layers are mixed effects of the wind in the higher atmosphere, coming from Jura mountains. They may be due to the orographically generated valley wind, as well as the effect of the land breeze. All these layers sink down till the mixed layer got developed and rose as an effect of the solar heating. Surface wind directions support this observation in the morning hours i.e. being directed to the site from Jura Mountains. Figure 64b) presents measurements performed on March 28-29, 2002 nighttime under (cold) anti-cyclonic weather. The results show the residual layer diminishing during all the night from 1.5km to 0.8km. Development of several layers seen throughout the night. These layers are seen developed till 3.5km. Meteorological observations show that till around 2100H of the first day, the wind directions for Neuchâtel and Chasseral were from North/Northeast, but after this time, Neuchâtel wind direction remained from Northeast, whereas at Chasseral the wind direction changed. This difference is expected to cause a circulation, and therefore, a disturbance in lidar observations. With the change in wind direction, relative humidity (RH) was increased for Chasseral from about 40% to about 80%, indicating wind from the lake. Neuchâtel site is showing low RH (expected from Mountain-peaks). Also, the temperature for Neuchâtel was decreasing for this event due to colder wind from Jura, whereas for Chasseral, it was increasing due to humid and warm wind from the lake; indicating a local circulation between the lake and the mountains during the observation period.

Figure 65 presents measurements performed on June 21-22, 2001 nighttime, under anti-cyclonic

98
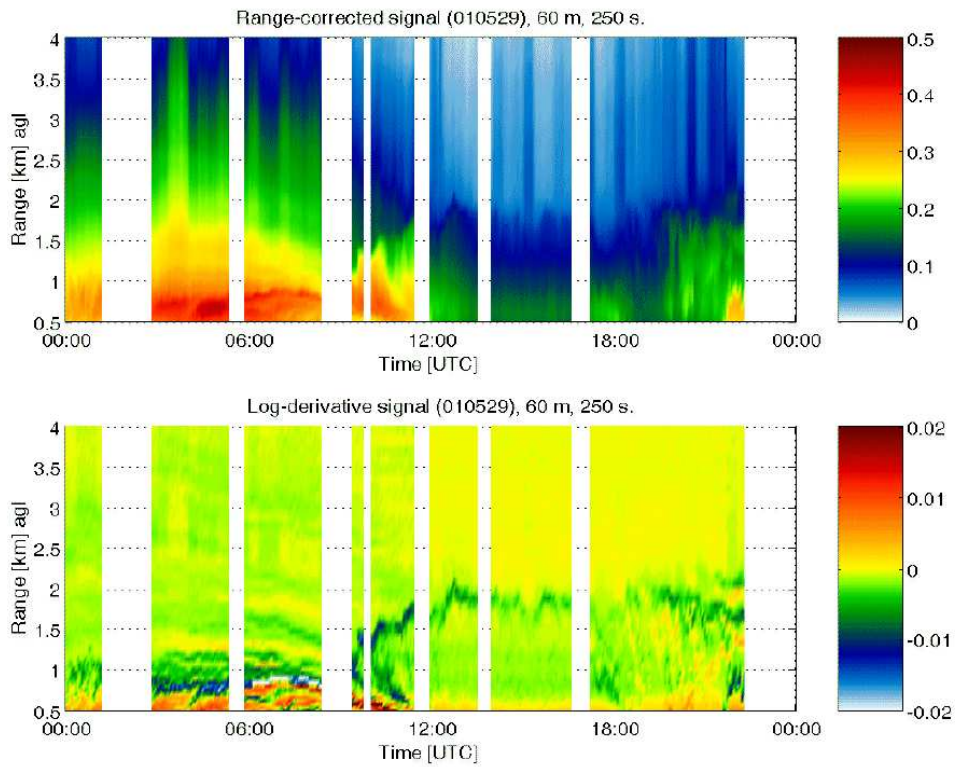
a)
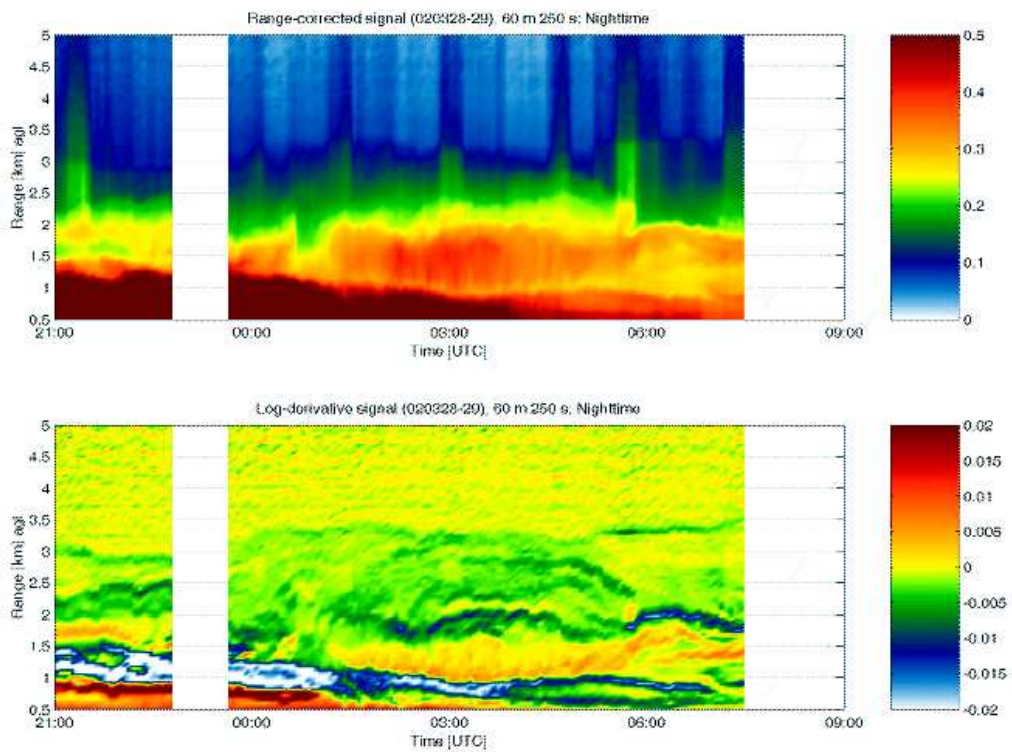
b)

Figure 64: a) Lidar observation of descending layers during the morning hours of May 29, 2001. b) Observation of uplifting of aerosol layers till around 3.5 km during nighttime; it seems to be an effect of local circulation of wind due to the presence of the lake and the mountains.
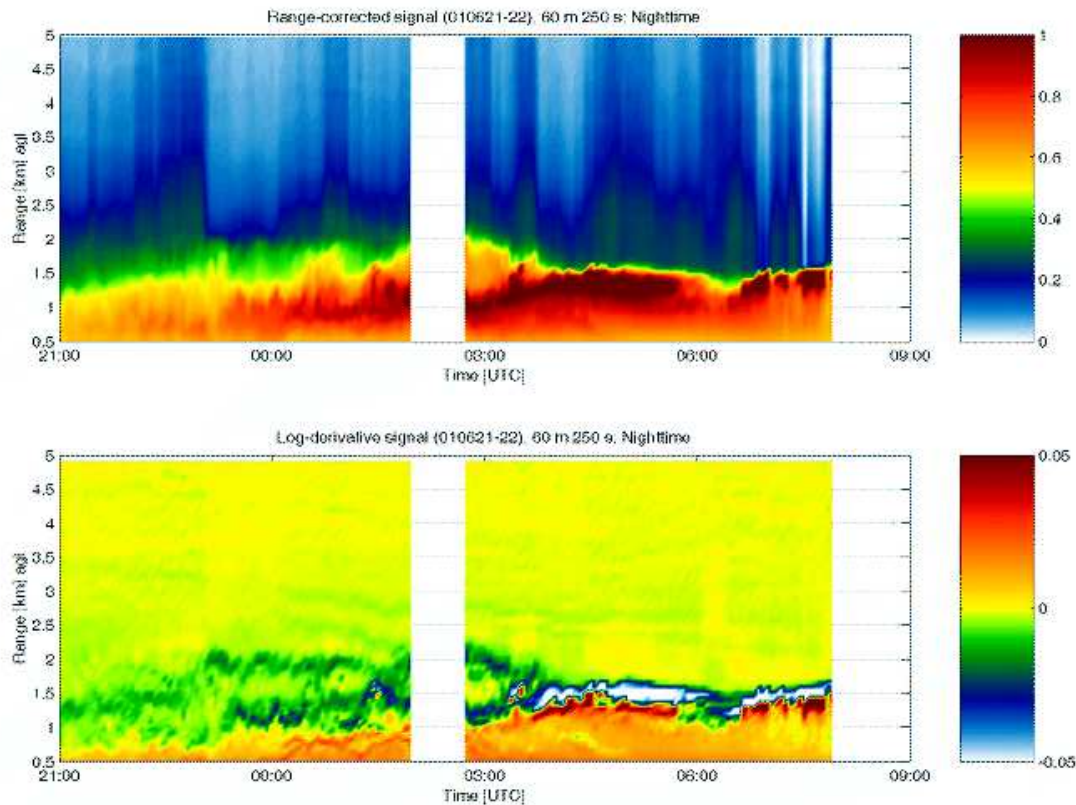
Figure 65: Mixing of various layers in the rising PBL.

warmer weather conditions and in clear vertical/horizontal visibility. The figure shows an uplift-ing of the AML during nighttime and the growth of the lowest layer after 0100H. Few other layers are seen mixed with the lowest layer in the early morning hours. Meteorological parameters show that this phase is the end of the anti-cyclonic phase. The wind direction for the region was from Southwest, the surface pressure was decreasing and RH was increasing. The lowest temperature for this night was reached around 0300H. Higher values in the range-corrected signal is around 0300H indicate the mixing of aerosols.

11.3.4 Vertical transport studies in the Alps around Garmisch-Partenkirchen

by H. Giehl, S. Kreipl, T. Trickl

The lidar measurements during the warm season before and during EARLINET have demonstrated pronounced daytime vertical transport of aerosol and to heights around 4000 m above the mountains next to IFU. In the morning an upvalley air stream forms in the PBL of the local Loisach valley ("valley wind") reaching IFU typically before noon and resulting in an increase of ozone and aerosol imported from outside the mountains. This flow rises along the slopes in the upper part of the valley and reaches heights of 1 to 1.5 km above the summits and crests of the adjacent mountains (2300 to 2962 m a.s.l.) under conditions of moderate humidity. A return flow may form at high altitudes (see Carnuth and Trickl (2000); Kreipl et al. (2001),Carnuth et al. (2002) and references therein); resulting in the generation of a second aerosol and ozone layer above the PBL. An example of a diurnal series of measurements is given in Fig. 66, showing the simultaneous mid-day increase of aerosol above 3000 m due to the formation of this return flow.

100

The aerosol backscatter coefficients in the layer around 3.7 km are not much lower than those in the PBL. In general, the aerosol backscatter coefficients in the upper layer rarely drop to values below one third of those found in the PBL. To some extent, the decrease may be explained by the increase in valley cross section for growing altitude. The upward-transport efficiency is expected to exceed 50 % which demonstrates the importance of the Alps (and other mountains) for the export of European air pollution from the PBL. Bimodal aerosol distributions as that shown in Fig. 66 have been found in a number of cases examined since 1991. Their formation is strongly influenced by the synoptic wind conditions. By comparisons with radiosonde wind data from Munich it was found that all observations of bimodal distributions took place under conditions of wind speeds below 5 m/s and mostly easterly to southerly advection (Table 12). A counter example is given in Fig. 67. Due too strong northerly advection with wind speeds of about 8 m/s at around 3000 m no local vertical transport could be observed. The maximum temperature was 11°C in the valley (730 m), favourable for the formation of a moderate orographic wind system. The radiosonde data reveal an unstable stratification. The upvalley wind speed maximum was 5 m/s. This demonstrates the strong interference of the synoptic wind.

It should be mentioned that the situation was different during the VOTALP field campaign in the Swiss Mesolcina valley (Furger et al., 2000; Carnuth and Trickl, 2000). This valley is substantially deeper (300 m to 3000 m; Loisach valley below Garmisch-Partenkirchen: 650 to 2000 m). As a consequence the return flow above the PBL was highly reproducible since it was, in part, channeled in the valley.

A more accurate estimate of the export efficiency for the Loisach valley has not been possible due
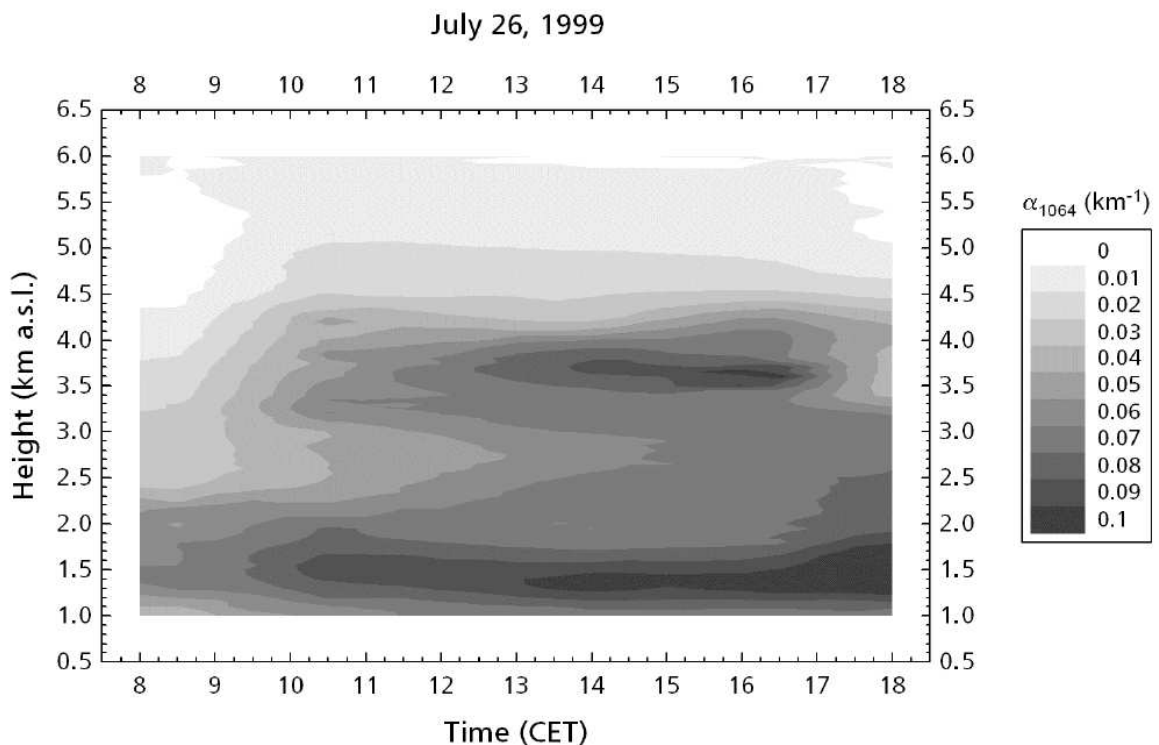
Figure 66: Diurnal cycle of the aerosol extinction coefficient above IFU on July 26, 1999, showing the characteristic bimodal distribution observed during the warm season under conditions of low synoptic wind speed or more southerly advection

Table 12: Maximum aerosol-layer height, wind direction and wind speed for seven diurnal cycles since 1991 showing bimodal vertical aerosol distributions

Date	Height (km asl)	Wind direction	Wind speed (m/s)	Remark
1991-09-03	4.0	S...E	0...3.6	
1998-05-11	3.5	E	0...1	
1998-05-13	3.9	ENE	4	
1999-03-31	3.6	ESE	5	
1998-07-26	4.3	NE	3	cf. Fig. 66
2001-09-03	3.4	SW	4	very weak structure
2002-07-09	3.7	ENE	3	cf. Fig. 11.3.4

to the absence of wind data. Wind measurements by research aeroplanes finally became possible during the 2002 VERTIKATOR campaign. In the following we briefly describe the lidar activities during this campaign and present the first results obtained. The analysis of the enormous number of angular scans with two aerosol lidar systems was not complete at the end of EARLINET.

Fig. 68 shows a map of the Loisach valley near Garmisch-Partenkirchen and the location and principal scan orientations of the two IFU aerosol lidars. The stratospheric lidar was operated at IFU and scanned along the valley and parallel to the Wetterstein mountains. Due to insuffcient overlap between laser beam and telescope field of view small elevation angles were preferred. Thus, the local vertical distribution at IFU was determined from the westerly scans. The mobile lidar was placed 6 km outside the mountains (Murnauer Moos) and scanned along the Loisach valley. In addition to the

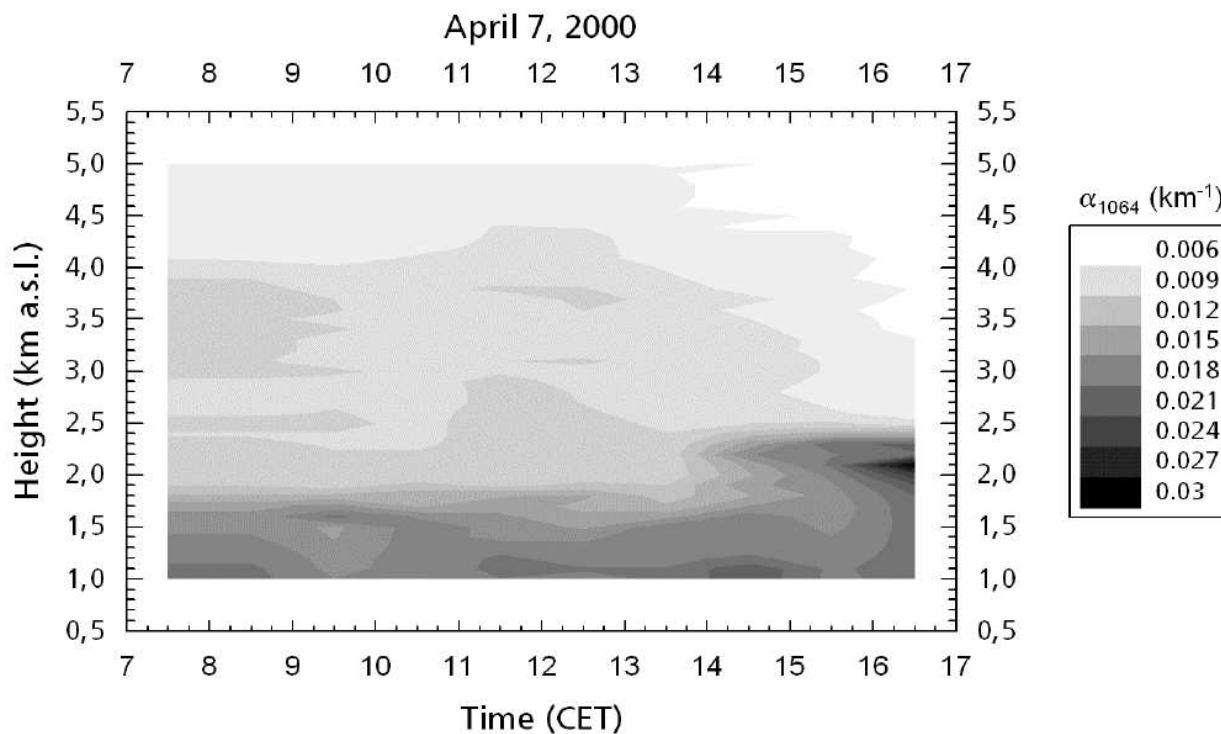Figure 67: Diurnal cycle of the aerosol extinction coefficient above IFU on April 7, 2000, during strong northerly advection; no orographic effects are seen.

Figure 68: Map of the mountains around Garmisch-Partenkirchen and the Loisach valley; the positions of the two aerosol lidars are marked by circles, the three principal scanning directions by arrows. From the scans along the valleys a two-dimensional map of the backscatter coefficients will be generated.

lidar measurements wind measurements were made on two aeroplanes. Wind-lidar measurements took place on board the DLR Falcon. Due to the limited horizontal resolution no flights along the valley were made. Some information might be extracted from the west-east flight legs outside the mountains, but the preliminary data available do not cover the lowest 200 m. In addition, some flights by the Do 127 aircraft of Forschungszentrum Karlsruhe yielded wind information along the Loisach valley and vertical wind profiles above Eibsee, i.e., next to the highest mountains of the area.

For this report we focus on the two subsequent campaign days July 8 and 9, 2002. Although warm fair-weather conditions had build up for several days prior to this period there are clear differences between the observations on both days. Figure 11.3.4 shows diurnal series of profiles at both lidar sites obtained by projecting the slant-path measurements for a selected angle onto the vertical axis. It is obvious that the influence of pronounced vertical transport to heights above the morning PBL is seen at both sites on July 9. On July 8 just a minor expansion of the PBL was observed at both locations. For July 8 there are wind-profile measurements above Eibsee (Fig. 70) a wind reversal is discernible above 2000 m (morning) or 2500 m (afternoon). According to the weather map and FLEXTRA backward trajectories the synoptic wind direction was west (270 degrees) which does not agree with the measured wind direction above the summit height (3000 m). On the other hand the wind speed aloft in the morning clearly exceeds that in the valley which indicates synoptic influence. The lidar profiles do not exhibit much structure and, thus, do not reflect the layering and layer positions seen in the wind profiles. This suggest an upward injection of PBL air rather than a separate mass flow. The similarities of the aerosol profiles above both lidar locations indicate that this injection is based on a vertical expansion of the PBL. The similarities, however, do not allow one to distinguish between local vertical expansion above both sites and advection of aerosol towards Murnauer Moos.
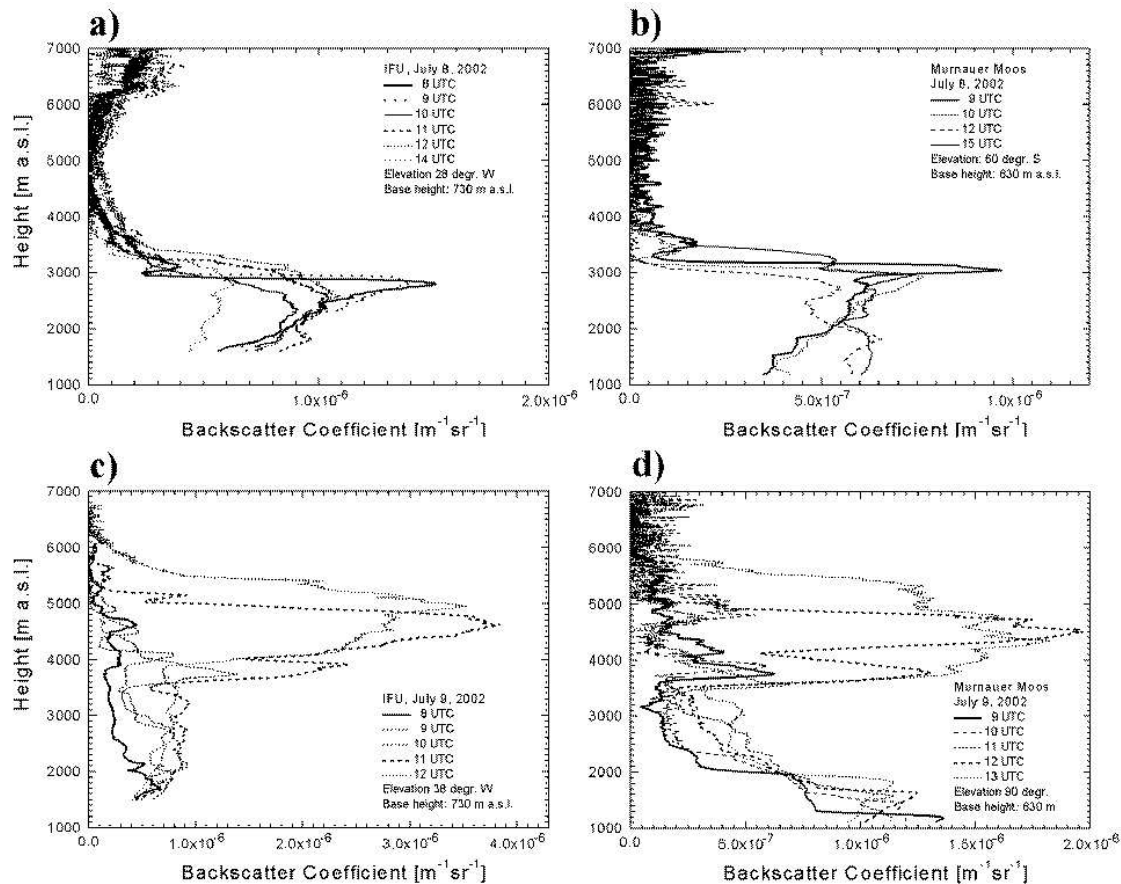
Figure 69: Four diurnal series of the two IFU lidars at the sites IFU and Murnauer Moos on July 8 and 9, 2002 (see inserts).

On July 9, the impact of a pronounced vertical redistribition was observed at both sites. Southerly winds prevail due to the approach of a minor front from the west resulting in a thunderstorm in the afternoon. As on July 8 extremely high temperatures were reached, 30 degrees already at about 10 UTC. This explains that also on July 9 the vertical transport near IFU resembles more a vertical expansion of the PBL than a valley-wind - anti-valley-wind circulation. The upward transport starts as early as at 9 UTC (or even before this) which is quite unusual. In contrast to this a bimodal distribution was observed above Murnauer Moos. In addition, the first observation of significant aerosol above the morning PBL occurred at 11 UTC, i.e., two hours later than above IFU. Both facts indicate that advection from the upper part of the valley should have caused the increase of aerosol above the height of the morning PBL. This is supported by the fact that the measured upper-level wind speed of 5 to 8 m/s (due to the parallel synoptic wind) would result in an air travel time of less than 2 h between the Wetterstein range and the Murnauer Moos site, in some agreement with the observed delay. We conclude that the transport above Alpine valleys may be rather complex and more different mechanisms must be distinguished than in the past. The measurements on July 9 were influenced by advection of North-American fire plumes and, at 3500 m (according to the FLEXTRA trajectories), maybe also by Saharan dust. Other situations are expected for the remaining days of the campaign not analysed so far. We also conclude that more detailed wind measurements (than possible during the VERTIKATOR campaign covering a larger area in the Bavarian Alps) are necessary to characterize fully the transport in and above the valley. Thus, these investigations will
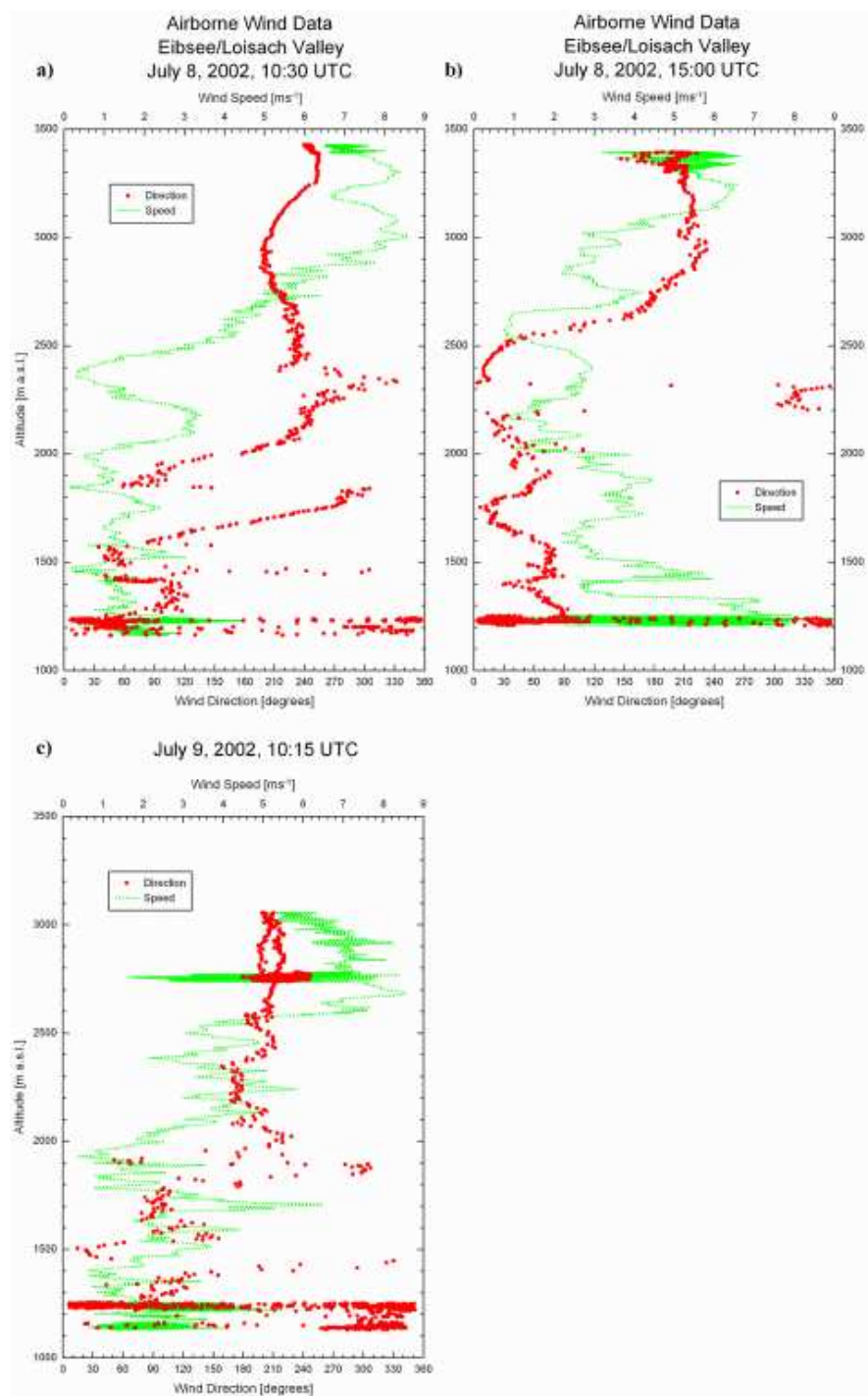
Figure 70: Vertical profiles of wind speed and wind direction above Eibsee (to the west of IFU) measured onboard the Do127 aircraft (data kindly provided by U. Corsmeier)

continue in the future.

11.4 Socio-economic Relevance and Policy Implications

The air-pollution export from the boundary layer to the free troposphere is crucial for the hemispherical redistribution of pollutants. Significant amounts of atmospheric trace constituents are transported from continent to continent. This should have severe implications for the most productive source regions for air pollution such as South-East Asia, North America and Europe. Due to the presence of numerous mountain ranges, in particular the Alps, the European export of trace gases and aerosol to the free troposphere might be strongly influenced by orographic "pumping". In addition, the Alpine ecosystem is affected by the upvalley flows advecting heavily polluted air from the surrounding urban and industrialized areas. Forest damages and the resulting increasing number of avalanches has already started to create substantial financial efforts by the local authorities.

11.5 Conclusions

Aerosol lidar measurements have been proved to yield valuable information on orographically induced vertical transport. The impact of the local wind systems on the diurnal cylce of vertical distribution of aerosol backscatter and/or extinction coefficients have been studied in some detail at the EARLINET partner stations Barcelona, Athens, Neuchâtel and Garmisch-Partenkirchen. Some of the basic concepts of the air flow reponsible for the structured aerosol distributions have been confirmed. The measurements so far carried out have yielded a host of information which will be further analysed after the end of the project. It is obvious that a number of open questions have emerged from these investigations. In particular, the Alpine wind system must be studied under quite a variety of different meteorological conditions, with more support from aircraft measurements and modelling. This is expected to yield typical boundary conditions for characteristic transport patterns.

12 Stratospheric aerosol

by Valentin Simeonov

12.1 Objectives

The primary goal of this work package is the coordination of stratospheric aerosol observations within the EARLINET project and detection of smaller scale features of stratospheric aerosol distribution and its interdependence with dynamics and heterogeneous chemistry.

At present, eight stations situated in Aberystwyth, Garmisch-Partenkirchen, Jungfraujoch, Kühlungsborn, L'Aquila, Leipzig, Minsk and Napoli are taking part in these observations. EPFL is in charge of the coordination of the measurements and has the responsibility to warn for special events, such as volcanic eruptions that may cause a change in the stratospheric aerosol content. Measurements of stratospheric aerosol were performed before the establishment of EARLINET network at three stations- Garmisch-Partenkirchen, Leipzig, and Minsk. The long-term record of lidar remote sensing of the stratospheric aerosol layer began at Garmisch-Partenkirchen in 1976 and has captured several major and minor volcanic eruptions with stratospheric impact.

Stratospheric aerosols are of natural and anthropogenic origin. Primary natural factors include, first, powerful volcanic eruptions, usually accompanied by massive emissions of sulfur gases into the stratosphere, which subsequently leads to the formation of sulfate aerosols. Atmospheric circulation plays a major role by influencing the thermodynamic conditions for aerosol formation and its transportation. The main anthropogenic sources include stratospheric aircraft flights and the transport to the stratosphere of long-living carbonyl sulfide gas (the product of fuel combustion) where it is oxidized to sulfuric acid vapor.

The last powerful volcanic eruption happened in June 1991 (Mount Pinatubo) and according to different lidar, satellite and sun photometer data (McCormick and Thomason, 1995; Rosen et al., 1994; Jäger et al., 1995; Ansmann et al., 1997) lead to a maximum stratospheric aerosol optical depth of approx. 0.2 at green wavelengths for the Northern hemisphere in the winter-spring of 1992. No other major volcanic eruptions affecting the stratosphere have occurred during the decay phase and in 1997, the stratospheric aerosol levels fell close to those of the pre-Pinatubo period or even lower - to the values of 1979. For example the total optical depth in December 1997 between 15 and 30 km at 532nm that is attributed to the combination effects of the molecular atmosphere, ozone and aerosol was 0.057, out of these only approximately 0.003 was due to aerosol (Kent and Hansen, 1998). Nowadays the aerosol content is considered to be close to the equilibrium background level observed in 1979 (Hofman and Rosen, 1981) and during the pre-Pinatubo period 1989-1991 since no significant eruptions able to perturb the stratosphere occurred after 1997.

12.2 Methods and scientific achievements

The results from the stratospheric measurements performed in the frame of the EARLINET project confirm the low aerosol load during the period 2000-2002. The individual backscatter profiles from the Minsk station taken in the period 2000-2002 shown in Fig.71 demonstrate a decrease in time of the backscatter coefficient especially for altitudes below 22-24 km. No significant seasonal variations of the backscatter coefficient can be observed for the whole period, despite a slight increase in the winter profiles as seen from the averaged seasonal profiles in Fig.72. The low values of the lidar scattering ratio (molecular+particle backscatter/molecular backscatter) also illustrate the very
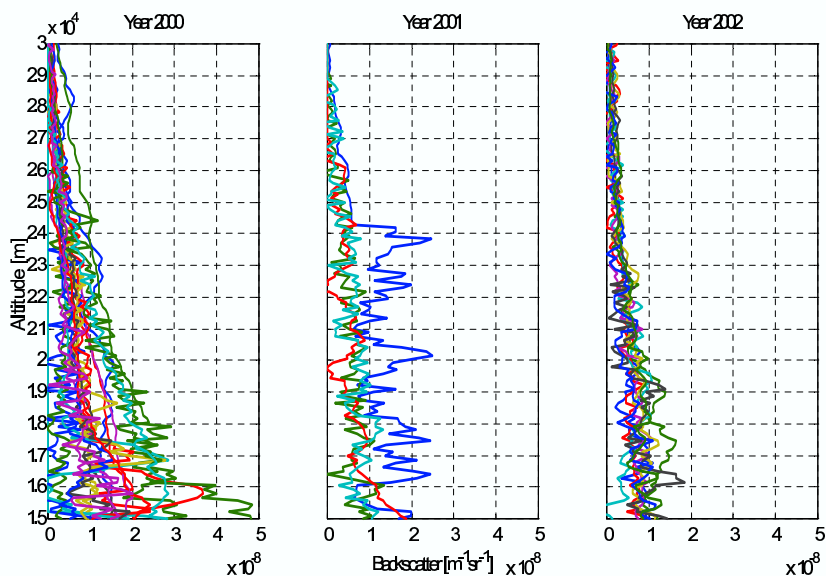
Figure 71: Individual profiles of the aerosol backscatter coefficient (Minsk).

low aerosol load in the stratosphere. Figure 73 shows a selection of summer and winter profiles of the lidar scattering ratio taken in Garmisch-Partenkirchen. The maximum value is about 1.05 and is found in the wide range of 16 to 27 km. Minimum backscatter for matching is found in these profiles above 27 km. The maximum of the lidar scattering ratio observed at Aberystwyth (Fig. 74 right) at altitude of 20km is around 1.07, while it reaches 1.135 over Minsk (Fig. 74 left) at about 23km.

The lidar-derived general pattern of temporal dynamics of stratospheric aerosol loading is characterized most completely by the integrated aerosol backscatter coefficient calculated for a certain altitude range. The integrated backscatter coefficient between 15 and 30 km for the Minsk station presented in Fig.75 shows low values - between 1 and $2 \cdot 10^{-4}$ sr^{-1} for the period 2000 - mid 2001 and lower than $1 \cdot 10^{-4}$ sr^{-1} till the end of 2002. The integrated particle backscatter coefficient measured
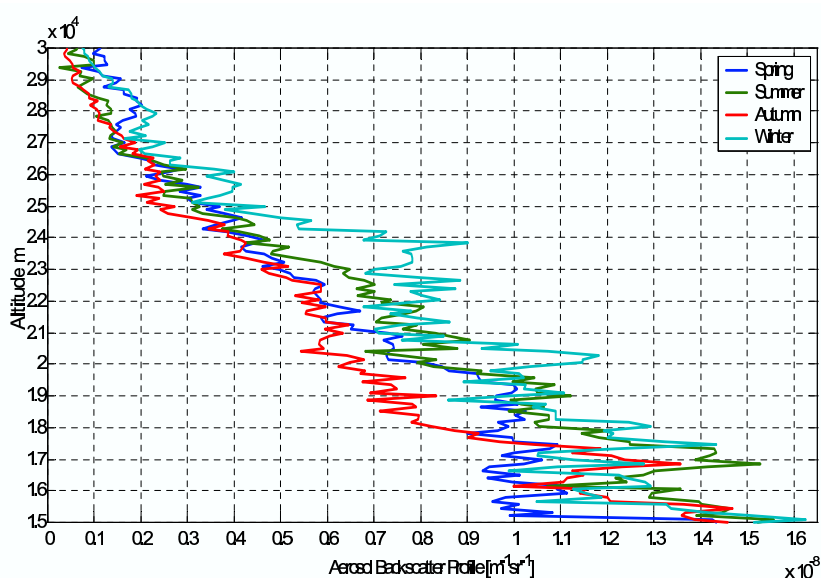
Figure 72: Averaged seasonal profiles of the aerosol backscatter profile (Minsk).
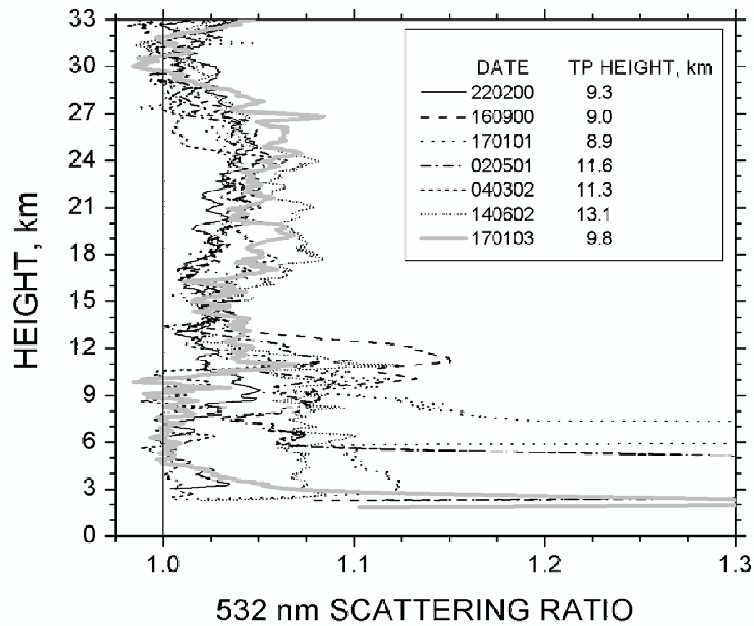
Figure 73: Selected profiles of the 532 nm scattering ratio (Garmisch-Partenkirchen).

in Garmisch-Partenkirchen and shown in Fig.76 is presented in three height ranges: tropopause (TP) to the top of the aerosol layer, tropopause to 15 km, and 15 km to layer top, plus tropopause heights for each lidar profile. The 15 km-top values represent the aerosol layer not disturbed by tropopause variations. The same figure also displays the 1999 averages of the TP-top and 15 km-top average integrals, which are regarded as minimum annual averages in the long-term record until 2000. The 2000 to 2003 measurements vary around the 1999 averages without a tendency to higher or lower values. Table 13 indicates that the 2000-2003 averages do not differ significantly from the 1999
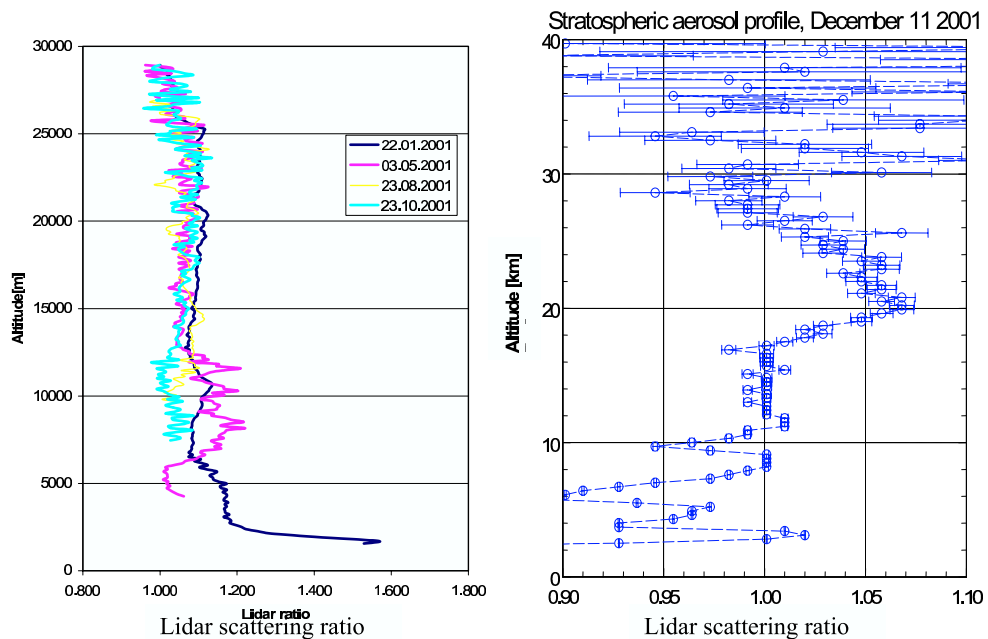
Figure 74: Lidar scattering ratio profiles taken at Minsk (left) and Aberystwyth (right).
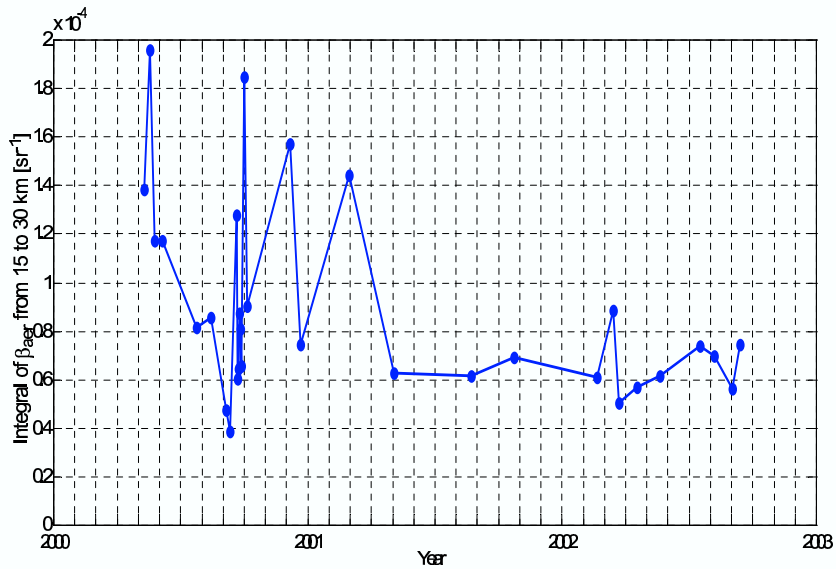
Figure 75: Integrated backscatter coefficient between 15 and 30 km (Minsk).

averages.

These results are consistent with the data obtained by other lidar groups i.e. from Tomsk (56.5°N, 85.0°E) (Zuev et al., 2001) and Mauna Loa (19.5°N, 157.7°W) (Barnes and Hofman, 2001). The sun photometer measurements of the stratospheric aerosol depth performed at Jungfraujoch (3560m ASL) also show low values of the aerosol optical depth - below 0.04 for the period after 1997 (Ingold et al., 2001). It must be concluded that the present stratospheric aerosol background has reached a minimum in 1999. The new minimum in the stratospheric aerosol content is below the lowest stratospheric aerosol load observed within two decades, that of 1979. It can be further concluded that the stratospheric aerosol layer as a whole is not affected by anthropogenic aerosol sources. Neither increasing industrial emissions nor increasing air traffic emissions are reflected in the integral values
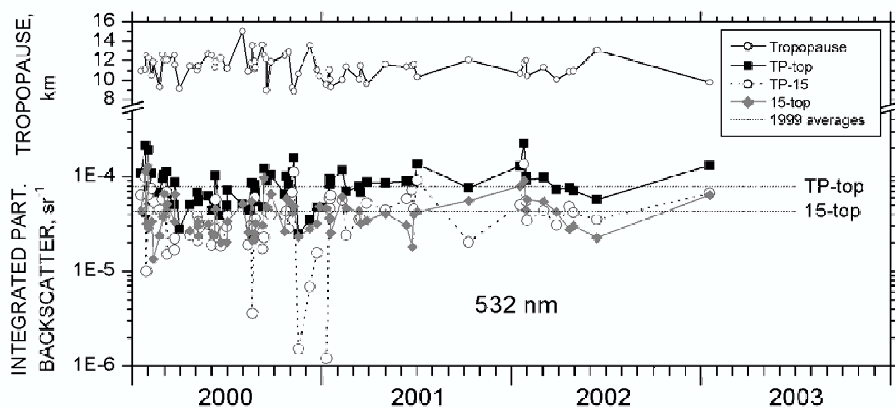
Figure 76: Integrated particle backscatter coefficient in three height ranges plus tropopause heights.

110

Table 13: Post-Pinatubo stratospheric aerosol background, average values of 532 nm integrated backscatter coefficient, sr^{-1} (Garmisch-Partenkirchen)

Year	1999	2000-2003
Tropopause to layer top	7.91e-5	7.98e-5
15 km to layer top	4.28e-5	4.11e-5

displayed. That does not exclude the possibility that in the very sensitive height range 8 to 13 km of the lowermost stratosphere an anthropogenic signal might exist. However, the extreme variability of atmospheric conditions and constituents in this region require adequate measurement strategies.

 All this data demonstrate that at present the stratospheric aerosol load is at its background level. For its correct measurement more sophisticated lidar methods and more precise data of the stratospheric air density and ozone distribution are needed. We have to note here that anomalous aerosol layers can episodically be observed even in periods of background state of the stratospheric aerosol. This may be attributed to clouds such as the polar stratospheric clouds (PSC) that form between 15 and 25 km at high and middle latitudes after rapid temperature decreases. Changes of the thermodynamic conditions in the stratosphere may also trigger the processes of aerosol nucleation at altitudes of 25 -35 km (Hofman et al., 1985).

These layers can be measured and even though they appear seldom, they are of scientific interest. What is more, statistical data from the last century shows that power volcanic eruptions occur in a period of 10 to 15 years. This shows the necessity of maintaining the ability to perform stratospheric measurements within the present EARLINET lidar network.

13 Differences between rural and urban aerosols

by Jacques Pelon, Volker Matthias and Alexandros Papayannis

13.1 Objectives

The objective of the work to be performed in this work package is close to the one of section 7, as focusing on the difference between urban and rural aerosols which can be observed during temporal cycles. The diurnal and seasonal cycle of the aerosols in the boundary layer is different in urbanised and agricultural areas as forcings and aerosol particle sources are different at the surface. In urban areas, the heat capacity of buildings is larger than the one of agricultural areas leading to the formation of a heat island, which modifies the dynamics of the boundary layer. Furthermore, important sources of pollution are present in or near cities as traffic is more important as well as industrial activity. Finally, in rural areas relative humidity is larger than in urban areas due to a larger available moisture from the soil and a larger cooling of the surface. All this impacts the optical parameters of the aerosol layers, which are different in urban and rural areas.

13.2 Methodology and scientific achievements

Methodology related to the modification of dynamics is similar to section 7 and implies to observe the transitions between the stable boundary layer observed during nighttime and the more convective one during daytime. We are aiming at the acquisition of observational sets in the morning growth period, and extend it to early afternoon and in the evening transitions. The behaviour of the urban boundary layer is different to the rural one, due to both an increase in roughness at the surface due buildings elevation, and to the anthropogenic heat flux caused by heat accumulation during daytime and manmade production in urban areas. The development of the boundary layer will thus be different in town and outside the built area and the optical properties may differ as well.

Convection in the boundary layer is important as particles and pollutants formed during daytime are mixed up to the top of the BL. After the reformation of a stable layer during nighttime, the pollutants are not removed from the upper part above called the residual boundary layer. They can be further possibly transported in the middle or upper troposphere. During the formation of the stable nocturnal layer, this layer may include less particles and pollutants as no photochemical production will occur. The erosion of the residual layer above it during the following cycle may lead to a pollution increase near the surface, as the residual layer is mixed with the new growing active boundary layer. The structural and optical properties of these aerosol layers are thus important to be measured especially in the transition phases. This is made easier by the fact that this can be achieved in night-time periods, when Raman lidar can be operated.

Additional measurements such as from radiosonde are also required for the analysis. For the comparison of optical properties in the boundary layer, it is important that the impact of the relative humidity (RH) is identified. This hygroscopicity of aerosol particles is depending on aerosol composition and above a given RH value the size of particles rapidly increases. This leads to an increase in scattering which should not be interpreted in terms of number of particles.

In order to assess these differences between urban and rural aerosols, pairs of stations where these comparisons can be done need to be identified. Five pairs of groups were initially involved in this work. During the project it appeared that the constraints were very important for the site identification and the required measurements, and that it would be difficult to achieve all the objectives of this
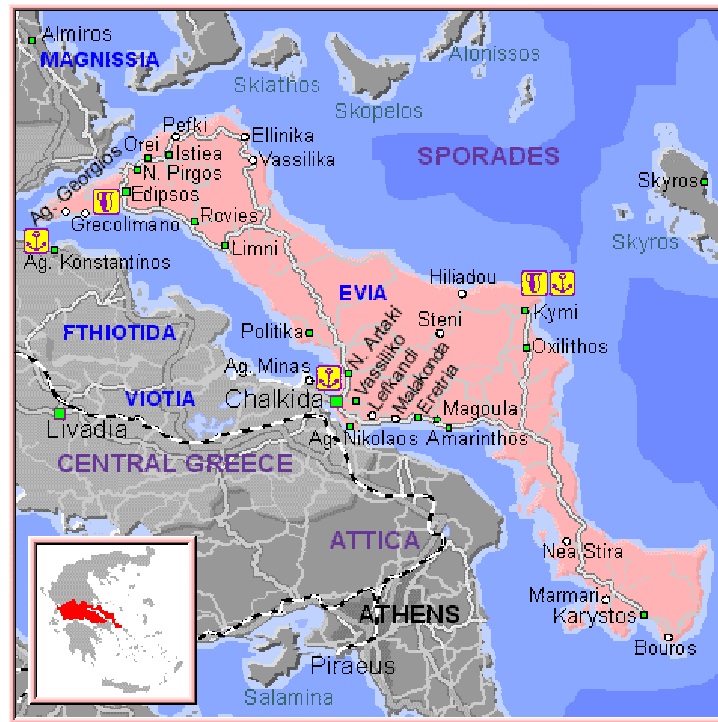
Figure 77: Map of Attica and Evia island.

work package. Due to the large difference in distance between the two eastern european sites (Minsk and Belsk), and between Italian sites moreover perturbed by orography, it has been decided to focus on sites providing close by measurements leading to a reduced number of fixed stations (Hamburg and Paris). Tests ware made over Athens area using a mobile system.

  The same remarks as for section 7 apply to this section for the data acquisition and analysis. Priority was given to setting the observations and first cases have been observed, which are presented herebelow.

13.2.1 Athens

During the fall of the year 2002 a mobile single-wavelength lidar system was completed and tested at NTUA. The system is equipped with a pulsed Nd:YAG laser emitting 12mJ/pulse at 532 nm. The receiver is a Cassegrainian telescope with 150mm diameter. The mobile lidar system was successfully inter-compared to the NTUA stationary lidar system, in the range height 0.7-3.5 km, at 532 nm.

A field campaign was organized at a rural site of the Evia island (135 asl., 38° 33' N, 24° 07' E) on November 16, 2002, 5 km far from the Oxylithos village, located 135 km northeast of the city of Athens (Figure 77). The rural site where the lidar measurements took place is located only 4 km from the seashore, therefore the air masses probed are strongly influenced by the sea spray and could be considered of maritime origin. The lidar measurements took place from 10:30 - 16:00 UT over Athens and Oxylithos sites, simultaneously. Synoptic meteorological conditions were similar over the two sites that day.

Figure 78 shows three lidar profiles taken between 12:00 and 14:00 UT over these two sites. It is
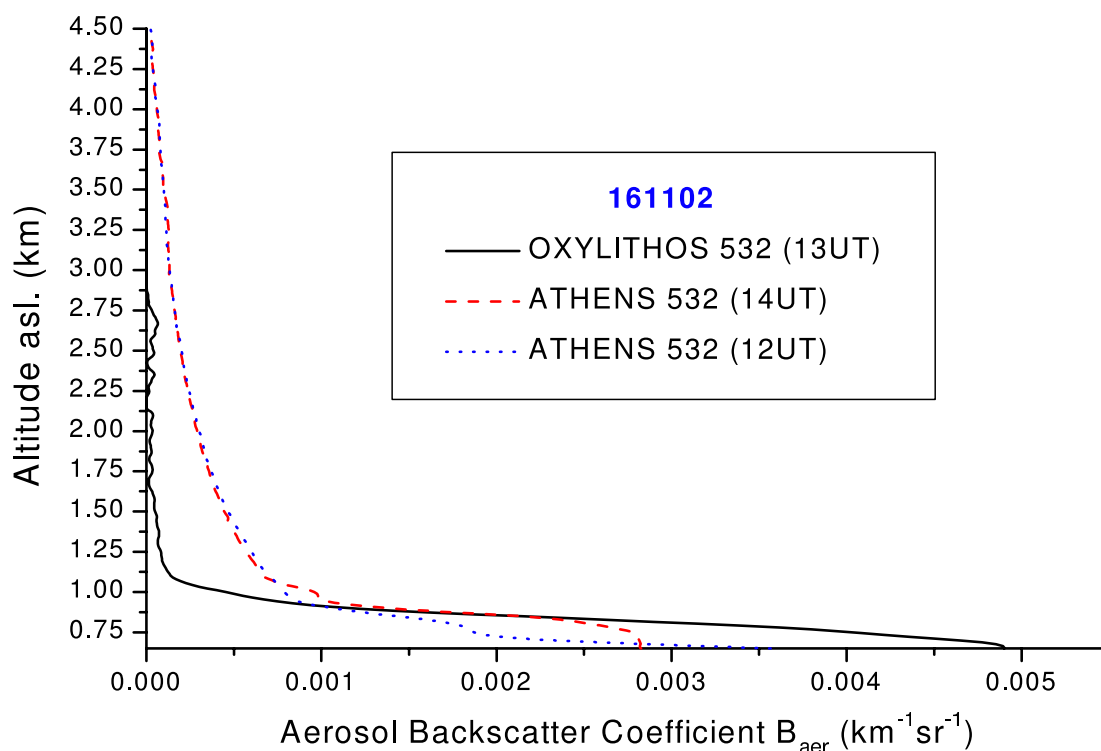
Figure 78: Lidar profiles taken over Athens (urban) and Oxylithos (rural-maritime) sites on November 16, 2002.

interesting to note the similar values of the PBL height at both sites (around 1 km), as well as the much higher values of β_{aer} (by a factor of 5-6) observed over Athens, in the free troposphere. This is due to the fact that Athens was influenced by synoptic western winds, thus bringing air pollutants from central Europe along the free troposphere. On the other hand, Oxylithos was influenced by a local winds regime of eastern direction, thus bringing maritime air to the lidar observing site. It is also interesting to note that, surprisingly, over the rural site, the β_{aer} values inside the PBL are of the order of 0.0035-0050 km^{-1}sr^{-1}, while over Athens they are of the order of 0.0025-0.0035 km^{-1}sr^{-1}. This could be explained by the fact that Oxylithos is considered as a maritime site (mixture of maritime and rural aerosols), therefore, the relative humidity values are higher than those in Athens (mixture of urban aerosols). This leads to higher values of the backscatter coefficient inside the PBL at Oxylithos than inside the city of Athens. However, both β_{aer} values are quite low compared to the mean values obtained yearly over Athens.

13.2.2 Paris

New systems have been developed in Paris to more directly combine observations with the existing station of Palaiseau. The objective was first put on the development of a microlidar with a French company. A prototype has been developed in 2001-2002, which has been tested in 2002 and involved in comparisons with the system at Palaiseau and with the reference lidar system at Neuchâtel. Good

114
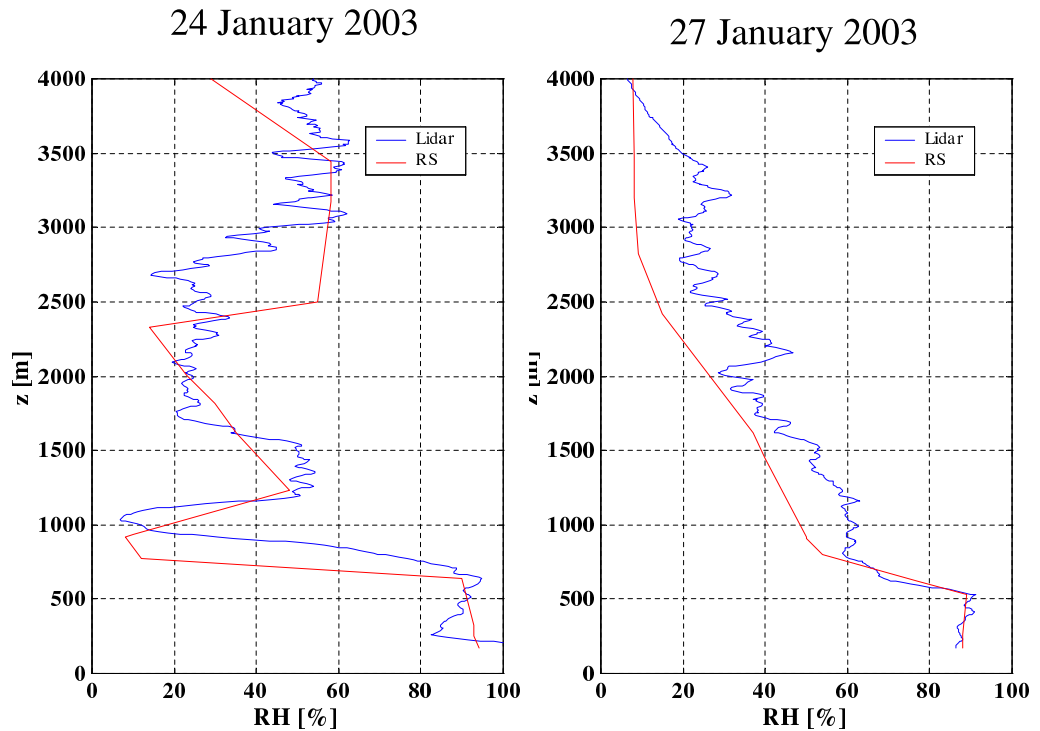
Figure 79: Comparisons of relative humidity profiles in Palaiseau and St Mand´e obtained from radiosonde and lidar (see text for details) a) on 24 January 2003 and b) on 27 January 2003.

comparisons were obtained, but the failure of the laser prevented the system to be installed in Paris. It was thus decided to switch to the use of the mobile Raman system developed in collaboration between Service d'A´eronomie at IPSL and Institut G´eographique National (IGN). This system could only be used after the end of the validation campaign held for Eumetsat in Toulouse end of 2002. The focus was thus put on the comparison of the maximum boundary layer height reached during the day and aerosol properties taking advantage that water vapor profiles could be measured simultaneously to check for relative humidity values over the Paris measurement site. This site was located in the eastern part of Paris on the IGN site in Saint Mand´e. Relative humidity in Palaiseau was determined from radiosonde measurements at the meteorological station of Trappes about 15 km west of Palaiseau. In order to retrieve relative humidity at Saint Mand´e, the temperature profiles measured at Trappes were used. Usually, only weak spatial variation of the temperature profile can be expected, but as only two temperature profiles are routinely obtained and as lidar measurements were taken at sunset, errors due to temporal mismatch may be significant (typically 10%). An example of comparison of relative humidity profiles is shown in Figure 79 for the 24 and 27 January 2003. Profiles agree reasonably well although some differences are observed in structures and absolute values. Relative humidity values are comparable over these two days. However as RH is larger than 90 %, a small error on RH may lead to a significant modification of the scattering coefficients. Backscattering profiles are deduced using the quotient of the elastically scattered and the Raman scattered signals (Ansmann et al., 1992b). Results show significant variations over the two days both in terms

24 January 2003   Paris/STM   27 January 2003
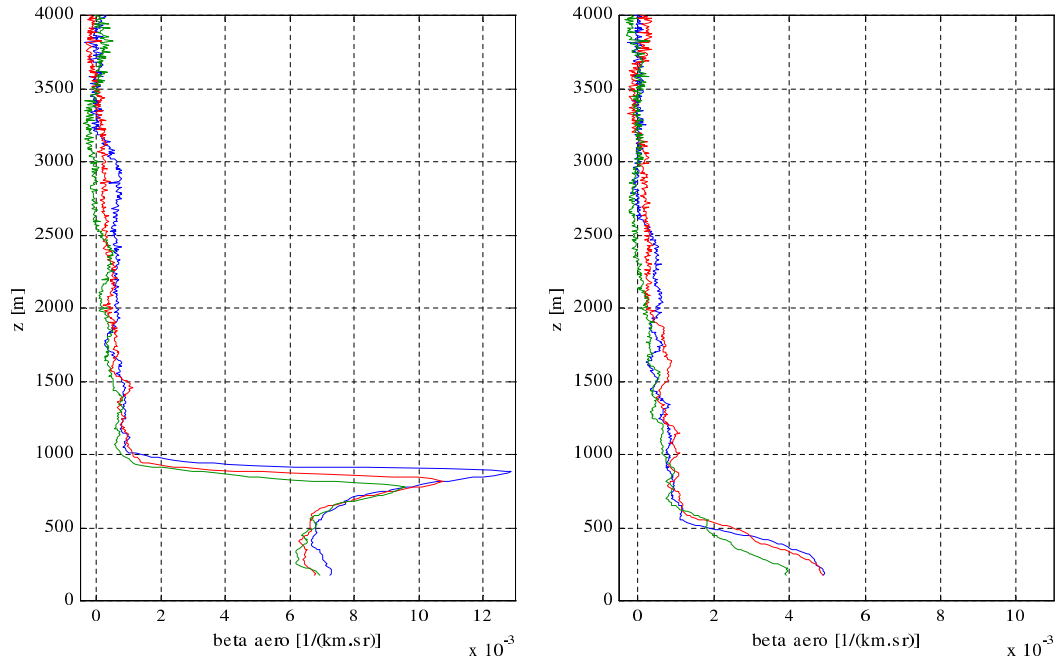
Figure 80: Comparison of backscattering coefficients derived from Raman lidar over Saint Mandé.

of height and scattering. On January 24, the ABL is more developed and the increase of humidity near saturation at ABL top (near 900 m) is the cause of the observed increase and of the modification of the vertical profile. On January 17, the ABL structure is different and the ABL height is reduced to a value closer to 600 m.

Values near the surface are comparable between both days although about 30 % larger on January 24. The ABL heights retrieved from Palaiseau lidar and reported in Table 14, are giving similar results in term of boundary layer heights and backscattering coefficient. When comparing the values of ABLh, one can see a slight difference between SM and Palaiseau stations, SM being slightly larger. Backscattering coefficients are also comparable on January 24.

On January 24, the wind was blowing from NNE (Palaiseau is under the influence of Paris) and the measurements of optical depth using the sun photometer in Palaiseau showed fairly constant values in the afternoon (about 0.18 at 440 nm) decreasing in the evening, as shown in Figure 81. Lidar integrated backscattering is about $810 \cdot 10^{-3}$ sr^{-1} at 350 nm during the evening, which would correspond to values about 15 in the lidar ratio. This rather low value, generally associated with large particles, would confirm the larger contribution of moisture.

On January 27, the sun-photometer is giving decreasing values (see Figure 81) as the wind is blowing from the north-west to the west and the influence of the urban area is decreasing. In the evening the total optical depth is smaller than 0.1 at 440 nm. This variation may be seen as a signature of the production of aerosol in the urban area.

Table 14: Results from the simultaneous lidar measurements at Palaiseau and Saint Mand´e in December 2002 and January 2003.

19/12/02	H CLA [m] Paris St-Mandé	HCLA Average (m) Palaiseau	β (350 nm) Average (m-1sr-1) ParisSt-Mandé	β (532 nm) Aver. ABL (km-1sr-1) Palaiseau	RH (%)	Wind Direction
SBL	550	620	4.75E-06	5.0E-06	90	SE
Residual layer	950	950	-	2.7E-06		SW
Free Troposph (<5 km)	2000	1700	5.90E-07	1.5E-06		W
06/01/03						
SBL	350		5.20E-06		95	NE
Residual layer	1050		5.0E-06			N
Free Troposph	2000		8.8E-07			NW
17/01/03						
SBL	530	500	5.0E-06	4.5E-06	95	SE→S
Residual layer	1520	1720	2.7E-06	3.5E-06		S→W
Free Troposph	2100		3.5E-07			S→ NW
24/01/03						
SBL	880	750	7.3E-06	7.8E-6	90	-
Residual layer	1700		7.1E-07	1.4E-6		NNE
Free Troposph	2500		4.30E-07			NNE
27/01/03						
SBL	550	450	2.9E-06	4.0E-06	85	WNW
Residual layer	1400	1400	8.0E-07	2.2E-6		NW→ W
Free Troposph	2300		4.10E-07			NW→ W
30/01/03						
SBL	600		3.5E-06		80	WNW→NNE
Residual layer	1550	1300	1.3E-06			NW→N
Free Troposph	2500		2.5E-07			NW→N

24 January 2003   27 January 2003
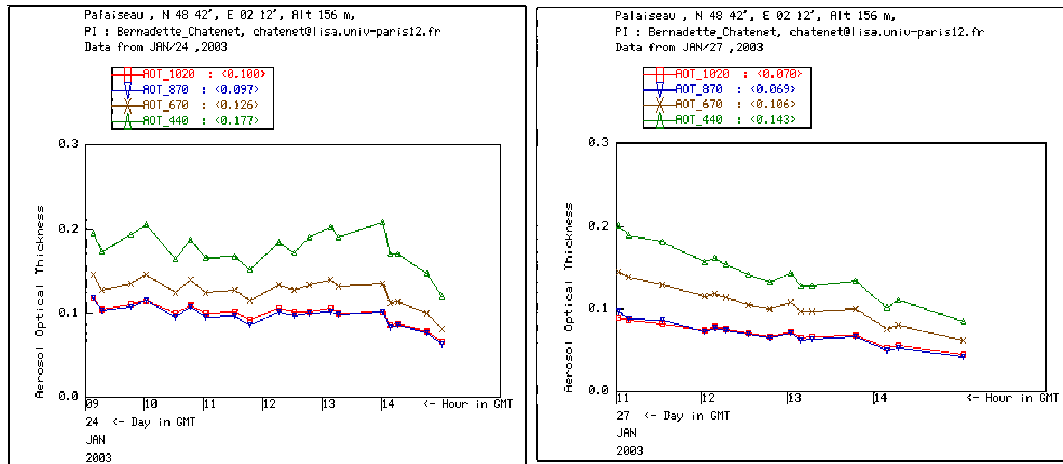
Figure 81: Optical depth measured by a CIMEL sun-photometer at Palaiseau a) on 24 January 2004 and b) 27 January 2003.

13.2.3   Hamburg

Lidars are probing a small volume of the air above the measuring system. Typical diameters of the emitted laser beam at the top of the troposphere are only a few meters and the field of view of the used telescopes is not much wider. Therefore, it is an important issue to investigate the representativity of a lidar profile for a larger area. Especially in the vicinity of large urban areas, aerosols are produced, transported and modified, so these areas are of special interest for studies on the small scale variability of the aerosol vertical distribution.

Small scale variability in a big city   For a period of one year, between December 2001 and December 2002, MPI Hamburg operated a second aerosol lidar system at the south-east border of the city, in Bergedorf. This system was a single wavelength backscatter system based on a XeF excimer laser emitting at 351 nm. The vertical coverage was similar to that from the 3-wavelengths Raman lidar system in the center of Hamburg and reached from ca. 300 m to ca. 10000 m above ground. The horizontal distance between the systems was ca. 25 km. The Hamburg area is a very flat terrain, the system in the center of Hamburg was on top of a building at 25 m asl while the system in Bergedorf was at 40 m asl.

118

Table 15: Integrated backscatter (IB) values taken from aerosol backscatter profiles at 351 nm (Bergedorf) and 355 nm (Hamburg center).

Date	IB City $[10^{-3}$ sr$^{-1}]$	IB Bergedorf 10^{-3} sr$^{-1}]$	Trajectory 19 UT	Morning	Noon	Evening
01/12/13	1.22	2.31	SE			x
02/01/03	1.34	1.40	SE			x
02/02/14	0.52	0.71	E			x
02/02/21	0.63	0.67	NW			x
02/03/28	3.58	4.30	SE			x
02/04/04	2.87	3.29	E		x	
02/06/03	1.99	2.57	SE			x
02/08/15	1.91	5.33	N		x	
02/08/19	10.99	10.81	SE			x
02/08/29	8.05	9.09	NW (950hPa) SW (850hPa)			x
02/09/02	2.09	2.86	E			x
02/09/12	1.58	2.53	E			x
02/09/30	10.74	10.14	SW			x
02/11/05	3.23	3.13	SE			x
mean	3.62	4.22				

The header for the "Time of Measurement" columns (Morning, Noon, Evening) spans above the last three columns.

Methods   Because the main goal of this campaign was to investigate the differences between urban and more rural aerosols, measurements have been performed on sunny days when spatial inhomogeneities due to passing fronts or local rainfall were not expected. Altogether, 14 days in different seasons and with different local wind fields have been investigated to get a good cross section of different meteorological conditions, with the restriction that all days were more or less cloud free. This permits optimum conditions for lidar measurements and allows the investigation of the temporal development of the aerosol vertical distribution throughout the day. On 6 days complete diurnal cycles have been observed and the development of the PBL between early morning and afternoon has been investigated at both sites.

Comparisons of the aerosol backscatter profiles taken in the late afternoon, when the planetary boundary layer (PBL) is usually well developed, have been performed on most of the chosen days. Only on two days, noon measurements had to be considered for the comparisons (see Table 15). The aerosol backscatter profiles have been calculated with common lidar ratios of usually 50 sr. Calibration of the profiles in a region with very low aerosol backscatter above the PBL was always possible, so systematic errors in the calculation of the aerosol backscatter profiles could be avoided. System intercomparisons with simultaneous measurements taken in the center of Hamburg showed that both systems work properly and that typical system differences are in the order of 10 % or less for the mean value of the aerosol backscatter in the PBL. The difference in the measuring wavelength accounts for maximum deviations of ca. 2%, depending on the observed aerosol.
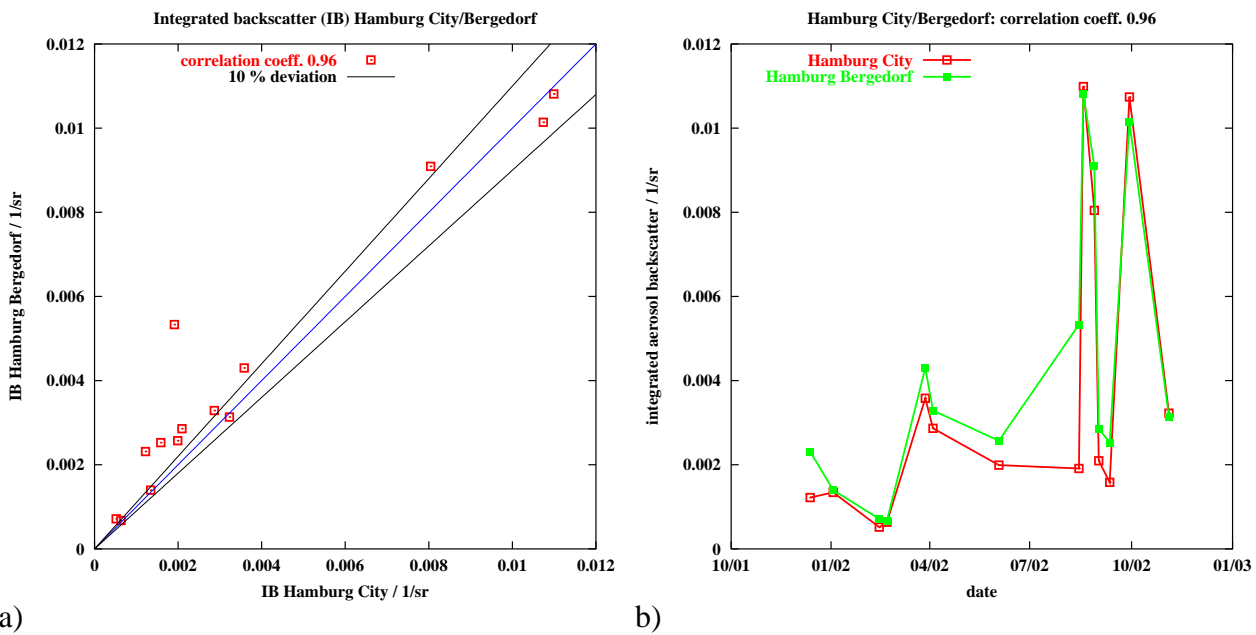
Figure 82: a) Comparison of the integrated backscatter values measured at Hamburg center and Bergedorf. b) Times series of integrated backscatter measurements at Hamburg center and Bergedorf.

Integrated backscatter results   Table 15 summarizes the measurements and shows the differences of the column backscatter in the PBL. In most of the cases, differences are quite small and do not exceed 20 %, often the values agree even within 10 % which has to be regarded as equal in terms of the estimated typical difference between the systems when probing the same aerosol (Fig. 82a). Nevertheless, also large differences were observed. On three days the integrated backscatter was more than 50 % higher at Bergedorf than at the city center. On August 15, 2002, the largest differences were found when northerly winds transported air masses over the city to Bergedorf. However it could not be proven that these were urban aerosols originating from the city of Hamburg. The other two cases with large differences between the measurements were connected with easterly and south easterly winds, when Bergedorf is at the windward side of the city. Interestingly, significantly higher values were always found at the border of the city, regardless of wind direction. On average, the integrated backscatter was about 17 % higher in Bergedorf than in the center of Hamburg. This result is surprising and should be investigated more in detail. It is speculated that humidity effects or local aerosol sources, e.g. from farming could play a major role in the explanation.

Despite this large differences on some of the days, the profiles are very similar in most of the cases. The correlation coefficient of the time series of the integrated backscatter values is with 0.96 very high (Fig. 82b). Systematic modifications of the aerosol between the both sites could not be observed, the difference in the mean value is mainly attributed to 2 or 3 outliers. E.g. if the measurements from 02/08/15 and 02/09/12 were not considered, the mean difference of the integrated backscatter would be less than 10 %. From this, one can conclude that under stable meteorological conditions, a lidar derived aerosol backscatter profile represents an area of a few tens of kilometers very well, even in an urban area. However, large differences can occur as it can be quite difficult to explain these differences without additional information on e.g. transport patterns and relative humidity.
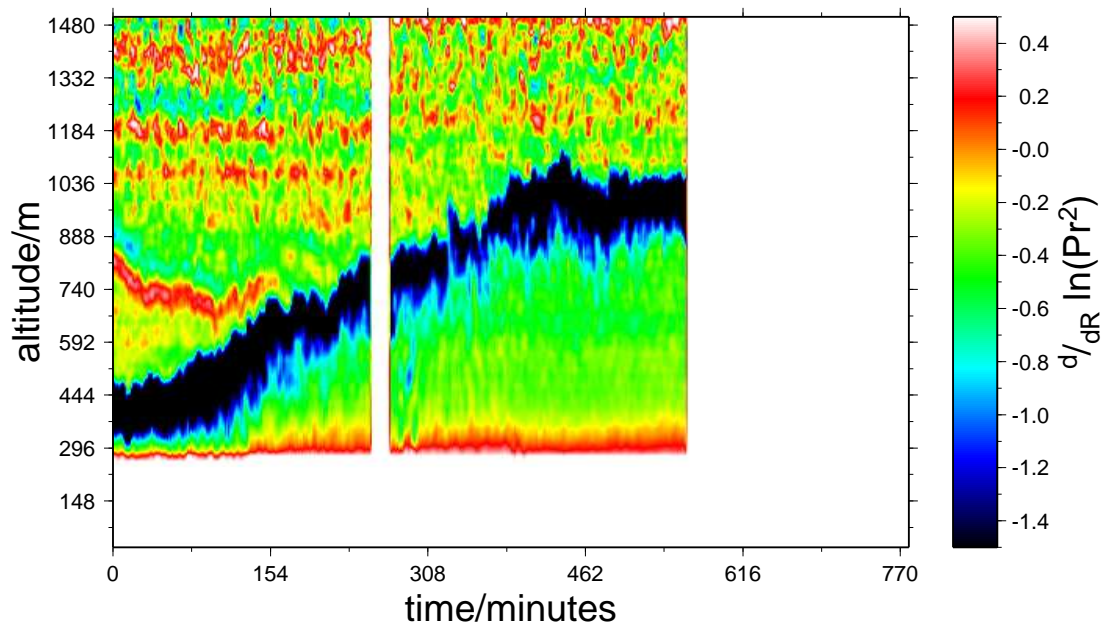
PBL development   Besides the integrated backscatter values, also the temporal development of the planetary boundary layer has been investigated. On 6 days measurements started already early in the morning, when turbulence is still low and the planetary boundary layer is not yet developed. Depending on season and meteorological conditions, it can take from one to six hours between the observation of the first turbulence elements breaking through the nocturnal boundary layer and the full development of a well mixed PBL. Examples of time series of $\frac{d}{dR} \ln Pr^2$, which represent the gradients in the aerosol distribution very well, are shown in Figure 83. The height of the mixing layer can be calculated from the lidar signals by taking the minimum of $\frac{d}{dR} \ln Pr^2$. This has been done for the data from the 6 days of simultaneous observations at Hamburg center and Hamburg Bergedorf. High correlation between the PBL-development at the two sites (see Fig. 83) could be observed on four of the days. Outliers cannot be avoided completely, if the layering is more complex or if weak aerosol gradients make it difficult to determine the mixing layer. Updrafts of warm air sometimes leads to much lower aerosol gradients in that air volume and the largest gradient is then detected in very high altitudes. Especially in situations with low aerosol backscatter and therefore low gradients in the $\ln Pr^2$, an accurate determination of the PBL height can be difficult and not precise enough with automatically working algorithms (see Fig. 84).

 On two days the layering was very complex with several aerosol layers in the morning and advection processes during the day. These days have not been chosen for quantitative investigations of PBL rise time and correlation coefficients. For the other days the PBL-height at Hamburg center and Bergedorf was calculated from lidar signal averages of 5 minutes and 60 m. Table 16 shows mean values of the PBL-height in the afternoon and their standard deviation from all six days of complete diurnal cycles. On four days additionally the correlation coefficients of the PBL-heights and the rise time of the PBL in the morning are given. In all cases, the PBL-height observed in Bergedorf was slightly higher than that in Hamburg center, but only in two cases the difference was higher than the vertical rersolution of the used data of 60 m. The variability of the PBL-height in the afternoon, given by the standard deviation is very similar at both sites. The cases shown in Figures 83 and 84 show very high correlations throughout the whole day of 0.89 (2002/06/03) and 0.96 (2002/04/04). The PBL rise times could only be compared in three cases. On January 3, 2002 the increase of the PBL in Bergedorf was connected with very low aerosol gradients which could not be determined by the used algorithm. The rise times were between 90 and 250 m/h and were comparable at both stations. Although the values at Hamburg centre were always higher than at Bergedorf, more investigations would be necessary to prove that result. The determination of the rise time is done by assuming a linear increase of the PBL height in a certain time frame. The results depend very much on the chosen time interval and on possible outliers within that time.

13.3   Conclusion

Observational configuration for observing the boundary layer height development is difficult to set, it requires two systems, two sites of operation in nearby rural and urban conditions. This set-up successfully operated for Hamburg site did not reveal any significant differences as could have been done for Paris in previous campaigns and in the last observations performed in this work package. This is really depending on the heat effect of the urban area, which is different from an urban area to another. Furthermore Hamburg is located near the sea and maritime influence may play a significant role.

This analysis is further more complicated when comparing backscattering or extinction coefficients, as it requires a control of relative humidity and the knowledge of the phase function (this means

$\mathrm{^d/_{dR}\,ln(Pr^2)}$, λ = 351 nm, starting time 2002/04/04 7:16 UT, Hamburg Bergedorf

a)

$\mathrm{^d/_{dR}\,ln(Pr^2)}$, λ = 355 nm, starting time 2002/06/03 7:02 UT, Hamburg City
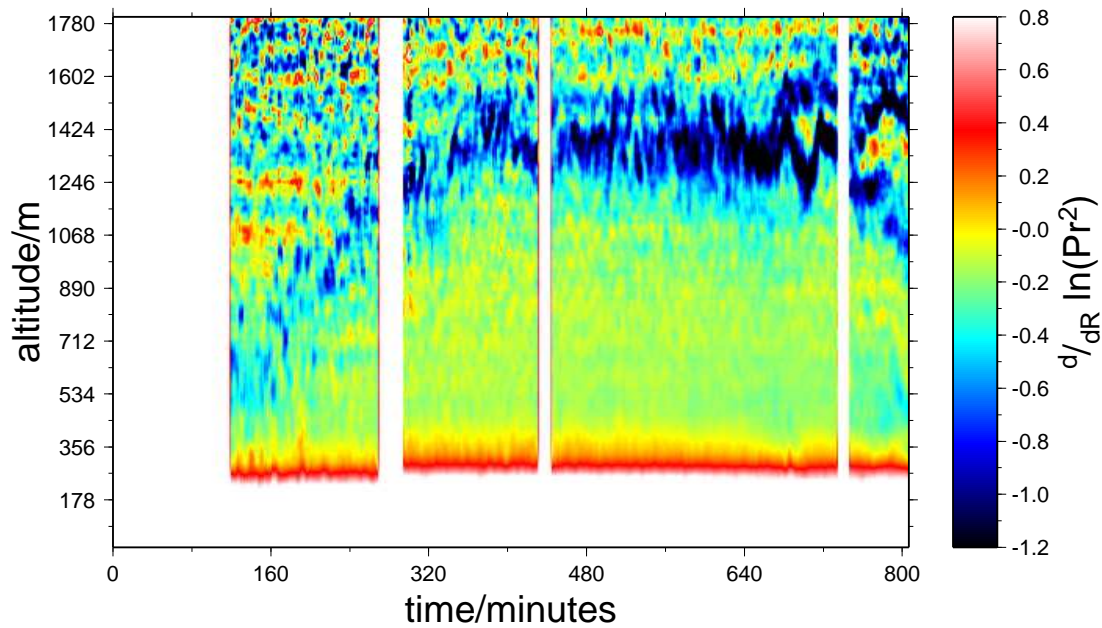
b)

Figure 83: $\frac{d}{dR} \ln Pr^2$ of the lidar signal at 355 nm taken on a) April 4, 2002 and b)June 3, 2002, both at Hamburg center.

122

Development of the planetary boundary layer in Hamburg City and Hamburg Bergedorf, 2002/04/04
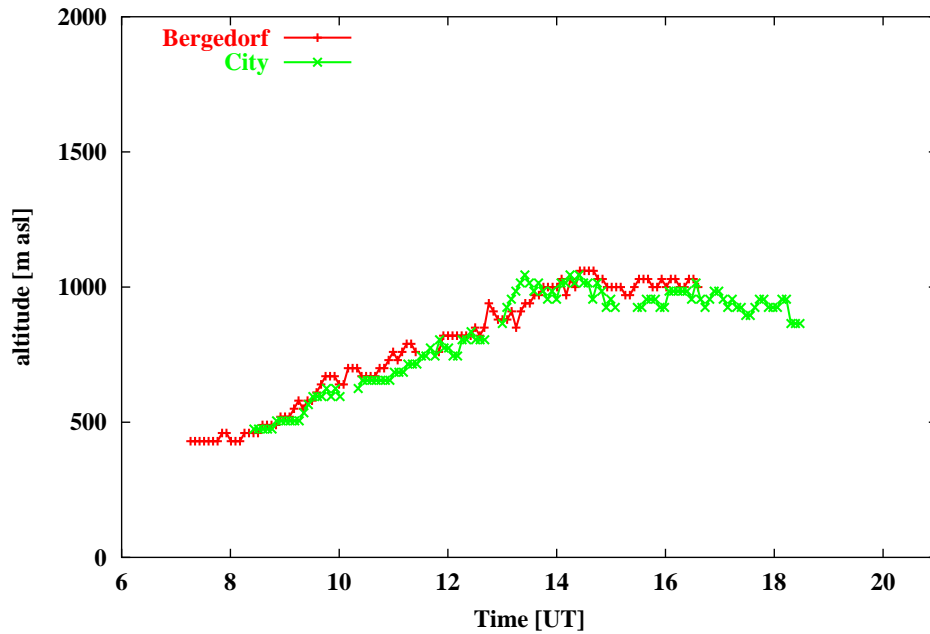
a)

b)

Development of the planetary boundary layer in Hamburg City and Hamburg Bergedorf, 2002/06/03
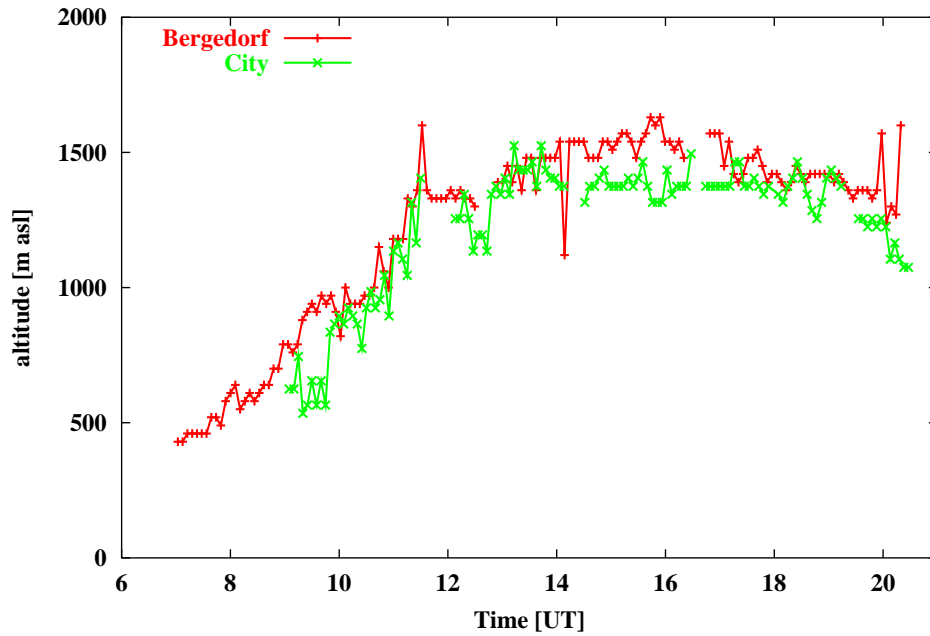
Figure 84: Development of the planetary boundary layer height in Hamburg center and Bergedorf on a) April 4, 2002 and b) June 3, 2002.

Table 16: Mean PBL-heights and their standard deviations, correlation coefficients and PBL rise times for simultaneous measurements at Hamburg center and Bergedorf.

Date	location	Mean PBL height [m]	Std. Dev [m]	correlation coeff.	PBL rise time [m/h]
2002/01/03	HH Center	767	29	0.78	380
	Bergedorf	804	33	(12:30 - 16:00 UT)	-
2002/02/14	HH Center	1212	-	0.52	250
	Bergedorf	1219	-	(9:00 - 17:00 UT)	200
2002/04/04	HH Center	976	37	0.96	100
	Bergedorf	1020	25	(8:30 - 16:30 UT)	90
2002/06/03	HH Center	1375	66	0.89	230
	Bergedorf	1459	89	(9:00 - 20:00 UT)	190
2002/08/29	HH Center	1405	-	-	-
	Bergedorf	1424	-	-	-
2002/09/30	HH Center	1249	-	-	-
	Bergedorf	1400	-	-	-

this cannot be done using backscattering lidar operating with a fixed elevation). An alternative can be proposed from what has been observed, as using a rural site which measurements could be influenced or not depending on the wind direction by the emissions of a nearby city. Difference in optical depth have been evidenced using such a procedure in similar relative humidity conditions which may attributed to the local production.

14 UV-B and optical properties

by Dimitris Balis

14.1 Objectives

The overall scope of this work package was to quantify the influence of aerosols on the UV-B radiation levels at ground using both measurements and model calculations. The main objectives were:

- To perform UV-B radiation measurements simultaneously with the lidar measurements.

- To validate a radiative transfer model against UV-B measurements, using additionally the lidar as input to the model calculations.

- To estimate the impact of different aerosol conditions on the UV-B radiation field, using both measurements and model calculations.

14.2 Methodology

At the Thessaloniki station (40.5°N, 22.9°E) two UV spectrophotometers (one single and one double monochromator) operated continuously and monitored the UV solar spectrum in the 285-366nm range with a 0.5 nm spectral resolution. In addition, measurements of global total, UV-A and UV-B radiation, direct and diffuse erythemal irradiance have been performed using broadband pyranometers and finally the Brewer instruments were used to monitor the columns on O_3. SO_2, the columns are being worked out. The information on the cloud cover was extracted from the 1-min resolution pyranometer data and from synoptic observations at the nearby airport. For the interpretation of the UV measurements the Tropospheric Ultraviolet and Visible (TUV) Version 4 model was used. During the first six months of the project the model was tested against spectral UV-B measurements and its accuracy was found to be better than 10% when the input parameters were well defined. The model is available through anonymous ftp, by Dr. Sasha Madronich (National Centre of Atmospheric Research). In order to solve the radiative transfer equation, we used the discrete-ordinates algorithm (DISORT) developed by Stamnes et al. (1988), using 16 streams. This routine is also used by other state of the art radiative transfer codes (e.g. UVSPEC). In TUV the atmosphere is divided in 50 adjacent and homogeneous layers. In each of them it is assumed that scattering and absorbing properties are constant, but are allowed to be different from layer to layer.

To estimate the impact of different aerosol conditions on the UV-B radiation field, measurements of the vertical distribution of the aerosol extinction coefficient were used, which were taken during routine observations and special events of high aerosol load (e.g. Sahara dust outbreaks, forest fires etc). Spectral and broadband UV-B irradiance measurements, as well as total ozone observations, were available whenever lidar measurements were obtained.

For the determination of the aerosol optical properties that are relevant to the transmission of the UV-B radiation through the atmosphere, we compared measured and modeled spectral UV-B irradiances using aerosol extinction and lidar ratio vertical profiles measured by a Raman lidar system, together with an indirect determination of the single scattering albedo, since there was no directly measured information of the size distribution and chemical composition of the measured aerosols. To derive estimates of the effective SSA at cloud-free days with different aerosol conditions we used measured spectral irradiances and aerosol optical depth at the stations of Thessaloniki and Lindenberg (Germany). Measurements of global and diffuse (the latter available only at Thessaloniki)
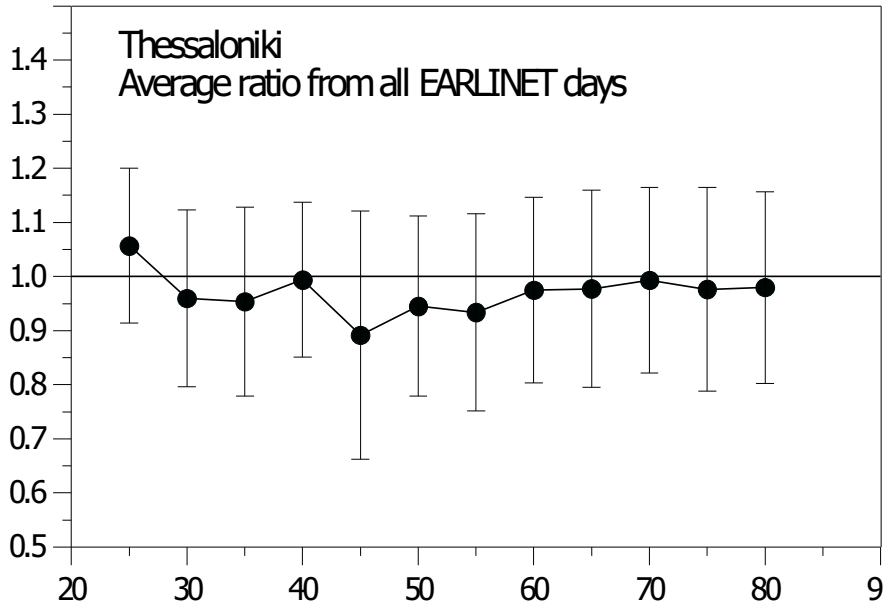
Figure 85: Average ratio of simulated to measured erythemal irradiance as a function of the solar zenith angle.

irradiance and of direct-to-diffuse irradiances ratio were compared with model calculations, which were based on the actually measured total ozone column and aerosol optical depth. From these comparisons we determined the values of SSA for which the model and the measurements were in agreement of better than 1%. The individual uncertainties of the measurements, modeling and aerosol optical depth determination contribute to the overall uncertainty in determining the single scattering albedo. A realistic estimate of the achievable accuracy is about 0.1 units of SSA for high aerosol optical depths and about 0.2 units for low aerosol conditions (Bais et al., 2002). For the theoretical determination of the aerosol optical properties that are relevant to the transmission of the UV-B radiation through the atmosphere we used the software package OPAC (Optical Properties of Aerosols and Clouds) (Hess et al., 1998), which provides optical properties in the solar and terrestrial spectral range of atmospheric particulate matter. Microphysical and optical properties of 10 aerosol components are considered as typical cases. The optical properties considered in this study were the extinction, scattering and absorption coefficients, the single scattering albedo and the lidar ratio at 355nm. These are calculated on the basis of the microphysical data (size distribution and spectral refractive index) under the assumption of spherical particles in case of aerosols. Backward trajectories at certain levels in the troposphere were provided in the frame of EARLINET by the German Weather Service (DWD) and were used to determine the origin of the aerosols observed.

14.3   Scientific achievements

All spectral measurements performed at Thessaloniki during the days when lidar measurements were available, were compared with model calculations using as input the total ozone measured by the Brewer spectrophotometer and the aerosol optical depth at 355 nm measured both with the Brewer (Santacesaria et al., 1997) and with the Raman lidar, assuming that there are background aerosol conditions in the stratosphere. For the selection of the single scattering albedo (SSA) a pre-
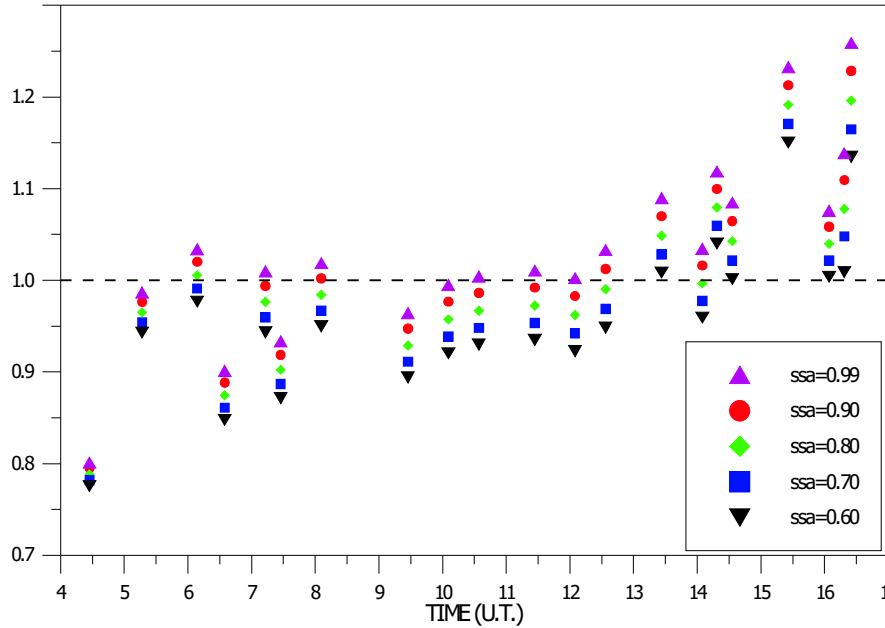
Figure 86: Ratios of simulated to measured global irradiance at 340 nm for various values of the single scattering albedo, for the 10th of August 1998 at Lindenberg.

calculated value of 0.8 was used initially, corresponding to a realistic assumption concerning the microphysical properties of the aerosols of an urban site (Shettle and Fenn, 1979). The resulting ratios of the measurements over the calculations were averaged over certain solar zenith angle intervals. These average ratios are shown in Fig. 85.

As it is clear from this figure the mean ratio is of the order of 0.98 and does not show any solar zenith angle (SZA) dependence, since the pseudospherical DISORT was used for the model calculations. This mean ratio indicates that in general the model simulates very satisfactory the measured UV spectra, when total ozone and aerosol optical depth are accurately known. However, the uncertainty in the choice of the appropriate SSA value introduces differences of about 15% for individual simulations performed for all the days when both UV and lidar measurements were available. This uncertainty is significant and limits our ability to use a radiative transfer model for the interpretation of the UV measurements for an area that can be influenced from various aerosol sources. For this reason we applied an indirect method for estimating the single scattering albedo, already described in the previous section. We applied the iterative procedure for the indirect determination of the single scattering albedo on a case extracted from the LACE98 experiment (Ansmann, 2002). We used global irradiance measurements performed with a single Brewer at Lindenberg and aerosol optical depth measurements at 399 nm performed with a sunphotometer during the 10th of August 1998. The reason for selecting this case is that during that period there were closures experiments conducted that allow the justification of the estimated values of the single scattering albedo. In Figure 86 we show the application of the method on the measurements of that day.

As it is evident from that figure there is variability during the day in the values of SSA that give ratios close to 1. In the morning hours the method indicates values larger than 0.9 while in the afternoon the SSA values decrease even down to 0.6. This change indicates the presence of different type of aerosols above the measuring site between the morning and the afternoon hours, when more absorbing aerosols are expected to be present. As described in Ansmann (2002) the flow was from
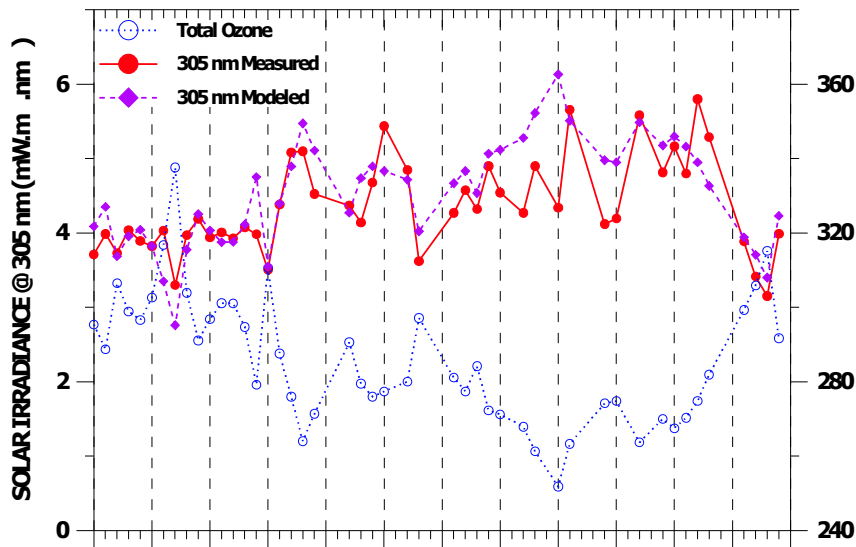
127

Figure 87: Total ozone, model and measured global irradiance at 305 nm for the period Sep-Oct 2001 at Thessaloniki, Greece.

the north during most of that day with low aerosol optical depth values, while in late afternoon the winds changed to east and southeast advecting air from the polluted western and southwestern parts of Europe. Aerosols from polluted (urban) regions are more absorbing in the UV (see e.g. Shettle and Fenn (1979)) and therefore smaller values of the SSA are expected. The estimated SSA values are consistent with this change in the meteorological situation and the source regions and thus we can claim that estimated change of the SSA during the day is confirmed by independent observations. Next from the available UV and lidar measurements at Thessaloniki we tried to identify clear sky cases that allow quantifying the effect of the different aerosol properties on the solar UV at the Earth's surface. For this purpose we used the total ozone measurements and aerosol optical depth measurements performed with the double Brewer spectroradiometer, the estimated SSA, profiles of the aerosol extinction coefficient and the lidar ratio, and backward trajectories. Since the Raman lidar measurements are performed only after sunset we examined here only spectral measurements performed during late afternoon hours in order to minimize the time difference between the two measurements. Comparisons were performed between measurements that corresponded to the same solar zenith angle. From all the available spectral UV measurements we selected to study in more detail three cases, which, according to the aerosol lidar measurements and to the trajectory analysis, corresponded to distinct aerosol conditions. These three cases were selected from the period September-October 2001 and are presented in Figure 87. This figure shows for the period of these two months the total ozone measurements and the measurements of the global irradiance at 305 nm, a wavelength where absorption by ozone is very strong with a Radiation Amplification Factor (RAF) of about 3 while the accuracy of the measurements is better than 5%.

The solid circles show the measured values of the UV irradiance, while the diamonds show the modeled values considering only the effect of ozone absorption in the calculations. The differences between the two curves show the effect of the aerosols on the attenuation of the UV irradiance at the surface. It is evident from this figure that day-to-day changes in the aerosol optical properties can cause changes in the UV of similar magnitude with changes induced from changes in the total ozone column. This effect is on the average about 4% but there are days when the aerosol effect can
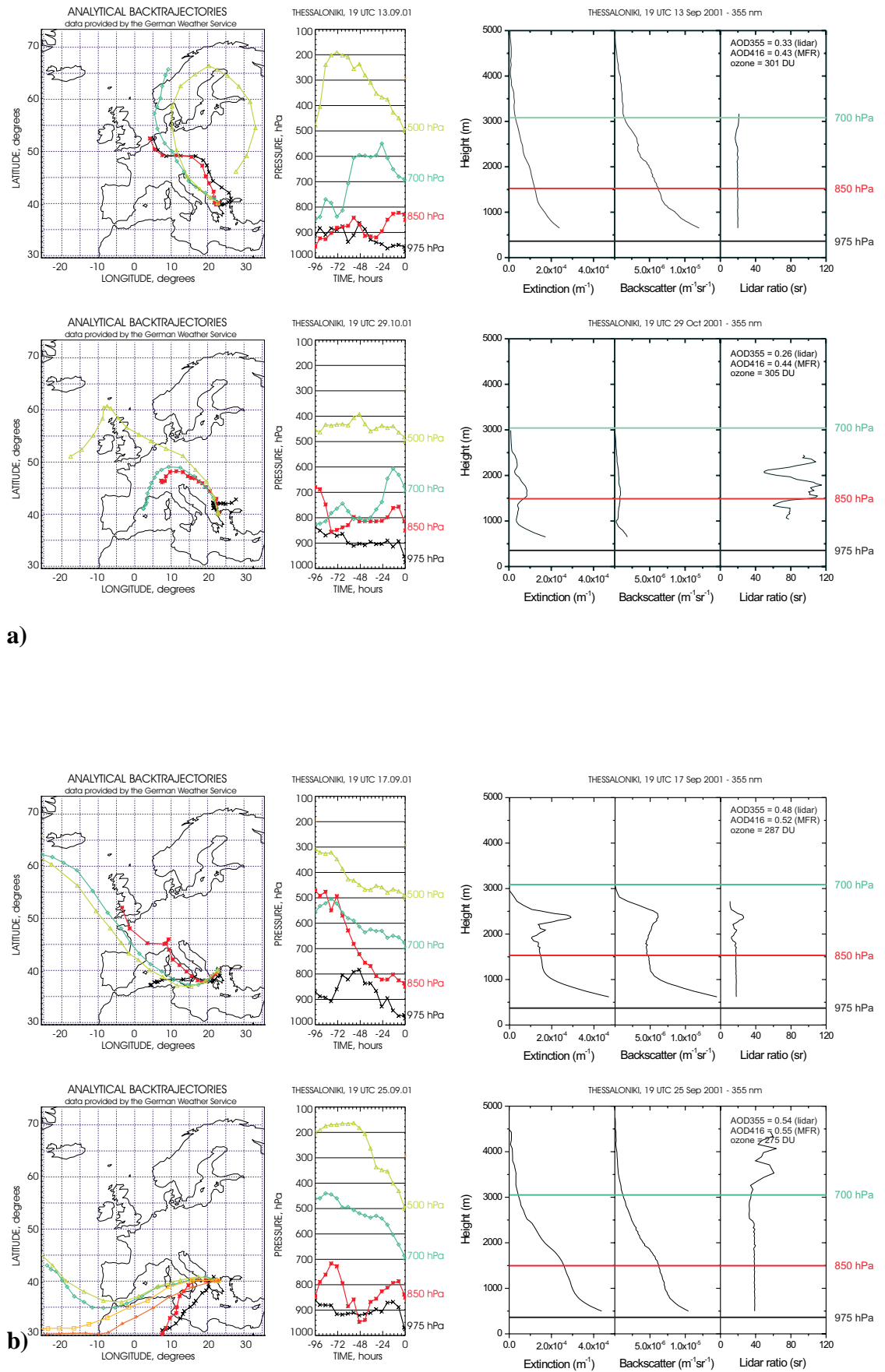
Figure 88: Profiles of the aerosol extinction and backscatter coefficients and the lidar ratio and backtrajectories for 13-9-2001 and 29-10-2001 and for 17-9-2001 and 25-9-2001.
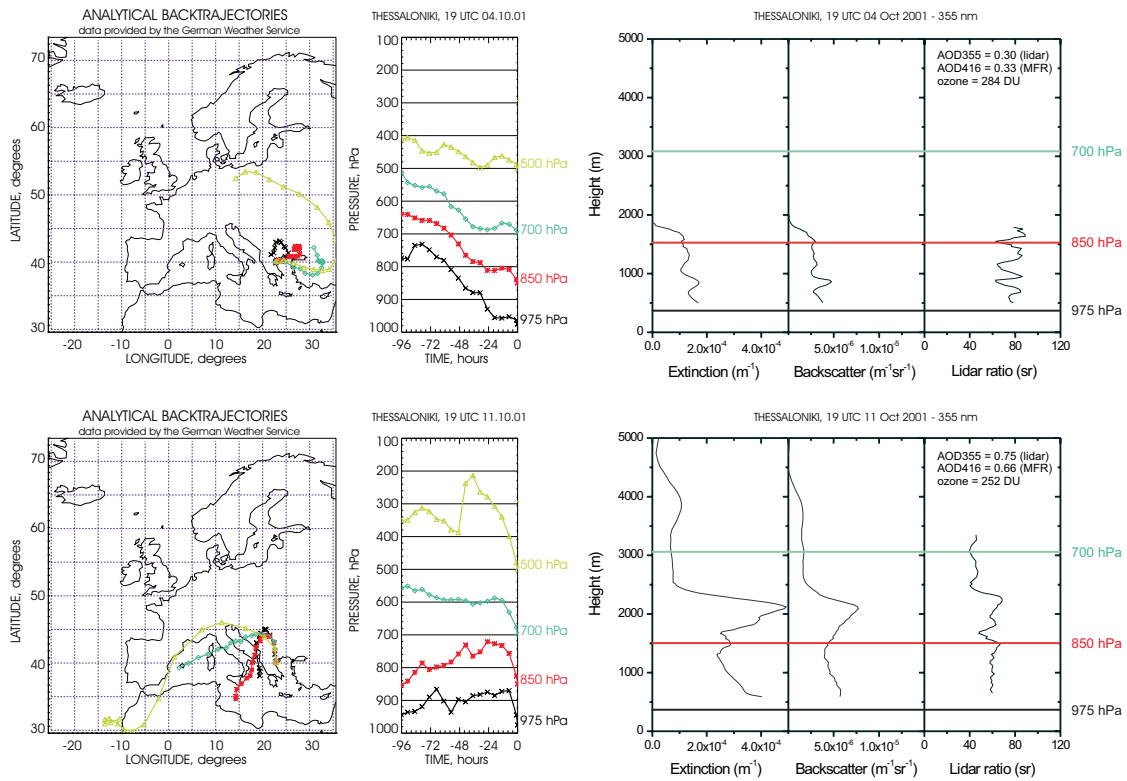
Figure 89: Profiles of the aerosol extinction and backscatter coefficients and the lidar ratio and backtrajectories for 4-10-2001 and 11-10-2001.

reach almost 30%. Kylling et al. (1998) found similar cases in measurements performed in a remote island in the Northern Aegean Sea during the PAUR experiment that took place in 1996. From this period we present the following three cases, because according to the trajectories they allow a distinct characterization of the air masses present over the measuring site:

Case 1: Two days with same total ozone and same aerosol optical depth but with different lidar ratio and UV irradiance (13-Sep-2001 versus 29-Oct-2001) (see Figure 88a)

Case 2: A Sahara dust event versus a clean (low) aerosol case with (25-Sep-2001 versus 17-Sep-2001) (see Figure 88b)

Case 3: A pollution episode, where the total ozone decline is accompanied by a decrease in UV irradiance, compared with a clean case (11-Oct-2001 versus 4-Oct-2001) (see Figure 89).

The three cases discussed above made it possible to quantify the effect of certain type of aerosols on the UV irradiance but left many uncertainties about the consistency between measured lidar ratio profiles and estimated SSA values. Therefore all the measurements (independent of their ozone values) of global and diffuse irradiance and of direct-to-diffuse irradiances ratio considered in Figure 85 were compared with model calculations, which were based on the actually measured total ozone column and aerosol optical depth. From these comparisons we estimated the values of SSA for which the model and the measurements were in agreement of better than 1%. Depending on the sensitivity of each quantity to changes in SSA, more than one value of SSA may satisfy the above condition. The mean of these values was considered the effective single-scattering albedo of the layer above the measuring site. For the same cases we calculated the mean lidar ratio as determined by the nearest in time measurement with the Raman lidar of LAP. The results are shown in Figure

90b.
For this purpose we also calculated with OPAC the SSA and the lidar ratio at 355nm for various

a)

b)
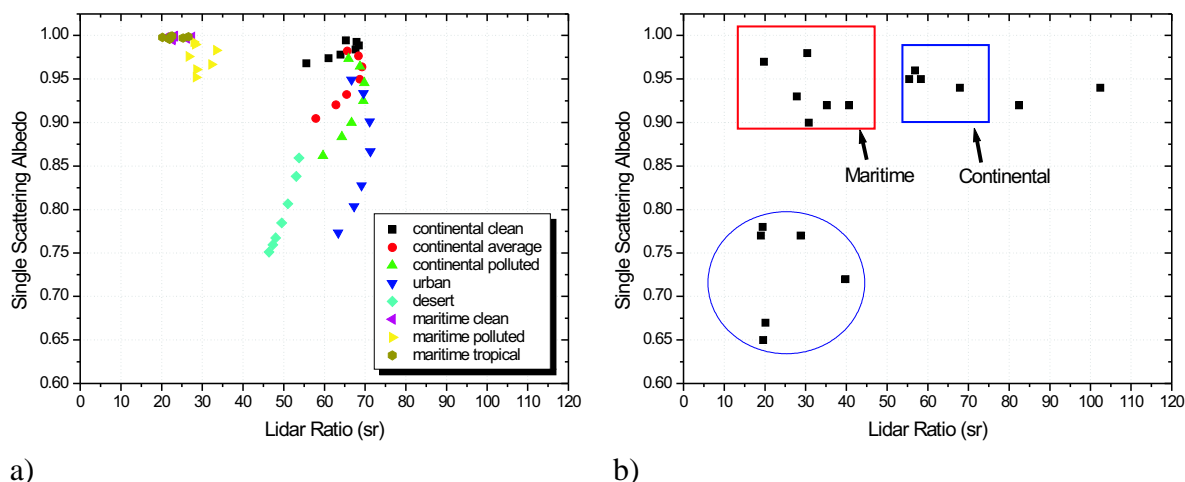
Figure 90: Estimates of the single scattering albedo and the lidar ratio at 355 nm for various aerosol models based (a) on OPAC (b) on measurements.

aerosol models and relative humidity classes. These calculations are demonstrated in Figure 90a. From both figures it is evident that similar SSA or LR values can correspond to different aerosol types. However the simultaneous knowledge of both parameters improves our ability in characterizing the aerosol type. For instance SSA values of 0.9 can correspond to both maritime and continental aerosols, which however have different LR values. Similarly urban and continental aerosols might have similar LR values but distinct SSA values. The comparison of the two figures indicates that the experimental determination of the SSA and the lidar ratio are consistent for the case of maritime and continental aerosols. This is verified also by checking the backward trajectories, with the OPAC estimations. Using SSA / lidar ratio connections make a better characterization of these aerosol cases possible. However for the cases of urban aerosols and desert dust the association of the low SSA estimated by measurements with small lidar ratios are not in agreement with the modeled values. Similar studies performed by Ferrare et al. (1998) using Raman lidar measurements and SSA estimations based on size distribution measurements concluded that higher SSA values correspond to lower lidar ratios, however highly depending on relative humidity and the real part of the refractive index.

15 Statistical analysis

by Volker Matthias

15.1 Data base

The statistical analysis of the aerosol vertical profiles derived in the EARLINET project is restricted to the regular measurements. These measurements have been taken three times a week on preselected days (Mondays and Thursdays) and time windows (Monday early afternoon and sunset, Thursday sunset). Additional measurements performed on other days, e.g. for the observation of diurnal cycles or Saharan dust events have not been considered for the statistical analysis to avoid a bias for those "special" situations and for fair weather periods. Only one profile in each of the predefined measurement windows has been considered.

All data has been taken between May 1, 2000 and November 30, 2002, the period for which all EARLINET stations had to deliver data. Nevertheless, the individual data sets can be quite different. Due to technical reasons, some groups have much smaller data sets than others. Raman channels for example have been included in some systems in the second half of 2000 and therefore measurements cover only the period from Oct/Nov 2000 to Nov. 2002. Weather conditions also restrict the availability of aerosol vertical profiles in the northern part of Europe.

As has been stressed before, aerosol extinction profiles can only be derived in a quantitative way from Raman measurements. Therefore the statistical analysis is mainly based on the data from 10 EARLINET stations which operated UV Raman channels for at least 24 months. The stations together with the covered time and the number of measurements which have been taken can be seen in Table 17. It has been distiguished between summer (April till September) and winter (October till March).

Additionally, investigations of the aerosol vertical distribution based on pure backscatter measurements have been performed. Mean summer and winter profiles have been calculated at 532 nm for all stations with data from more than 24 months. Also here the stations and the number of available profiles are listed in Table 18.

Table 17: Number of measurements and covered time period for EARLINET Raman lidars stations

Station	covered time	all	summer	winter
Aberystwyth	5/00 - 10/02	55	34	21
Athens	11/00 - 11/02	81	45	36
Hamburg	5/00 - 11/02	109	71	38
Kühlungsborn	5/00 - 11/02	62	39	23
L'Aquila	5/00 - 11/02	75	41	34
Lecce	5/00 - 8/02	166	94	72
Leipzig	5/00 - 9/02	77	55	22
Naples	10/00 - 12/02	135	62	73
Potenza	5/00 - 11/02	88	60	28
Thessaloniki	02/01 - 08/02	57	31	26

Table 18: Number of measurements and covered time period for EARLINET stations with 532 nm backscatter measurements

Station	covered time	all	summer	winter
Athens	11/00 - 11/02	165	109	56
Belsk	10/00 - 9/02	124	72	52
Hamburg	11/00 - 12/02	186	107	79
Kühlungsborn	5/00 - 11/02	123	62	61
Leipzig	5/00 - 9/02	84	57	27
Minsk	5/00 - 9/02	183	126	57
Munich	5/00 - 11/02	139	83	56
Neuchâtel	5/00 - 11/02	137	78	59
Potenza	5/00 - 9/02	182	112	70
Thessaloniki	6/00 - 11/02	107	64	43

15.2   Methods

The statistical evaluation follows the methods described in Matthias and Bösenberg (2002). It has been mainly used for the planetary boundary layer (PBL) where most of the aerosol particles can be found. Seven out of ten stations deliver profiles from ca. 500 m agl upwards. The other three stations can deliver only a limited number or even no extinction values in the lowest 1000 m above ground. (see Fig. 15.2). The aerosol optical depth (AOD) in the PBL has been derived by extrapolating the lowest data point down to ground and then integrating over the whole layer. In most cases, this assumption can be made without large errors because the boundary layer is usually still well mixed at sunset when the measurements are taken. However in some winter cases the lowest measurement height is above the boundary layer and representative extinction values can not be determined for the lowest layer. Fortunately those cases are rare. They have been excluded for this statistics.

The determination of the boundary layer height out of the lidar data is done looking at the most significant gradient in the range corrected lidar signal, which is due to a high decrease in aerosol backscatter caused by lower particle concentration and humidity above the PBL. This method is well proven (Flamant et al., 1997) and delivers accurate values of the PBL height under well mixed conditions.

The aerosol optical depth (AOD) has additionally been calculated in fixed layers of 0-1 km, 1-2 km, 2-5 km. Higher layers have not been considered here because they are often not covered by the Raman lidar measurements and the statistics would be based on only few measurements. Additionally, elastic lidar measurements show that the contribution of aerosol in those very high layers can be regarded as rather small (see section 15.3.4).

For the lowest layer, the optical depth values have been calculated by assuming the extinction value closest to ground to represent the extinction in the missing layer. For the other layers, only profiles which cover the whole height range have been taken. Low and midrange clouds have been excluded in all aerosol profiles, cirrus clouds are usually optically thin and they are sometimes included in the aerosol profiles. To distinguish cirrus clouds from aerosol, the names of all files containing cirrus clouds are stored in a separate list and can therefore be sorted out.

The error which is introduced by the used extrapolation method has been investigated by Ina Mattis from IfT. She compared the method with two potentially more accurate methods which rely on
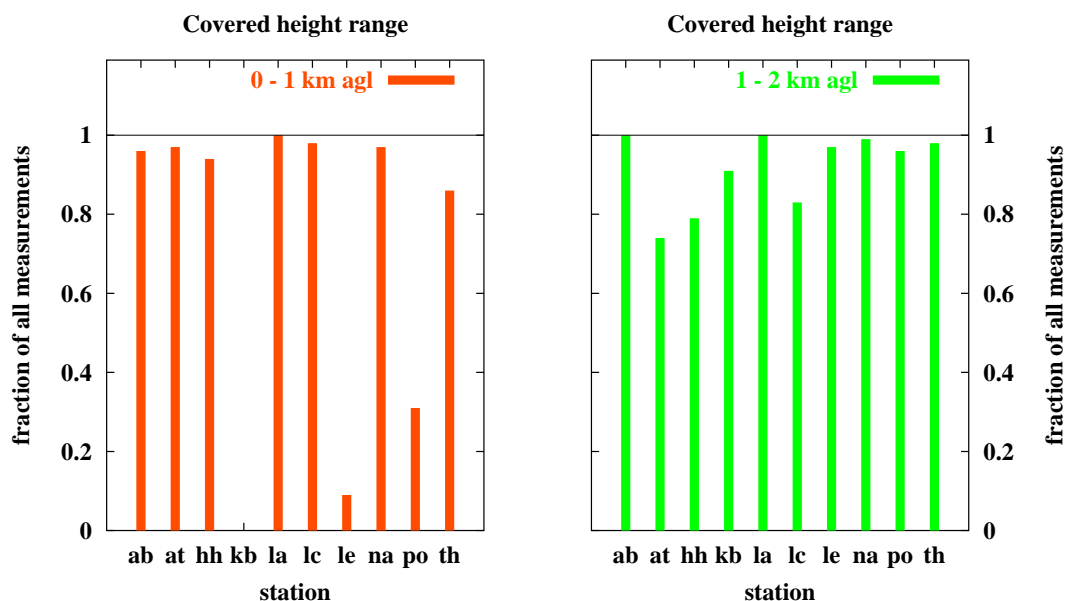
Figure 91: Coverage of the lowest 1000 m agl and the layer between 1000 and 2000 m agl by aerosol extinction profiles from the considered stations.

the possibility to derive the aerosol backscatter profile also in low altitudes where the overlap between laser beam and telescope field of view is still incomplete. Figure 92 illustrates three different methods of extrapolation of the extinction profile from its lowest calculated point z_{ovl} down to the ground.

A Under the assumption of a well mixed dust layer, the profile is extrapolated with the constant value of $\alpha(z_{\mathrm{ovl}})$. In the example of Figure 92 z_{ovl} is 1.5 km and $\alpha(z_{\mathrm{ovl}}) = 62\,\mathrm{Mm}^{-1}$. The resulting dust layer mean extinction coefficient $\overline{\alpha}$ is $60\,\mathrm{Mm}^{-1}$.

B Under the assumption of a height constant lidar ratio, the extinction profile is extrapolated parallel to the backscatter profile $\beta(z)$ with the use of the actual layer-mean lidar ratio $\overline{LR}_{020626} = 48\,\mathrm{sr}$ for the range from z_{ovl} to the dust-layer height $z_{\mathrm{dl}} = 2.55\,\mathrm{km}$. The resulting $\overline{\alpha}$ is $65\,\mathrm{Mm}^{-1}$.

C Similar to B but with the use of the climatological mean lidar ratio $\overline{LR}_{\mathrm{climatol}}$ which was found to be 59 sr for Leipzig in the EARLINET period. In this case $\overline{\alpha}$ is $75\,\mathrm{Mm}^{-1}$.

Under real nighttime conditions, methods B and C are more realistic than method A since some hours after sunset the assumption of a well mixed dust layer often is not true. The aerosol backscatter and extinction in the lowest few hundred meters should be enhanced because of the stratification usually is stable during nighttime and humidity increses significantly. This increase of the aerosol load is represented by the backscatter profiles which can be observed down to the ground.
 The three methods A, B, and C were applied to 30 test cases, which were observed over Leipzig in 2001 and in 2002. The average value of all 30 dust-layer mean extinction coefficients is $88\,\mathrm{Mm}^{-1}$ without any extrapolation. The average values of $\overline{\alpha}$ derived with the methods A, B, and C are $97\,\mathrm{Mm}^{-1}$, $110\,\mathrm{Mm}^{-1}$, and $107\,\mathrm{Mm}^{-1}$, respectively. The $\overline{\alpha}$ values are underestimated by 20% if no extrapolation is applied. If method A is used the difference is in the order of 10 %. Methods B and C differ only by a few percent which indicates that for averages the climatological mean lidar ratio
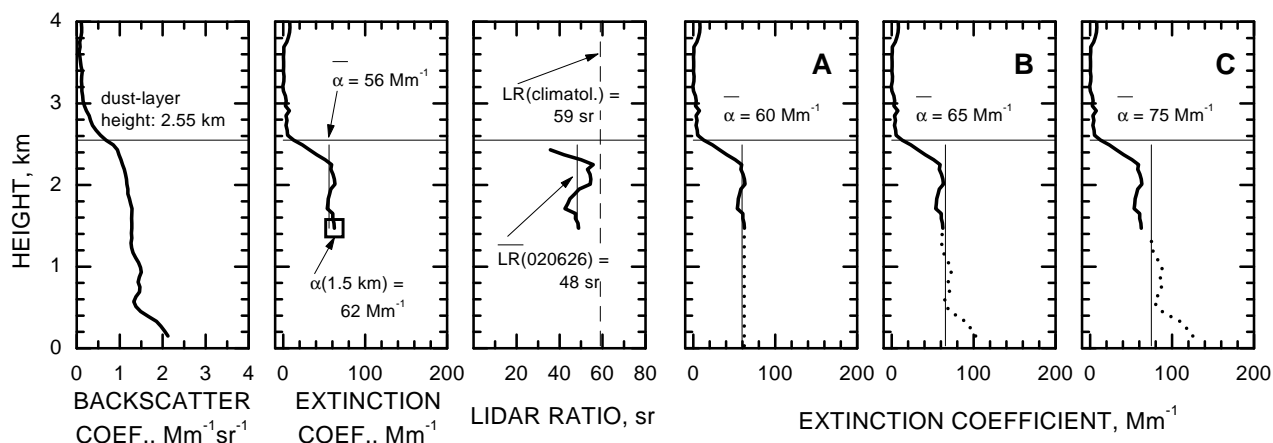
Figure 92: Profiles of the backscatter and extinction coefficients, and of the lidar ratio (all at 532 nm) observed on June 26, 2002 over Leipzig, Germany. The three right panels show the extended extinction profiles (dotted) and the resulting dust-layer mean values (thin lines) corresponding to the three extrapolation methods A, B, and C.

can be used for a rough estimate of dust-layer mean extinction coefficients even in cases where only a backscatter profile but no extinction profile can be derived for the dust layer because of $z_{dl} < z_{ovl}$.

15.3 Results

Aerosol extinction measurements from the 10 aforementioned EARLINET stations were the basis for investigations about the PBL-height, aerosol optical depth in the PBL and the statistical parameters of the distribution functions. Elastic backscatter measurements at 532 nm show mean vertical distribution of the aerosol in winter and summer seasons.

15.3.1 PBL-height

The PBL-height shows in most cases a clear annual cycle with higher values in summer than in winter. E.g. for Hamburg it has been shown that on average this cycle follows quite well a sinus function with maximum values in the beginning of July and lowest values around beginning of January (Matthias and Bösenberg, 2002). The variability of the PBL-height is high, usually with a relative standard deviation in the order of 0.4.

  Nevertheless there are also stations where the annual cycle of the PBL-height shows only a weak dependence on season (e.g. Athens) or even lower values in summer than in winter (Lecce), see Fig. 93. The reasons for the surprising feature in Lecce could not yet be found. Possible reasons which are under investigation are land-sea-breeze effects influencing the aerosol distribution in the PBL in summer and very low PBL-heights in winter which cannot be detected. The results from Kühlungsborn are clearly influenced by the difficulty of the lidar system to cover the lowest 1500 m of the troposphere, which leads to an overestimation of the PBL height and a rather low variability. High mean PBL-heights and low variabilty can also be found for L'Aquila and Potenza, both mountain stations at 683 m and 829 m above sea level, resepectively. All measurements showed that the top of the PBL is rarely above 3000 m agl, therefore mountain stations have a cutoff for maximum values compared to low level stations. Additionally, the Potenza lidar system does not cover the lowest 1000 m above ground. Low mean values and also low variability are found for Athens, which can be
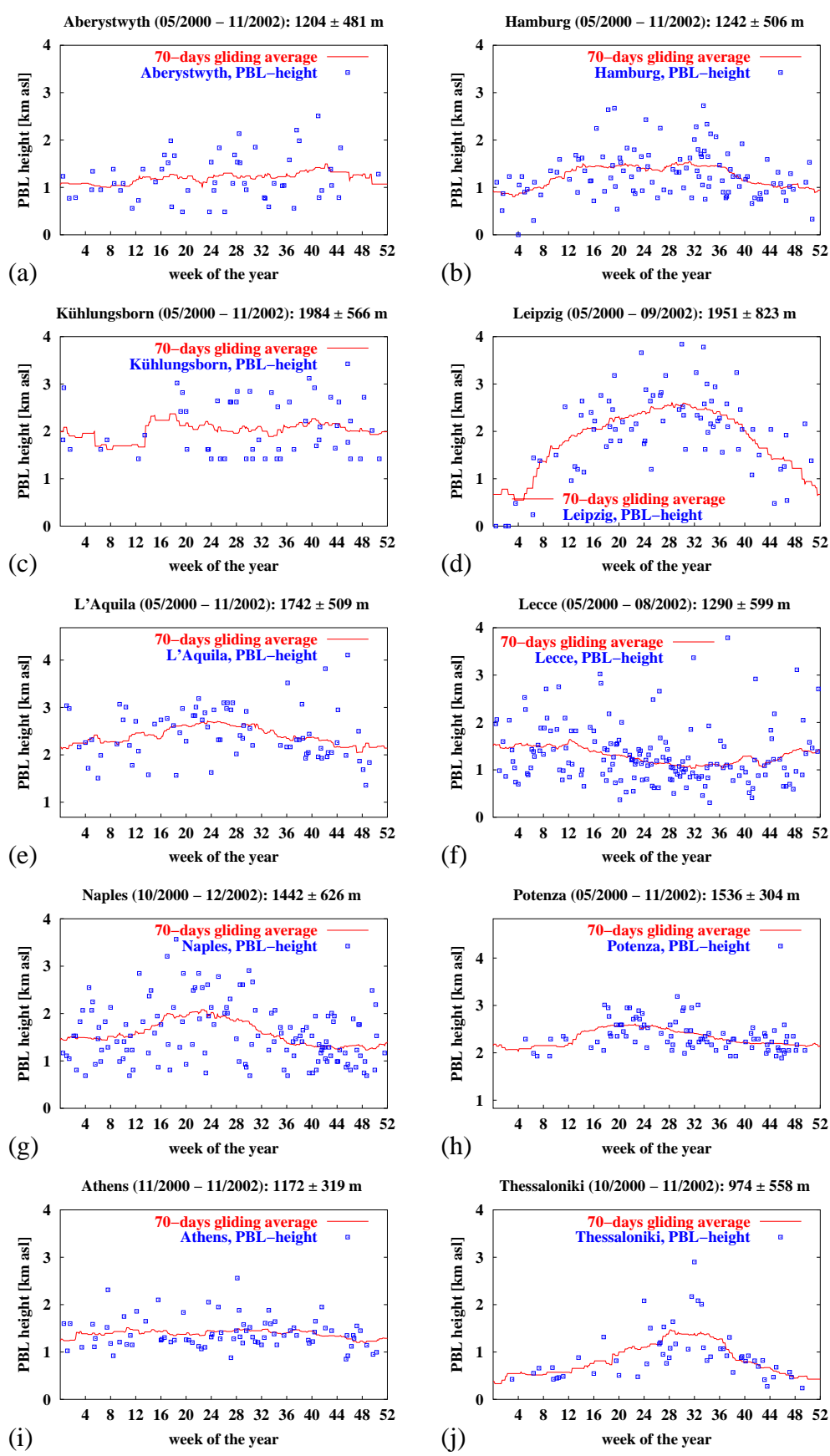
Figure 93: Annual cycle of the planetary boundary layer height for ten EARLINET stations

136

Table 19: Statistical parameters of the PBL-height for ten EARLINET stations

Station	PBL-height / m agl	Std. Dev / m	Rel. Std. Dev	Skewness
Aberystwyth	1204	481	0.40	0.62
Hamburg	1242	506	0.41	0.62
Kühlungsborn	1984	566	0.29	0.36
Leipzig	1951	823	0.42	-0.39
L'Aquila	1742	509	0.29	0.18
Lecce	1261	599	0.48	1.29
Napoli	1442	626	0.43	0.70
Potenza	1542	304	0.20	0.69
Athens	1172	319	0.27	1.16
Thessaloniki	899	538	0.60	1.47

explained by the strong influence of local circulation patterns due to the surrounding mountains. A frequent occurence of very low PBL-heights are detected in Thessaloniki leading to the lowest mean value of all stations and the largest variability. The effect could not be explained up to now and will be further investigated with additional measurements. Possibly also a land-see-breeze affects the aerosol layering in the lowest few hundred meters.

15.3.2 Aerosol optical depth

For all ten considered stations the aerosol optical depth has been calculated in the planetary boundary layer and in fixed layers of 0-1 km, 1-2 km and 2-5 km above ground level.

For all ten considered stations the aerosol optical depth has been calculated in the planetary boundary layer and in fixed layers of 0-1 km, 1-2 km and 2-5 km above ground level. AOD-values in the PBL range from 0.16 (Aberystwyth) to 0.3 (Athens and L'Aquila) with high variability throughout the whole year (Table 20). The relative standard deviation is typically between 0.4 for southern European sites and 0.8 for northern European ones. Again, Kühlungsborn is an exception with lowest values and highest variability which is again explained by missing values for PBL-heights below 1.5 km.

Generally, higher values of the aerosol optical depth can be found in summer compared to winter, which is at least partly due to higher PBL-heights in summer. Hamburg, Kühlungsborn and Leipzig show an interesting annual cycle of the AOD with two maxima, one in spring and one in late summer/early fall (Fig. 94). It can only be speculated whether e.g. typical flow patterns in Germany or humidity effects are responsible for this feature.

All distribution functions show positive skewness. Again higher values are found for the Northern stations (0.8 - 1.9) and lower values for the South-European ones (0.5 to 1.1) (Table 20). Again Kühlungsborn differs for known reasons from the general pattern with exceptionally high values for both standard deviation and skewness. The high skewness already indicates that the frequency distribution is not Gaussian. In fact it has been shown that the lognormal distribution represents the cumulative frequency distribution of the AOD much better than a Gaussian distribution does (see Fig. 95). Two tests have been applied to check the quality of the fitted distribution function, the χ^2-test and the Kolmogorov-Smirnov-test. The χ^2-test looks for quadratic deviations of the measurements
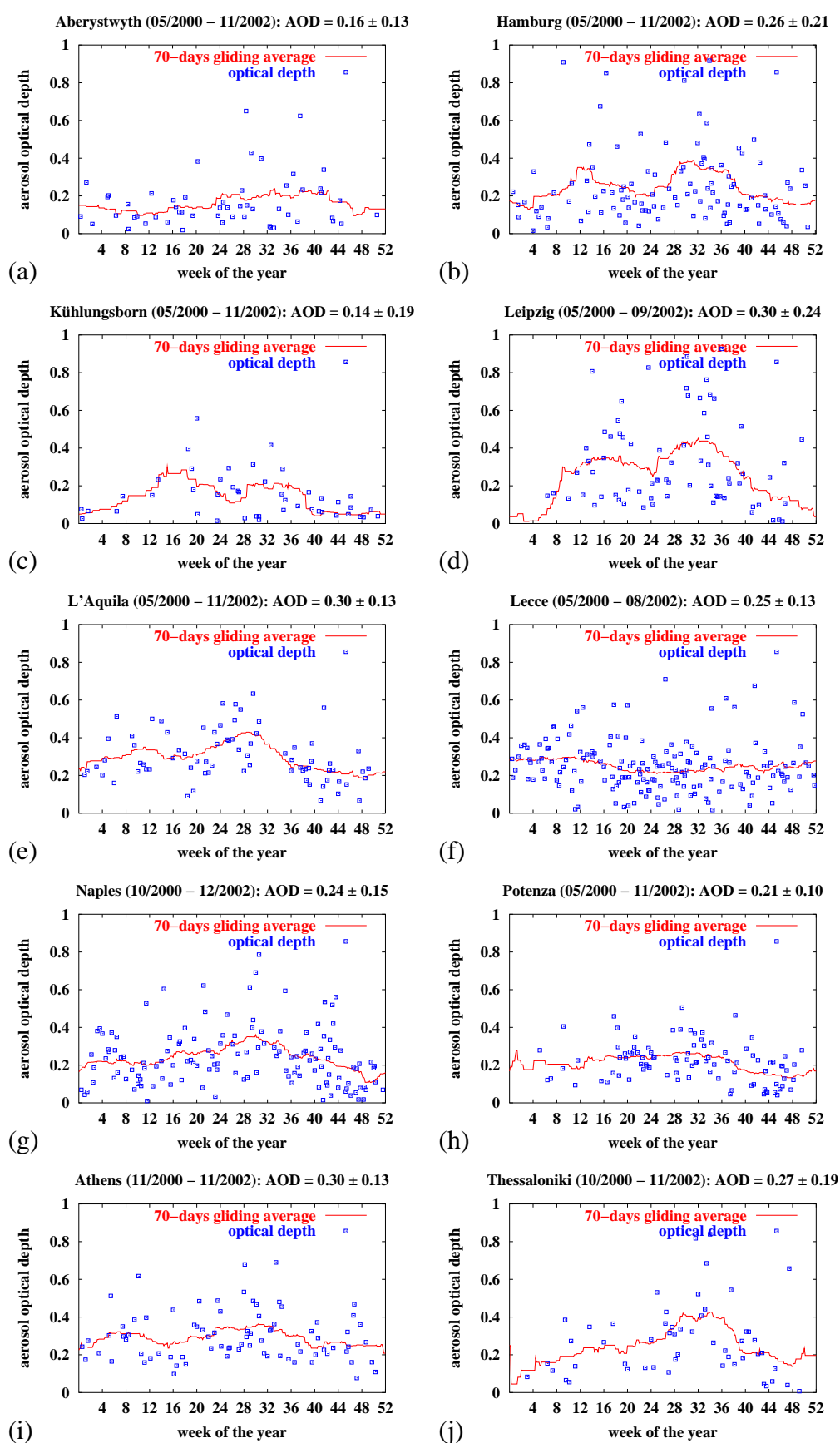
Figure 94: Annual cycle of the aerosol optical depth in the planetary boundary layer height for ten EARLINET stations

138

Table 20: Statistical parameters of the aerosol optical depth in PBL for ten EARLINET stations

Station	Mean AOD	Std. Dev	Rel. Std. Dev	Skewness
Aberystwyth	0.16	0.13	0.81	1.86
Hamburg	0.26	0.22	0.83	1.90
Kühlungsborn	0.14	0.19	1.38	2.82
Leipzig	0.30	0.24	0.81	0.83
L'Aquila	0.30	0.13	0.43	0.55
Lecce	0.25	0.13	0.54	0.92
Napoli	0.24	0.15	0.62	1.02
Potenza	0.22	0.10	0.44	0.48
Athens	0.30	0.13	0.44	0.94
Thessaloniki	0.27	0.19	0.70	1.10

Table 21: Statistical parameters of cumulative frequency distribution of the aerosol optical depth in PBL for ten EARLINET stations

Station	Median of AOD (meas.)	Median of AOD (fitted)	Std. Dev (in log scale)	1σ-interval
Aberystwyth	0.135	0.125	0.77	0.06 - 0.27
Hamburg	0.20	0.19	0.79	0.09 - 0.42
Kühlungsborn	0.125	0.11	1.00	0.04 - 0.31
Leipzig	0.245	0.235	0.89	0.10 - 0.57
L'Aquila	0.27	0.27	0.48	0.17 - 0.44
Lecce	0.235	0.21	0.67	0.11 - 0.41
Napoli	0.215	0.185	0.79	0.08 - 0.41
Potenza	0.215	0.19	0.57	0.11 - 0.33
Athens	0.27	0.28	0.43	0.18 - 0.42
Thessaloniki	0.265	0.20	0.90	0.08 - 0.50

from the fitted distribution while the Kolmogorov-Smirnov-test looks for maximum deviations. For both tests, threshold values for e.g. a significance level of 95 % are given in tables (Johnson and Leone, 1964). Following these tests on a 95 % level, the Kolmogorov-Smirnov-test is passed by all stations except one (Naples). For the χ^2-test the result depends on the number of classes (optical depth intervals) defined for the test calculations. Since it is recommended to have at least 5 elements in each class, in the beginning 9 classes have been defined and 6 of the 10 groups passed the test. After reducing the number of classes to 7, two additional groups passed the test. Only for the frequency distributions of Naples and Lecce the lognormal distribution does not represent the measurements on a 95 % significance level.

In Table 21 the median values and the 69%-(1σ-) intervals of the distribution functions are given. Calculated medians fit the measurements quite well, the 1σ-intervals are usually very broad and cover values from ca. 0.08 to 0.45. Only in Thessaloniki and Leipzig, higher values of 0.5 and more can be found in the 1σ-interval. This clearly demonstrates the large variability of possible aerosol
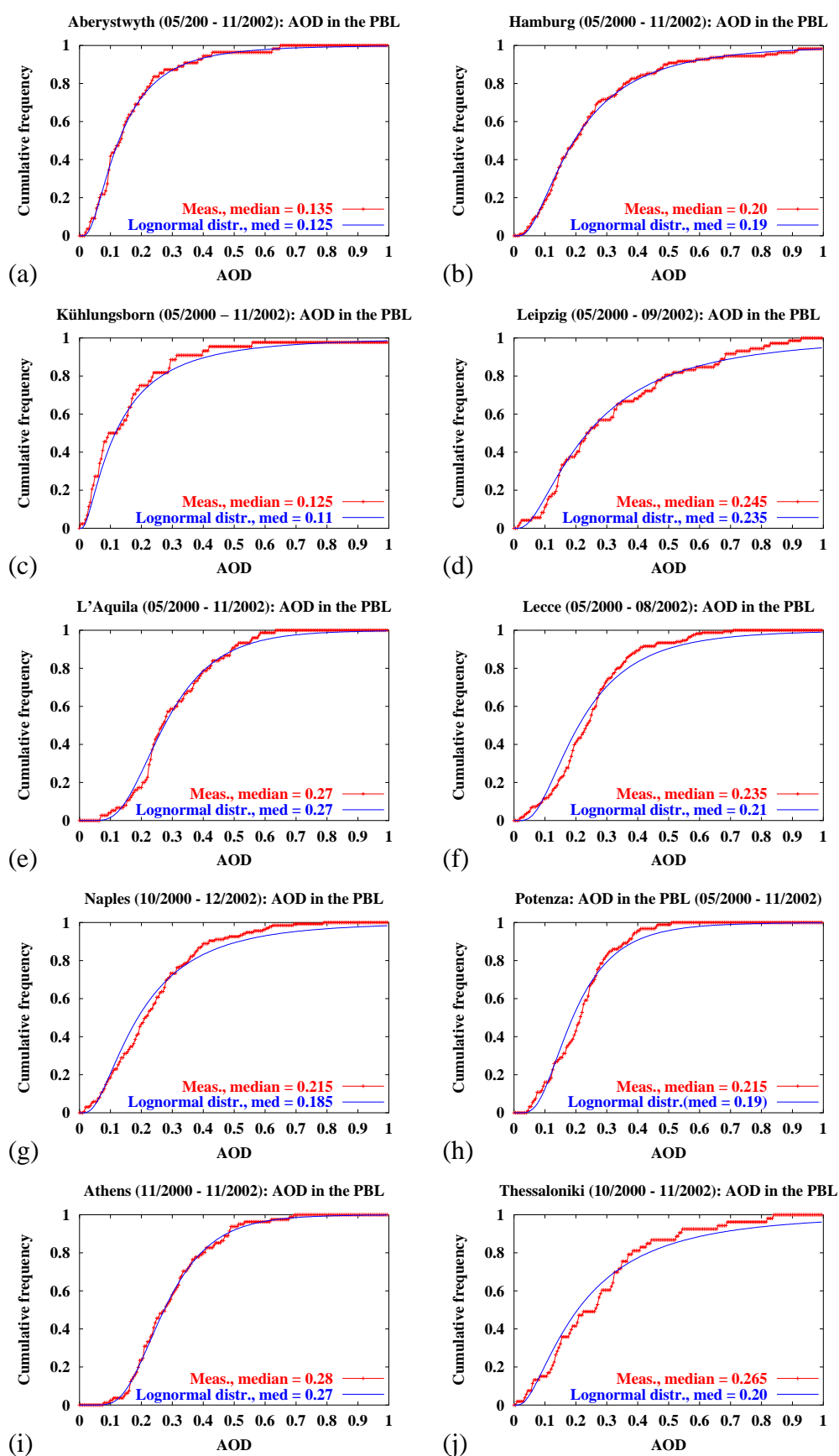
Figure 95: Cumulative frequency distribution of the aerosol optical depth in the PBL for ten EAR-LINET stations
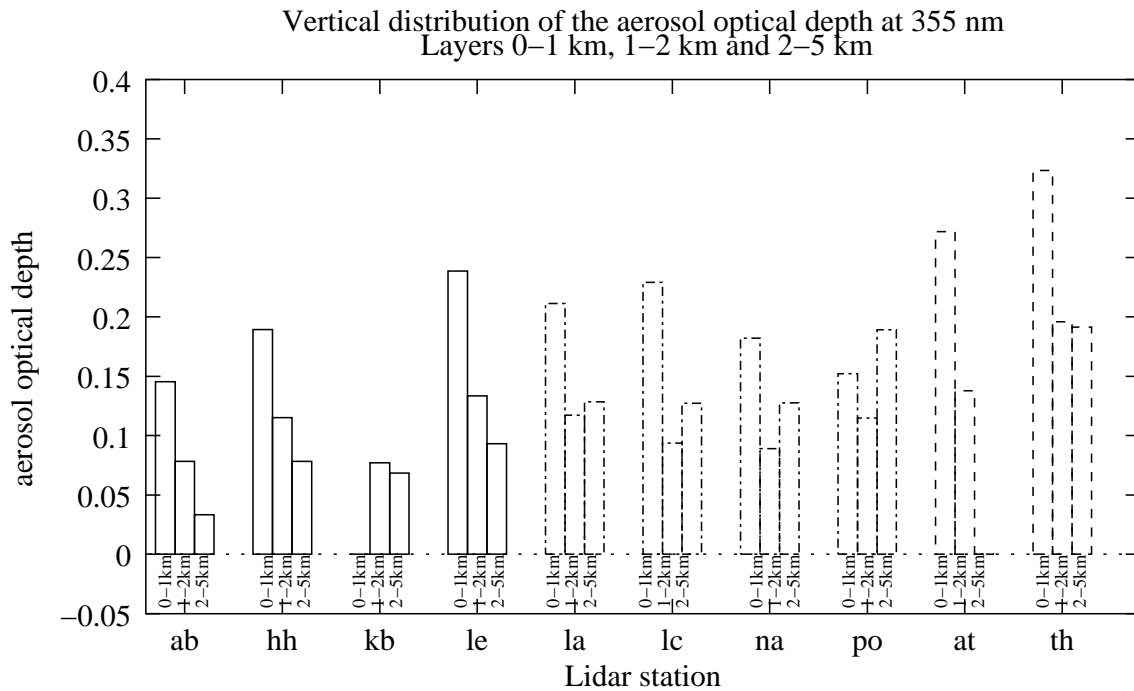
140

Figure 96: Aerosol optical depth in three layers, 0-1 km, 1-2 km and 2-5 km above ground level.

optical depth values, even in the planetary boundary layer where some aerosol is always present. Only long-term measurements on a regular basis can give information about the real variability and about trends in the aerosol distribution over Europe.

Additional to the column values, the vertical distribution of the aerosol optical depth has been investigated for the three layers 0-1km, 1-2 km and 2-5 km. The mean values shown here represent different numbers of profiles. Three stations cover the 0-1 km range only with few measurements, in the range 1-2 km the coverage is very good for all stations, but also the layer 2-5 km is in some cases only represented by a few profiles. Kühlungsborn has no extinction profiles below 1000 m and Athens cannot deliver values up to 5000 m. The corresponding means have been omitted in Figure 96. The mean extinction values can be calculated by dividing mean AOD by the thickness of the layers.

Figure 96 gives interesting results about the vertical aerosol distribution in northern Europe (represented by Aberystwyth, Hamburg, and Leipzig) and in southern Europe, especially Italy. The northern stations show more or less the same vertical distribution of the AOD, about 80 % is accumulated in the lowest 2000 m. All Italian stations show larger AOD values for the 2-5 km layer than for the 1-2 km layer, nevertheless mean extinction values in the 2-5 km layer are significantly lower than in the 1-2 km layer. The high values in the upper layer represents frequent transport of aerosol in higher altitudes, e.g. from Saharan dust outbreaks and other continental sources. Here about 60 - 70 % of the AOD can be found in the lowest 2 km. The two Greek stations show highest values in the lower two layers compared to all other stations. AOD is larger than 0.4 in the lowest 2 km and also the 2-5 km layer shows a large amount of aerosol in Thessaloniki.

15.3.3 Correlation analysis

If the aerosol profiles of two nearby lidar stations are compared, they sometimes reveal very similar profiles. This, of course, depends on weather conditions and will not always be the case. For some
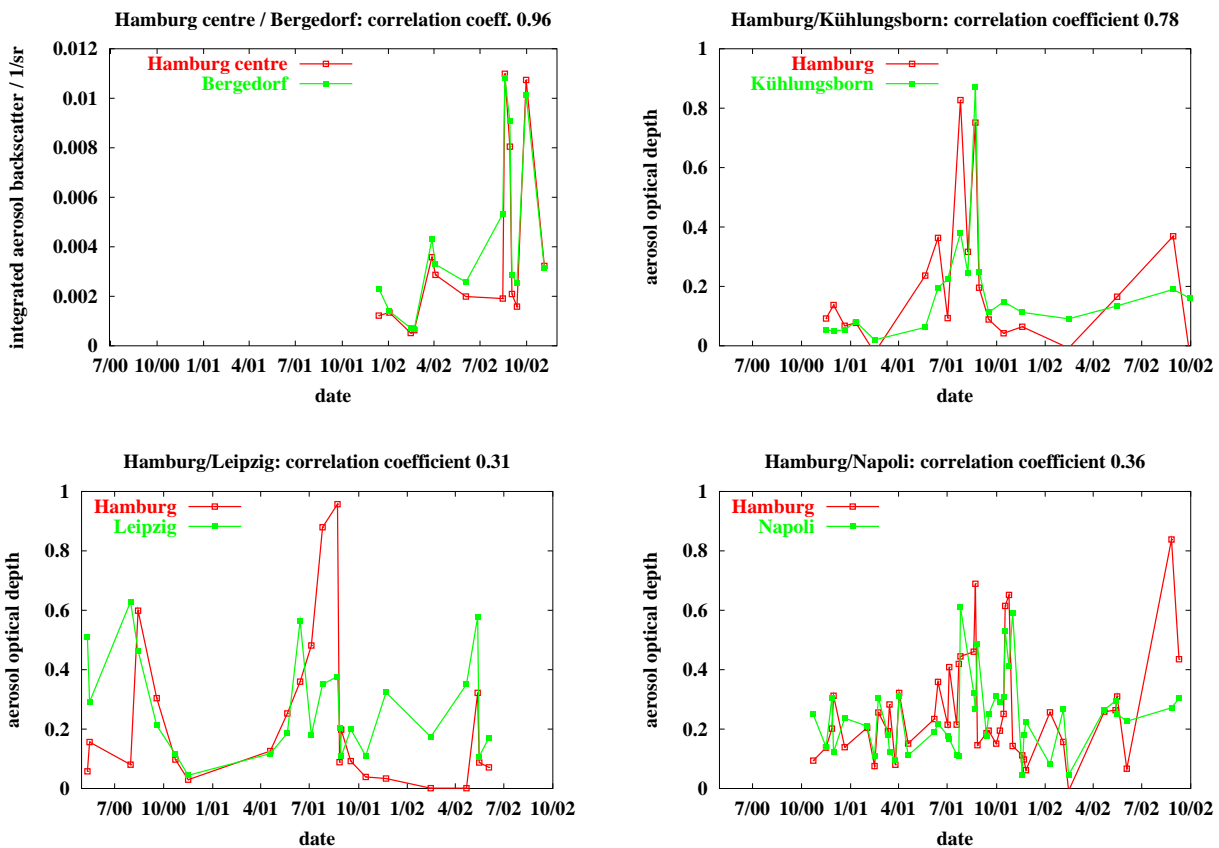
Figure 97: Correlations between aerosol optical depth for measurements on common days and in common height ranges for Hamburg/Bergedorf, Hamburg/Kühlungsborn, Hamburg/Leipzig and Hamburg/Naples.

of the EARLINET Raman lidar stations it has been investigated how large the correlation between optical depth values of nearby lidar stations are. For this purpose, only those days have been considered when both compared stations took measurements. The correlation has been calculated based on the optical depth in the common height range of the stations. This has been done to avoid large errors due to insufficient coverage of the lowest 1 km of the atmosphere.

The results are shown for Hamburg, compared to Leipzig (horizontal distance 300 km), Kühlungsborn (horizontal distance 130 km) and Bergedorf (horizontal distance 25 km). The latter station has been operated for one year in the frame of section 13 to investigate the differences between rural and urban aerosols and the representativity of aerosol lidar measurements for a larger area. For comparison Hamburg data has also been correlated to the data from Naples, which is in distance of ca. 1500 km and where only accidental correlations would be expected.

The four German stations are not much influenced by orography or local wind fields. This also true for Kühlungsborn, which is directly at the shore of the Baltic Sea, because the measurements do not cover the lowest heights which are mostly influenced by land-sea-breeze effects. Since additionally the distances between the stations cover a range from a few tens to a few hundreds of km, they are well suited for correlation studies. Assuming the aerosol distribution is not only depending on local sources and sinks, some correlation between them would be expected.

Hamburg and Bergedorf have only been compared in 2002. They show very high correlation of

about 0.96, while for Hamburg and Kühlungsborn the correlation in a 2 years period decreases to 0.78. Although Hamburg and Leipzig show similar patterns in the plotted time series (Fig. 97, the correlation coefficient is only 0.31, which is even lower than for Hamburg and Naples (0.36). It can be concluded, that if measurements at two correlated stations are possible they show high correlations at distances up to at least ca. 150 km and are therefore representative for a larger area. However, it has to be noted, that the individual correlations can be highly dependent on the location of the lidar system, because e.g. orographic effects can largely influence the results.

15.3.4 Vertical distribution of aerosol backscatter

To derive information on the vertical distribution of the aerosol backscatter at different EARLINET sites, the profiles from ten sites taken at 532 nm have been considered. The time series of all stations include at least 24 months of measurements with 60 - 130 profiles in summer and 30 to 80 profiles in winter (see Table 18). Average profiles have been calculated for summer (April till September) and winter (October till March). Because not all profiles cover the same height range (e.g. due to clouds), the combined profile is only given in those heights where at least half of all profiles contributed to the average. Heights above 5000 m are not shown because in many cases the aerosol backscatter is dominated by cirrus clouds, which have not been excluded for this statistics.

  Aerosol can be found up to 3-4 km in northern and central Europe and up to 4 -5 km in southern and eastern Europe (Fig. 98). Most of the aerosol is located in the lower altitudes, the average value smoothly decreases with height. This is an effect of the averaging procedure, usually the height dependence of the aerosol backscatter follows a more or less stepwise function with a sharp decrease in aerosol backscatter at the top of the PBL.

The EARLINET stations in the eastern and southern part of Europe, especially Athens and Thessa-
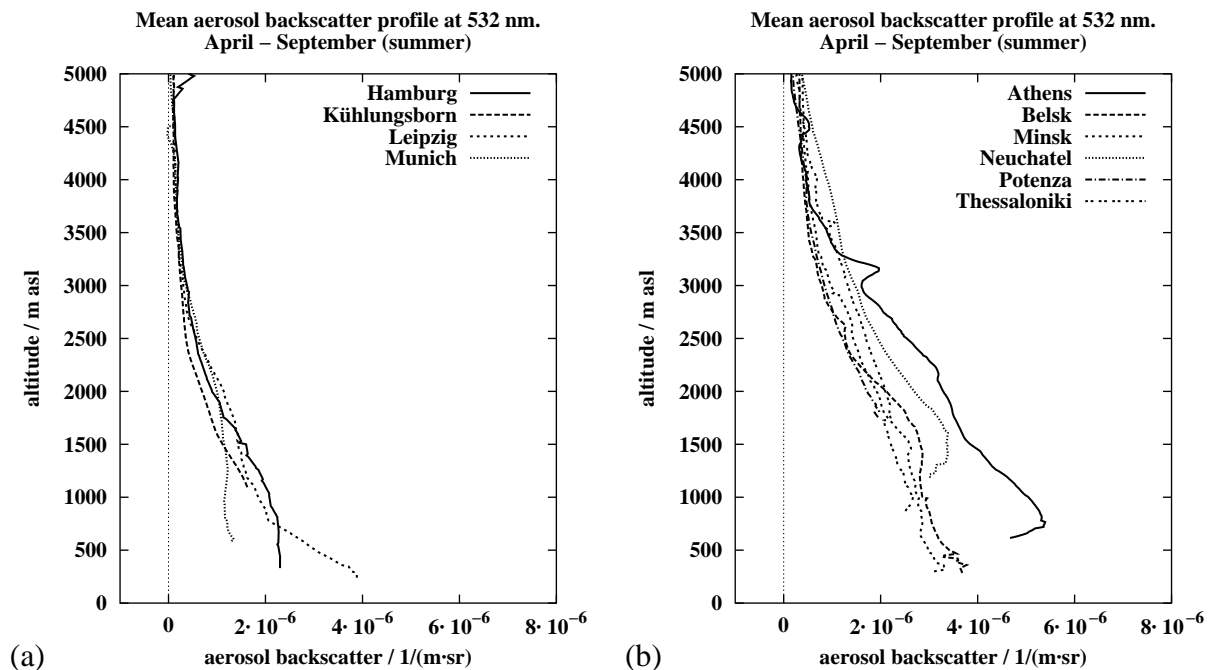

Figure 98: Mean aerosol backscatter profile at 532 nm for April till September. Northern and central European stations (a) and southern and eastern European stations (b).

loniki show clearly higher values of the aerosol backscatter. This result was already obvious in the extinction measurements at 355 nm.

The differences between the two sets of stations holds also for the winter months (Fig. 99). The shape of the profiles is clearly different, the aerosol is much more concentrated in below 1.5 km in southern and eastern Europe and below 1 km in northern and central Europe. Close to the ground mean backscatter values are higher in winter than in summer, which is an effect of the accumulation of aerosol in a low stable PBL in winter.

Comparisons of the absolute values of the aerosol backscatter at 532 nm can only be done in a very limited way. The measured aerosol backscatter depends on the chosen lidar ratio and the calibration value, so differences in the order of 20 - 30 % can easily be caused by the systematic use of different lidar ratios. Nevertheless, the vertical distribution of the aerosol is not much affected by these difficulties in the data evaluation and also the differences between the northern and central European stations and the southern and eastern ones are larger than the estimated uncertainties of the mean profiles.
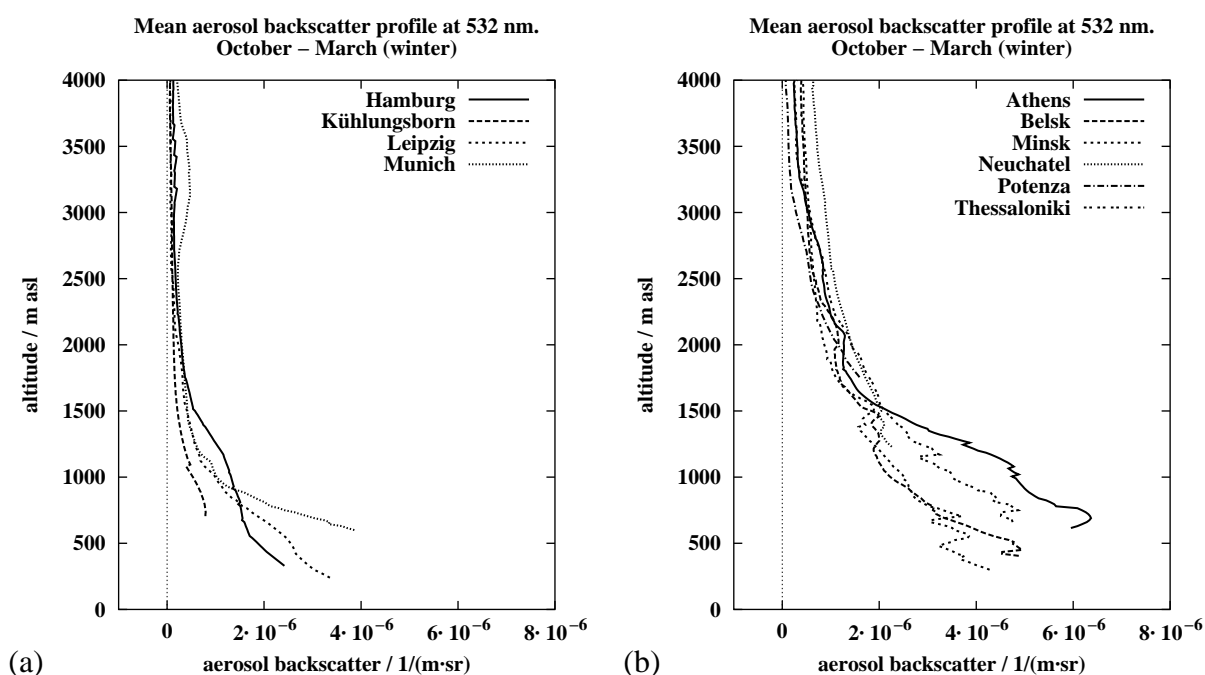
Figure 99: Mean aerosol backscatter profile at 532 nm for October till March. Northern and central European stations (a) and southern and eastern European stations (b).

15.4 Individual station statistics

The statistical evaluation of EARLINET data for several sites has been done at MPI Hamburg with identical criteria on the data quality and data evaluation to assure the comparibility of the results. Besides that, some stations performed individual evaluations of their data using slightly different approaches or looking at different quantities. Selected results of those efforts are presented in this section.

Table 22: Statistical parameters of the aerosol backscatter (351 nm) and the lidar ratio at L'Aquila. Maximum limits for the test are given in paranthesis.

	aerosol backscatter 10^{-6} (m·sr)$^{-1}$	lidar ratio sr
Mean	3.39	54
Std. Dev	1.85	9
Median	3.03	53
Skewness	1.06	0.33
Kolm.-Smirnov-test	0.068 (0.133)	0.083 (0.155)
χ^2-test	3.36 (9.5)	2.2 (6.0)
Number of profiles	108	75

15.4.1 L'Aquila

by Marco Iarlori

For L'Aquila, additional parameters have been statistically evaluated. The procedure also follows closely to what is applied in the previous section and is published in Matthias and Bösenberg (2002). Mean and median values, standard deviation and skewness have also been calculated for the aerosol backscatter at 351 nm and for the lidar ratio. The aerosol backscatter and the dust layer height (which corresponds to the PBL-height used in the previous section) have been investigated for frequency distribution. As already shown for Hamburg (Matthias and Bösenberg, 2002) the dust layer height follows a normal (Gaussian) distribution while the aerosol backscatter also follows a log-normal distribution. For L'Aquila, also the lidar ratio can be represented by a Gaussian distribution. The distribution functions have been tested with both the χ^2-test and the Kolmogorov-Smirnov-test and fulfilled the given limits for 95 % confidence. Statistical parameters for the aerosol backscatter and the lidar ratio are displayed in Table 22.

15.4.2 Potenza

by Gelsomina Pappalardo

Additional to the optical depth, in Potenza also statistics of the integrated backscatter at 355 nm and 532 nm and the lidar ratio (see also section 16 on lidar ratio) have been carried out. The dust layer height has been obtained from both, daytime (afternoon) and nighttime (sunset) measurements. The measurements together with a six-weeks sliding average are shown in Figure 100. The annual cycle shows higher values in summer than in winter. In particular in the summer period the mean height of the daytime dust layer is higher (2700 m asl) compared to that calculated from the night time measurements (2500 m asl). In winter time no significant difference between the dust layer heights are observed.

  The statistical analysis for the integrated backscatter and the lidar ratio have been carried out in the dust layer as well as in four fixed ranges of height above lidar station: 0-1 km, 1-2 km, 2-5 km and 5-12 km. The mean and median values, the standard deviation and the skewness related to the integrated backscatter and the lidar ratio are reported in the Table 23. The annual cycle is displayed in Figure 100. As shown for the optical depth in the previous section, also the integrated
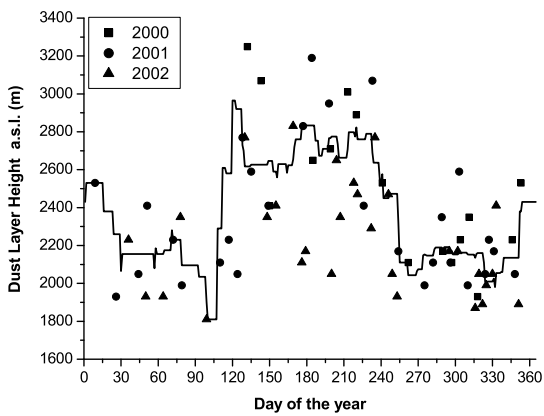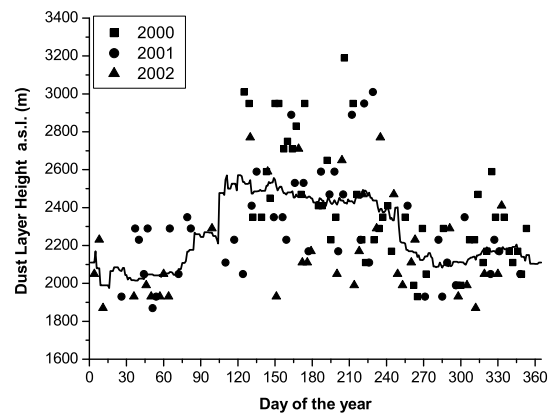
| (a) | (b) |

Figure 100: Annual cycle of the daytime dust layer height (a) and the night time dust layer height (b) in Potenza for the period May 2000 - December 2002. Data points and six weeks sliding average are plotted.

backscatter shows high values of the skewness in layers with significant aerosol content. This again emphasizes that the distribution function cannot be represented by a Gaussian distribution and the median represents the most likely value much better than the mean does. On the other hand, the lidar ratio shows only low skewness. Interesting to note is also that on average the vertical distribution of the lidar ratio in Potenza does not change significantly with height.
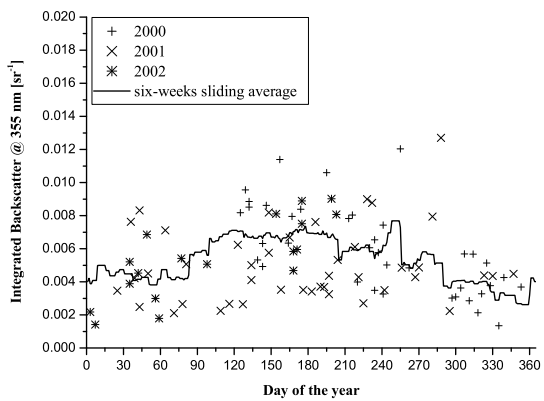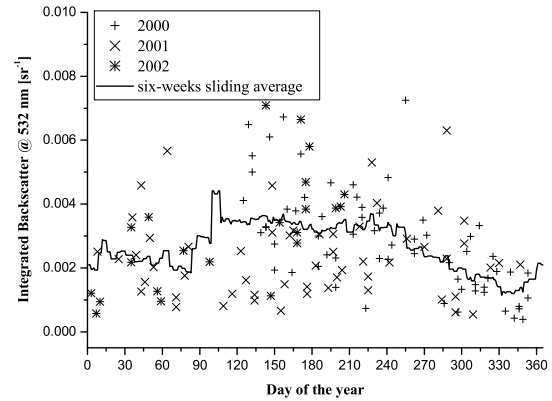
| (a) | (b) |

Figure 101: Annual cycle of the integrated aerosol backscatter at 355 nm (a) and 532 nm (b) in the dust layer in Potenza for the period May 2000 - December 2002. Data points and six weeks sliding average are plotted.

146

Table 23: Statistical parameters of the integrated backscatter at 355 nm and 532 nm and the lidar ratio at 355 nm taken at Potenza between May 2000 and December 2002.

Integrated backscatter at 355 nm					
Layer	Mean 10^{-3} sr^{-1}	Std. dev. 10^{-3} sr^{-1}	Skewness	Median 10^{-3} sr^{-1}	Number of meas.
0 - 1 km	3.76	1.66	0.71	3.50	87
1 - 2 km	2.00	1.41	1.53	1.67	150
2 - 5 km	1.41	1.79	2.28	0.76	149
5 - 12 km	0.17	0.24	2.75	0.08	46
Dust Layer	5.10	2.39	0.66	4.53	141
Integrated backscatter at 532 nm					
Layer	Mean 10^{-3} sr^{-1}	Std. dev. 10^{-3} sr^{-1}	Skewness	Median 10^{-3} sr^{-1}	Number of meas.
0 - 1 km	1.82	0.99	0.98	1.67	163
1 - 2 km	1.11	0.82	1.28	0.99	185
2 - 5 km	0.79	1.12	2.53	0.32	186
5 - 12 km	0.08	0.10	2.99	0.04	150
Dust Layer	2.63	1.50	0.85	2.49	181
Lidar ratio at 355 nm					
Layer	Mean sr	Std. dev. sr	Skewness	Median sr	Number of meas.
0 - 1 km	45.3	12.7	-0.38	48.0	19
1 - 2 km	43.5	12.4	0.50	40.9	79
2 - 5 km	45.0	15.6	0.47	43.0	76
5 - 12 km	41.6	26.2	0.24	35.2	9
Dust Layer	42.6	12.0	-0.06	42.9	66

16 Lidar ratio data base

by Gelsomina Pappalardo

16.1 Objectives

One of the main objectives of the EARLINET project is the compilation of a statistically significant data set concerning the ratio of aerosol extinction to backscatter (lidar ratio) starting from both regular and special measurements. Lidar ratio data are retrieved from simultaneous and independent lidar measurements of aerosol extinction and backscatter (Ansmann et al., 1992a). Lidar ratio is a parameter strongly related to the microphysical properties of the aerosols depending on the aerosol type and aerosol size distribution; moreover, lidar ratio is important in estimating the climate impact of aerosols. For this reason a statistically significant data set of systematic lidar ratio measurements on the European scale is a very powerful tool for the study of tropospheric aerosols. In particular, these measurements, in conjunction with information on the air masses characteristics, provide information on microphysical properties of the aerosol on a wide range of meteorological conditions on a continental scale and can be very useful for investigating the climate impact of aerosols. Moreover, this data set can be used to improve the quality of a number of satellite retrieval systems that are affected by the presence of aerosols, and will provide the necessary basis for future satellite missions that employ laser remote sensing.

16.2 Methodology

Lidar techniques are mature enough to provide quantitative measurements, in particular, the combination of the Raman elastic-backscatter lidar technique allows the independent retrieval of the aerosol extinction and backscatter profiles (Bösenberg et al., 2001b).

Within EARLINET, ten lidar stations have the capability of measuring Nitrogen Raman scattering in the UV simultaneously to the elastic backscatter; among these lidar stations, two have the capability to measure nitrogen Raman scattering also in the visible domain (Kühlungsborn and Leipzig).

To achieve the objectives of this work package, all the EARLINET lidar stations providing simultaneous aerosol extinction and backscatter measurements have been selected.

In order to assure a high quality for the aerosol extinction data, an intercomparison of the Raman algorithms used by each group has been performed. Good results of this experiment demonstrate the capability of each participating group to obtain lidar ratio profiles in the whole dust layer with good accuracy (see also section 4) (Matthias et al., 2002).

For the lidar ratio evaluation, extinction and backscatter are obtained with the Raman method and are processed with the same averaging in space and time. These aerosol extinction and backscatter data have been delivered to the EARLINET data base, for all involved stations, in the common format.

16.3 Scientific achievements

At the moment, the lidar ratio data set consists of about 1100 Raman files from regular measurements covering the period May 2000 - October 2002. Further lidar ratio data, present in the database are related to special events (Saharan dust outbreaks, forest/industrial fires, photochemical smog episodes, volcanic eruptions, etc.) occurred over Europe.

All lidar ratio data delivered to the EARLINET database have been collected and a statistical analysis has been performed.

Figure 102 and 103 report the mean values of the lidar ratio calculated in the dust layer above each lidar station for all the regular measurements at 355 nm and 532, respectively. The seasonal variation and the frequency distribution of the mean value of the lidar ratio in the dust layer have also been studied for each station. Mean values of the lidar ratio have been calculated in the dust layer because this height range is representative for the main aerosol load in the planetary boundary layer and the residual layer for each station. The number of measurements is not the same for each station, mainly reflecting quite different weather conditions but also the technical availability and capabilities of the systems. Besides, in Thessaloniki Raman measurements started in March 2001 because it is one of the lidar stations that upgraded the system with Raman channels during the project.

Mean values of the lidar ratio, for the whole period of measurement, have been calculated in the dust layer above each lidar station starting from the routine measurements establishing the climatology. These values are reported in Table 24 together with the mean values obtained for autumn-winter and spring-summer periods.

This is the first time that mean values of the lidar ratio have been measured on a continental scale

Table 24: Mean values of the lidar ratio calculated in the dust layer above each lidar station

Station	Wavelength [nm]	Mean value [sr]	Winter mean value [sr]	Summer mean value [sr]
ABERYSTWYTH	355	46	44	48
ATHENS	355	32	37	29
HAMBURG	351	55	54	55
KÜHLUNGSBORN	355	41	30	45
	532	36	23	35
L'AQUILA	351	48	47	49
LECCE	351	47	52	43
LEIPZIG	355	64	74	61
	532	58	61	58
NAPOLI	351	76	82	71
POTENZA	355	39	41	38
THESSALONIKI	355	46	39	48

starting from a large data set covering more than two years of systematic observations. Therefore there will be significant interest in the scientific community to use these data for the improvement of both global/regional atmospheric and climate prediction models. Moreover, these data will be important for aerosol studies performed by future space based lidar.

Lidar ratio values present a large variability along the profile in the dust layer; the mean variability for the lidar ratio value for each station has been evaluated as the mean of the standard deviations of the mean value of the lidar ratio for each profile and results of this analysis show that lidar ratio values can vary up to 30 sr from the mean value in the dust layer.

An analysis of the correlation between lidar ratio measurements and air mass has been performed using back-trajectories calculated by the German Weather Service (section 5). In particular, the mean values of lidar ratio calculated in the dust layer have been correlated to the air masses origin divided into 9 classes: north (N), northeast (NE), east (E), southeast (SE), south (S), southwest (SW), west (W), northwest (NW) and local (L). Higher lidar ratio values measured in the South of Europe are
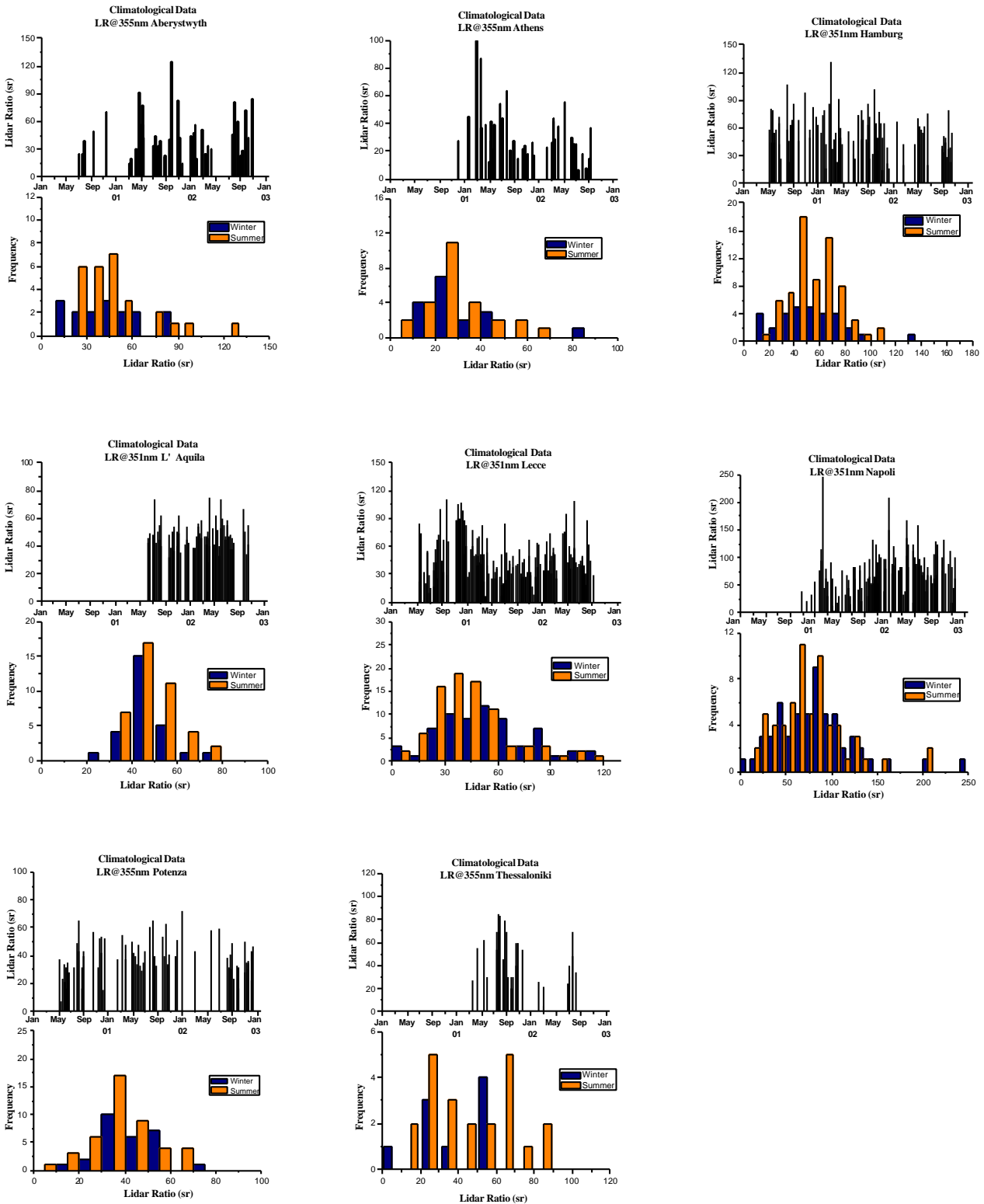
Figure 102: Mean values of the lidar ratio data in the dust layer above each lidar station starting from all the climatological data and frequency distribution for winter and summer periods.
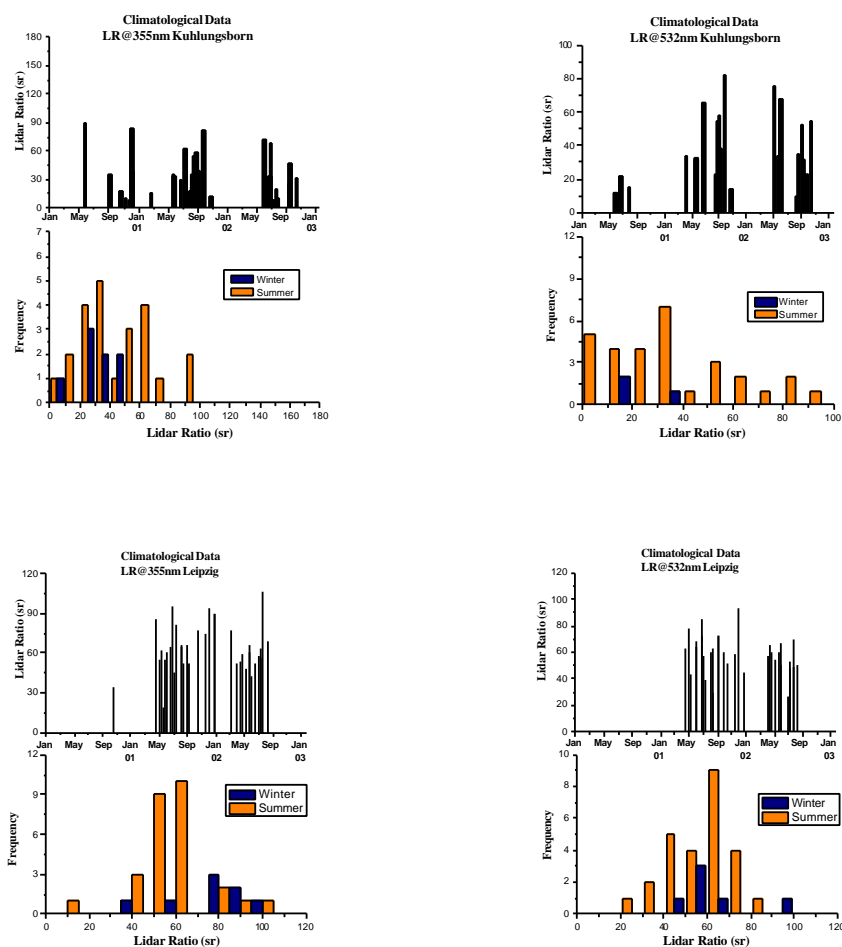
Figure 103: Mean values of the lidar ratio data in the dust layer for Khlungsborn and Leipzig stations starting from all the climatological data at 355 nm and 532 nm and frequency distribution for winter and summer periods.

correlated with air masses coming from southerly direction, and this could be related to aerosols originated from Saharan regions (Papayannis et al., 2002). Higher lidar ratio values measured in central Europe seem to be correlated with air mass coming from easterly directions representing more continental aerosols (Ackermann, 1998), while lower values are related to air masses coming from the ocean in connection with sea salt aerosols (Pappalardo et al., 2002).

Lidar ratio values have been studied also starting from special measurements. In particular, lidar ratio values measured in cirrus clouds are around 10 sr for all the stations for more than 50 different cases. Anomalous high values of the lidar ratio (50-60 sr) have been measured in southern Italy, above the dust layer around 3-4 km of height during the last two eruptions of the Etna volcano and these values are consistent with theoretical lidar ratio values for sulphate aerosol (Evans, 1988).

The first preliminary results of the statistical analysis performed on the lidar ratio measurements provide useful input for climate models. Anyway the observed large variability of this parameter demonstrates how important it is to continue the systematic lidar observations on a continental scale.

17 Analysis of source regions

Thomas Trickl (IFU)

17.1 Objectives

This work package focusses on long-range transport of aerosol and the identification of its principal source regions inside and outside Europe. The investigations concentrate on transport pathways which advect aerosol or trace gases to the European sites on a more regular basis. The activities were expected to yield information on the influence of different source regions on the optical coefficients measured at the EARLINET stations and on the transport itself by regarding the aerosols as a highly suitable tracer for boundary-layer air or air pollution.

17.2 Methods

The analyses are based on lidar measurements within EARLINET and the EU projects VOTALP and STACCATO, but also on the existing long-term series for the free troposphere at the NDSC (Network for the Detection of Stratospheric Change) station Garmisch-Partenkirchen, as well as on backward trajectories provided by the German Weather Service (DWD), NOAA-CMDL and A. Stohl's group at TU München. The DWD trajectories, which were available to all partners, are given for four subsequent days and are suitable for transport studies of Saharan dust and within Europe. For intercontinental transport the FLEXPART trajectories (TU München) and the NOAA trajectories are more suitable since they are calculated for periods of ten days. However, they were accessible by two EARLINET groups only. For longer periods and for simulating lidar results the tracer model FLEXPART (TU München) has been applied. The FLEXPART model can be run in both a forward and a backward mode and yields clearer results since the entire tracer plume may be visualized. The tracer plume may be also folded with data from emission inventories. In the backward mode this allows one to determine the relative importance of different source region. The analysis has been also based on satellite images (TOMS, SeaWIFS, GOES East), EPA station data and data from MOZAIC flights. For Saharan dust meteorological and model forecasts have been used for initiating measurements within the network (see Work Package 7).

17.3 Scientific Achievements

17.3.1 European Source Regions

Although source regions within Europe were initially considered in the proposal it was soon realised that this goal had been too ambitious due to the low density of EARLINET stations, the absence of stations in some of the most heavily polluted regions as well as in many rural areas, and the lack of transport-modelling groups within EARLINET contributing to this subject. The EARLINET activities concerning European source regions were mostly confined to the analysis of air-mass modification over Europe which is treated in Work Package 9.

For IFU, a statistical analysis was carried out. IFU is located in the Bavarian Alps and is rather central within Europe. Thus, contributions from different European source regions may be observed. Mostly, quite clean conditions prevail due to the nighttime catabatic air flow admixing air from the free troposphere. As a consequence, the aerosol observations at IFU are highly indicative of air-mass

Figure 104: The SeaWiFS satellite image taken in the visible channel on August 04, 2001 at 12:00UT

advection. For the three years 2000-2002 the mean daily maximum 532-nm extinction coefficient in the lower boundary layer was 0.035 km^{-1} under conditions excluding Saharan dust, corresponding to a visual range of 111 km. During just 16.8 % of the 77 measurement days (14.5 % of the climatology days) 0.050 km^{-1} was exeeded for air advection from principal European pollution source areas, namely Spain, North-west Germany, Great Britain, Northern Italy, but also the area to the north of the Black Sea which is identified in the following section to be an important source of air pollution. Extinction coefficients of 0.10 m^{-1} and more (visual range 39 km and less) were reached on just 4 days. The source areas were Spain, the Black Sea and (as a special case) the greater Moskow area on two days during the fire period in September 2002.

The high visibility in recent years (which differs from the situation in and before the early 1990s) is remarkable and might reflect the improvement of the air quality in central and eastern Europe after 1990. It is planned to harden this observation by analysing visibility data for the monitoring stations near IFU.

17.3.2 A European source area relevant for south-eastern Europe: The northern shore of the Black Sea

by A. Papayannis

Among the lidar data available during the EARLINET period a total of 11 days was selected to determine possible source regions of aerosol particles outside the geographical EARLINET domain. Among the available lidar data within this Work Package an interesting case study was identified, where combined lidar, satellite and trajectory analysis was performed to identify long-range transport of aerosol over the Aegean Sea. This case concerns the period of August 2 to 30, 2001. Figure 104 shows the SeaWiFS satellite image taken in the visible channel on August 04, 2001 at 12:00UT. In this Figure the Black Sea region is shown covered by (black carbon and/or soot?) aerosol.

  The series of lidar measurements are shown in Fig. 105 for selected days in the aforementioned time period of August 2 to 30, 2001. All lidar measurements (taken at 532 nm at 12:00 UT) do show the existence of important aerosol loads between 1.5 and 4 km height asl. The most spectacular case is the day of August 7, 2001 where an aerosol backscatter coefficient of the order of 0.0025 $km^{-1}sr^{-1}$ is observed at 4 km height. Although the high aerosol loads found inside the PBL (below 1.5 km) are due to the local air pollution sources over Athens, the aerosol particles found above 1.5
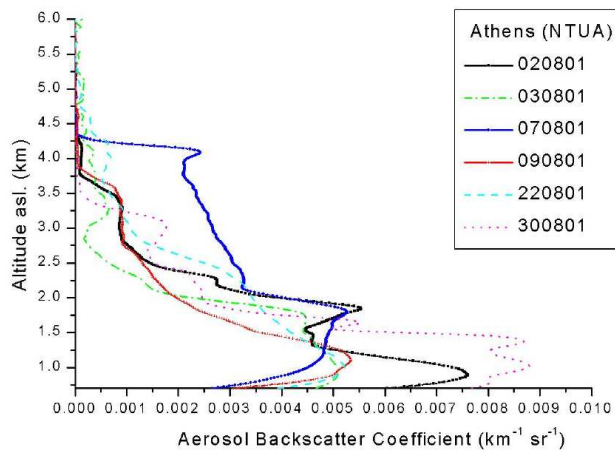
153

Figure 105: Aerosol backscatter lidar profiles for selected days in the time period of August 2 to 30, 2001 (taken at 532 nm at 12:00 UT).

km height asl could be attributed to long-range transport mechanisms, which take part in the free troposphere over the Aegean Sea.

To identify long-range transport mechanisms over the Aegean Sea a 96-hours back-trajectory analysis was performed for selected days in the before mentioned this time period (Fig. 106). This analysis showed that the majority of the air masses ending over Athens (between 975 and 500 hPa) had previously over-passed Ukraine, Romania and the Black Sea, where the SeaWiFS instrument had detected high aerosol loads (see Fig. 104).

The ATSR/ESA satellite data reporting wild fires over the globe for August 2001 are shown in Figure 107 together with air mass back-trajectory analysis for air masses ending over Athens on 090801 at 19:00 UT. In fact this figure shows that around the Black Sea region and especially in Ukraine, a large number of wild (forest) fires is identified during August 2001. Therefore, this could be the most plausible reason for the observation of such high quantities of aerosols over Athens during that month. One has also to consider the large coal-burning power plants over the same region which also emit important quantities of soot particles into the atmosphere, which, once in the free troposphere are transported over the Aegean Sea towards Greece, during the August period, when the regional Etesian winds (Meltemi) prevail. Therefore, the aerosol load found above 1.5 height over Athens during August 2001, would be a mixture of Pyrogenic aerosols and soot particles.

17.3.3 Saharan Dust

by A. Papayannis, T. Trickl (IFU) The most important extra-European aerosol source region is the Sahara desert. The transport of Saharan dust to Europe is mostly associated with prefrontal air streams in the case of sufficiently long frontal systems or Mediterranean storms. Thus, the frequency of these events is of the order of one to three per month. The influence of the Saharan dust plumes is the strongest in Southern Europe, but also Central Europe may be quite significantly affected. In particular, Saharan dust episodes are well known in the Alps where, in winter, the colour of the snow surface takes on yellow-red traces during periods of pronounced southerly advection. Lidar mea-
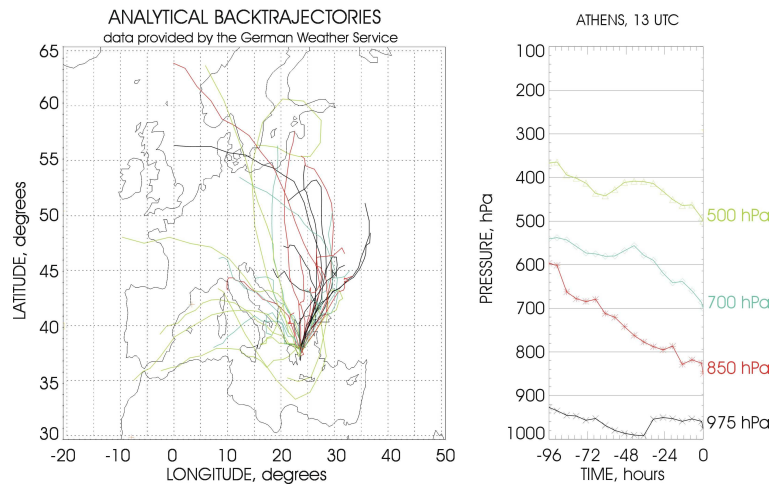
Dates: 30/07 - 2,3,6,7,9,15,22,30/08/2001

Figure 106: 96-hours back-trajectory analysis performed for air masses ending over Athens (between 975 and 500 hPa) for selected days in the time period July 30 to August 30, 2001.

surements at Garmisch-Partenkirchen (IFU) during prefrontal advection from Africa have a rather long tradition and have revealed a typical vertical extension of the dust plume up to more than 5 km (Jäger et al., 1988; Kreipl et al., 2001).

It has been one of the main results within EARLINET that Saharan dust is transported over most of the European continent, with observations even in Poland and Belarus. To the north the dust layers reach altitudes of up to 10 km.

Co-ordinated measurements of Saharan dust were carried out in the frame of Work Package 7. More than 105 cases have been successfully predicted since May 1, 2000, and measurements have taken place by network stations during most of them. Details on the activities may be found in the report on Work Package 7.
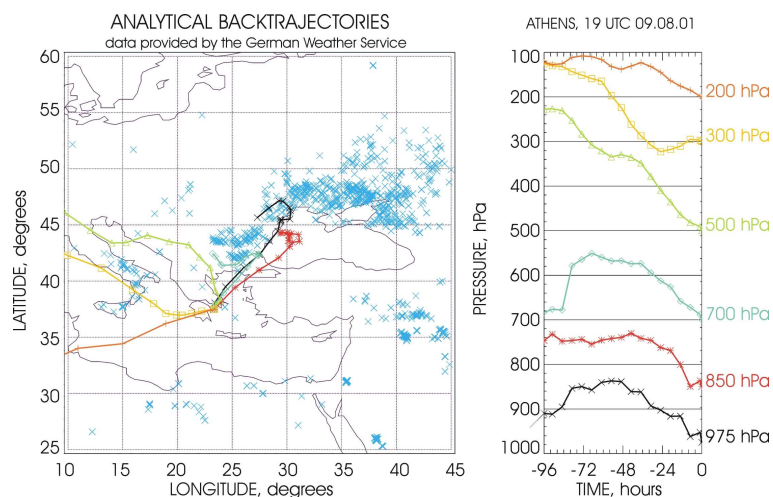

Figure 107: ATSR/ESA satellite data reporting wild fires over the globe for August 2001 (blue crosses) together with an air mass back-trajectory analysis for air masses ending over Athens on 090801 at 19:00 UT.

155

It should be mentioned that Saharan dust has dominated the aerosol budget above Garmisch-Parten-kirchen in recent years. As mentioned in Sec. 17.3.1 the average visibility at IFU is high. Within the EARLINET period the mean extinction coefficient was 0.049 km^{-1}, 0.035 km^{-1} for the days without Saharan dust and 0.085 km^{-1} for those with Saharan dust (climatology days only). Extinction coefficients of 0.10 km^{-1} were approximately reached or exceeded on 41 % of the days with advection from the desert. This clearly demonstrates the impact of the African aerosol plumes for the visibility conditions even beyond the Mediterranean region.

17.4   Intercontinental Transport

by T. Trickl

A lot of the lidar studies at IFU in recent years have been devoted to the investigation of the trans-Atlantic transport of air pollution. After the first observation of the North American ozone plume over Europe with the IFU ozone lidar in 1996 a number of case studies have been carried out. A lot of this analysis has taken place within the EU projects VOTALP, STACCATO and EARLINET, as well as within the German ATMOFAST project, see e.g. Stohl and Trickl (1999); Trickl et al. (2002). The investigation of intercontinental transport has become a key topic in atmospheric research in recent years.

 Most of the air from the heavily polluted boundary layer of the United States (U.S.) seems to be exported in the warm conveyor belts (WCBs) of frontal systems ending a pollution episode. The air mass is, thus, lifted to the upper troposphere where it is rapidly transported to Europe in the jet stream. There is evidence from our work and the NARE results that the trans-Atlantic air pollution transport in the lowermost few kilometres of the atmosphere is not important. This explains the lack of clear observations of North American signatures at surface stations in western Europe.

The upward transport in WCBs does not significantly affect the ozone concentrations. The analysis shows that ozone mixing ratios between 80 and 110 ppb are found on both sides of the Atlantic as well as in the WCB outflow region which are intersected by MOZAIC flights in the North-Atlantic
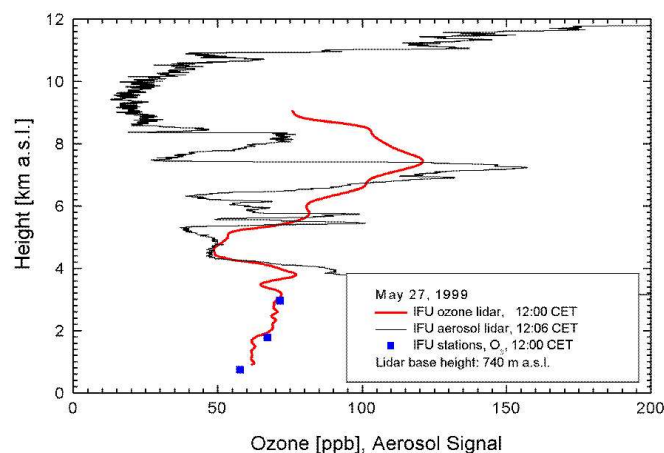

Figure 108: Simultaneous ozone and aerosol lidar measurements at IFU on May 17, 1999, showing a positive correlation between both constituents in a rather wide layer above 5 km a.s.l..
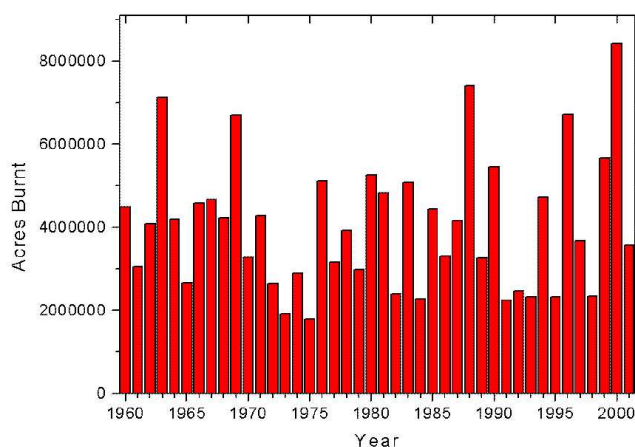
156

Figure 109: Acres of forests burnt per year in the United States during the period 1960-2000 (from http:// www.nifc.gov)

flight corridor. However, the frontal systems do affect the aerosol density by washout. In none of the 313-nm backscatter profiles of the ozone lidar so far obtained during typical North America episodes there are clear indications of aerosol within the high-ozone layers. This does not mean that the aerosol does not exist. Simultaneous free-tropospheric measurements with the big NDSC aerosol lidar of IFU during some of the relevant episodes have, indeed, revealed small amounts of particles in these layers. This is explained by the much higher sensitivity for particles of a 532-nm aerosol lidar. One example is shown in Fig. 108 taken from a four-day measurement period in May 1999 which was analysed in detail by transport modelling during the past two years. During this period the highest ozone values occurred ever observed with the IFU ozone lidar in a layer advected from across the Atlantic (up to 130 ppb). The ozone maxima are positively correlated with the aerosol which demonstrates the presence of boundary layer air. Indeed, the FLEXTRA backward trajectories verify import from a source region to the south-west of the Great Lakes. A forward tracer calculation with the FLEXPART model initialised with tracers released in the North American boundary layer nicely reproduces the vertical structure of the lidar measurements. On the other hand the ozone mixing ratio is far above the values reported for that source region. Simultaneously measured humidity profiles (Paul-Scherrer-Institut) show very dry air above 5 km. Since this air mass did not subside during the passage across the Atlantic one has to invoke an admixture of stratospheric air. Another possibility suggested by the arrival of some of the air components from the Pacific Ocean is pollution import from East Asia. However, at present there is no way to distinguish between these possibilities.

Much more aerosol signal is expected in the case of advection of North American forest-fire plumes (Forster et al., 2001). Huge forest areas in Canada and Siberia are burnt every year. It has been emphasized that these fires might significantly contribute to the CO_2 budget in the northern hemisphere (G. Wotawa, private communication). During the observational period of EARLINET there were two summers with extended fires in the U.S., 2000 and 2002. The fire statistics for the U.S. for the period 1960 to 2000 is given in Fig. 109. During this fourty-year period 2000 is the year with the highest damage. Data for 2002 are not available so far.

Although warnings were issued in 2000 no positive observations of North American fire plumes
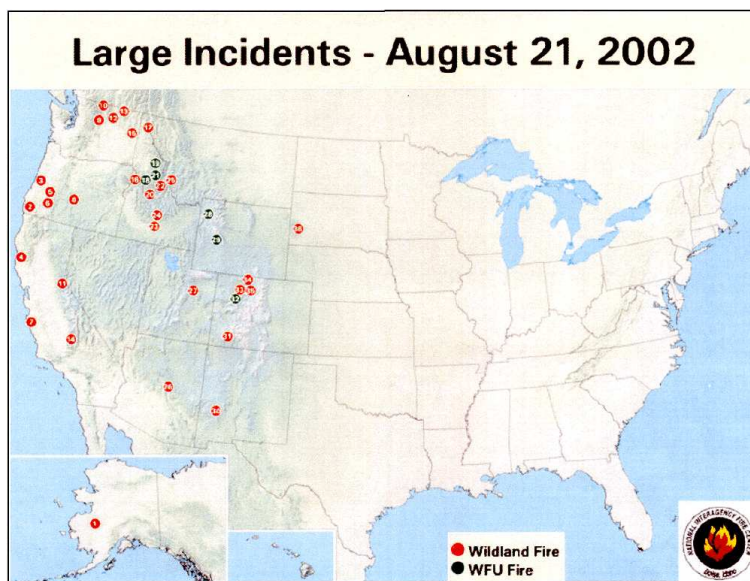
Figure 110: Map of the U.S. fires on August 21, 2002 (from http:// www.nifc.gov /fire-info/firemap.html)

have been reported by the EARLINET partners. In 2002 many observations were made, but the backscatter coefficients at 532 nm were usually below the Rayleigh value. This is a strange fact since from June to September a huge number of fires were reported throughout the western U.S., caused by exceptionally dry conditions. This is documented in Fig. 110 which shows a fire map for August 21, 2002. The first observation within the lidar network was reported on June 27, 2002. During the following weeks observations were made every few days and reported by stations from Sweden to Bulgaria (e.g., Fig. 111). The typical height range was 4 to 6 km. Despite the ongoing fires the number of observations strongly decreased towards September. This could be explained by FLEXPART trajectories which mostly overpass the U.S. at high altitude or shifted to the north during this period.

July 9 was rather exceptional since much higher backscattering was observed. Fig. 111 shows the diurnal series for the site Murnauer Moos (about 22 km to the north of Garmisch-Partenkirchen, see Work Package 10). Above 3.5 km an intense layer with aerosol from North American was advected shortly before a thunderstorm leading to south-westerly to southerly advection. The possibility of Saharan dust as an explanation is almost fully excluded from the FLEXTRA trajectories calculated for every three hours. Only for a single time and the single height of 3.5 km some Saharan dust could have been admixed. A full explanation of the observations is still missing. Further model runs with the FLEXPART tracer model are necessary and planned. FLEXPART simulations are also necessary in order to identify the reasons for the low backscatter coefficients in the fire plumes in summer 2002.

17.4.1   Aerosol statistics in the free troposphere (1992-2002)

by H.Giehl, H. Jäger, T. Trickl

As mentioned, aerosol is an excellent tracer of boundary-layer air. As a consequence valuable information on long-range transport in the free troposphere may be obtained from lidar measurements. However, an inspection of many years of free-tropospheric lidar measurements at IFU has
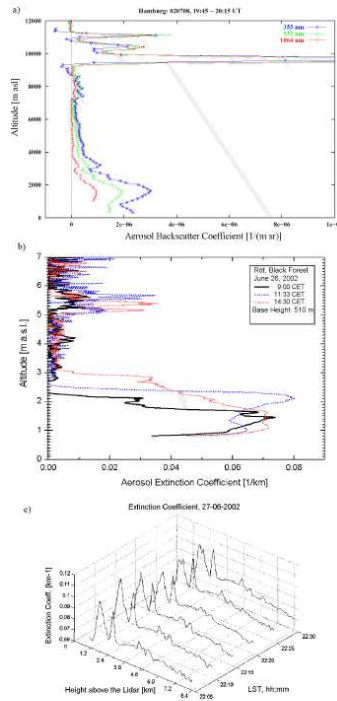
Figure 111: Observations of North American fire plumes at three selected EARLINET stations after the first warning on June 27, 2002 a) Hamburg (July 2, 2002), b) Röt, Black Forest (June 27, 2002), c) Sofia (June 27, 2002); the fire plumes were observed between 3 and 6 km.

revealed very low aerosol-induced backscatter signals, exceptions mostly occurring during Saharan dust events. The low aerosol density above the boundary layer may, to a major extent, be ascribed to washout in frontal systems as described above. However, this means that the aerosol budget obtained by lidar sounding is not representative of the air pollution advected. The presence of aerosol in a certain layer is, nevertheless, indicative of long-range advection. It yields information on how frequently air from remote boundary layers are advected in the free troposphere. Therefore, a climatology of free-tropospheric aerosol observations and potential source regions was attempted.

For the evaluation of source regions backward trajectories are necessary. The trajectories available to the EARLINET stations did not exceeed four days in time. This is not sufficient in the case of intercontinental transport. Only two stations had access to trajectories covering at least ten days (FLEXTRA model accessible by the groups at Leipzig and Garmisch-Partenkirchen). The analysis was finally carried out for Garmisch-Partenkirchen where 27 years of aerosol measurements are available, which have covered the entire free troposphere starting in 1992. The IFU NDSC lidar is optimized for stratospheric measurements and, therefore, has exceptional sensitivity for the sometimes tiny amounts of aerosol in the free troposphere.

Since at the time of this report just four years of trajectories have been completed the analysis so far has been limited to deriving the fraction of days on which aerosol was observed in the free troposphere (related to all measurement days per month or per year). A total of 478 vertical profiles for 532 nm have been inspected for 1992 to 2002. 2001 and 2002 were finally excluded due to an increasing number of missing months yielding obvious deviations from the results of the other years. This limited the total number of measurements analysed to 449.
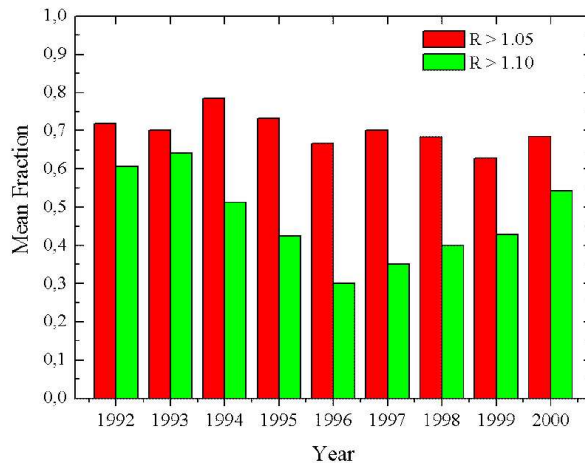
Figure 112: Annual averages of the fraction of days with free-tropospheric aerosol for the two tresholds 5 % and 10 % above Rayleigh (532 nm); for the 10 % threshold the Mt. Pinatubo period and the period afterwards were treated separately in addition.

The number of measurements included were further reduced by about 83 because of an unclear interpretation. Criteria for discarding measurements were

1. no free-tropospheric structure beyond spikes or cirrus clouds in the upper troposphere (vast majority of cases); measurements with potential upper tropospheric cloud influence were rejected anyway if the structures occurred above 10 km. It should be mentioned that a few of these cases with exceptional layer thickness were analysed with backward trajectories and related to the outflow of a WCB.

2. data available only for altitudes above 5 km (mostly limited to 1992)

3. potential extensions of the boundary layer may not be distinguished.

4. leaking of stratospheric air into the upper troposphere (mostly during the Mt.-Pinatubo period)

5. No clear structure (e.g., potential drift of evaluation base line)

Thresholds for accepting aerosol structures were selected. Since the aerosol-related signals were mostly very low these thresholds were chosen as 5 % and 10 % of the Rayleigh values at 532 nm. It is very interesting that these two tresholds yield a completely different behaviour of both the long-term trend and the average seasonal cycle for this period (Figs. 112 and 113).

 For the lower threshold there is no obvious trend. This is quite different for the 10 % treshold. In this case there is a pronounced negative trend in the early 1990s. From the synchronous decay of the stratospheric aerosol load after the Mt.-Pinatubo eruption we tentatively ascribe this behaviour to stratosphere-troposphere transport. Stratospheric air intrusion are associate with dry conditions which should yield a high probabilty for survival of the particles, in contrast to the situation for the upward transport of boundary layer air which may be accompanied by washout. This could explain that the signature of the stratospheric component is easier to observe for the 10-% threshold. This interpretation is hardened by the differences in seasonal cycle before and the end of the Pinatubo period: After the volcanic period not much aerosol is observed outside the warm season which might
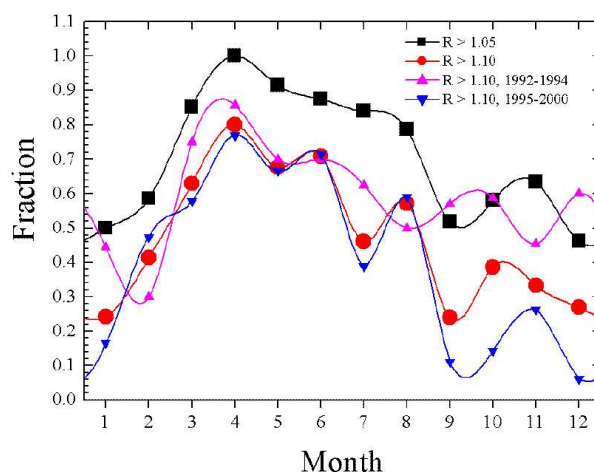
160

Figure 113: Seasonal cycles (monthly means) for the two treshold conditions selected; for the 10 % threshold the Mt. Pinatubo period and the period afterwards were treated separately in addition.

be due to the lower convective activity and less upward transport from the boundary layer.

The seasonal cycle is characterized by a rather early maximum in March. This resembles the late-winter maximum for stratospheric air influence in the lower troposphere (Stohl et al., 2000; James et al., 2002). This indicates that subsidence of dry upper-tropospheric and lower-stratospheric air and may influence the free-tropospheric aerosol distribution. The aerosols advected may originate in rather remote source regions, even in East Asia where air pollution is known to have a pronuonced positive trend. Indeed, there is some indication of a positive trend in the data for the 10-% threshold. The observation of an aerosol spring maximum reminds one of the frequently mentioned spring maximum of ozone (Monks, 2000). It cannot be excluded that long-range transport is one of the keys to both phenomena.

17.5   Socio-economic Relevance and Policy Implications

Long-range transport is one of the key topics of current atmospheric research. Both the European air-pollution import and export are in the focus of major international efforts. The impact of emission reductions in Europe and emission growth in other regions of the world, such as East Asia, on the overall distribution of trace constituents in the atmosphere must be understood in detail as the prerequisite for future abatement strategies and their control.

17.6   Conclusions

The following conclusions may be drawn from the results obtained within EARLINET:

1. There is some indication that maxima in the boundary-layer aerosol load are related to air-mass passage over polluted regions in Europe

2. Saharan dust strongly influences the European aerosol budget, not only in the Mediterranean area, but also in parts of Central Europe. Observations of Saharan dust within EARLINET have been made in coutries as distant from the desert as Belarus.

161

3. The influence of the North American fire periods on the EARLINET observation was astonishingly low with typical 532-nm backscatter coefficients rarely exceeeding the Rayleigh values.

4. The background aerosol load in the free troposphere is very low, apart from Saharan-dust episodes. Nevertheless, aerosol is a valuable tracer for long-range transport of air pollution.

5. The fraction of days with free-tropospheric aerosol exhibits a pronounced maximum in March which roughly coincides with the maximum of stratosphere-troposphere transport in the lower troposphere.

Substantially more work is needed to quantify the European contributions. Additional lidar stations are needed in rural and industrialized regions not covered by EARLINET. Future activities must be accompanied by extensive modelling studies. It will be also an important task for well-equipped lidar stations to measure simultaneously several constituents such as aerosol, ozone and water vapour which yields complementary information on atmospheric transport.

18 EARLINET - Microphysical parameters from optical lidar data

by Christine Böckmann, Detlef Müller, Anatoli Chaikovsky, Irina Mironova, Lars Schneidenbach, Andreas Kirsche, Alexander Mekler

18.1 Introduction

Aerosols have a direct radiative forcing because they scatter and absorb solar and infrared radiation in the atmosphere. Aerosols also alter warm, ice and mixed-phase cloud formation processes by increasing droplet number concentrations and ice particle concentrations. They decrease the precipitation efficiency of warm clouds and thereby cause an indirect radiative forcing associated with these changes in cloud properties. The size distribution is critical to all climate influences. Submicrometer aerosols scatter more light per unit mass and have a longer atmospheric lifetime than larger aerosols. The number of cloud condensation nuclei per mass of aerosol also depends on the chemical composition of aerosols as a function of size. IPCC (2001) states that chemical and physical properties of aerosols are needed to estimate and predict direct and indirect climate forcing.

Raman lidar systems provide optical properties - backscatter β and extinction α coefficient profiles independently - on a highly resolved vertical and temporal scale. These systems detect the elastically backscattered light at the emitting wavelengths as well as the light inelastically backscattered by certain molecules, e.g., nitrogen. These facts opened the possibility to retrieve microphysical properties from the optical ones (Böckmann, 2001; Böckmann and Wauer, 2001) by solving an inverse ill-posed problem via specially developed regularization techniques.

In more detail, by regularized inversion of the ill-posed first kind Fredholm integral system which relates the optical to the physical particle properties

$$\alpha(\lambda) = \int_0^\infty \pi r^2 Q_{ext}(r, \lambda; m) n(r) \ \mathrm{d}r, \ \ \beta(\lambda) = \int_0^\infty \pi r^2 Q_\pi(r, \lambda; m) n(r) \ \mathrm{d}r \qquad (17)$$

one is able to determine the size distribution function $n(r)$ and to capture the complex refractive index m without any knowlegde of the shape of the function $n(r)$ in advance. Here r denotes the particle radius, λ is the wavelength and Q_π and Q_{ext} are the backscatter and extinction efficiencies, see Eqs. (20) and (22). Mainly spherical particles are assumed, i.e., optical lidar data with small depolarization ratios.

Two inversion algorithms exist or were developed one at the Institute of Mathematics of the Potsdam University (IMP) and one at the Institute of Tropospheric Research Leipzig (IfT).

18.2 Developed regularization methods

18.2.1 IMP algorithm

The hybrid regularization technique developed at IMP is designed to work with different kind and number of optical data, i.e., experimental data obtained with different systems at various wavelengths can be evaluated (Böckmann, 2001). The algorithm does neither require any *a priori* information on the analytical shape of the investigated distribution function nor an initial guess of it. Even bimodal and multimodal distributions can be retrieved without any knowledge of the number of modes in advance.

The first regularization step in this method is performed via discretization, in which the investigated distribution function is approximated with variable B-spline functions. The projection dimension (number of base function) and the order of the used B-splines serve as regularization parameters. In the second step, regularization is controlled by the level of truncated singular-value decomposition performed during the solution process of the resulting linear equation system. In order to reduce the computer time, a collocation projection is used.

The highly nonlinear problem of the complex refractive index as a second unknown is handled by introducing a grid of a wavelength- and size-independent mean complex refractive index and by enclosing the area of possible real/imaginary-part combinations through inversion and back-calculation of optical data.

18.2.2 Developed software for the IMP algorithm

We developed a user-friendly software to invert the Eq. (17).

Firstly, one has the choice to get results from measurements or from simulated data. Figure 114 shows a screenshot with results of a simulated calculation with a 40x40 grid for the complex refractive index concerning example 5 of Table 25.

To start a simulation every parameter (used wavelengths, refractive index, noise level, grid parameters, shape of the particles, number of modes and kind of the distribution) can be manipulated with the parameter interface. A noise level can be added to simulated data and multiple runs with different randomly created errors are possible.

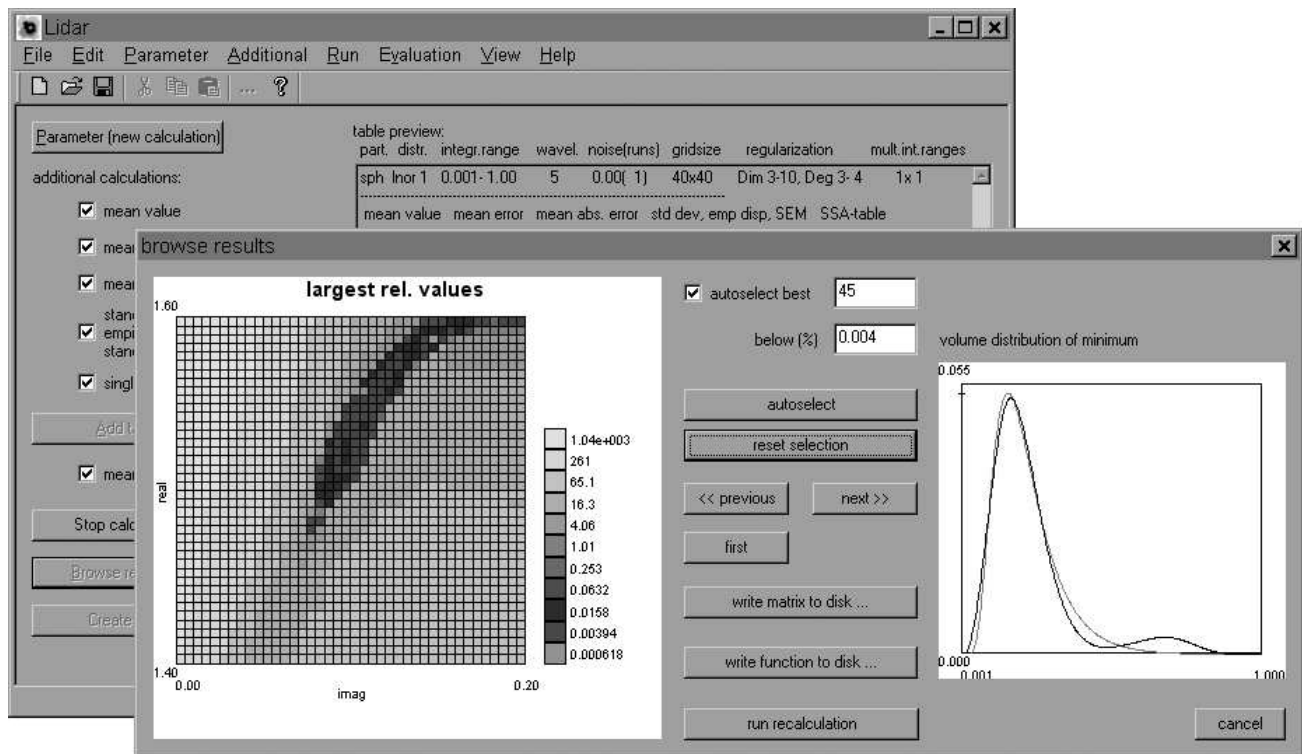One can specify any number of calculations to keep the computer busy a whole night, a weekend or

Figure 114: Screenshot of the developed software. The foreground shows the result browser with results from a simulation concerning example 5 of Table 25. The background provides a partial view on the main window.

164

more. The software writes checkpoints regularly. So the calculation state can be recovered in case of a crash. At any time one has the possibility to stop the calculation and save the current state and to continue later.

If the calculation is done a result browser provides a visual evaluation of the results. In case of an unknown refractive index one can see a result matrix of the grid as briefly described in the last subsection, see the left hand side of Fig. 114. On the right hand side the volume distribution function of the corresponding minimum point of the result matrix is given.

Secondly, one can mark a number of points from the matrix to recalculate its volume distribution and to retrieve the microphysical parameters. Finally, a table of all calculated microphysical parameters is created. It includes mean values and standard deviations of all retrieved parameters as well as in case of simulations relatives errors.

The software is still in alpha-state, not all features around the computation are stable, yet. The numerical routines where tested together with an older, less comfortable version and are working fine.

18.2.3   IfT algorithm

The IfT scheme, which is described in detail in Müller et al. (1999), uses a Tikhonov regularization with constraints to invert the eight optical data measured with the IfT multiwavelength lidar. The strength of regularization, which determines the degree of smoothness of the solution, is found from generalized cross-validation. The investigated volume concentration distribution is approximated with a discrete set of eight base functions, which have the shape of B-splines of the first degree. Fifty inversion windows of variable width are defined through variation of the lower and upper limits of the base-function range from 0.01 to 0.2 and from 1 to 10 μm, respectively. The base functions are distributed logarithmically equidistant within the windows. The inversion is performed for every window and for refractive indices that vary from 1.33 to 1.8 in real and from 0 to 0.7 in imaginary part.

From the inversion solutions only those are selected, for which the back-calculated optical data agree with the original data within the limits of the measurement error.

From extended simulation studies, it was shown that an appropriate reconstruction of the volume distribution together with a mean complex refractive index is found from the eight optical data derived with the IfT multiwavelength lidar (Müller et al., 2001). It was demonstrated that information on particle extinction is necessary at two wavelengths at least and that the optical data must be determined with errors of $\leq$10%–20%.

18.3   Simulation studies

In this section we present an extensive simulation study concerning an error analysis of the IMP algorithm by using the backscatter coefficients β at 355, 532 and 1064 nm and the extinction coefficients α at 355 and 532 nm (case: 3+2) in comparison with three additional backscatter coefficients β at 400, 710, and 800 nm (case: 6+2) with the aim to find a minimal or optimal data set of wavelengths. First case studies of retrieving from only 3-wavelength Raman-lidar observations were shown in Böckmann et al. (2001), Müller et al. (2001), and Eixmann et al. (2002).

After retrieving the size or volume distribution function one can determine the microphysical parameters as, e.g., the effective radius, i.e., the surface-area weighted mean radius, the total surface-area,

Table 25: Different typical examples of monomodal lognormal size distribution functions

Example	1	2	3	4	5
Radius r_{mod} [μ m]	0.05	0.1	0.1	0.3	0.1
Mode width σ	1.8	1.4	1.8	1.6	1.6

volume and number concentrations

$$r_{\text{eff}} = \frac{\int n(r)\, r^3\ \mathrm{d}r}{\int n(r)\, r^2\ \mathrm{d}r}, \quad a_{\text{t}} = 4\pi \int n(r)\, r^2\ \mathrm{d}r, \tag{18}$$

$$v_{\text{t}} = \frac{4\pi}{3} \int n(r)\, r^3\ \mathrm{d}r, \quad n_{\text{t}} = \int n(r)\ \mathrm{d}r \tag{19}$$

and the single scattering albedo (SSA).

Firstly, we investigate in an extensive simulation study with known complex refractive index by computing 90 examples with lognormal size distributions of Table 25 with different real parts (1.4,
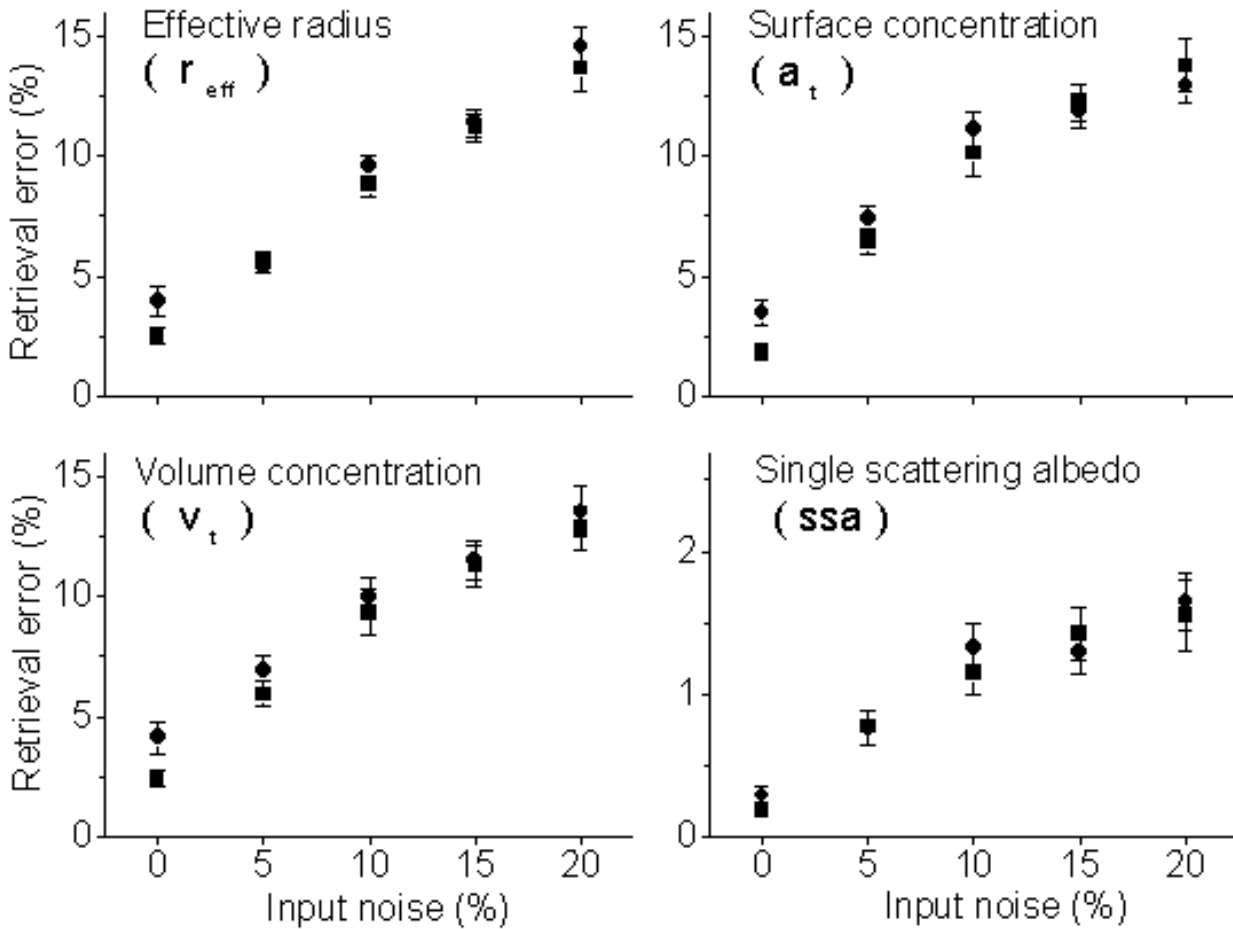

Figure 115: Simulation study with known refractive index and 90 examples (circles: case 3+2, squares: case 6+2).
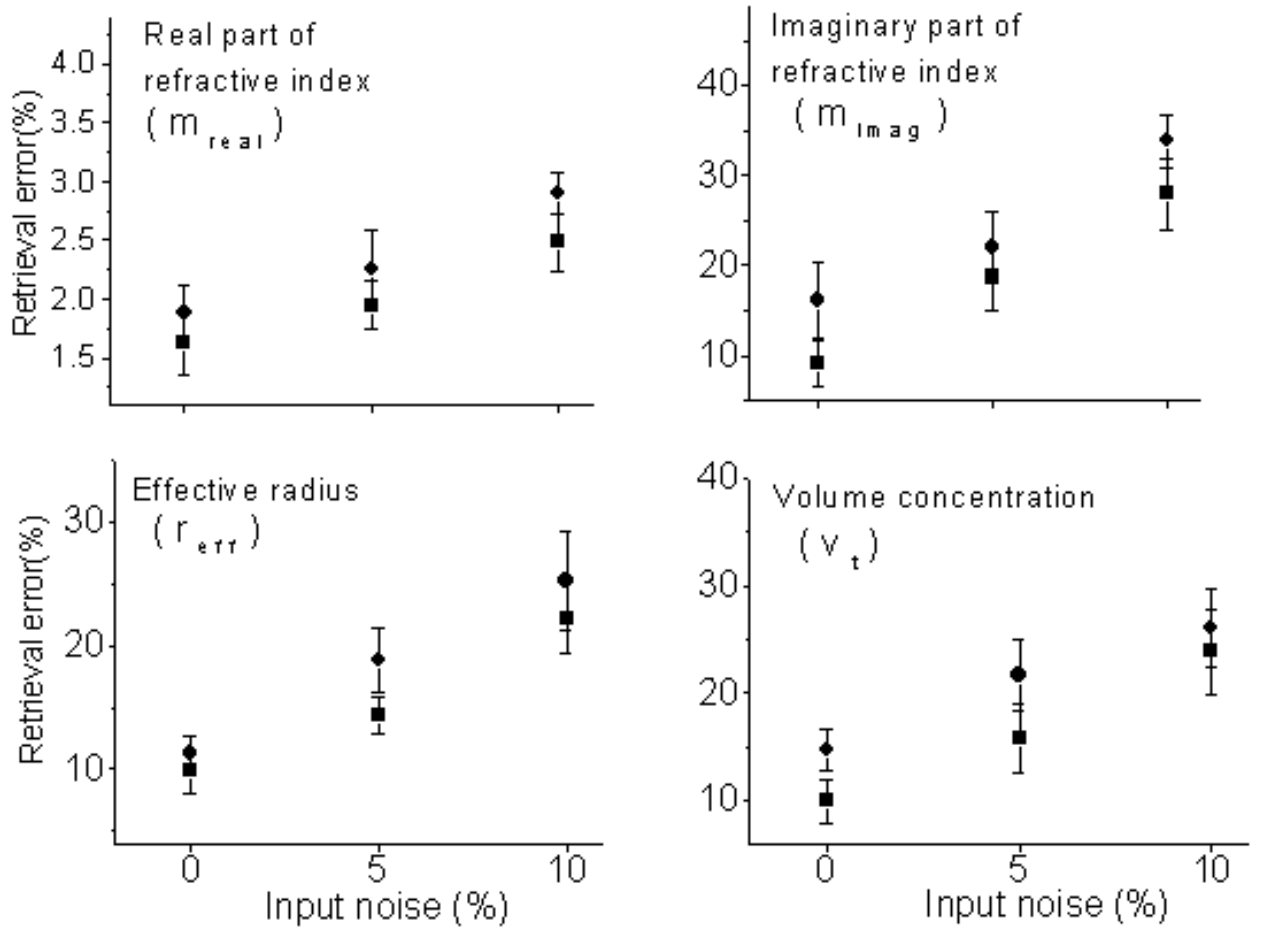
166

Figure 116: Simulation study with unknown refractive index and 26 examples (circles: case 3+2, squares: case 6+2).

1.55, 1.7), imaginary parts of refractive indices (0.0, 0.005, 0.01, 0.05, 0.1, 0.5) and normally distributed noise levels (0, 5, 10, 15, 20%) with 10 runs per noise level. Therefore, we compare the relative errors of the retrieved microphysical particle properties between the 3+2 case and the more extensive case 6+2, see Fig. 115. In the noiseless case for 6+2 coefficients the errors stay well below 2.5% for the effective radius, the surface and volume concentration and about 0.2% for the SSA which is mainly influenced by the imaginary part of the refractive index which is known here.
For 3+2 coefficients the errors increase to well below 5% and 0.4%, respectively. However, with increasing noise level on the input parameters α and β the retrieval errors grows up to 15% and to 2%, respectively, in the 20%-noise level in both cases (3+2, 6+2). In general, one observes that in all noisy data levels it is not important to make use of three additional backscatter coefficients. Therefore, by knowing the refractive index from, e.g., *in situ* chemical examinations or sunphotometer almucantar measurements a 3-wavelength Raman lidar is suitable for retrieving microphysical particle properties from the optical ones.
 Secondly, we investigate in the unknown complex refractive index case. Since in the previous case we observed that different real parts of the refractive index influence only slightly the retrieval errors this simulation study is justified with 26 examples for 5 and 10% input noise. In the noiseless case the retrieval errors are situated between 1 and 15% for the first four microphysical parameters and

167

for the SSA the error is again very small about 4%, see Figs. 116,119. This result is remarkable if one has in mind that from a mathematical point of view in those cases the operators (17), i.e., the kernel functions $\pi r^2 Q_{\pi/ext}(r, \lambda; m)$ are not exactly known. The complex refractive index m is a second unknown with two parts in Eq. (17). For 10% input noise the retrieval errors are situated between 20 and 35% and about 8%, respectively.

The 3+2 results in comparison with the 6+2 case show the same behavior as in the previous case. In the unknown refractive index case a 3-wavelength Raman lidar is also suitable for retrieving microphysical properties from the optical ones but only if special care is taken concerning the measurement errors and conditions. It is favourable to take the Raman measurements during night-time operations but this is not absolutely necessary. It is more important to make additionally depolarization measurements to classify the particle shape (Böckmann and Wauer, 2001). Otherwise this hybrid regularization method could fail because of ill-posedness of the integral operators (17) and using only a few noisy input data.

Summarising, the retrieval errors, e.g., for the effective radius and the volume concentration are between 20 and 25% in the 6+2 case and from 25 to 30% in the 3+2 case as well as about 10% with known refractive index in both cases for 10% input noise. Therefore, it is not absolutely necessary to operate with a six-wavelength lidar.

18.4 Measurement examples

The inversion algorithms from IMP (Böckmann, 2001) and IfT (Müller et al., 1999) were tested for experimental data sets, too.

18.4.1 LACE 98

As a first measurement example we chose the six-wavelength lidar observation of the Institute for Tropospheric Research in Leipzig from 9. August 1998 of Lindenberg Aerosol Characterization Experiment (LACE 98) (Wandinger et al., 2002b). The physical particle properties retrieved with our hybrid method could be validated by particle *in situ* measurements performed aboard the aircraft
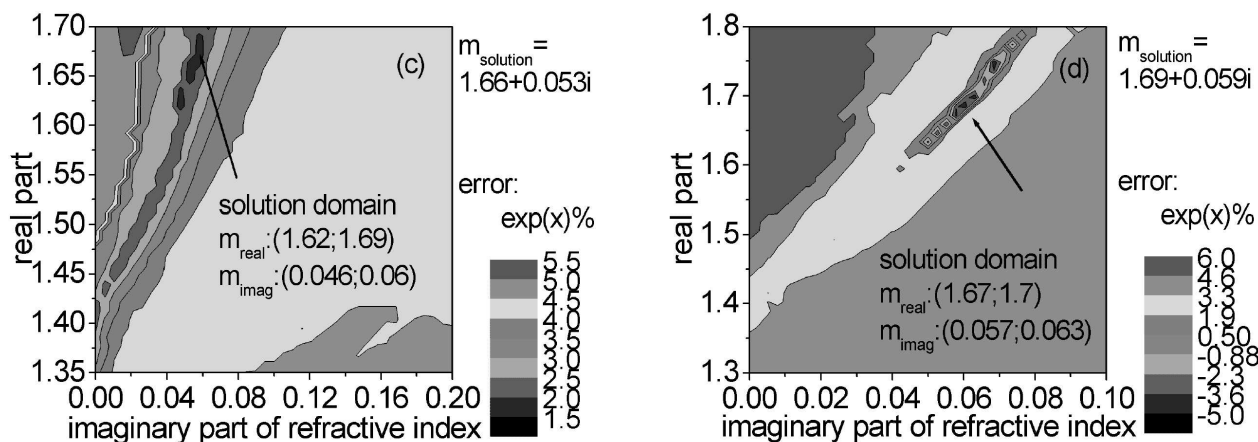

Figure 117: Retrieval of the refractive index domain from LACE 98 measurements from 3.5-4 km, 2200-2400 UTC, for the 3+2 case (right) and for the case 6+2 (left) with the IMP algorithm.

Table 26: Microphysical particle properties retrieved from lidar data by regularized IMP inversion in comparison with *in situ* measurements aboard the Falcon from 3.4-3.9 km. (A) airborne measurements on the basis of the complete particle size distribution, (B) under omission of the particle in the Aitken mode. The value in brackets is the volume-weighted complex refractive index of two internal components in contrast to two external detected components: 30-35% sootlike material: $1.75 + 0.45i$, 65-70% ammonium-sulfatlike material: $1.53 + 0i$ (Müller et al., 2001).

Parameter	*in situ* (A): $r \geq 1.5$ nm	*in situ* (B): $r \geq 50$ nm	case 3+2	case 6+2
r_{eff} (μm)	0.24±0.06	0.25±0.07	0.23 ±0.01	0.24±0.01
v_t (μm^{3}cm^{-3})	9±5	8±5	11±1	11±1
a_t (μm^{2}cm^{-3})	110±50	95±55	136±5	136±5
n_t (cm^{-3})	640±174	271±74	563±186	506±131
m_{real}	(1.56)	(1.56)	1.69±0.03	1.66±0.02
m_{imag}	(0.07)	(0.07)	0.059±0.005	0.053±0.004
$ssa(532$ nm$)$	0.78±0.02	0.79±0.02	0.78±0.01	0.79±0.01
$ssa(355$ nm$)$	-	-	0.72±0.01	0.74±0.01

Falcon (German Aerospace Center) in the vicinity of the field site during the time of the lidar observations. The measurement was characterized by an elevated biomass-burning particle layer between 3 and 6 km height. The origin was tracked back to intense forest fires in western Canada.

Firstly, the retrieved effective radius is in excellent agreement with the one from the *in situ* measurements whereas the volume and surface-area concentrations are slightly larger. There is a large deviation in particle number concentration. This value is critical in simulations, too. This is an ongoing work, see next section.

Secondly, comparing the results of the 3+2 case with the 6+2 case the first three parameters of Table 26 are in excellent agreement. Note that there is also very good agreement with the IfT inversion method (Müller et al., 2001).

Thirdly, the real and imaginary part are slightly larger in the 3+2 case. This inaccuracy is caused by a larger possible solution domain, see Fig. 117 (right), as in the 6+2 case (left). Almost all simulation retrievals show the same behavior that the retrieved solution domain for the refractive index in the 3+2 case is larger. However, the values of the refractive index are not directly comparable with the *in situ* data, see caption of Table 26 .

Finally, the parameter set permits calculation of the SSA, which is a key parameter in climate impact studies.

18.4.2 INDOEX

Second experimental tests were made with the optical data sets of six backscatter and two extinction coefficients, which are provided by IfT's six-wavelength aerosol lidar (Althausen et al., 2000). The IfT algorithm has been successfully used for this combination of data, which were obtained in large international field experiments such as the Indian Ocean Experiment (INDOEX; Indian Ocean/Maldives, February/March 1999) (Ramanathan et al., 2001). The optical data have undergone extensive quality checks and to date present the best available data set for testing the capabilities of the inversion algorithms.

Figure 118 presents the measurement example from March 10, 1999. At that time airmasses were advected from the Indian subcontinent to the field site of the six-wavelength lidar at Hulhule island

Table 27: Mean values of the physical particle parameters and the respective standard deviations for 13 individual measurement cases. Left column shows the results from the IfT algorithm. Right column shows the results from the IMP algorithm. r_{eff} denotes the effective radius, v the volume concentration, and s the surface-area concentration. m_{real} is the real part and m_{imag} the imaginary part of the complex refractive index. SSA denotes the single-scattering albedo at 532 nm.

	IFT	IMP
r_{eff}, μm	0.20 ± 0.00	0.18 ± 0.05
v, μm^{3}cm^{-3}	21 ± 11	19 ± 13
s, μm^{2}cm^{-3}	351 ± 188	394 ± 343
m_{real}	1.54 ± 0.11	1.54 ± 0.15
m_{imag}	0.022 ± 0.014	0.027 ± 0.026
SSA	0.90 ± 0.06	0.87 ± 0.11

(4.1° N, 73.3° E) in the Maldives. The Maldives are approximately 700 km to the southwest of the Indian subcontinent. During the northeast monsoon in northern hemispheric winter huge amounts of pollution are advected from South Asia out over the tropical Indian Ocean.

The particle backscatter coefficient shows particles in several layers. For the inversion the optical data were averaged across two height ranges. Effective particle radii were around 0.14 μm. There is excellent agreement of the results obtained with the two algorithms. The single-scattering albedo varies between 0.85 and 0.95. The IfT algorithm shows a larger uncertainty, but agrees very well to the results from IMP. With respect to volume- and surface-area concentration there is good agreement in the lower layer. Considerable difference is found with respect to the upper layer.

At present a statistical analysis of the different data sets obtained during INDOEX is performed with the two algorithms. These data sets cover highly different aerosol conditions, e.g., large marine particles, and small anthropogenic particles, produced from biomass and fossil fuel combustion. Table 27 summarizes the results. Shown are the mean values representing polluted condition during the northeast monsoon over the tropical Indian Ocean.

Both algorithms agree rather well in the average values of the microphysical particle properties. The large standard deviations are determined by the variability among the mean values of individual measurement cases. The IMP algorithm shows a larger variability compared with the results obtained with the IfT algorithm.

18.4.3 Arctic Haze

Another test was made with respect to the reduced data set of three backscatter and two extinction coefficients obtained during a period of advection of Arctic haze over north and Central Europe in April 2001 (Heintzenberg et al., 2003). This case not only presents the example of long-range transport of an important aerosol type from outside of Europe into the observational area of EARLINET. The combination of three backscatter and two extinction coefficients also presents the minimum data set necessary for the trustworthy retrieval of microphysical particle properties from lidar observations.

According to backward trajectory analysis airmasses were advected from the polar regions to Leipzig, Germany, in the first two weeks of April 2001. Figure 120 shows the results for the optical properties. The particle backscatter profile shows that this layer of Arctic haze extended to approxi-
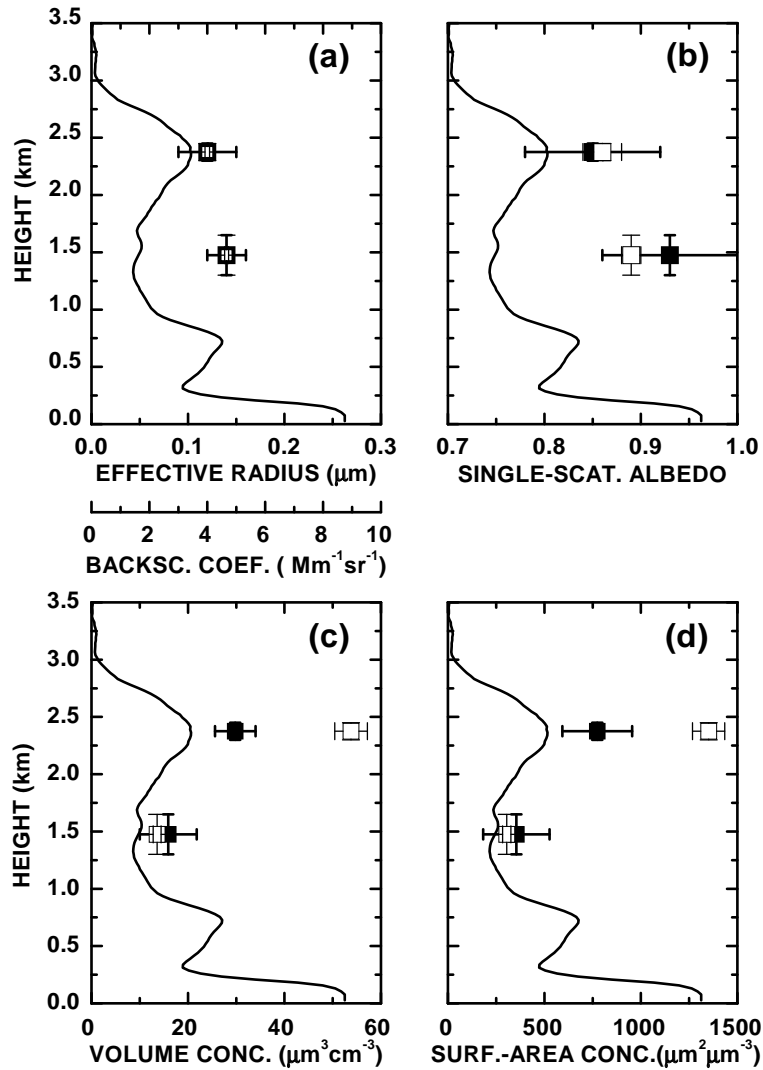
Figure 118: Measurement case from 1454-1647 UTC on March 10, 1999. Comparison of microphysical particle properties obtained with the IfT algorithm (closed squares) and the IMP algorithm (open squares). Shown are (a) effective radius, (b) single-scattering albedo at 532 nm, (c) volume concentration, and (d) surface-area concentration. Also shown in each case is the profile of the particle backscatter coefficient (solid line). Error bars denote statistical uncertainty. Vertical errors bars denote the height ranges across which the optical data were averaged for the inversion.
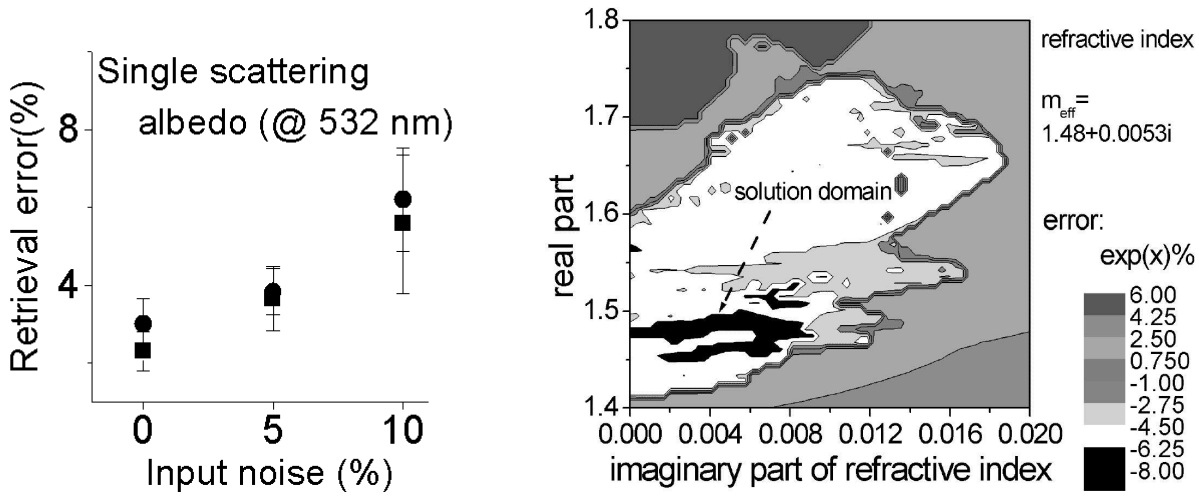
Figure 119: Left: Retrieval errors for the single scattering albedo with unknown refractive index: same notation as in Fig. 116; Right: Retrieval of the refractive index domain with the IMP algorithm for the Artic haze observed over Leipzig.

mately 3-km height. The particle lidar ratio was 40-60 sr at 532 nm in 2-km height. The Ångström exponents in the wavelength range from 355-532 nm varied around 1.8-2.0, which indicates the presence of small particles. The profile of the Ångström exponents calculated from the profiles of the backscatter coefficients at 355 and 532 nm remains rather constant below 2 km height. The Ångström exponent is a good indicator of the relative size of the particles. It has to be concluded that the mean particle size remained rather constant throughout the particle layer. In-situ observations performed at IfT showed the presence of Arctic haze near the surface (Heintzenberg et al., 2003).

Table 28 presents the results for the microphysical particle properties obtained with the two algorithms. Effective radius is approximately 0.13 μm in the case of the IfT algorithm. The algorithm from IMP is at the lower end of the uncertainty range given by the IfT algorithm. Both values are in agreement with the comparably large Ångström exponents. According to the in-situ observations the effective radius was approximately 0.14 μm.

The volume concentration obtained with the IMP algorithm is larger by a factor of two, and surface-area concentration by a factor of three compared with the results from the IfT algorithm. It has to

Table 28: Mean values of the physical particle parameters and the respective standard deviations for Arctic haze observed over Leipzig. Left column shows the results from the IfT algorithm. Right column shows the results from the IMP algorithm.

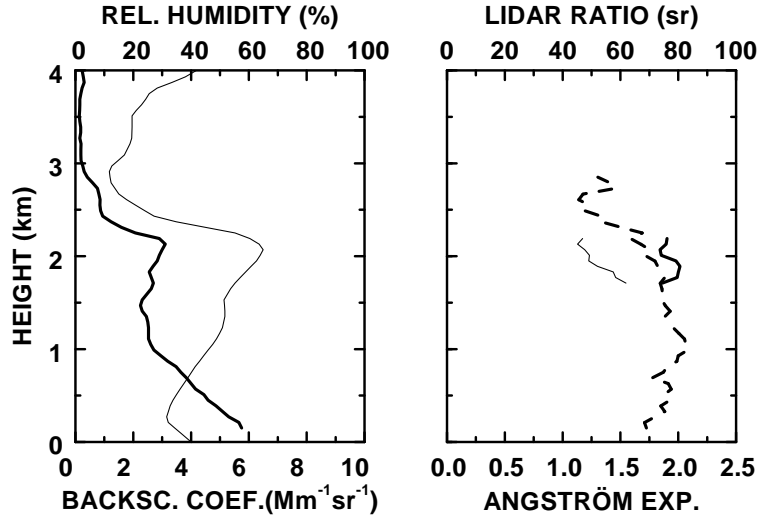|	IFT	IMP
r_{eff}, μm	0.13$\pm$0.06	0.07$\pm$0.002
v, μm^{3}cm^{-3}	23$\pm$8	42$\pm$3
s, μm^{2}cm^{-3}	560$\pm$120	1859$\pm$175
m_{real}	1.51$\pm$0.13	1.48$\pm$0.02
m_{imag}	0.004$\pm$0.004	0.005$\pm$0.003
SSA	0.970$\pm$0.04	0.96$\pm$0.02

Figure 120: Lidar observations of (a) the particle backscatter coefficient (thick solid line), relative humidity (thin solid line), (b) particle lidar ratio (thin solid line), Ångström exponent from the extinction coefficients at 355 and 532nm (thick solid line), and Ångström exponent from the backscatter coefficients at 355 and 532 nm (dashed line).

be observed that this measurement presents a difficult example with respect to the inversion. The inversion codes become unstable for effective radii around 0.1 μm.

The real part of the complex refractive index is similar in both cases. However the IfT algorithm shows a large uncertainty. The imaginary parts agree well. Both algorithms yield almost the same single-scattering albedo which is one of the most important parameters in climate-impact studies.

18.5   Further improvements

18.5.1   Reduction of computing time

The following formulas hold for the extinction and backscatter kernels of spherical particles (Bohren and Huffman, 1983):

$$
\begin{cases}
K_\pi^{(m)} = \pi r^2 Q_\pi(r, \lambda; m) = \frac{\pi}{\nu^2} | \sum_{n=1}^{\infty} (2n+1)(-1)^n (a_n - b_n)|^2, \\[2mm]
K_{ext}^{(m)} = \pi r^2 Q_{ext}(r, \lambda; m) = \frac{\pi}{\nu^2} Re \sum_{n=1}^{\infty} (2n+1)(a_n + b_n),
\end{cases}
\tag{20}
$$

where ν denotes the wave number defined by $\nu = 2\pi/\lambda$.

It was shown in Mekler et al. (2000) that both of the series in (20) are uniformly (=absolutely) convergent in every bounded subdomain of the definition domain (21). Moreover, the kernel functions can be represented in form of power series with respect to the product $x = r\nu$ of the particle radius and the wave number, respectively. This is useful by practical calculations because the new representation will reduce the runtime.

The restrictions on the real variables r, ν and on the complex parameter m may be written in the form

$$
0 < x < \infty, \ m^2 \notin M_\varepsilon,
\tag{21}
$$

173

where $0 < \varepsilon$ is an arbitrary small fixed number and M_ε denotes the domain $\{m : |\frac{m-1}{m}| < 2 - \varepsilon\}$ on the complex plain. For the Fredholm operators the values of the parameter m lie in fact strictly inside M_ε.

The functions a_n and b_n $(n \geq 1)$ in (20) are expressed by Sommerfeld spherical harmonics ψ and ζ as follows (Bohren and Huffman, 1983):

$$
\begin{cases}
a_n = a_n(x; m) = \frac{m\psi_n(mx)\psi_n'(x) - \psi_n(x)\psi_n'(mx)}{m\psi_n(mx)\zeta_n'(x) - \zeta_n(x)\psi_n'(mx)}, \\[2mm]
b_n = b_n(x; m) = \frac{\psi_n(mx)\psi_n'(x) - m\psi_n(x)\psi_n'(mx)}{\psi_n(mx)\zeta_n'(x) - m\zeta_n(x)\psi_n'(mx)},
\end{cases}
\tag{22}
$$

where the denominators in (22) do not turn into zero in the definition domain of the kernels.

The Taylor expansion with respect to m of the extinction kernel of the Fredholm operators at the point $m = 1$ has (up to the second order) the following form

$$
K_{ext}^{(m)}(r, \nu) = 2\pi\nu^{-2} Re \sum_{n=1}^{\infty} (2n+1)(a_n(m, x) + b_n(m, x)) =
$$

$$
2\pi\nu^{-2} Re \Big(-\pi\mathbf{i}(m-1) \sum_{n=1}^{\infty} \left\{ \sum_{k=0}^{n-1} [(2n - 2k + 1)V_{k,n-k}] \right\} \left(\frac{x}{2}\right)^{2n+1} +
$$

$$
+ (-\frac{\pi}{2})\mathbf{i}(m-1) \sum_{n=1}^{\infty} \left\{ \sum_{k=0}^{n-1} [(2n - 2k + 1)U_{k,n-k}] \right\} \left(\frac{x}{2}\right)^{2n+3} +
$$

$$
+ \frac{\pi}{2}\mathbf{i}(m-1)^2 \sum_{n=1}^{\infty} \left\{ \sum_{k=0}^{n-1} [(2n - 2k + 1)\left(-2\pi(-1)^{n-k}\Delta_{k,n-k} - N_{k,n-k}\right)] \right\} \left(\frac{x}{2}\right)^{2n+1} +
$$

$$
+ \frac{\pi}{4}\mathbf{i}(m-1)^2 \sum_{n=1}^{\infty} \left\{ \sum_{k=0}^{n-1} [(2n - 2k + 1)\left(-4\pi(-1)^{n-k}\Upsilon_{k,n-k} - \Omega_{k,n-k}\right)] \right\} \left(\frac{x}{2}\right)^{2n+3} +
$$

$$
+ \pi^2(m-1)^2 \sum_{n=1}^{\infty} \left\{ \sum_{k=0}^{n-1} [(2n - 2k + 1)\Psi_{k,n-k}] \right\} \left(\frac{x}{2}\right)^{4n+2} +
$$

$$
+ \frac{\pi^2}{4}(m-1)^2 \sum_{n=1}^{\infty} \left\{ \sum_{k=0}^{n-1} [(2n - 2k + 1)\Phi_{k,n-k}] \right\} \left(\frac{x}{2}\right)^{4n+6} + \{\text{remainder}\},
$$

where the values $V, U, N, \Delta, \Upsilon, \Omega, \Psi, \Phi$ do not depend on m in contrast to a_n and b_n. A similar expansion holds for the backscatter kernel. Therefore, those representations are favourable in reducing the computational runtime.

18.5.2 Inversion technique with nonnegativity constraints

To improve the retrieval of the microphysical parameters especially of the total number concentration which is often very unstable in the retrieval process as mentioned in the previous section we startet to apply a regularization technique with nonnegativity constraints.

Imposing a priori constraints can sometime dramatically improve the quality of the solution to inverse problems. This is particulary true in applications, where nonnegativity is important. From
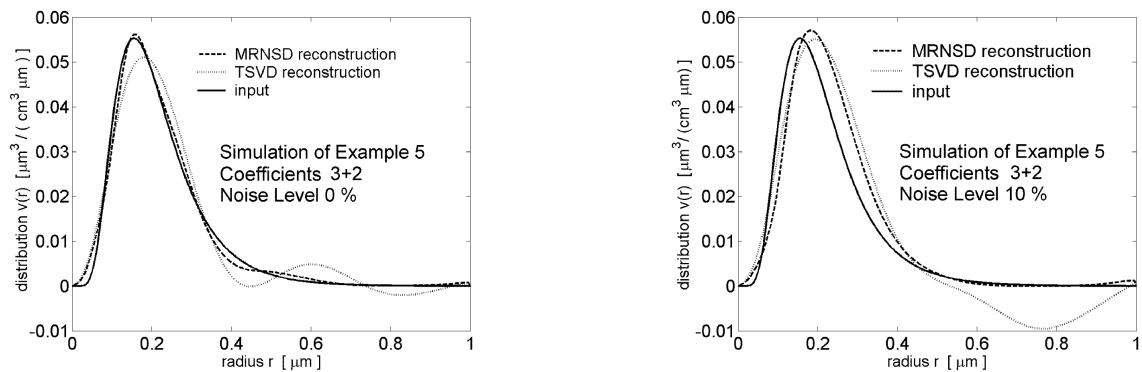
Figure 121: Retrieval of the volume distribution function of example 5 (solid line) of Table 25 via an unconstraint method (grey solid line) in comparison with a constraint method (dashed line) with noiseless data (left) and noisy data (rigth).

the mathematical point of view the known methods fall into two broad categories - variational and iterative.

In terms of computational cost, if a good a priori value of the regularization parameter is not available, one may have to solve several variational problems and then select the best one using an a posteriori regularization parameter selection technique. Iterative regularization techniques are then likely to be much cheaper, assuming the cost of determining when to stop the iteration is relatively low. The iterative methods use iteration count as regularization parameter. We select a modified residual norm steepest descent (MRNSD) algorithm which converges to a solution $n(r) \geq 0$, i.e. the nonnegativity condition is always satisfied. For more details see Vogel (2002).

First applications to Eq. (17) and simulations show very good results. We compared the new retrieval results (dashed line) with those from unconstraint regularized inversion via truncated singular value decomposition (TSVD), see Fig. 121 (grey solid line). One observes that the oscillations of the unconstraint solution which often lie also in the negative range are suppressed in the constraint solution. This fact shall be favourable in retrieving the total number concentration. Those examinations are an ongoing work. Moreover, first observations show also very good results especially for only 3+2 coefficients in the noisy case, see Fig. 121 (right).

18.6 Methodology to retrieve atmospheric aerosol parameters by combining multi-wavelength lidar and Sun-sky radiance measurements

18.6.1 Introduction

The remote monitoring of atmospheric aerosol is now made in the European region by two measurement networks. The effective Aerosol Robotic Network (AERONET) for remote aerosol monitoring is created on the base of the sun sky-scanning radiometer CIMEL (Holben et al., 1998). Data processing of the radiometric measurements provides the retrieval of aerosol size distributions integrated over the whole atmospheric layer and the estimation of particle complex refractive indices (Dubovik and King, 2000). Lidar systems give the information on altitude distributions of aerosol parameters. Routine multiwavelength lidar observations are made within the scope of the lidar network EAR-LINET (Bösenberg et al., 2001a). Now a number of scientific centers make routine observations by both of these instruments. Scientific and practical interest is to arrange a comprehensive ex-

periment using a sun scanning radiometer and a multi-frequency lidar and to design algorithms for data processing, which will provide the construction of vertically stratified models of atmospheric aerosols. The methodology of coordinated multi-frequency lidar and radiometric investigations of atmospheric aerosols has been developed and was tested in real-life experiments.

18.6.2 Equation set description

The mathematical statement of the problem and the starting set of equations were proposed by Chaikovsky et al. (2002). A base equation system is constructed as an equation set including the relationships of data vectors of lidar and radiance measurements with aerosol parameters of the atmospheric layer as well as additional conditions on the smoothness of altitude profiles of aerosol parameters retrieved. The equation set includes three following subsystems:

- aerosol optical thickness from radiance measurements defined by the integral value of the aerosol extinction coefficient,

- multi-wavelength lidar equations containing information on vertical aerosol parameter profiles,

- smoothness constraints on vertical aerosol parameters distributions.

$$
\begin{aligned}
\tau^{*a}(\lambda_i) &= \tau^{a,i}(\lambda_i, C_\nu, m_j) + \Delta_\tau^i \\
L^*(\lambda_j, \theta, z) &= L(\lambda_j, \theta, C_\nu, m_j, z) + \Delta_L^j \\
0_\nu^* &= S_2 C_\nu + \Delta_{0_\nu}
\end{aligned}
\tag{23}
$$

Here $\tau^{*a}(\lambda_i)$ are the vectors of aerosol optical thickness from radiometric measurements at wavelength λ_i, $i = 1, ..., I$ and $L^*(\lambda_j, \theta, z)$ is the lidar signal at wavelength λ_j, $j = 1, ..., J$, and zenith angle θ normalized by its value at point z_N.

$$
L^*(\lambda_j, \vartheta, z) = \frac{P^*(\lambda_j, \theta, z) z^2}{P^*(\lambda_j, \theta, z_N) z_N^2}
\tag{24}
$$

where $P^*(\lambda_i, \theta, z)$ is the measured lidar signal.
On the right hand of Eqs. (23), $\tau^a(\lambda_i, C_\nu, m_j)$ and $L(\lambda_j, \theta, C_\nu, m_j, z)$ are non-linear functions of parameters C_ν of aerosol particles size distribution and m_j is the particle complex refractive index.

$$
\tau^{a,i} = \int_0^{z_N} \varepsilon^a(\lambda_i, z') \, dz' \,,
\tag{25}
$$

where $\varepsilon^a(\lambda_i)$ are the aerosol extinction coefficients at wavelengths λ_i.

$$
L(\lambda_j, \theta, C_\nu, z_N, z) = \frac{R(\lambda_j, C_\nu, z)}{R_N(\lambda_j, C_{\nu,N}, z_N)(T^a(\lambda_j, \theta, C_\nu, z))^2} \times \frac{\beta^m(\lambda_j, z)}{\beta^m(\lambda_j, z_N)(T^m(\lambda_j, \theta, C_\nu, z))^2}
\tag{26}
$$

where

$$
R(\lambda_j, C_\nu, z) = 1 + \frac{\beta^a(\lambda_j, C_\nu, z)}{\beta^m(\lambda_j, z)}
\tag{27}
$$

$$
T^a(\lambda_j, \theta, C_\nu, z) = \exp(-\int_0^z \frac{1}{\cos\theta} \varepsilon^a(\lambda_j, z') \, dz')
\tag{28}
$$

176

$$T^m(\lambda_j, \theta, z) = \exp(-\int_0^z \frac{1}{\cos\theta}\varepsilon^m(\lambda_j, z')\, dz')\,. \tag{29}$$

$\beta(\lambda_i, z)$ and $\varepsilon(\lambda_i, z)$ are the backscatter and extinction coefficients, respectively; superscripts "a" and "m" represent the values for aerosols and air molecules.

Equation $0_\nu^* = S_2 C_{\nu,n} + \Delta_{0_\nu}$ is a vector analogue of smoothness constraints with respect to vertical distributions of parameters C_ν, 0_ν^* is a null-vector corresponding to preliminary estimation of 2-nd order finite differences, Δ_x is a vector that characterizes uncertainties in the vector x of measurements or specifications.

Aerosol parameters will be retrieved similar to Dubovik and King (2000) by the maximum likelihood method. The likelihood function for the chosen model (23) can be written as

$$P(C_\nu | L^*, \tau^*, 0_\nu^*) \sim$$
$$\exp\{-\frac{1}{2}[\sum_{n=1}^{N-1}\sum_{j=1}^{J}(L_n^{j*} - L_n(C_\nu))^T \Omega_L^{-1}(L_n^{j*} - L_n(C_\nu)) +$$
$$\sum_{i=1}^{I}(\tau^{a,i*} - \tau^{a,i}(C_\nu))^T \Omega_\tau^{-1}(\tau^{a,i*} - \tau^{a,i}(C_\nu)) + \frac{E_m}{\sigma_\nu^2}]\} \tag{30}$$

where Ω_L is the covariance matrix of errors in the measured value L^{j*}, Ω_τ is the covariance matrix of errors in the measured value τ^{a*} and $\sigma_n u^2$ is the variance of finite-difference a priori estimation for vertical distribution C_ν.

According to the method of maximum likelihood, the best estimation of unknown values $\tilde{C}_\nu$ correspond to the maximum of the likelihood function

$$P(\tilde{C}_\nu | L_1^*, \tau^*, 0_\nu^*) = \max \tag{31}$$

that corresponds to the minimum of the form in the exponent of Eq. (30).

A mathematical simulation has shown that the direct application of the procedure to find the maximum of the function of Eq. (31) provides the optimal solution only for small measurement errors. A "first guess" for retrieving a concentration profile (input parameters for an optimization subroutine used) has to be close to "true" values. The difficulty is that standard optimization codes seek, as a rule, a local minimum of a function near the "first guess". Under a large number of parameters being optimized and a poor first guess, a chance to get a valid solution is small.

To improve the convergence of the profiles of aerosol parameters retrieved to the optimal ones, the processing algorithm was rearranged, so that the solution was normalized at each step of the optimization to correspond to integral aerosol parameters provided by the radiometric data. This procedure is essentially an analog of the preliminary calibration of lidar data by using radiometric measurements.

18.6.3 Retrieval of aerosol parameters by field measurements

The designed procedure was refined during combined field radiometric and lidar measurements at the two stations of Minsk (Belarus) and Belsk (Poland), which are constituents of both the AERONET (PHOTON) and EARLINET. The lidar systems of Minsk and Belsk have three working wavelengths (532, 694, and 1064 nm). Their specifications enable an aerosol layer to be sounded during day hours up to altitudes about 10 km and making measurements along slanted ranges. The data processing algorithm includes following main procedures:
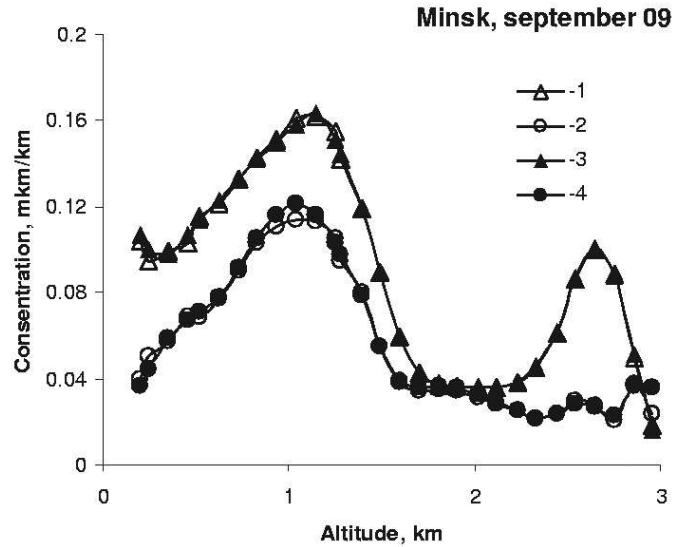
Figure 122: Volume concentrations of the fine (curves 1 and 3) and coarse (2 and 4) modes retrieved by measurements in Minsk on September 9, 2002 prior to (1 and 2) and after (3 and 4) the final correction.

- pretreatment of the CIMEL and LIDAR data,

- normalizing of lidar data,

- calculation of approximate altitude profiles of aerosol fraction concentrations,

- correction of altitude profiles of aerosol fraction concentrations.

At the final stage, the correction of parameters C_ν is made on the base of minimizing the expression in the exponent of the function of Eq. (30).

Combined lidar and radiometric measurements are being made in Belsk since April, 2002, in Minsk since July, 2002. An aerosol model as a set of two fractions is used during measurement processing. The parameters of the fractions are determined by the CIMEL data. The retrieved parameters are the concentrations of the fractions.

The retrieved profiles of the concentration of the two fractions are given in Fig. 122. The proportion of the fine and coarse fractions changes essentially with the altitude. The profiles $C_{f,n}$ and $C_{c,n}$ are shown prior to and after the correction at the final stage of the data processing.

Figure 123 shows measured lidar signals $L^*(\lambda_j)$ as well as quantities $L(\lambda_j)$ calculated by the retrieved aerosol parameters. The distributions of $\ln(L^j/L^{*j})$ are also given here. For Minsk measurements on September 09, the difference between the observed and measured quantities is rather small. It is less than 15% for the wavelengths 532 and 1064 nm and is of the order of 30% for 694 nm. Except for the boundary points, these differences are close to the calculated measurement errors of $L^*(\lambda_j)$.

Generalizing the results of the data processing for the series of September 09, we can conclude that in this case the two-fraction model of the aerosol layer with altitude-constant microstructure of each fraction and varying their concentrations is adequate to describe the whole data set for the performed optical measurements.
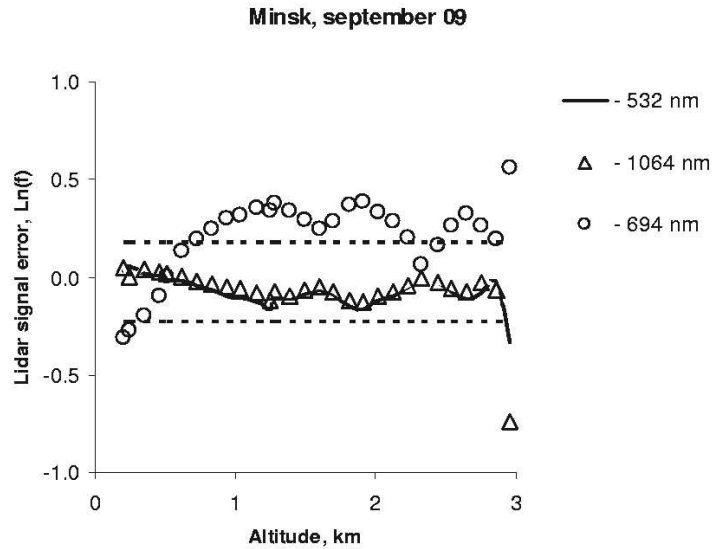
Figure 123: Accuracy of the retrieved experimental lidar signals, Minsk, September 9, 2002. Dashed lines correspond to retrieval errors of $\pm$ 20%.

18.6.4 Conclusion

Field measurements carried out at Minsk and Belsk stations in 2002 by combined usage of the CIMEL and multi-frequency lidars have provided the basis to design the described procedure of correlated radiometric and lidar observations. The methods of performing the experiments and formats of input data presentation have been worked out to correspond to the main requirement of adequate representation of aerosol layer parameters during measurements.

The main difficulties of data processing were multiple parameters of the problem, rather high measurement errors, and a limited number of spectral channels of multi-frequency lidars. The data processing algorithm is based on successive estimations and corrections of aerosol characteristics. "Hard" parameterization of a solution desired is implemented here. The algorithm operates under comparatively high measurement errors and in presence of other disturbing factors.

Apparently, the procedure of correlated radiometric and lidar observations should be further developed towards expanding the spectral range and increasing the number of working wavelengths of a lidar and the inclusion of Raman systems in an observation cycle to directly measure altitude profiles of aerosol extinction. This will enable one to use a more general model of the aerosol layer and to go into details of aerosol microstructure. The procedure of data processing in this case can be arranged as an additional correction of the solution with a large number of desired parameters.

19 Modeling and forecasting of dust events

by Slobodan Nickovic

19.1 Objectives

The major objective of the Package is to improve the quantitative assessment of the spatio-temporal distribution of mineral dust using the atmospheric dust aerosol model DREAM. The objectives also include dust cycle components of soil erosion physics, multiple-particle size effects, turbulent diffusion, advection and deposition of dust. Finally, it anticipates tuning and validation of the model using EARLINET lidar measurements.

19.2 Methodology

The objectives of this work package were performed through the following specific tasks. Two model domain were specified in order to cover both lidar sites and Saharan sources: a) the finer-resolution Mediterranean region and b) the coarser-resolution European region. The both dust model versions were operationally implemented by providing daily dust forecasts covering 3-day periods. A set of predicted vertical concentration profiles were calculated and archived on a daily base for most of the EARLINET network points. Also, other dust and conventional atmospheric parameters of interest were calculated and archived: dust load, dust surface concentration, wet and dry deposition, cloudiness, wind, temperature, moisture, and precipitation. A selection of dust forecasting output data were put and available to the scientific community at a specially established web page: http://www.icod.org.mt/modeling/forecasts/dust_med.htm (see Fig. 124).

19.3 Scientific achievements

Saharan dust model   The ICoD group established dust model operational forecasts from the very beginning of the EARLINET-NAS project official start (April 2002). The NCEP/Eta regional atmospheric model drives the DREAM model on an on-line basis. The atmospheric model provides at each iteration time step driving parameters such as wind, temperature, humidity and precipitation. The model simulates all major phases of the atmospheric dust life such as production, diffusion, advection and removal of dust by solving the following concentration equation:

$$\frac{\partial C_k}{\partial t} = -u\frac{\partial C_k}{\partial x} - v\frac{\partial C_k}{\partial y} - (w - v_{gk})\frac{\partial C_k}{\partial z} - \nabla(K_H \nabla C_k) - \frac{\partial}{\partial z}\left(K_Z \frac{\partial C_k}{\partial z}\right) + \left(\frac{\partial C_k}{\partial t}\right)_{SOURCE} - \left(\frac{\partial C_k}{\partial t}\right)_{SINK}$$
(32)

Here, dust concentration C is considered as a radiative and chemically passive tracer. The model also includes effects of the particle size distribution on aerosol dispersion. The dust concentration governing equation is given by permitting no inter-particle interactions. In the model, there are 4 particle size classes determined by clay, small silt, large silt and sand. The total concentration is assumed as a weighted sum of concentrations of particle size classes. Fig. 125 schematically show processes represented in the model.

  The desert dust sources are specified using high-resolution data on vegetation and soil types. The dust production scheme that estimates the amount of dust injected into the atmosphere takes into account effects of ground wetness, the impact of prolonged fluxes due to inertial forces, and effects
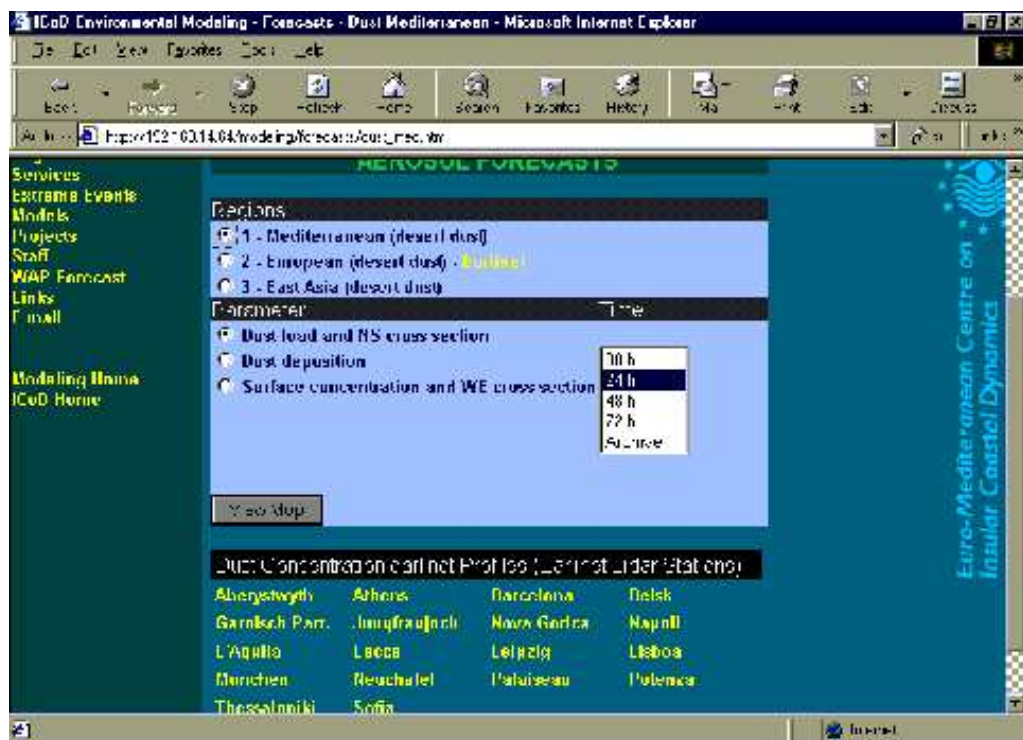
Figure 124: ICoD web page with operational dust forecasts

of the viscous sub-layer mixing. The model also simulates injection of dust under shear-free flow conditions characterized by strong convection and narrow uprising motion (overheated surfaces). The dry deposition scheme treats separately deposition process over sea, bare and ice surfaces, and surfaces covered by vegetation, and deposition by gravitational settling. Wet deposition scheme uses precipitation supplied by the atmospheric part of the model.

Model vs. lidar comparisons   For the selected dust storm case (October 2001), a validation of the model against lidar and other measurements has been provided. The case is characterized with strong injection of dust in the Western Sahara and subsequent long-range transport of dust deep towards Western and Northern Europe. We run the model over the extended period from 6-17 October 2001 in order to well represent the dust cycle from its initial phase till the end of the process. For the comparison reasons, dust concentration vertical profiles have been recorded for the EARLINET lidar stations over the whole simulation period. Fig. 126 shows that the model-predicted dust loads generally well compare with values observed at different lidar stations.

 In addition, a comparison of model profiles against a number of EARLINET stations was performed. Fig. 127 shows an example of observed and predicted profiles of the backscatter coefficients. The model simulation results indicated that the October dust storm case, after significant initial injection of the mineral aerosol from the Western Sahara, was transported by the large-scale atmospheric circulation first over the Western Mediterranean (Fig. 128) and then advancing towards north, covering large parts of the Western and Northern Europe.

  ICoD modelling experiments were performed in order to contribute to quantitative assessment of temporal and spatial mineral aerosol distribution and to improve planning activities of EARLINET lidar groups by indicating time and location of forthcoming dust storms.
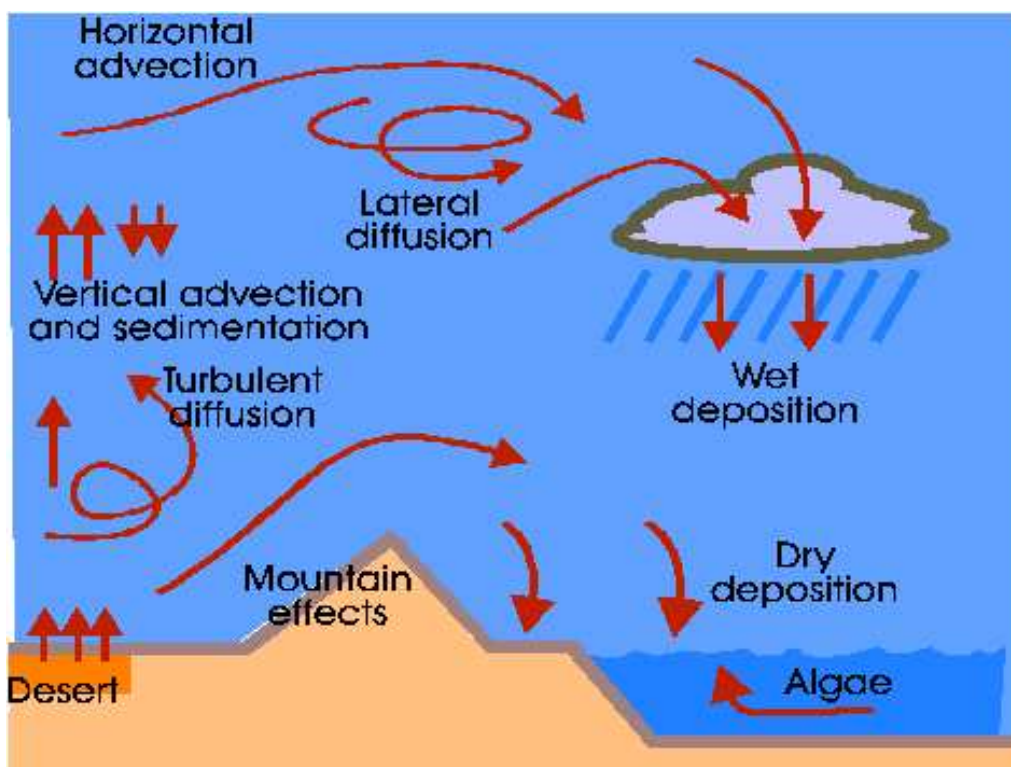
181

Figure 125: Dust cycle in the model.

19.4   Socio-economic relevance and policy implication

Modelling aspect incorporated through the work packages described in section 8, 17 and this work package in the project brought a complementary information to EARLINET lidar measurements, thus contributing to better understanding of the overall atmospheric cycle of the mineral dust originating from the Sahara desert. Being one of key climate forcing factors and affecting the natural environment, dust has numerous social-economic impacts and policy implications. Models such as DREAM used within the project contributes to better specification of spatial and temporal distribution of mineral dust.

ICoD's participation in the project was a unique opportunity to collaborate with lidar observation groups setting conditions for close future cooperation inn the field of data assimilation in the modelling structure.

19.5   Discussion and conclusion

ICoD completed all the planned tasks with no delay. Operational dust forecasts were established from the very beginning of our project participation in order to support other project participants and to archive the raw model results over as much as longer period. Close cooperation was established with several EARLINET groups, especially with colleagues from Leipzig and Munich. In collaboration with them and thanks to the method for conversion of concentration to lidar measurements and vice versa (A. Ansmann, personal communication) we were able to perform a comparison of model results against observations.
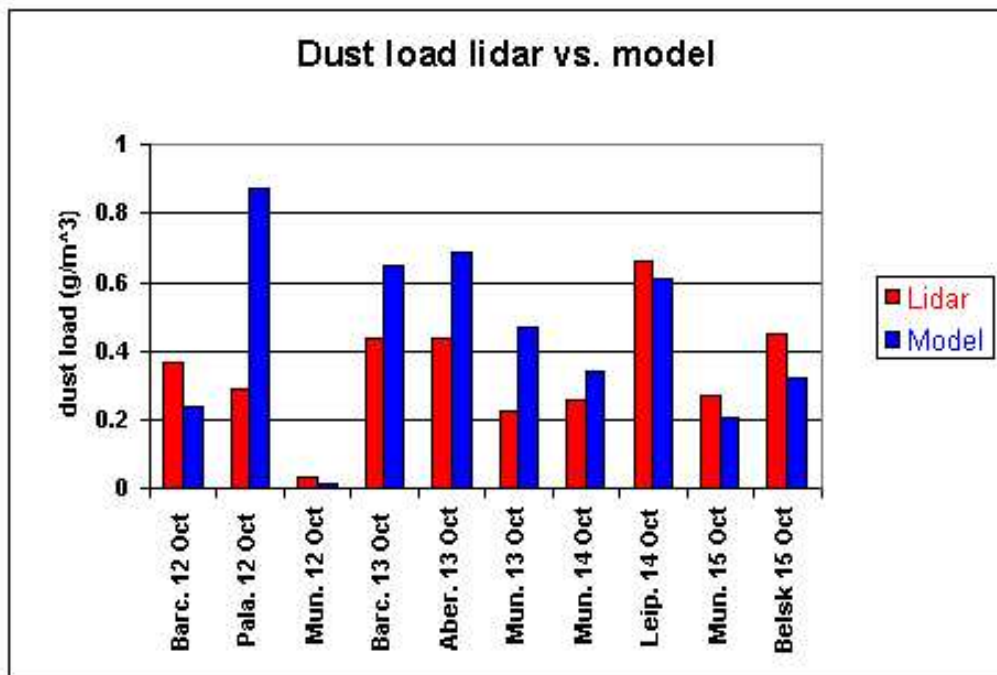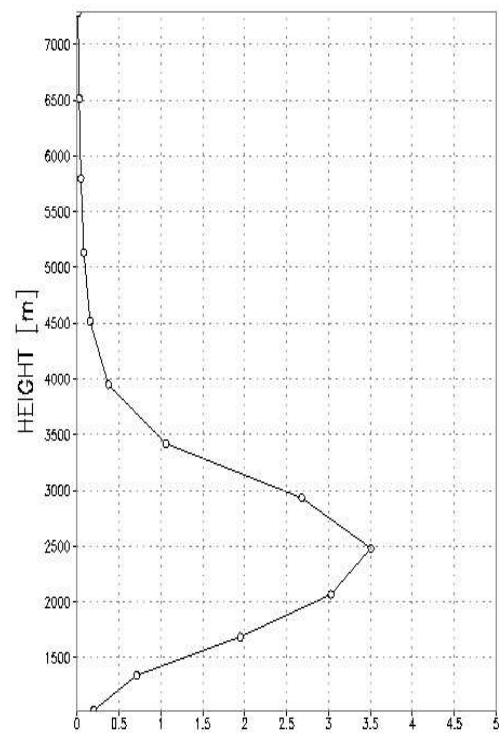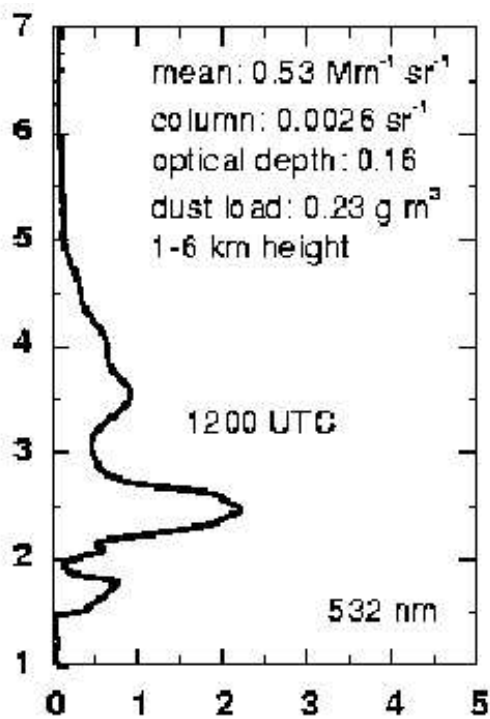
Figure 126: Dust load: lidar vs. model

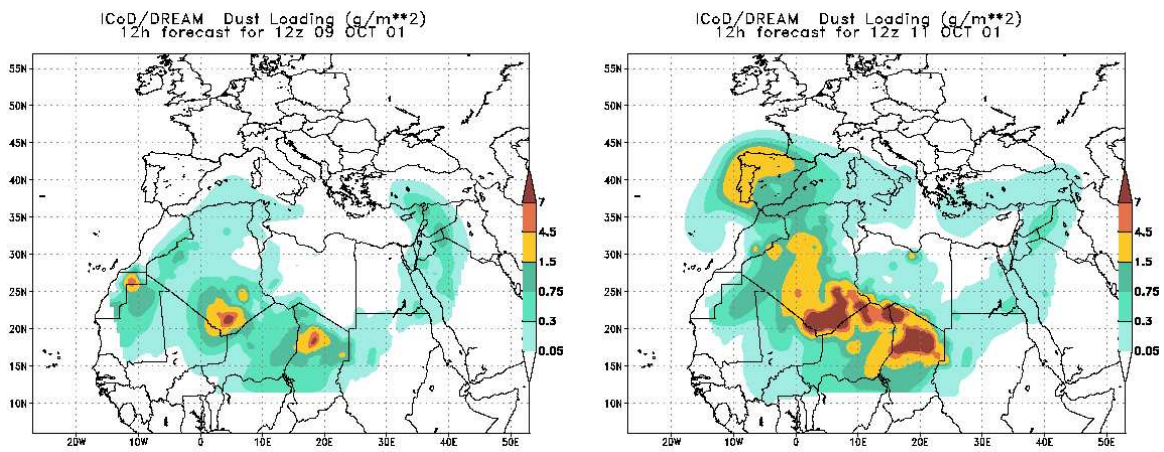Figure 127: Observed (left) and predicted (right) vertical profiles of aerosol in Leipzig 13 October 2001.

183

Figure 128: Spatial and temporal evaluation of the October 2001 dust storm

References

Ackermann, J. (1998). The extinction-to-backscatter ratio of tropospheric aerosols: A numerical study. *Journal of Atmospheric and Oceanic Technology*, 15:1043 – 1050.

Althausen, D., Müller, D., Ansmann, A., Wandinger, U., Hube, H., Clauder, E., and Zörner, S. (2000). Scanning six-wavelength eleven-channel aerosol lidar. *Journal of Atmospheric and Oceanic Technology*, 17:1469–1482.

Ansmann, A. (2002). Lindenberg Aerosol Characterization Experiment (LACE'98): Overview and main results. *Journal of Geophysical Research*, 10.1029/2000JD000233.

Ansmann, A., Mattis, I., Wandinger, U., Wagner, F., Reichardt, J., and Deshler, T. (1997). Evolution of the Pinatubo aerosol: Raman lidar observations of particle optical depth, effective radius, mass, and surface area over central Europe at 53.4°N. *Appl. Opt.*, 31:7113–7131.

Ansmann, A., Riebesell, M., Wandinger, U., Weitkamp, C., Voss, E., Lahmann, W., and Michaelis, W. (1992a). Combined Raman Elastic-Backscatter LIDAR for Vertical Profiling of Moisture, Aerosol Extinction, Backscatter, and LIDAR Ratio. *Applied Physics*, B 55:18–28.

Ansmann, A., Riebesell, M., and Weitkamp, C. (1990). Measurement of atmospheric aerosol extinction profiles with a Raman lidar. *Optics Letters*, 15.

Ansmann, A., Wandinger, U., Riebesell, M., Weitkamp, C., and Michaelis, W. (1992b). Independent measurement of extinction and backscatter profiles in cirrus clouds by using a combined Raman elastic-backscatter lidar. *Appl. Opt.*, 31:7113–7131.

Bais, A., Kazantzidis, A., Kazadzis, S., Balis, D., Zerefos, C., and Meleti, C. (2002). Effects of aerosol optical depth and single scattering albedo on surface UV irradiance. In *SPIE proceedings*.

Baldasano, J. M., Cremades, L., and Soriano, C. (1994). Circulation of Air Pollutants over the Barcelona Geographical Area in Summertime. In Angeletti, G. and Restelli, G., editors, *Proceedings of the Sixth European Symposium on Physico-Chemical Behavior of Atmospheric Pollutants, Environmental Research Program of the European Community, Air Pollution Research Report EUR 15609/1*, pages 474–479.

Barnes, J. and Hofman, D. (2001). Variability in the background aerosol over Mauna Loa. *Geoph. Res. Lett.*, 28:2895–2898.

Barros, N., Borrego, C., Toll, I., Soriano, C., Jimnez, P., and Baldasano, J. M. (2003). Urban photochemical pollution in the Iberian Peninsula: Lisbon and Barcelona airsheds. *J. Air & Waste Manage. Assoc.*, 53:347–359.

Batcharova, E. and Gryning, S.-E. (1998). Wind climatology, atmospheric turbulence and internal boundary-layer development in Athens during the medcaphot-trace experiment. *Atmos. Environ.*, 32:2055–2069.

Böckmann, C. (2001). Hybrid regularization method for the ill-posed inversion of multiwavelength lidar data in the retrieval of aerosol size distributions. *Appl. Opt.*, 40:1329–1342.

Böckmann, C., Müller, D., and Wandinger, U. (2001). Microphysical Particle Properties from 3-Wavelength Raman Lidar. *Journal of Aerosol Science*, 32:393–394.

Böckmann, C. and Wauer, J. (2001). Algorithms for the inversion of light scattering data from uniform and non-uniform particles. *J. Aerosol Sci.*, 32:49–61.

Bodhaine, B., Wood, N., Dutton, E., and Slusser, J. (1999). On Rayleigh Optical Depth Calculations. *J. Atmospheric and Oceanic Technol.*, 16:1854–1861.

Bohren, C. F. and Huffman, D. R. (1983). *Absorption and scattering of light by small particles*. John Wiley & Sons, New York.

Bösenberg, J. (1998). Ground-based differential absorption lidar for water vapor and temperature profiling: methodology. *Appl. Opt.*, 37:3845 – 3860.

Bösenberg, J., Alpers, M., Althausen, D., Ansmann, A., Böckmann, C., Eixmann, R., Franke, A., Freudenthaler, V., Giehl, H., Jäger, H., Kreipl, S., Linn´e, H., Matthias, V., Mattis, I., Müller, D., Sarközi, J., Schneidenbach, L., Schneider, J., Trickl, T., Vorobieva, E., Wandinger, U., and Wiegner, M. (2001a). The German Aerosol Lidar Network: Methodology, Data, Analysis. MPI-Report 317, Max-Planck-Institut für Meteorologie, Hamburg.

Bösenberg, J., Ansmann, A., Baldasano, J., Balis, D., Böckmann, C., Calpini, B., Chaikovsky, A., Flamant, P., Hågård, A., Mitev, V., Papayannis, A., Pelon, J., Resendes, D., Schneider, J., Spinelli, N., Vaughan, T. T. G., Visconti, G., and Wiegner, M. (2001b). EARLINET: A European Aerosol Research Lidar Network. In Dabas, A., Loth, C., and Pelon, J., editors, *Laser Remote Sensing of the Atmosphere. Selected Papers of the 20th International Laser Radar Conference*, pages 155–158. Edition Ecole Polytechnique, Palaiseau.

Bösenberg, J., Brassington, D., and Simon, P., editors (1997). *Instrument Development for Atmospheric Research and Monitoring. Lidar Profiling, DOAS and Tunable Diode Laser Spectroscopy*, volume 8 of *Transport and Chemical Transformation of Pollutants in the Troposphere*. Springer-Verlag, Berlin Heidelberg.

Bösenberg, J. and Theopold, F. (1988). Evaluation of DIAL measurements in presence of signal noise. In *Proceedings of the 14th International Laser Radar Conference, San Condilo, Italy*, pages 209–211.

Carnuth, W. and Trickl, T. (2000). Transport studies with the IFU three-wavelength aerosol lidar during the VOTALP Mesolcina experiment. *Atmos. Environ.*, 34:1425–1434.

Carnuth, W., Trickl, T., and Kempfer, U. (2002). Highlights of the tropospheric lidar studies at IFU within the TOR project. *Tellus 54B*, pages 163–185.

Chaikovsky, A., Dubovik, O., Holben, B., and Bril, A. (2002). Methodology to retrieve atmospheric aerosol parameters by combining ground-based measurements of multi-wavelength lidar and sun sky-scanning radiometer. In Zherebtsov, G. A., Matvienko, G. G., Banakh, V. A., and Koshelev, V. V., editors, *Eight International Symposium on Atmospheric and Ocean and Ocean Optics: Atmospheric Physics. Proceeding of SPIE, Vol. 4678*, pages 257–268.

Diak, G. R. and Stewart, T. R. (1986). Assessment of surface turbulent fluxes using geostationary satellite surface skin temperature and a mixed layer planetary boundary layer model scheme. *J. Geophys. Res.*, 94, D5:6357–6373.

Dorling, S., Davies, T., and Pierce, C. (1992). Cluster analysis: A technique for estimating the synoptic meteorological controls on air and precipitation chemistry-method and applications. *Atmos. Environ.*, 26A:2575–2581.

Driedonks, A. G. M. (1982). Models and observations of the growth of the atmospheric boundary layer. *Boundary-Layer Meteorol.*, 23:283–306.

Dubovik, O. and King, M. (2000). A flexible inversion algorithm for retrieval of aerosol optical properties from sun and sky radiance measurements. *J. Geophys. Res.*, 105(D16):20673–20696.

Edlen, B. (1953). The dispersion of standard air. *Journal of the Optical Society of America*, 43:339.

Eixmann, R., Böckmann, C., Fay, B., Matthias, V., Mattis, I., Müller, D., Kreipl, S., Schneider, J., and Stohl, A. (2002). Tropospheric aerosol layers after a cold front passage in January 2000 as observed at several stations of German lidar network. *Atmospheric Research*, 63:39–58.

Evans, B. T. N. (1988). Sensitivity of the backscatter/extinction ratio to changes in aerosol properties: implications for lidar. *Appl. Opt.*, 27:3299–3306.

Fernald, F. G. (1984). Analysis of atmospheric lidar observations: Some comments. *Appl. Opt.*, 23:652–653.

Ferrare, R., Melfi, S. H., Whiteman, D. N., Evans, K. D., Leifer, R., and Kaufman, Y. J. (1998). Raman lidar measurements of aerosol extinction and backscattering, 2 Derivation of aerosol real refractive index, single-scattering albedo, and humidification factor using Raman lidar and aircraft size distribution measurements. *Journal of Geophysical Research*, 103, D16:19673–19689.

Flamant, C., Pelon, J., Flamant, P., and Durand, P. (1997). Lidar determination of the entrainment zone thickness at the top of the unstable marine atmospheric boundary layer. *Boundary-Layer Meteorol.*, 83:247–284.

Forster, C., Wandinger, U., Wotawa, G., James, P., Mattis, I., Althausen, D., Simmonds, P., O'Doherty, S., Jennings, G., Kleefeld, C., Schneider, J., Trickl, T., Kreipl, S., Jäger, H., and Stohl, A. (2001). Transport of boreal forest fire emissions from Canada to Europe. *J. Geophys. Res.*, 106, D19:22887–22906.

Furger, M., Dommen, J., Graber, W. K., Poggio, L., Prvt, A., Emeis, S., Grell, G., Trickl, T., Gomiscek, B., Neininger, B., and Wotawa, G. (2000). The VOTALP Mesocina Valley Campaign 1996 (concept, background and some highlights). *Atmos. Environ.*, 34:1395–1412.

Godin, S., Carswell, A., Donovan, D., Claude, H., Steinbrecht, W., McDermid, I., McGee, T., Gross, M., Nakane, H., Swart, D., Bergwerff, H., Uchino, O., von der Gathen, P., and Neuber, R. (1999). Ozone differential absorption lidar algorithm intercomparison. *Appl. Opt.*, 38:6225–6236.

Heintzenberg, J., Tuch, T., Wehner, B., Wiedensohler, A., Wex, H., Ansmann, A., Mattis, I., Müller, D., Wendisch, M., Eckhardt, S., and Stohl, A. (2003). Arctic Haze over Central Europe. *Tellus (in press)*.

Hess, M., Köpke, P., and Schult, I. (1998). Optical properties os aerosols and clouds: the software package OPAC. *Bulletin of the American Meteorological Society*, 79:831 – 844.

Hofman, D. and Rosen, J. (1981). On the background stratospheric aerosol layer. *J. of Atm. Sci.*, 38:168–181.

Hofman, D., Rosen, J., and Grindel, W. (1985). Delayed production of sulfuric acid condensation nuclei in the polar stratosphere from El Chichon volcanic vapors. *J. of Geoph. Res.*, 90 D1:2341–2354.

Holben, B. N., Eck, T. F., Slutsker, I., Tanr´e, D., Buis, J. P., Setzer, A., Vermote, E., Reagan, J. A., Kaufman, Y. J., Nakajima, T., Lavenu, F., Jankowiak, I., and Smirniov, A. (1998). AERONET-A Federated Instrument Network and Data Archive for Aerosol Characterization. *Remote Sens. Environment*, 66:1–16.

Ingold, T., Mätzler, C., Kämpfer, N., and Heimo, A. (2001). Aerosol optical depth measurements by means of a Sun photometer network in Switzerland. *J. of Geoph. Res.*, 106:27537–27554.

IPCC (2001). Climate change 2001: The science of climate change. Technical Summary of the Working Group I Report, World Meteorological Organization, Genf.

Jäger, H., Carnuth, W., and Georgi, B. (1988). Observations of Saharan Dust at a North Alpine Mountain Station. *J. Aerosol Sci.*, 19:1235–1238.

Jäger, H., Uchino, O., Nagai, T., Fujimoto, T., Freudenthaler, V., and Homburg, F. (1995). Ground based remote sensing of the decay of the Pinatubo eruption cloud at three northern hemisphere sites. *Geoph. Res. Lett.*, 22:607–610.

James, P., Scheel, H. E., Stohl, A., and Trickl, T. (2002). Deep Stratospheric Air Intrusions-Case studies and Climatology, Contribution TOR-12 (6 pp. on CD ROM). In Midgley, P. M. and Reuther, M., editors, *Transport and Chemical Transformation in the Troposphere, Proceedings of EUROTRAC Symposium 2002, Garmisch-Partenkirchen (Germany), March 11 to 15, 2002*. Markgraf.

Johnson, N. and Leone, F. C. (1964). *Statistics and Experimental Design in Engineering and the Physical Sciences* , volume 1. John Wiley & Sons, New York.

Kent, G. and Hansen, G. (1998). Multiwavelength lidar observations of the decay phase of the stratospheric aerosol layer produced by the eruption of Mount Pinatubo in June 1991. *Appl. Opt.*, 37:3861–3872.

Klett, J. D. (1981). Stable analytical inversion solution for processing lidar returns. *Appl. Opt.*, 20:211–220.

Kottmeier, C. and Fay, B. (1998). Trajectories in the Antarctic lower troposphere. *Journal of Geophysical Research*, 103, D9:10947 – 10959.

Kreipl, S., Mücke, R., Jäger, H., Trickl, T., and A.Stohl (2001). Spectacular Cases of Vertical and Long-range Ozone and Aerosol Transport. In Dabas, A. and Pelon, J., editors, *Laser Remote Sensing of the Atmosphere, Selected Papers of the 20th International Laser Radar Conference, Vichy (France), July 10 to 14, 2000,*, pages 455–458.

Kylling, A., Bais, A., Blumthaler, M., Schreder, J., Zerefos, C., and Kosmidis, E. (1998). Effect of aerosol on solar UV irradiances during the Photochemical Activity and Solar Ultraviolet Radiation campaign. *J. Geophys. Res*, 103:26,051–26,060.

Matthias, V., Böckmann, C., Freudenthaler, V., Pappalardo, G., Bösenberg, J., Amiridis, V., Amodeo, A., Ansmann, A., Balis, D., Boselli, A., Chaykovski, A., Chourdakis, G., Comer´on, A., Delaval, A., Tomasi, F. D., Eixmann, R., Frioud, M., Hågård, A., Iarlori, M., Komguem, L., Kreipl, S., Larchevêque, G., Matthey, R., Mattis, I., Papayannis, A., Persson, R., Rizi, V., Rocadenbosch, F., Rodriguez, J., Schneider, J., Schumacher, R., Shcherbakov, V., Simeonov, V., Wandinger, U., Wang, X., and Wiegner, M. (2002). Lidar intercomparisons on algorithm and system level in the frame of EARLINET. MPI-Report 337, Max-Planck-Institut für Meteorologie, Hamburg.

Matthias, V. and Bösenberg, J. (2002). Aerosol climatology for the planetary boundary layer derived from regular lidar measurements. *Atmospheric Research*, 63:221 – 245.

Matthias, V., Freudenthaler, V., Amodeo, A., Balin, I., Balis, D., Chaykovski, A., Chourdakis, G., Comer´on, A., Delaval, S., de Tomasi, F., Eixmann, R., Hågård, A., Konguem, L., Kreipl, S., Matthey, R., Mattis, I., Rizi, V., Rodrigues, J., and Wang, X. (2003). Aerosol lidar intercomparison in the frame of EARLINET. Part I: Instruments. *Applied Optics (submitted)*.

Mattis, I. (2002). *Aufbau eine Feuchte-Temperatur-Aerosol-Ramanlidars und Methodenentwicklung zur kombinierten Analyse von Trajektorien und Aerosolprofilen (Construction of a humidity temperature aerosol Raman lidar and development of a method for a combined analysis of trajectories and aerosol profiles)*. PhD thesis, Universität Leipzig.

Mattis, I., Müller, D., Ansmann, A., Wandinger, U., Forster, C., and Stohl, A. (2001). Major Saharan-dust outbreak observed with Raman lidar over Leipzig (Germany). *J Aerosol Science*, 32:289–390.

McCormick, M. and Thomason, L. (1995). Atmospheric effects of the Mt. Pinatubo eruption. *Nature*, 373:399–404.

Measures, R. M. (1984). *Laser remote sensing*. John Wiley & Sons, New York.

Mekler, A. A., Böckmann, C., and Sokolovskaia, N. (2000). Particle distribution from spectral Mie-scattering: kernel representation and singular-value spectrum. Technical Report NLD-058, Preprint Series of Universität Potsdam. ISSN 1432-2935.

Monks, P. (2000). A review of the observations and origins of the spring ozone maximum. *Atmos. Environ.*, 34:3545–3561.

Müller, D., Wandinger, U., Althausen, D., and Fiebig, M. (2001). Comprehensive particle characterization from three-wavelength Raman-lidar observations: case study. *Appl. Opt.*, 40:4863–4869.

Müller, D., Wandinger, U., and Ansmann, A. (1999). Microphysical particle parameters from extinction and backscatter lidar data by inversion with regularization: Simulation. *Appl. Opt.*, 38:2358–2368.

Papayannis, A., Balis, D., Chaikovsky, A., Comer´on, A., Eixmann, R., Hågård, A., Iarlori, M., Komguem, L., Mattis, I., Mitev, V., Pandolfi, M. ., Rodrigues, J., Sauvage, L., Simeonov, V., Sobolewski, P., Spinelli, N., De Tomasi, F., Tsaknakis, G., and Wiegner, M. (2002). Two Years of continuous observations of Saharan dust events over the European continent sing a coordinated LIDAR Network in the frame of the EARLINET Project. In *ILRC Lidar Remote Sensing in Atmospheric and Earth Sciences Reviewed and revised papers presented at the 21st International Laser Radar Conference*, pages 309–312.

Pappalardo, G., Bösenberg, J., Balis, D., Boselli, A., Komguem, L., Larchevêque, G., Matthias, V., Mona, L., Mattis, I., Papayannis, A., Perrone, M., and Rizi, V. (2002). EARLINET Measurements of the Aerosol Extinction-to-Backscatter Ratio. In *ILRC Lidar Remote Sensing in Atmospheric and Earth Sciences Reviewed and revised papers presented at the 21st International Laser Radar Conference*, pages 301 –304.

Ramanathan, V., Crutzen, P., Lelieveld, J., Mitra, A. P., Althausen, D., Anderson, J., Andreae, M. O., Cantrell, W., Cass, G. R., Chung, C. E., Clarke, A. D., Coakley, J. A., Collins, W. D., Conant, W. C., Dulac, F., Heintzenberg, J., Heymsfield, A. J., Holben, B., Howell, S., Hudson, J., Jayaraman, A., Kiehl, J. T., Krishnamurti, T. N., Lubin, D., MacFarquhar, G., Novakov, T., Ogren, J. A., Podgorny, I. A., Prather, K., Priestley, K., Prospero, J. M., Quinn, P. K., Rajeev, K., Rasch, P., Rupert, S., Sadourny, R., Satheesh, S. K., Shaw, G. E., Sheridan, P., and Valero, F. P. J. (2001). The Indian Ocean Experiment: An integrated analysis of the climate forcing and effects of the great Indo-Asian haze. *J. Geophys. Res.*, 106:28,371–28,398.

Rosen, J., Kjoome, N., McKenzie, R., and J.Liley (1994). Decay of mount pinatubo aerosol at midlatitudes in the northern and southern hemispheres. *J. of Geoph. Res.*, 99:25733–25739.

Santacesaria, M. F. V., Bais, A., Balis, D., Sarra, A. D., Papayannis, A., and Zerefos, C. (1997). Optical properties of tropospheric aerosols determined by lidar and spectrophotometric measurements (PAUR campaign). *Appl. Opt.*, 36:6875–6886.

Sasano, Y., Browell, E. V., and Ismail, S. (1985). Error caused by using a constant extinction/backscattering ratio in the lidar solution. *Appl. Opt.*, 24:3929–3932.

Shettle, E. P. and Fenn, R. W. (1979). Models for the aerosols of the lower atmosphere and the effects of humidity variations on their optical properties. Env. Res. Papers, No. 676, Air Force Geoph. Lab., Proj. 7670, AFGL-TR-79-0214.

Soriano, C., Baldasano, J. M., Buttler, W. T., and Moore, K. (2001). Circulatory Patterns of Air Pollutants within the Barcelona Air Basin in a Summertime situation: Lidar and Numerical Approaches. *Boundary-Layer Meteorol*, 98(1):33–55.

Stamnes, K., Tsay, S.-T., Wiscombe, W., and Jayaweera, K. (1988). Numerically stable algorithm for discrete-ordinate-method radiative transfer in multiple scattering and emitting layered media. *Appl. Opt.*, 27:2502–2509.

Stohl, A. (1998). Computation, accuracy and applications of trajectories – a review and bibliography. *Atmospheric Environment*, 32:947 – 966.

Stohl, A., Spichtinger-Rakowsky, N., Bonasoni, P., Feldmann, H., Memmesheimer, M., Scheel, H. E., Trickl, T., Hübener, S., Ringer, W., and Mandl, M. (2000). The influence of stratospheric intrusions on Alpine ozone concentrations. *Atmos. Environ.*, 34:1323–1354.

Stohl, A. and Trickl, T. (1999). A textbook example of long-range transport: Simultaneous observation of ozone maxima of stratospheric and North American origin in the free troposphere over Europe. *J. Geophys. Res.*, 104:30445–30462.

Stohl, A., Wotawa, G., Seibert, P., and Kromp-Kolb, H. (1995). Interpolation errors in wind fields as a function of spatial and temporal resolution and their impact on different types of kinematic trajectories. *J. Appl. Meteor.*, 34:2149–2165.

Toll, I. and Baldasano, J. (2000). Photochemical modeling of the barcelona area with highly disaggregated anthropogenic and biogenic emissions. *Atmos Envir*, 34(19):3069–3084.

Trickl, T., Cooper, O. R., Eisele, H., James, P., Mücke, R., and Stohl, A. (2002). Intercontinental transport and its influence on the ozone concentrations over Central Europe -three case studies. *Journal of Geophysical Research (submitted)*.

United States Committee on Extension to the Standard Atmosphere (1976). *U. S. Standard Atmosphere, 1976*. Washington: National Oceanic and Atmospheric Administration.

Vogel, C. R. (2002). *Computational Methods for Inverse Problems*. Siam, Philadelphia.

Wandinger, U. (1998). Multiple-scattering influence on extinction-and backscatter-coefficient measurements with Raman and high-spectral-resolution lidars. *Appl. Opt.*, 37:417–427.

Wandinger, U., Mattis, I., Komguem, L., Vaughan, G., Matthias, V., and Bösenberg, J. (2002a). Air-Mass modification over Europe observed within the European Aerosol Research Lidar Network (EARLINET). In *ILRC Lidar Remote Sensing in Atmospheric and Earth Sciences 21st International Laser Radar Conference*, pages 317–320.

Wandinger, U., Müller, D., Böckmann, C., Althausen, D., Matthias, V., Bösenberg, J., Weiß, V., Fiebig, M., Wendisch, M., Stohl, A., and Ansmann, A. (2002b). Optical and microphysical characterization of biomass-burning and industrial-pollution aerosols from multiwavelength lidar and aircraft measurements. *J. Geophys. Res.*, 107, 10.1029/2000JD000202.

Whiteman, D. (1999). Application of statistical methods to the determination of slope in lidar data. *Appl. Opt.*, 38, 15:3360 – 3369.

Zuev, V. V., Burlakov, V., El'nikov, A., Ivamov, A., Chaikovski, A., and Scherbakov, V. (2001). Processes of long-term relaxation of stratospheric aerosol layer in northern hemisphere midlatitudes after powerful volcanic eruption. *Atm. Env.*, 35:5059–5066.